Electronic Structure and Transport in Molecular and Nanoscale Electronics

by

Xiaofeng Qian

Submitted to the Department of Nuclear Science and Engineering
in partial fulfillment of the requirements for the degree of

Doctor of Philosophy in Nuclear Science and Engineering

at the

MASSACHUSETTS INSTITUTE OF TECHNOLOGY

February 2008

Author .....
Department of Nuclear Science and Engineering
Nov 30, 2007

Certified by .....
Sidney Yip
Professor of Nuclear Science and Engineering
and Professor of Materials Science and Engineering
Thesis Supervisor

Certified by .....
Nicola Marzari
Associate Professor of Materials Science and Engineering
Thesis Reader

Accepted by .....
Jacquelyn C. Yanch
Professor of Nuclear Science and Engineering
Chairman, Department Committee on Graduate Students

Electronic Structure and Transport in Molecular and Nanoscale Electronics

by

Xiaofeng Qian

Submitted to the Department of Nuclear Science and Engineering
on Nov 30, 2007, in partial fulfillment of the
requirements for the degree of
Doctor of Philosophy in Nuclear Science and Engineering

Abstract

Two approaches based on first-principles method are developed to qualitatively and quantitatively study electronic structure and phase-coherent transport in molecular and nanoscale electronics, where both quantum mechanical nature of electrons and dimensionality of systems play the critical roles in their electronic, magnetic and optical properties.

Our first approach is based on Green's function method with *ab initio* quasi-atomic orbitals within Landauer formalism. To efficiently and accurately apply Green's function method, we develop a minimal basis-set of quasiatomic orbitals from plane-wave density functional theory (DFT) results. This minimal basis-set resembles quasi-angular momentum characteristics in solid state systems and it further validates Slater's original idea of linear combinations of atomic orbitals. Based on their *ab initio* tight-binding matrices, the accuracy, efficiency and stability of our scheme are demonstrated by various examples, including band structure, Fermi surface, Mülliken charge, bond order, and quasiatomic-orbitals-projected band structure and quasiatomic-orbitals-projected Fermi surface. Remarkably these quasiatomic orbitals reveal the symmetry and chemical bonding nature of different molecular, surface and solid systems. With this minimal basis-set, quantum conductance and density of states of coherent electron transport are calculated by Green's function method in the Landauer formalism. Several molecular and nanoscale systems are investigated including atomic wires, benzene dithiolate, phenalenyl dithiolate and carbon nanotube with and without different types of defects. Conductance eigenchannel decomposition, phase-encoded conductance eigenchannel visualization, and local current mapping are applied to achieve deeper understandings of electron transport mechanism, including spin dependence, dimensionality dependence, defect dependence, and quantum loop current induced by time-reversal symmetry breaking.

Our second approach naturally arises due to the fact that electron transport is an excited state process. Time-dependent density functional theory (TDDFT) is a fundamental approach to account for dynamical correlations of wave functions and correct band gap in DFT. In our second approach, we mainly focus on the mathematical

formulation and algorithm development of TDDFT with ultrasoft pseudopotentials and projector augmented wave method. Calculated optical absorption spectrum gives correct positions and shapes of excitation peaks compared to experimental results and other TDDFT results with norm-conserving pseudopotentials. Our method is further applied to study Fermi electron transmission through benzene dithiolate molecular junction sandwiched by two gold chains. It is first verified that group velocity of Fermi electron in the gold chain obtained by TDDFT agrees with that from band structure theory. Then under rigid band and zero bias approximations, a tiny Fermi electron wave packet from the chain is injected into the molecular junction. Transmission coefficient evaluated after the scattering process is around 5%. This is in agreement with the result from Green's function method. The two methods also show similar characteristic propagation channel. This nice agreement verifies that Green's function approach based on DFT reaches the TDDFT result without dynamical electron correlations in the linear response region.

With further development, our quasiatomic orbitals can serve as a minimal basis-set to combine non-equilibrium Green's function and TDDFT together with GW quasi-particle corrections. The unified method will provide a more accurate and efficient way to explore various molecular and nanoscale electronic devices such as chemical sensor, electromechanical device, magnetic memory, and optical electronics.

Thesis Supervisor: Sidney Yip
Title: Professor of Nuclear Science and Engineering
and Professor of Materials Science and Engineering

Acknowledgments

I would like to express my deepest thanks to my advisor and mentor, Professor Sidney Yip, for his unlimited support, inspiration and encouragement in the past five years. His great passion and deep insight on scientific research are invaluable to me. More importantly, his great support as a mentor guided me through the years at MIT in science and life.

I would like to thank Professor Ju Li for his endless patience, outstanding instruction, and uncompromisingly high academic standard for which he motivated me to work on this interesting thesis project. Without the countless discussions with him, I could not go this far successfully. Hopefully his ability to identify the essence of scientific problems will pass on me.

I have also benefited a lot from the members of my thesis committee, Professors Nicola Marzari and Troy Van Voorhis. Their invaluable suggestions and deep insights lead my work to a next higher level after each meeting and discussion.

Many thanks to our MMM group members for their help and support that made my graduate experience a pleasant one. Professor Xi Lin at Boston University, Dr. Akihiro Kushima, Dr. Clemens Först, and Professor Ting Zhu at Georgia Institute of Technology provided so much help and insightful discussions about fundamental mechanism of electronic and atomistic transport. I am very grateful to Dr. Jacob Eapen, Dr. Robert Boyer, Dr. Emilio Silva, Dr. Mukul Kabir, Timothy Lau, and Paul Monasterio, and visiting scientist Dr. Satoshi Izumi. I would also like to thank my collaborators, Liang Qi at University of Pennsylvania, Professor Cai-Zhuang Wang and Professor Kai-Ming Ho at AMES lab, for their technical and scientific support.

Last, but by no means least, I would like to express my heartfelt appreciation to my parents, my wife Shuning, and our lovely daughter Rosanna, for their deepest and everlasting love and care. I wish to thank my wife Shuning, who is the most precious gift that MIT has given to me. My research work is obviously much less significant than the love we share, and even less important than every meal that she cooked at all the late nights.

Contents

List of Figures

List of Tables

Chapter 1

Electronic structure of solids

1.1 Many-body problem of atoms

The nature never stops astonishing us from the very big, such as the universe, to the very small, such as atoms. It is due to the fact that the physical world consists of numerous interacting many-body systems over different length and time scales. The complexity of the interacting many-body problem at different scale gives rise to the emergence of new types of phenomena and patterns.

A simple example is the emergence of quantum mechanics. Although classical mechanics had been established for a long time, it was not until the beginning of the last century that people became aware of a whole new world - the world of quantum mechanics, where wave nature of particles such as electrons, plays an important role in both ground state and excited state properties. This small world has become the playground of condensed matter physics, modern chemistry, nano-materials science, and etc. Most problems in the above areas are many-body problems involving both nuclei and electrons. Interacting many-body system of nuclei and electrons is governed by Schrödinger equation, which is the central equation of quantum mechanics. For a given set of nuclei at position $\mathbf{R} \equiv \{\mathbf{R}_I\}$ and electrons at position $\mathbf{r} \equiv \{\mathbf{r}_i\}$, the Schrödinger equation of the system without considering the relativistic effect is

$$\hat{H}\Psi(\mathbf{r}, \mathbf{R}) = E\Psi(\mathbf{r}, \mathbf{R}), \tag{1.1}$$

where $\hat{H}$ is the Hamiltonian operator, E is total energy and $\Psi(\mathbf{r}, \mathbf{R})$ is many-body wave-function of all nuclei and electrons. $\hat{H}$ contains their kinetic energy and interacting potential operators,

$$\hat{H} = \hat{H}_e + \hat{H}_n + \hat{H}_{ne}. \tag{1.2}$$

Without taking account of external electric and magnetic fields, electron Hamiltonian $\hat{H}_e$, nucleus Hamiltonian $\hat{H}_n$ and electron-nucleus interaction Hamiltonian $\hat{H}_{en}$ are defined in the following equations

$$\hat{H}_e(\mathbf{r}) = \hat{T}_e + \hat{V}_e = -\sum_{i=1}^{N_e} \frac{\hbar^2}{2m}\nabla^2 + \sum_{i=1}^{N_e}\sum_{j>i}^{N_e} \frac{e^2}{|\mathbf{r}_i - \mathbf{r}_j|} \tag{1.3}$$

$$\hat{H}_n(\mathbf{R}) = \hat{T}_n + \hat{V}_n = -\sum_{I=1}^{N_n} \frac{\hbar^2}{2M_I}\nabla^2 + \sum_{I=1}^{N_n}\sum_{J>I}^{N_n} \frac{Z_I Z_J e^2}{|\mathbf{R}_I - \mathbf{R}_J|} \tag{1.4}$$

$$\hat{H}_{en}(\mathbf{r}, \mathbf{R}) = \hat{V}_{en} = -\sum_{I=1}^{N_n}\sum_{i=1}^{N_e} \frac{Z_I e^2}{|\mathbf{R}_I - \mathbf{r}_i|}. \tag{1.5}$$

$\hbar$, m, e, M_I, Z_I, N_e and N_n are Dirac constant, electron mass, electron charge, nucleus mass, nucleus charge, number of electrons and number of nuclei respectively. The opposite sign of electron and nucleus's charges are taken into account by the minus sign in Eq.(1.5). Eq.(1.1) looks very simple at first glance. It is nothing else but kinetic energy and Coulomb interaction. However, currently the largest number of many-body system that people can solve is no more than one hundred. To accurately solve this equation for many-particle system at larger scale without any approximation is extremely challenging. Therefore, to solve Eq.(1.1) efficiently with reasonable accuracy, various physical approximations have to be introduced.

1.1.1 Born-Oppenheimer approximation

The first approximation is Born-Oppenheimer (BO) approximation[1, 2] or adiabatic approximation. Since nucleus mass M_I is much larger (more than 1,800 times) than electron mass m and nucleus velocity is about $(m/M_I)^{3/4}$ of Fermi electron velocity, nucleus motion and electron motion can be often treated as two decoupled motions.

Under this approximation, electrons adjust their positions *adiabatically* with respect to nuclei's configuration, and thus many-body wave function can be written as the product of wave functions of nuclei and electrons. That is,

$$\Psi(\mathbf{r},\mathbf{R}) = \sum_n \Phi_n(\mathbf{R})\Psi_{en}(\mathbf{r},\mathbf{R}), \tag{1.6}$$

where $\Phi_n(\mathbf{R})$ and $\Psi_{en}(\mathbf{r},\mathbf{R})$ describe the states of nuclei and electrons respectively, subject to the orthogonality condition,

$$\langle\Phi_n|\Phi_m\rangle = \delta_{n,m}, \tag{1.7}$$

$$\langle\Psi_{en}|\Psi_{em}\rangle = \delta_{n,m}. \tag{1.8}$$

With Eq.(1.6), (1.7) and (1.8) it is easy to prove that many-body wave function is normalized to be 1, which means total probability to find the given set of nuclei and electrons in the whole space is one. Since operators $\hat{H}_e$ and $\hat{H}_{en}$ only affect the electronic wave function $\Psi_{en}(\mathbf{r},\mathbf{R})$, Eq.(1.1) can be re-written as

$$\begin{aligned} E\Psi(\mathbf{r},\mathbf{R}) &= \big(\hat{H}_e + \hat{H}_n + \hat{H}_{en}\big)\Psi(\mathbf{r},\mathbf{R}) & (1.9)\\ &= \hat{H}_n\Psi(\mathbf{r},\mathbf{R}) + \sum_n \Phi_n(\mathbf{R})\Big[\big(\hat{H}_e + \hat{H}_{ne}\big)\Psi_{en}(\mathbf{r},\mathbf{R})\Big] & (1.10)\end{aligned}$$

Assuming E_{en} is eigen-energy of electronic wave function $\Psi_{en}(\mathbf{r},\mathbf{R})$ subject to the Hamiltonian operator $\hat{H}_e + \hat{H}_{en}$, we then have a set of equations to replace Eq. (1.1),

$$\begin{aligned} \sum_n \big(\hat{H}_n + E_{en} - E\big)\Phi_n(\mathbf{R})\Psi_{en}(\mathbf{r},\mathbf{R}) &= 0, & (1.11)\\ \big(\hat{H}_e + \hat{H}_{en} - E_{en}\big)\Psi_{en}(\mathbf{r},\mathbf{R}) &= 0. & (1.12)\end{aligned}$$

In a more simple form they are

$$\begin{aligned} E &= \sum_n E_n, & (1.13)\\ \big(\hat{H}_n + E_{en}\big)\Phi_n(\mathbf{R}) &= E_n\Phi_n(\mathbf{R}), & (1.14)\end{aligned}$$

$$\left(\hat{H}_e + \hat{H}_{en}\right)\Psi_{en}(\mathbf{r},\mathbf{R}) \;=\; E_{en}\Psi_{en}(\mathbf{r},\mathbf{R}), \tag{1.15}$$

where E_n is eigen-energy of nuclear wave function $\Phi_n(\mathbf{R})$.

With the BO approximation, the original Schrödinger equation for interacting many-body system including nuclei and electrons is transformed into a set of decoupled equations of motion for nuclei and electrons respectively. It greatly simplifies the original problem and the effect of a given set of nuclei at $\{\mathbf{R}_I\}$ has been incorporated into electronic Hamiltonian as a fixed set of parameters. However, Eq. (1.15) still tells us nothing about how to solve this equation efficiently and accurately. The remaining problem is still a many-electron system. Meanwhile, the Pauli exclusion principle for fermions needs to be considered.

1.1.2 Fock space for N-identical-particle system

To include the Pauli exclusion principle, we need to first establish the Fock space - the Hilbert space of N-identical-particle system.

Identical particles: bosons and fermions

The objects here that we deal with are atoms and electrons. They are identical particles which can not be distinguished from each other by their intrinsic properties, such as mass, charge and spin. That means any physical measurement on many-body state Ψ of identical particles and permuted (exchanged) many-body state $\hat{P}_{ij}\Psi$ will have the same results. Here permutation operator $\hat{P}_{ij}$ is defined as exchange operation on the positions of particle i and particle j,

$$\hat{P}_{ij}\Psi(\mathbf{r}_1,\mathbf{r}_2,\cdots,\mathbf{r}_i,\mathbf{r}_j,\cdots,\mathbf{r}_N) = \Psi(\mathbf{r}_1,\mathbf{r}_2,\cdots,\mathbf{r}_j,\mathbf{r}_i,\cdots,\mathbf{r}_N). \tag{1.16}$$

The above statement implies that Hamiltonian $\hat{H}$ of many-body system and permutation operator $\hat{P}_{ij}$ commute with each other: $[\hat{H},\hat{P}_{ij}] = 0$. Many-body state Ψ is

eigenstate of $\hat{H}$ and $\hat{P}_{ij}$ for any i and j simultaneously,

$$\hat{P}_{ij}\Psi(\mathbf{r}_1, \mathbf{r}_2, \cdots, \mathbf{r}_i, \mathbf{r}_j, \cdots, \mathbf{r}_N) = p_{ij}\Psi(\mathbf{r}_1, \mathbf{r}_2, \cdots, \mathbf{r}_j, \mathbf{r}_i, \cdots, \mathbf{r}_N), \tag{1.17}$$

where p_{ij} is eigenvalue of operator $\hat{P}_{ij}$. It is easy to see that many-body state after two successive permutations will be the same as original many-body state,

$$\hat{P}_{ij}^2\Psi = p_{ij}^2\Psi = \Psi, \tag{1.18}$$

which gives

$$p_{ij} = \pm 1. \tag{1.19}$$

Therefore, p_{ij} divides identical particles into two groups,

$$p_{ij} = +1: \quad \hat{P}_{ij}\Psi = +\Psi \quad \text{(bosons)}, \tag{1.20}$$

$$p_{ij} = -1: \quad \hat{P}_{ij}\Psi = -\Psi \quad \text{(fermions)}. \tag{1.21}$$

The antisymmetry of fermion wave function in the above equation gives rise to the Pauli exclusion principle.

Fock space for bosons and fermions

Up to now we are still dealing with many-body wave function Ψ as a function of all the space spanned by N interacting identical particles. However, a good starting point will be a system consisting of N non-interacting particles. The state of each identical particle is assumed to be given by single-particle Hilbert space - an element in a Hilbert space $\mathcal{H}$. The Fock-space of N identical particles is the Hilbert space to describe the space spanned by an unknown number of identical particles. Then the Fock space is the direct sum of tensor products of all N single-particle Hilbert spaces $\mathcal{H}$,

$$\mathcal{F}_\nu = \bigoplus_{n=0}^{N} S_\nu \mathcal{H}^{\otimes n}, \tag{1.22}$$

where S_ν is either the symmetrization operator for bosons with $\nu = +1$ or the anti-symmetrization operator for fermions with $\nu = -1$. A state in Fock space, for example, can be written as

$$|\Psi\rangle = |\phi_1, \phi_2, \cdots, \phi_N\rangle, \tag{1.23}$$

It is a good basis for bosonic system, but it is not a good basis to represent N-fermion system since permutation of any two particles in the above many-body state will not give anti-symmetric wave function. However the Slater determinant of all single-particle states can fulfill the requirement of the Pauli exclusion principle. The more elegant way to describe the Fock space of fermions is to use second quantization representation.

1.1.3 Second quantization

The original quantum mechanics is expressed in first quantization, where particles are treated as quantum wave functions and their surrounding environment is taken to be classical field. However, it is much more convenient to describe the interacting many-body fermion system and their quantum statistics in second quantization.

In second quantization, the environment of many-body system is further quantized. Classical fields in first quantization become quantum operators acting on quantum state to create new particles or destroy existing particles in the system. Quantum state of the vacuum is often denoted by $|0\rangle$, which stands for a state containing zero particle. Vacuum state is the starting point of any other quantum state which contains particles. Quantum state of an interacting many-body system is obtained through creation or annihilation of particles with single-particle creation operator $a_i^\dagger$ and annihilation operator a_i,

$$|n_1, n_2, \cdots\rangle = a_1^\dagger a_2^\dagger \cdots |0\rangle. \tag{1.24}$$

which describes number of n_1 particles in single-particle state $|1, 0, 0, 0 \cdots\rangle$, number of n_2 particles in single-particle state $|0, 1, 0, 0 \cdots\rangle$ and so on. Quantum statistics

of bosons and fermions are embedded in the commutation and anti-commutation relations of creation and annihilation operators. For bosons, $a_i^\dagger$ and a_i commute with each other

$$[a_i, a_j^\dagger] = a_i a_j^\dagger - a_j^\dagger a_i = \delta_{ij}, \tag{1.25}$$

while for fermions two operators anti-commute with each other

$$\{a_i, a_j^\dagger\} = a_i a_j^\dagger + a_j^\dagger a_i = \delta_{ij}. \tag{1.26}$$

The number of particles in state i is

$$\hat{N} = \sum a_i^\dagger a_i. \tag{1.27}$$

For fermions n_i is either 0 or 1 because single-particle state $\phi(\mathbf{r}_i\sigma_i)$ can at most hold one fermion (σ_i is singe particle spin state) by the Pauli exclusion principle.

One way to construct an N-electron wave function which satisfies the Pauli exclusion principle is the determinant of single-particle wave functions $\phi(\mathbf{r}_i\sigma_i)$. In first quantization notation, it is

$$\Psi(\mathbf{r}_1\sigma_1, \mathbf{r}_2\sigma_2, \cdots, \mathbf{r}_N\sigma_N) = \frac{1}{\sqrt{N!}}(-1)^P \sum_P P[\phi(\mathbf{r}_1\sigma_1)\phi(\mathbf{r}_2\sigma_2)\cdots\phi(\mathbf{r}_N\sigma_N)], \tag{1.28}$$

where P is permutation operator defined in Eq.(1.16). In second quantization, however, we never need to explicitly sum over all the possible permutations of single-particle state. Similar to Eq. (1.24), an N-electron wave function is written as

$$|n_1, n_2, \cdots, n_N\rangle = a_1^\dagger a_2^\dagger \cdots a_N^\dagger |0\rangle. \tag{1.29}$$

The states described in above second quantization notation form the basis vectors of Fock space $\mathcal{F}_\nu$ of N-fermion system.

Once second quantization is applied, immediately Hamiltonian operator involving multi-body interactions can be represented by annihilation and creation operators. For example, one-body and two-body Hamiltonian operators are simply reformulated

into

$$\hat{H}_1 = \sum_{i,j} \langle i|\hat{H}_1|j\rangle a_i^\dagger a_j \tag{1.30}$$

and

$$\hat{H}_2 = \frac{1}{2} \sum_{i,j,k,l} \langle ij|\hat{H}_2|kl\rangle a_i^\dagger a_j^\dagger a_l a_k. \tag{1.31}$$

It is obvious that Hamiltonian acting on electron wave function in Eq. (1.15) only contains one-body and two-body Hamiltonian operators. *From now on, we use $\hat{H}_e$ as full electronic Hamiltonian to represent ($\hat{H}_e + \hat{H}_{en}$) in Eq. (1.15).* Then we have the following new electronic Hamiltonian of interacting N-electron system in the second quantization form

$$\hat{H}_e = \sum_{i,j} \langle i|\hat{H}_1|j\rangle a_i^\dagger a_j + \frac{1}{2} \sum_{i,j,k,l} \langle ij|\hat{H}_2|kl\rangle a_i^\dagger a_j^\dagger a_l a_k, \tag{1.32}$$

where

$$\hat{H}_1 = \hat{T}_1 + \hat{V}_{en}(\mathbf{r}_1) = -\frac{\hbar^2}{2m}\nabla^2 - \sum_{I=1}^{N_n} \frac{Z_I e^2}{|\mathbf{R}_I - \mathbf{r}_1|}, \tag{1.33}$$

$$\hat{H}_2 = \hat{V}_{ee}(\mathbf{r}_1, \mathbf{r}_2) = \frac{e^2}{|\mathbf{r}_1 - \mathbf{r}_2|}. \tag{1.34}$$

In momentum space single-particle plane-wave states will diagonalize the electronic kinetic energy,

$$\phi_k(\mathbf{r}) = e^{-i\mathbf{kr}}/\sqrt{V}. \tag{1.35}$$

Then the field creation operator which creates an electron at $\mathbf{r}$ with spin σ is defined as

$$\hat{\phi}_\sigma^\dagger(\mathbf{r}) = \sum_{\mathbf{k}} e^{-i\mathbf{kr}} a_{\mathbf{k}\sigma}^\dagger/\sqrt{V}. \tag{1.36}$$

1.2 Hartree-Fock theory

With second quantization of many-body electronic Hamiltonian and wave function, we can continue to solve the Schrödinger equation of N-electron quantum system

with additional approximations beside the BO approximation.

1.2.1 Hartree approximation

The first straightforward assumption in addition to the BO approximation, known as Hartree approximation, is that the ground state of many-body system is the same as the ground state of non-interacting system. Then the original interacting many-body problem is approximately mapped to a non-interacting many one-body problem and each single-particle state feels the averaged interacting potential from all the other single-particle states.

First we only consider one-body Hamiltonian $\hat{H}_i = \hat{H}_1(\mathbf{r}_i\sigma_i)$ term in total electronic Hamiltonian in Eq. (1.32), then we have

$$\hat{H}_e \approx \sum_i \hat{H}_i \tag{1.37}$$

and

$$\sum_i \hat{H}_i \Psi(\mathbf{r}_1\sigma_1, \mathbf{r}_2\sigma_2, \cdots, \mathbf{r}_N\sigma_N) = E\Psi(\mathbf{r}_1\sigma_1, \mathbf{r}_2\sigma_2, \cdots, \mathbf{r}_N\sigma_N). \tag{1.38}$$

Consequently the solution of many-body wave function $\Psi(\mathbf{r}_1\sigma_1, \mathbf{r}_2\sigma_2, \cdots, \mathbf{r}_N\sigma_N)$, called Hartree wave function, is the product of all single-particle wave functions,

$$\Psi(\mathbf{r}_1\sigma_1, \mathbf{r}_2\sigma_2, \cdots, \mathbf{r}_N\sigma_N) = \phi_1(\mathbf{r}_2\sigma_2)\ \phi_2(\mathbf{r}_2\sigma_2) \cdots \phi_N(\mathbf{r}_N\sigma_N). \tag{1.39}$$

Therefore, many-electron Schrödinger equation Eq. (1.38) is reformulated into single-electron Schrödinger equation,

$$\hat{H}_i\phi_i(\mathbf{r}_i\sigma_i) = E_i\phi_i(\mathbf{r}_i\sigma_i). \tag{1.40}$$

Then total energy including both one-body interaction term $\hat{H}_1$ and two-body interaction term $\hat{H}_2$ is written as

$$E = \sum_i \langle\phi_i|\hat{H}_1|\phi_i\rangle + \frac{1}{2}\sum_{i,j}\langle\phi_i\phi_j|\hat{H}_2|\phi_i\phi_j\rangle \tag{1.41}$$

In second quantization notation, it is

$$E = \sum_i \langle i|\hat{H}_1|i\rangle\langle a_i^\dagger a_i\rangle + \frac{1}{2}\sum_{i,j}\langle ij|\hat{H}_2|ij\rangle\langle a_j^\dagger a_j\rangle\langle a_i^\dagger a_i\rangle, \tag{1.42}$$

$$= \sum_i \langle i|\hat{H}_1|i\rangle n_i + \frac{1}{2}\sum_{ij(i\neq j)}\langle ij|\hat{H}_2|ij\rangle n_j n_i. \tag{1.43}$$

From the variational principle, the minimum of total electronic energy is the energy at stationary point in the variational space,

$$\delta\Big[E - \sum_i E_i(\langle\phi_i|\phi_i\rangle - 1)\Big] = 0, \tag{1.44}$$

where E_i is Lagrangian multiplier and single-particle state ϕ_i satisfies orthogonality condition $\langle\phi_i|\phi_j\rangle = \delta_{ij}$. It is worth to mention that E_i in Eq. (1.44) is different from E_i in Eq. (1.40) which only considers one-body interaction term. Then Hartree equation for single-particle state ϕ_i is written as

$$\Big(\hat{H}_1 + \sum_{j(j\neq i)} n_j\langle\phi_j|\hat{H}_2|\phi_j\rangle\Big)|\phi_i\rangle = E_i|\phi_i\rangle. \tag{1.45}$$

1.2.2 Hartree-Fock approximation

Hartree equation Eq. (1.45) faces a fundamental problem that many-electron wave function obtained from the product of single-electron states is not anti-symmetric with respect to the interchange of any two single-electron states. One simple solution to this problem is to use the Slater determinant of single-particle states $\phi(\mathbf{r}_i\sigma_i)$ described in Eq.(1.28), which automatically satisfies the requirement of anti-symmetry. Then the expectation value of electronic Hamiltonian $\hat{H}_e$ is

$$E = \Big\langle\Psi(\mathbf{r}_1\sigma_1, \mathbf{r}_2\sigma_2, \cdots, \mathbf{r}_N\sigma_N)\Big|\hat{H}_e\Big|\Psi(\mathbf{r}_1\sigma_1, \mathbf{r}_2\sigma_2, \cdots, \mathbf{r}_N\sigma_N)\Big\rangle \tag{1.46}$$

$$= \sum_i \langle i|\hat{H}_1|i\rangle n_i + \frac{1}{2}\sum_{ijkl}\langle ij|\hat{H}_2|kl\rangle\langle a_i^\dagger a_j^\dagger a_l a_k\rangle. \tag{1.47}$$

Since a_k and a_l will only affect $|n_k\rangle$ and $|n_j\rangle$ respectively, the expectation value of four creation and annihilation operators can be evaluated,

$$\langle a_i^\dagger a_j^\dagger a_l a_k\rangle = \langle n_k n_l|a_i^\dagger a_j^\dagger a_l a_k|n_k n_l\rangle = (\delta_{jl}\delta_{ik} - \delta_{il}\delta_{jk})n_k n_l \tag{1.48}$$

Therefore, the Hartree-Fock energy is rewritten into

$$\begin{aligned} E &= \sum_i \langle i|\hat{H}_1|i\rangle n_i + \frac{1}{2}\sum_{ijkl}\langle ij|\hat{H}_2|kl\rangle(\delta_{jl}\delta_{ik} - \delta_{il}\delta_{jk})n_l n_k & (1.49)\\ &= \sum_i \langle i|\hat{H}_1|i\rangle n_i + \frac{1}{2}\sum_{ij}\Big(\langle ij|\hat{H}_2|ij\rangle - \langle ij|\hat{H}_2|ji\rangle\Big)n_j n_i. & (1.50)\end{aligned}$$

From the comparison between Eq.(1.50) and Eq.(1.43), it is clear to us that, beside one-body interaction Hamiltonian $\langle i|\hat{H}_1|i\rangle$ and two-body repulsive Coulomb interaction Hamiltonian $\langle ij|\hat{H}_2|ij\rangle$, Hartree-Fock energy contains another important term — exchange interaction $\langle ij|\hat{H}_2|ji\rangle$. Notice that the Coulombic kernel $e^2/|\mathbf{r}_1 - \mathbf{r}_2|$ in exchange interaction only involves the distance between two particles. With explicit expression of single-particle wave function in both position space and spin space $\phi_i(\mathbf{r}\sigma) = \varphi_i(\mathbf{r})\chi_i(\sigma)$, we can further simplify the exchange interaction Hamiltonian

$$\langle ij|\hat{H}_2|ji\rangle = \langle\varphi_i\varphi_j|\hat{H}_2|\varphi_j\varphi_i\rangle\langle\chi_i|\chi_j\rangle = \delta_{\sigma_i\sigma_j}\langle\varphi_i\varphi_j|\hat{H}_2|\varphi_j\varphi_i\rangle = \delta_{\sigma_i\sigma_j}\langle ij|\hat{H}_2|ji\rangle, \tag{1.51}$$

which means exchange interaction only have effect on the interchange of two electrons with the *same* spin. Therefore, Hartree-Fock energy is

$$\begin{aligned} E &= \sum_i \langle i|\hat{H}_1|i\rangle n_i + \frac{1}{2}\sum_{ij}\Big(\langle ij|\hat{H}_2|ij\rangle - \delta_{\sigma_i\sigma_j}\langle ij|\hat{H}_2|ji\rangle\Big)n_j n_i, & (1.52)\\ &= \sum_i \langle i|\hat{H}_1|i\rangle n_i + \frac{1}{2}\sum_{ij}\Big(U_{ij} - \delta_{\sigma_i\sigma_j}J_{ij}\Big)n_j n_i. & (1.53)\end{aligned}$$

Here U_{ij} and J_{ij} are Coulomb energy and exchange energy respectively,

$$U_{ij} = \langle ij|\hat{H}_2|ij\rangle, \tag{1.54}$$

$$J_{ij} = \langle ij|\hat{H}_2|ji\rangle. \tag{1.55}$$

Similar to the derivation of Hartree equation - Eq.(1.45), we apply variational principle to obtain Hartree-Fock equation for Hartree-Fock Hamiltonian and single-particle states,

$$\Big(\hat{H}_1 + \sum_j n_j \langle\phi_j|\hat{H}_2|\phi_j\rangle\Big)|\phi_i\rangle - \sum_j \delta_{\sigma_i\sigma_j} n_j \langle\phi_j|\hat{H}_2|\phi_i\rangle|\phi_j\rangle = E_i|\phi_i\rangle. \tag{1.56}$$

Remarkably, Hartree-Fock approximation treats exchange interaction between like-spin particles exactly. More importantly this exchange effect is attractive with negative energy, which means electrons with the same spin will attract each other. To clearly see it, let us do more analysis on the second and third terms of Eq.(1.56) in first quantization. The second term $\sum_j n_j \langle\phi_j|\hat{H}_2|\phi_j\rangle|\phi_i\rangle$ is pure repulsive Coulomb interaction due to the presence of electron density from each single-particle state $|j\rangle$ with $\rho_i^{\mathrm{C}}(\mathbf{r}') = \sum_j n_j \phi_j^*(\mathbf{r}')\phi_j(\mathbf{r}')$, while the third term $-\sum_j \delta_{\sigma_i\sigma_j} n_j \langle\phi_j|\hat{H}_2|\phi_i\rangle|\phi_j\rangle$ introduces an extra charge density due to exchange of two like-spin particles. Similar to $\rho_i^{\mathrm{C}}(\mathbf{r}')$, we can reformulate the third term to see this exchange charge density explicitly,

$$\begin{aligned} -\sum_j \delta_{\sigma_i\sigma_j} n_j \langle\phi_j|\hat{H}_2|\phi_i\rangle|\phi_j\rangle &= -\sum_j \delta_{\sigma_i\sigma_j} n_j \frac{\langle\phi_i|}{\langle\phi_i|}\langle\phi_j|\hat{H}_2|\phi_i\rangle\frac{|\phi_i\rangle}{|\phi_i\rangle}|\phi_j\rangle & (1.57)\\ &= -\sum_j \delta_{\sigma_i\sigma_j} n_j \left\langle \frac{\phi_i\phi_j}{\phi_i}\middle|\hat{H}_2\middle|\frac{\phi_j\phi_i}{\phi_i}\right\rangle\middle|\phi_i\Big\rangle, & (1.58)\end{aligned}$$

therefore, exchange density for single-particle $|i\rangle$ is

$$\rho_i^{\mathrm{X}}(\mathbf{r},\mathbf{r}') = -\sum_j \delta_{\sigma_i\sigma_j} n_j \frac{\phi_i^*(\mathbf{r})\phi_j^*(\mathbf{r}')\phi_j(\mathbf{r})\phi_i(\mathbf{r}')}{\phi_i^*(\mathbf{r})\phi_i(\mathbf{r})}. \tag{1.59}$$

Here are several remarks for the above results:

1. When $j = i$, the term in $\rho_i^{\mathrm{X}}(\mathbf{r},\mathbf{r}')$ will *exactly cancel* the term in $\rho_i^{\mathrm{C}}(\mathbf{r})$, therefore Hartree-Fock approximation automatically avoids unphysical self-interaction error.

2. In Hartree-Fock approximation, each single-particle state $|i\rangle$ "sees" the same

Coulomb interaction potential and *different* exchange potential since the latter depends on the position of the state $|i\rangle$.

3. It is easy to show that integration of both Coulomb charge density and exchange charge density over $\mathbf{r}'$ will be equal to -1,

$$\int \rho_i^{\mathrm{C}}(\mathbf{r}')d\mathbf{r}' = \int \rho_i^{\mathrm{X}}(\mathbf{r},\mathbf{r}')d\mathbf{r}' = -1. \tag{1.60}$$

$\rho_i^{\mathrm{X}}(\mathbf{r},\mathbf{r}')$ (negative sign) attracts particles with the same spin and creates an exchange hole, while Coulomb charge density $\rho_i^{\mathrm{C}}(\mathbf{r}')$ (positive sign) is always repulsive and it keeps electrons away from each other no matter if they are in the same spin state or not. The probability to find two electrons in any two single-particle states at the same position $\mathbf{r}$ and the same spin σ is zero. This is given by

$$\left[\rho_{ij}^{\mathrm{C}}(\mathbf{r}') + \rho_{ij}^{\mathrm{X}}(\mathbf{r},\mathbf{r}')\right]\Big|_{\mathbf{r}=\mathbf{r}',\sigma_i=\sigma_j} \tag{1.61}$$

$$= \left[n_j\phi_j^*(\mathbf{r}')\phi_j(\mathbf{r}') - \delta_{\sigma_i\sigma_j}n_j\frac{\phi_i^*(\mathbf{r})\phi_j^*(\mathbf{r}')\phi_j(\mathbf{r})\phi_i(\mathbf{r}')}{\phi_i^*(\mathbf{r})\phi_i(\mathbf{r})}\right]\Big|_{\mathbf{r}=\mathbf{r}',\sigma_i=\sigma_j} \tag{1.62}$$

$$= n_j\phi_j^*(\mathbf{r})\phi_j(\mathbf{r}) - n_j\phi_j^*(\mathbf{r})\phi_j(\mathbf{r}) \tag{1.63}$$

$$= 0. \tag{1.64}$$

The above result is very important since it points out that under Hartree-Fock approximation we will have an exchange hole around the electron at position $\mathbf{r}$ for filling other like-spin electrons nearby. This exactly comes from the Pauli exclusion principle.

4. In Hartree-Fock approximation the Coulomb energy term is always positive and increases eigen-energy E_i, while the exchange term is always negative and lowers eigen-energy E_i.

With the use of $\rho_i^{\mathrm{X}}(\mathbf{r},\mathbf{r}')$ and $\rho_i^{\mathrm{C}}(\mathbf{r})$, we have a more simplified version of Hartree-Fock equation

$$\left[\hat{T}+\hat{V}_{en}+\hat{V}_{ee,i}^{\mathrm{HF}}\right]\Big|\phi_i\Big\rangle = E_i\Big|\phi_i\Big\rangle, \tag{1.65}$$

where $\hat{V}_{ee,i}^{\mathrm{HF}}$ is defined as

$$V_{ee,i}^{\mathrm{HF}}(\mathbf{r}) = \int d\mathbf{r}' \frac{\rho_i^{\mathrm{C}}(\mathbf{r}')+\rho_i^{\mathrm{X}}(\mathbf{r},\mathbf{r}')}{|\mathbf{r}-\mathbf{r}'|}. \tag{1.66}$$

Eq.(1.66) explicitly shows that original complicated electron-electron interaction Hamiltonian in Eq.(1.56) can be viewed as orbital-dependent effective electron-electron potential. However it will be more convenient for practical calculations to have an orbital-independent effective potential. To achieve this goal, Slater [3] proposed an averaged exchange charge density $\bar{\rho}^{\mathrm{X}}(\mathbf{r},\mathbf{r}')$ for single-particle state $|i\rangle$ at position $\mathbf{r}$ by averaging $\rho_i^{\mathrm{X}}(\mathbf{r},\mathbf{r}')$ with charge density of state $|i\rangle$ at position $\mathbf{r}$ as the weighting factor

$$\bar{\rho}^{\mathrm{X}}(\mathbf{r},\mathbf{r}') = \frac{\sum_i \rho_i(\mathbf{r})\rho_i^{\mathrm{X}}(\mathbf{r},\mathbf{r}')}{\sum_i \rho_i(\mathbf{r})} \tag{1.67}$$

with single-particle density $\rho_i(\mathbf{r}) = \phi_i^*(\mathbf{r})\phi_i(\mathbf{r})$. Then the new effective potential for state $|i\rangle$ in the modified Hartree-Fock equation does not explicitly depend on state $|i\rangle$.

It is important to notice that the sum of all the eigen-energies E_i of occupied single-particle state $|i\rangle$ is *not* equal to total energy $E(N)$ of N-electron system with $N = \sum_i n_i$. Instead they are related by the following equation

$$E(N) = \sum_i n_i E_i - \frac{1}{2}\sum_{ij}\Big(U_{ij} - \delta_{\sigma_i\sigma_j}J_{ij}\Big)n_j n_i, \tag{1.68}$$

with

$$E_i = \langle i|\hat{H}_1|i\rangle + \sum_j \Big(U_{ij} - \delta_{\sigma_i\sigma_j}J_{ij}\Big)n_j. \tag{1.69}$$

The physical meaning of E_i is given by Koopmans' theorem by adding or subtracting one electron in Eq.(1.53). It simply states that the energy of Hartree-Fock single-particle state, E_i, is the energy needed to add an electron into the original unoccupied

state $|i\rangle$ or remove one from the original occupied state $|i\rangle$.

From the above derivations, we can see that Hartree-Fock approximation has exactly included exchange interaction between electrons with the *same* spin. Hartree-Fock wave functions in the Slater determinant automatically satisfies anti-symmetric property with any interchange between two electrons. Exchange effect can be viewed as one type of correlations. However, other important correlations are not considered in Hartree-Fock approximation. For example, there is no appropriate treatment about the interaction between two electrons with *opposite* spins beside the pure Coulomb interaction.

1.2.3 Feynman diagram view of Hartree-Fock method

Up to this section, we have applied Born-Oppenheimer approximation and Hartree-Fock approximation to solve interacting many-electron problem. Mathematically under these approximations we have mapped interacting many-body problem onto non-interacting many one-body problem and that leads us to solve electronic Hamiltonian for single-particle state with nuclear Coulomb potential and other single-electron states as the parameters. However, it is worth to re-visit Hartree-Fock approximation by using Feynman diagram, which can give us a more direct view of many-body problem.

In general we can use perturbation theory to solve many-body problem step by step. We can extract those most important perturbation terms by physical intuition and use Green's function to evaluate one by one. This method will be very hard when dealing with high-order perturbations. Feynman diagram developed by Richard Feynman, however, gives an extremely simple way to evaluate perturbations and it is a pictorial interpretation of perturbative terms of scattering phenomena in quantum field theory.

Three pictures

Before going into the details of Green's function and Feynman diagrams, it is necessary for us to study three important pictures of the Schrödinger equation, including Schrödinger picture, interaction picture and Heisenberg picture.

The Schrödinger picture is the traditional description of the Schrödinger equation, where Hamiltonian $\hat{H}$ is usually time-independent and wave function $\Psi_{\mathrm{S}}(t)$ evolves with time,

$$i\hbar\frac{\partial}{\partial t}|\Psi_{\mathrm{S}}(t)\rangle = \hat{H}|\Psi_{\mathrm{S}}(t)\rangle, \tag{1.70}$$

$$|\Psi_{\mathrm{S}}(t)\rangle = e^{-i\hat{H}(t-t_0)/\hbar}|\Psi_{\mathrm{S}}(t_0)\rangle. \tag{1.71}$$

In the interaction picture both operator and wave function are time dependent. Suppose we have Hamiltonian

$$\hat{H} = \hat{H}_0 + \hat{V}, \tag{1.72}$$

where $\hat{H}_0$ is unperturbed Hamiltonian and $\hat{V}$ is the perturbation on $\hat{H}_0$. Then operator and wave function will be

$$|\Psi_{\mathrm{I}}(t)\rangle = e^{i\hat{H}_0 t/\hbar}|\Psi_{\mathrm{S}}(t)\rangle = e^{i(\hat{H}_0-\hat{H})t/\hbar}|\Psi_{\mathrm{S}}(0)\rangle = e^{-iVt/\hbar}|\Psi_{\mathrm{S}}(0)\rangle, \tag{1.73}$$

$$\hat{O}_{\mathrm{I}}(t) = e^{i\hat{H}_0 t/\hbar}\hat{O}_{\mathrm{S}}e^{-i\hat{H}_0 t/\hbar}. \tag{1.74}$$

Then time evolution operator $\hat{U}(t,t_0)$ is defined as the operator to bring wave function from time t_0 to time t in the interaction picture so that $|\Psi_{\mathrm{I}}(t)\rangle = \hat{U}(t,t_0)|\Psi_{\mathrm{I}}(t_0)\rangle$. By a simple derivation we have

$$\hat{U}(t,t_0) = e^{i\hat{H}_0 t/\hbar}e^{-i\hat{H}(t-t_0)/\hbar}e^{i\hat{H}_0 t_0/\hbar}. \tag{1.75}$$

Differentiating on the above equation, we have

$$i\hbar\frac{\partial}{\partial t}\hat{U}(t,t_0) = \hat{V}(t)\hat{U}(t,t_0). \tag{1.76}$$

And the solution will be

$$\hat{U}(t,t_0) = 1 - \frac{i}{\hbar}\int_{t_0}^{t} dt_1 \hat{V}(t_1)\hat{U}(t_1,t_0). \tag{1.77}$$

By iterative operation we have the final integrated form of $\hat{U}(t,t_0)$

$$\hat{U}(t,t_0) = \sum_{n=0}^{\infty}\left(\frac{-i}{\hbar}\right)^n \frac{1}{n!}\int_{t_0}^{t} dt_1 \cdots \int_{t_0}^{t} dt_n \hat{\mathcal{T}}\left[\hat{V}(t_1)\cdots\hat{V}(t_n)\right], \tag{1.78}$$

where $\hat{\mathcal{T}}$ is time-ordering operator which arranges all the operators in bracket in time-ordered series. It will put the operator in the earliest time on the right and so on.

In the Heisenberg picture the wave function is time independent,

$$|\Psi_{\rm H}(t)\rangle = e^{i\hat{H}(t-t_0)/\hbar}|\Psi_{\rm S}(t)\rangle = |\Psi_{\rm S}(t_0)\rangle, \tag{1.79}$$

then correspondingly any operator $\hat{O}_{\rm S}$ in the Schrödinger picture will transform into $\hat{O}_{\rm H}$ in the Heisenberg picture

$$O_{\rm H}(t) = e^{i\hat{H}(t-t_0)/\hbar}\,\hat{O}_{\rm S}\,e^{-i\hat{H}(t-t_0)/\hbar}. \tag{1.80}$$

It should be kept in mind that although we can work in any picture the expectation value of physical operators will remain unchanged simply due to the unitary transformation.

Single-particle Green's function

Single-particle Green's function can be viewed as the resolvent of Hamiltonian of many-body system. At zero temperature single-particle Green's function in real space and time, or *propagator*, is defined in the Heisenberg picture as the following

$$G(\mathbf{r}_2t_2,\mathbf{r}_1t_1) = -i\langle\Psi_0|\,\hat{\mathcal{T}}[\hat{\psi}(\mathbf{r}_2t_2)\hat{\psi}^\dagger(\mathbf{r}_1t_1)]\,|\Psi_0\rangle \tag{1.81}$$

$$= -i\langle\Psi_0|\,\hat{\psi}(\mathbf{r}_2t_2)\hat{\psi}^\dagger(\mathbf{r}_1t_1)\,|\Psi_0\rangle \quad (t_2 > t_1, \text{electron propagator}) \tag{1.82}$$

$$= +i\langle\Psi_0|\ \hat{\psi}^\dagger(\mathbf{r}_1 t_1)\hat{\psi}(\mathbf{r}_2 t_2)\ |\Psi_0\rangle \quad (t_2 < t_1, \text{hole propagator}), \tag{1.83}$$

in which $|\Psi_0\rangle$ is the normalized Heisenberg ground state wave function and $\hat{T}$ is time-ordering operator including a factor of $(-1)^P$ due to permutation of operators. P is the number of permutations to bring a series of operators into the time-ordered form. Single-particle Green's function for $t_2 > t_1$ in Eq.(1.83) is called retarded Green's function $G^r(\mathbf{r}_2 t_2, \mathbf{r}_1 t_1)$ and the other for $t_2 < t_1$ in Eq.(1.83) is called advanced Green's function $G^a(\mathbf{r}_2 t_2, \mathbf{r}_1 t_1)$. $\hat{\psi}(\mathbf{r}t)$ in Eq.(1.82) is Heisenberg field operator defined by

$$\hat{\psi}(\mathbf{r}t) = e^{i\hat{H}t/\hbar}\hat{\psi}_S(\mathbf{r})e^{-i\hat{H}t/\hbar}. \tag{1.84}$$

The physical meaning of single-particle Green's function, for example in the case of $t_2 > t_1$, is that if at time t_1 an electron is added into N-electron ground state at position $\mathbf{r}_1$, then the probability amplitude to find the added electron at position $\mathbf{r}_2$ and time t_2 is $+iG(\mathbf{r}_2 t_2, \mathbf{r}_1 t_1)$. For $t_2 < t_1$, if at time t_2 a hole is added into N-electron ground state at position $\mathbf{r}_2$, then the probability amplitude to find the added hole at position $\mathbf{r}_1$ and time t_1 is $-iG(\mathbf{r}_2 t_2, \mathbf{r}_1 t_1)$.

Green's function is not restricted in position eigenstates $\mathbf{r}$ and time space t. We can define Green's function in arbitrary single-particle eigenstates $\phi_k(\mathbf{r})$ and frequency space ω. Here k labels quantum number for an arbitrary eigenstate $\phi_k(\mathbf{r})$. One simple choice of $\phi_k(\mathbf{r})$ is eigenstates of the unperturbed Hamiltonian $\hat{H}_0$

$$\hat{H}_0|\phi_k\rangle = \varepsilon_k|\phi_k\rangle. \tag{1.85}$$

Therefore, we will have the corresponding single-particle Green's function $G(k_2, k_1, t_2 - t_1)$ in time space or $G(k_2, k_1, \omega)$ in frequency space. Then we can directly evaluate free-field propagator of unperturbed system,

$$G_0^{r,a}(k, \omega) = \frac{1}{\omega - \varepsilon_k \pm i\delta}, \tag{1.86}$$

where δ is a positive infinitesimal. $G_0^r(k, \omega)$ is retarded free-field Green's function and

$G_0^a(k,\omega)$ is advanced free-field Green's function. It is important to notice that $\omega = \varepsilon_k$ is the pole of retarded Green's function. In general the pole of single-particle Green's function is the energy difference between excited state energy of the interacting $(N+1)$-particle system and ground state energy of the N-particle system. Therefore, single-particle Green's function is extremely useful for the study of single-particle excitation spectra, which can be directly compared to experiment results.

Obviously it is almost impossible to directly calculate Green's function of many-body system since the above definition of Green's function is still built on many-body wave function and full Hamiltonian. However we can use perturbation theory and Wick's theorem to evaluate Green's function. Without the detailed derivation of Wick's theorem, we simply give its conclusion here. By Wick's theorem, the perturbation expansion of Green's function only involves the contracted field operators (free field propagator G_0) and interaction potential V in interaction picture.

Feynman diagrams

Feynman diagrams are directly related to Green's function defined in the previous section. Instead of writing single-particle Green's function explicitly, Feynman used a simple straight line and a wavy line to represent G_0 and interaction potential V respectively. (For general introduction, see Ref. [4])

In Fig. 1-1 we list four basic ingredients of Feynman diagrams for fermions: (a) single-particle unperturbed Green's function, (b) single-particle perturbed Green's function, (c) interaction potential, and (d) non-propagating Green's function. Their physical values are listed in Table 1.1. According to Wick' theorem the perturbed retarded Green's function (Fig. 1-1(b)) is the sum of all possible connected Feynman diagrams with only two external lines. Therefore, we can use this table to evaluate the perturbed retarded Green's function.

As an example we use Feynman diagram to carry out eigen-energy in Hartree-Fock approximation. Assume that the unperturbed Hamiltonian is one-electron Hamiltonian $\dot{H}_0$ and perturbation is two-electron Coulomb interaction potential $V_{klmn} = \int d^3\mathbf{r}_1 \int d^3\mathbf{r}_2 \phi_k^*(\mathbf{r}_1)\phi_l^*(\mathbf{r}_2)\frac{e^2}{|\mathbf{r}_1-\mathbf{r}_2|}\phi_m(\mathbf{r}_1)\phi_n(\mathbf{r}_2)$. We simply show Feynman diagram of

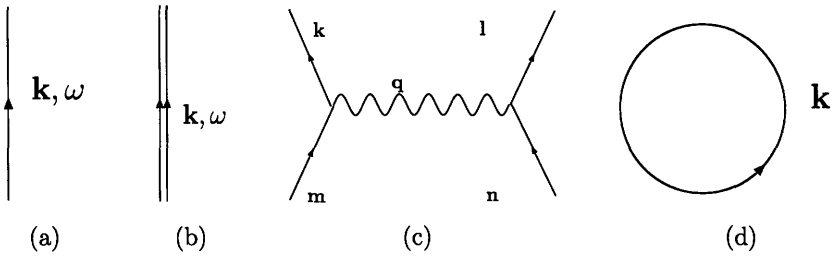

Figure 1-1: Four types of basic Feynman diagrams

Table 1.1: Feynman rules of Feynman diagrams

diagram	description	value
Fig. 1-1(a)	unperturbed retarded Green's function	$iG_0^r(\mathbf{k},\omega) = \frac{i}{\omega-\varepsilon_k+i\delta}$
Fig. 1-1(b)	perturbed retarded Green's function	$iG^r(\mathbf{k},\omega)$
Fig. 1-1(c)	interaction potential	$-iV_{klmn} = -i\langle kl\|\hat{V}\|mn\rangle$
Fig. 1-1(d)	non-propagating Green's function	$iG_0^a(\mathbf{k}) = -1(\|\mathbf{k}\| < k_F)$, or 0
	each Fermion loop	-1

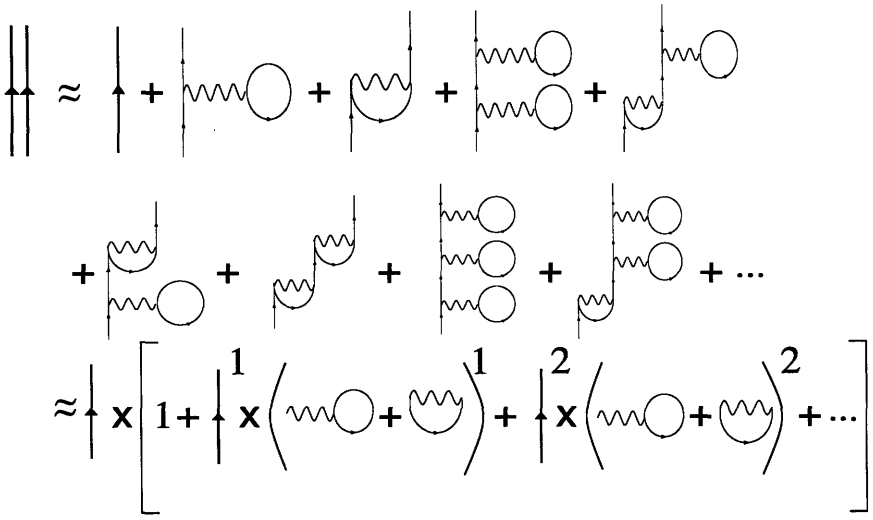

Figure 1-2: Feynman diagram for Hartree-Fock approximation

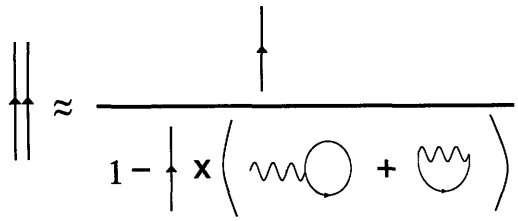

Figure 1-3: Feynman diagram for Hartree-Fock approximation after partial sum

perturbed Green's function Hartree-Fock approximation in Fig. 1-2. The main correction comes from two diagrams: one is *bubble* diagram corresponding to Hartree Coulomb interaction and the other is *oyster* diagram corresponding to like-spin exchange interaction. Fig. 1-2 has infinite number of perturbation terms which only contain bubble and oyster diagrams, however by partial sum we can obtain the infinite sum result as shown in Fig. 1-3. Using the Feynman rules in Table 1.1 we can evaluate this perturbed Green's function in Fig. 1-3,

$$iG^r(k,\omega) = \frac{1}{\left[iG_0^r(k,\omega)\right]^{-1} - \sum_{l<k_F}\left[(-1)(-iV_{klkl})(-1) + (-iV_{lkkl})(-1)\right]}, \quad (1.87)$$

then the final form of Green's function $G^r(k,\omega)$ is

$$G^r(k,\omega) = \frac{1}{\omega - \varepsilon_k - \sum_{l<k_F}\left(V_{klkl} - V_{lkkl}\right) + i\delta}, \quad (1.88)$$

with quasi-particle energy equal to $\omega = \varepsilon_k + \sum_{l<k_F}\left(V_{klkl} - V_{lkkl}\right) - i\delta$. Comparing this quasi-particle energy with the eigen-energy in Eq.(1.69), we immediately see that real part of ω, ε_k, V_{klkl} and V_{lkkl} correspond to E_i, $\langle i|H_1|i\rangle$, U_{ij} and J_{ij} of Eq.(1.69) respectively. Therefore, the energy correction from Hartree-Fock approximation can be treated as one type of self-energy correction to the original Hamiltonian H_0. Since the imaginary part of ω is inversely proportional to life time of quasi-particle, Hartree-Fock quasi-particle is infinity life time. This is because Hartree-Fock approximation only considers time-independent first-order correction and it does not include dynamical correlations due to the motion of other electrons, which will in turn give rises to dynamically screened Coulomb interaction. The latter gives the finite imaginary part of quasi-particle energy ω and the consequent finite life-time of quasi-particles.

1.3 Density functional theory

Density functional theory(DFT) [5, 6], developed by Hohenberg, Kohn and Sham, is another method to solve many-body problem by mapping interacting many-body

problem onto non-interacting many one-body problem. Briefly speaking DFT allows people to use 3-dimensional particle density as basic variable instead of $3N$-dimensional many-body wave functions to solve many-body problem. DFT has achieved great success in solid state systems including bulks, surfaces and molecules [7], where ground state properties can be easily obtained from DFT calculations such as atomistic structures, lattice constant, elastic constants, phonon spectra, and simulated STM images.

1.3.1 Hohenberg-Kohn theorem

Theorem I

The first Hohenberg-Kohn theorem [5] states that *ground-state energy E of interacting many-body system is determined by the ground state density $n(\mathbf{r})$.*

(a) *Ground state electron $n(\mathbf{r})$ is uniquely determined by external potential $V_{\text{ext}}(\mathbf{r})$.* Since Hamiltonian of interacting N-particle system with a given external potential $V_{\text{ext}}(\mathbf{r})$ consists of kinetic energy, electron-electron Coulomb interaction and external potential, the external potential $V_{\text{ext}}(\mathbf{r})$ completely fixes the Hamiltonian. Therefore, ground state wave function Ψ is fully determined by $V_{\text{ext}}(\mathbf{r})$. Obviously ground state electron density $n(\mathbf{r})$ is determined by $n(\mathbf{r}) = \Psi^*\Psi$, hence $n(\mathbf{r})$ is uniquely determined by external potential $V_{\text{ext}}(\mathbf{r})$.

(b) *Conversely, except a trivial additive constant, external potential $V_{\text{ext}}(\mathbf{r})$ is a unique functional of $n(\mathbf{r})$.* Assume that there exists another external potential $V'_{\text{ext}}(\mathbf{r})$ and ground state wave function Ψ' such that $n(\mathbf{r}) = n'(\mathbf{r})$. Then the new ground state energy is $E' = \langle\Psi'|T + V_{ee} + V'_{\text{ext}}(\mathbf{r})|\Psi'\rangle$, which should be lower than the energy $\langle\Psi|T + V_{ee} + V'_{\text{ext}}(\mathbf{r})|\Psi\rangle$. Ψ' and Ψ will not be same unless two external potentials differ by a constant. Consequently,

$$E' < E + \int d^3\mathbf{r} n(\mathbf{r})(V'_{\text{ext}} - V_{\text{ext}}). \tag{1.89}$$

Similarly, we will have another equation

$$E < E' + \int d^3\mathbf{r} n(\mathbf{r})(V_{\text{ext}} - V'_{\text{ext}}). \tag{1.90}$$

The sum of the above two equations leads to the inconsistency

$$E' + E < E + E'. \tag{1.91}$$

The above derivation proves that external potential $V_{\text{ext}}(\mathbf{r})$ is a unique functional of $n(\mathbf{r})$ except a trivial additive constant, and so is Hamiltonian H. Therefore the full many-body ground state is a unique functional of $n(\mathbf{r})$.

Theorem II

The second HK theorem [5] shows *the existence of variational principle for the total energy density functional* $E[n]$. Based on the first HK theorem, we can define F as the sum of kinetic energy and electron-electron Coulomb interaction energy with $F[n] \equiv \langle \Psi | T + V_{ee} | \Psi \rangle$. Obviously it is a universal functional of electron density $n(\mathbf{r})$ and it does not dependent on external potential V_{ext}.

For a given external potential V_{ext}, we can write down the total energy functional E_V

$$E_V[n] \equiv \int n(\mathbf{r}) V_{\text{ext}}(\mathbf{r}) + F[n]. \tag{1.92}$$

It is known that, for a given interacting N-electron system, the total energy functional of Ψ' defined by $\mathcal{E}_V[\Psi'] \equiv \langle \Psi' | T + V_{ee} + V_{\text{ext}} | \Psi' \rangle$ has the minimum at the correct ground state $\Psi' = \Psi$. Suppose we have ground state Ψ' with a different external potential V'_{ext}, then we will have the following conclusion,

$$\mathcal{E}_V[\Psi'] = \int n'(\mathbf{r}) V_{\text{ext}}(\mathbf{r}) + F[n'] > \mathcal{E}_V[\Psi] = \int n(\mathbf{r}) V_{\text{ext}}(\mathbf{r}) + F[n]. \tag{1.93}$$

Therefore, we have the variational principle for total energy

$$E_0 = E_V[n] \leq E_V[n'], \tag{1.94}$$

in which E_0 and n is the ground state energy and electron density and n' is arbitrary trial electron density.

Hohenberg-Kohn theorem establishes the following one-to-one mapping,

$$V_{\text{ext}}(\mathbf{r}) \Longrightarrow H \Longrightarrow \Psi \Longrightarrow n(\mathbf{r}) \Longrightarrow V_{\text{ext}}(\mathbf{r}) \Longrightarrow E_V[n]. \tag{1.95}$$

It provides a theoretical foundation to obtain the ground state properties by searching 3-dimensional ground state electron density based on the variational principle without dealing with $3N$-dimensional many-body wave functions if the exact form of energy density-functional $F[n]$ is known. It has also been extended to several other theories:

- spin density functional theory with spin degree of freedom included
- finite temperature and ensemble density functional theory for many-body system in thermal equilibrium
- density and current density functional theory to include electromagnetic field

However, Hohenberg-Kohn theorem does not tell us how to systematically obtain the universal energy density functional $F[n]$ and there is no rigorous proof to show that DFT is directly related to excited state properties of many-body system.

1.3.2 Kohn-Sham method

Kohn and Sham(KS) [6] suggested a practical approach to deal with unknown energy functional $F[n]$ which Hohenberg-Kohn theorem does not solve.

First they map the interacting many-body problem with true potential onto a non-interacting many one-body problem with effective potential assuming that ground state density of the original interacting many-body system can be represented by that of auxiliary system of non-interacting single-particles. Then they use N single-particle state $\psi_i(\mathbf{r})$ as the main variables to obtain the density of the non-interacting system

$$n(\mathbf{r}) = \sum_{i=1}^{N} |\psi_i(\mathbf{r})|^2. \tag{1.96}$$

Similar to the Hartree-Fock case, the exact ground-state wave function of this system is the Slater determinant of single-particle states,

$$\Psi_{\rm s}(\mathbf{r}) = \frac{1}{\sqrt{N!}}(-1)^P \sum_P P\Big[\psi_1\psi_2\cdots\psi_N\Big]. \tag{1.97}$$

The N single-particle states $\psi_i(\mathbf{r})$ are the N lowest eigenstates of one-electron Hamiltonian $\hat{H}_{\rm s}$

$$\hat{H}_{\rm s}|\psi_i\rangle = \varepsilon_i|\psi_i\rangle, \tag{1.98}$$

$$\hat{H}_{\rm s} = -\frac{\hbar^2}{2m}\nabla^2 + v_{\rm s}. \tag{1.99}$$

and $v_{\rm s}$ is the Kohn-Sham effective potential for single-particle states. In this single-particle representation, kinetic energy functional $T_{\rm s}[n]$ is simply defined by

$$T_{\rm s}[n] = T_{\rm s}[\{\psi_i\}] = -\sum_{i=1}^{N}\frac{\hbar^2}{2m}\langle\psi_i|\nabla^2|\psi_i\rangle. \tag{1.100}$$

Consequently the original exact universal energy functional $F[n]$ is decomposed into three terms

$$F[n] = T_{\rm s}[n] + E_{ee}^{s}[n] + E_{\rm xc}[n], \tag{1.101}$$

$$E_{\rm xc}[n] \equiv T[n] - T_{\rm s}[n] + E_{ee}[n] - E_{ee}^{s}[n]. \tag{1.102}$$

$E_{\rm xc}$, known as exchange-correlation energy functional, includes two parts: (a) the difference between true kinetic energy functional $T[n]$ and fictitious single-particle kinetic energy functional $T_{\rm s}[n]$ and (b) the difference between true electron-electron interaction energy functional $E_{ee}[n]$ and single-particle electron-electron Hartree energy functional $E_{ee}^{s}[n]$. Hence by this transformation the original problem of searching universal energy functional $F[n]$ has been moved into the searching of exchange correlation energy functional $E_{\rm xc}[n]$.

From Eq.(1.92) and Eq.(1.101), the single-particle Kohn-Sham effective potential

v_s can be obtained

$$v_s \equiv V_{ext} + \frac{\delta E_{ee}^s[n]}{\delta n} + \frac{\delta E_{xc}[n]}{\delta n} = V_{ext}(\mathbf{r}) + v_H(\mathbf{r}) + v_{xc}(\mathbf{r}) \tag{1.103}$$

with single-particle Hartree potential v_H

$$v_H(\mathbf{r}) = \int \frac{n(\mathbf{r}')}{|\mathbf{r} - \mathbf{r}'|} d\mathbf{r}' \tag{1.104}$$

and exchange-correlation potential v_{xc}

$$v_{xc} = \frac{\delta E_{xc}[n]}{\delta n}. \tag{1.105}$$

So far the Kohn-Sham approach does not solve many-body problem at all, and actually it just moves the difficulty of finding $F[n]$ into another difficulty of finding $E_{xc}[n]$. However, it has three major advantages:

- After Kohn-Sham single-particle transformation, two unknown functionals, including the original kinetic energy functional $T[n]$ and electron-electron interaction functional $E_{ee}[n]$, has been squeezed into one energy functional $E_{xc}[n]$.

- Single-particle kinetic energy functional $T_s[n]$ is much better than that in early Thomas-Fermi theory of energy functional of Fermi gas, which does not include the gradients of wave functions.

- Compared to Hartree and Hartree-Fock approximations, Kohn-Sham approach is still an exact theory and it provides an elegant and rigorous way to systematically improve the accuracy of total energy by searching better exchange-correlation functional since $E_{xc}[n]$ only depends on electron density.

1.3.3 Exchange-correlation functionals

From the Kohn-Sham method it is clear that once we have a suitable exchange-correlation energy functional $E_{xc}[n]$, self-consistent calculation can be easily per-

formed based on Eq.(1.96), Eq.(1.98), and Eq.(1.103). In another word, the key task of DFT is the search for good exchange-correlation energy functional $E_{\rm xc}[n]$.

Kohn and Sham use a simple but useful exchange-correlation energy functional with *Local Density Approximation*(LDA)[6, 8, 9, 10]. For a slowly varying electron density $n(\mathbf{r})$, they show that

$$E_{\rm xc}[n] = \int n(\mathbf{r})\, \varepsilon_{\rm xc}[n(\mathbf{r})]\, d\mathbf{r}, \tag{1.106}$$

in which one replaces the true exchange-correlation energy density with that $\varepsilon_{\rm xc}[n(\mathbf{r})]$ of uniform electron gas. Then exchange-correlation potential in the Kohn-Sham effective potential Eq.(1.103) is approximated by

$$v_{\rm xc} = \frac{\delta E_{\rm xc}[n]}{\delta n} \approx \varepsilon_{\rm xc}[n(\mathbf{r})] + n(\mathbf{r}) \frac{d\varepsilon_{\rm xc}[n(\mathbf{r})]}{dn}. \tag{1.107}$$

One further step to improve LDA is to include the dependence of gradient of electron density into $E_{\rm xc}[n]$. This approach is called *Generalized Gradient correction Approximation*(GGA) [11, 12, 13]. However, both LDA and GGA give wrong asymptotic behavior of total energy since their potential decays exponentially at large distance instead of correct $-\frac{e^2}{r}$ behavior. The intrinsic reason is the presence of incorrect self-interaction in both approximations where electrons interact with themselves. Consequently the first ionization energy from $\varepsilon_{\rm homo}$ is too small. Meanwhile their excitation spectra do not show discrete Rydberg series of bound states, instead they often give continuous spectra. Noting this problem, Becke [11] suggests a self-interaction corrected GGA to give the correct $-\frac{e^2}{r}$ asymptotic behavior and greatly improve the previous results from LDA and GGA.

Another popular hybrid exchange-correlation potential, called *B3LYP* [14, 15, 16, 17], is widely used for molecular systems in the quantum chemistry society. It combines the contributions from the local spin density approximation(LSDA), Hartree-Fock and GGA together. It gives much better agreement with experiments. The success of B3LYP reminds us that in molecules the exchange potential is more important than other correlations. However B3LYP does fail for metals and other

extended systems with small band gap while B3PW91 works better[18]. It is because the prescription of B3LYP functional underestimates the correlations of homogeneous electron gas, which is very important for systems with a significant itinerant character such as metals and small gap semiconductors. However, it should be mentioned even with exact exchange-correlation functional we still can not obtain correct band gaps since the exact Kohn-Sham band gap is not the true band gap. This problem will be discussed in the next section.

1.3.4 Band gap

Although density functional theory is a theory for ground state, people usually want to compare DFT Kohn-Sham band gap with experiments and results from expensive quantum chemistry methods such as HF, MP2, CCSD, CCSDT, CCSDTQ and etc. Unfortunately DFT calculations often underestimate band gap by $30\% - 100\%$.

Initially people tried to argue that the discrepancy came from non-exact exchange-correlation functionals such as LDA and GGA. It is shown by the work of Sham and Schlüter [19] and that of Perdew and Levy [20] that true band gap Δ is the sum of two components: Kohn-Sham band gap Δ_{KS} and the gap Δ_{XC} from the derivative discontinuity of exchange-correlation functional:

$$\Delta = \Delta_{\mathrm{KS}} + \Delta_{\mathrm{XC}}, \tag{1.108}$$

with

$$\Delta_{\mathrm{XC}} = \lim_{\delta \to 0} \left[\left. \frac{\delta E_{\mathrm{xc}}}{\delta n(\mathbf{r})} \right|_{N+\delta} - \left. \frac{\delta E_{\mathrm{xc}}}{\delta n(\mathbf{r})} \right|_{N-\delta} \right]. \tag{1.109}$$

That implies: (a) exchange-correlation potential v_{xc} should have derivative discontinuity at integer number of electrons, which is not true for LDA and GGA; (b) even with exact exchange-correlation energy functional which contains the correct discontinuity, Kohn-Sham gap Δ_{KS} itself is still not the true band gap; (c) the success of current exchange-correlation functionals such as LDA, GGA, or hybrid functional B3LYP is due to the error cancellation.

1.3.5 Relation between Kohn-Sham method and Hartree-Fock method

Kohn and Sham realize that exchange-correlation potential in general should be non-local. One typical nonlocal term is exchange potential of single particle states with the same spin state. They suggested in their method to replace exchange-correlation energy functional $E_{\rm xc}[n]$ with exchange energy $E_{\rm X}[n]$ of Hartree-Fock approach plus the remaining correlation part $E_{\rm c}[n]$

$$E_{\rm xc}[n] = E_{\rm x}[n] + E_{\rm c}[n] \tag{1.110}$$

with

$$E_{\rm x}[n] = -\frac{1}{2}\sum_{ij}\int \delta_{\sigma_i\sigma_j}\psi_i^*(\mathbf{r})\psi_j^*(\mathbf{r}')\frac{e^2}{|\mathbf{r}-\mathbf{r}'|}\psi_j(\mathbf{r})\psi_i(\mathbf{r}')\,d\mathbf{r}d\mathbf{r}' \tag{1.111}$$

and

$$E_{\rm c}[n] = \int n(\mathbf{r})\varepsilon_{\rm c}(\mathbf{r})\,d\mathbf{r}. \tag{1.112}$$

Correspondingly we obtain the new Kohn-Sham equation

$$\left[-\frac{\hbar^2}{2m}\nabla^2+v_{\rm H}+\frac{\delta E_{\rm c}[n]}{\delta n}\right]\psi_i+\sum_{j=1}^{N}\left[\int \delta_{\sigma_i\sigma_j}\psi_j^*(\mathbf{r}')\frac{e^2}{|\mathbf{r}-\mathbf{r}'|}\psi_i(\mathbf{r}')\,d\mathbf{r}'\right]\psi_j(\mathbf{r}) = \varepsilon_i\psi_i \tag{1.113}$$

The new Kohn-Sham equation, Eq. (1.113), is almost the same as the Hartree-Fock equation Eq.(1.56) except one additional correlation potential term. From this point the Kohn-Sham equation goes beyond the Hartree-Fock approximation.

The above conclusion leads us to a possible way to systematically and visually improve exchange-correlation functional $E_{\rm XC}[n]$. In Sec. (1.2.3) we apply perturbation theory on many-body problem in the non-interacting many single-particle picture, express the first order time-independent terms in infinite Feynman diagrams and finally obtain the Hartree-Fock approximation by partial sum of all those Feynman diagrams. Similarly, we may incorporate other important energy contributions into Feynman diagrams including time-independent and time-dependent perturbation terms, and then find the corresponding form of additional correlation energy functionals from the pole

of Green's function. Indeed this idea shares the same essence as several cases including random phase approximation(RPA) for van der Waals dipolar interactions and GW approach for quasi-particles. In principle it will go beyond static DFT as long as perturbation theory in single-particle picture does not break down.

1.4 Practical methods of density functional theory calculations

To perform practical DFT calculations of realistic systems such as molecules, surfaces and solids, there are two big problems we have to address: (a) how to deal with such large number of atoms and electrons? and (b) how to treat so many electrons even in one atom? These will be answered by Bloch theorem and pseudopotential method respectively in the next three small sections. In the last part, we will formulate Kohn-Sham equation with ultrasoft pseudopotentials in plane-wave basis-set.

1.4.1 Bloch theorem and Brillouin sampling

When electron moves in a crystal, it feels a periodic potential $U(\mathbf{r})$ with

$$U(\mathbf{r}) = U(\mathbf{r}+\mathbf{R}) \tag{1.114}$$

for all $\mathbf{R}$ in a Bravais lattice. Then the corresponding Schrödinger equation for electrons in the crystal is written as

$$\hat{H}\psi_n = \varepsilon_n\psi_n, \tag{1.115}$$

$$\hat{H} = -\frac{\hbar^2}{2m}\nabla^2 + U(\mathbf{r}), \tag{1.116}$$

in which ε_n and ψ_n are eigen energy and eigenstate of crystal Hamiltonian $\hat{H}$. It is easy to prove that translation operator $\hat{T}_{\mathbf{R}}$ and crystal Hamiltonian $\hat{H}$ commute with

each other: $[\hat{T}_{\mathbf{R}}, \hat{H}] = 0$. That means they simultaneously share the same eigenstates

$$\hat{T}_{\mathbf{R}}\psi_n = C_{\mathbf{R}}\psi_n. \tag{1.117}$$

Since two successive translation operations, $\hat{T}_{\mathbf{R}_1}$ and $\hat{T}_{\mathbf{R}_2}$, are equivalent to one operation $\hat{T}_{\mathbf{R}_1+\mathbf{R}_2}$

$$\hat{T}_{\mathbf{R}_1}\hat{T}_{\mathbf{R}_2} = \hat{T}_{\mathbf{R}_1+\mathbf{R}_2} \tag{1.118}$$

or

$$C_{\mathbf{R}_1}C_{\mathbf{R}_2} = C_{\mathbf{R}_1+\mathbf{R}_2}. \tag{1.119}$$

The only non-trivial solution of the above equation is

$$C_{\mathbf{R}} = e^{i\mathbf{k}\mathbf{R}}, \tag{1.120}$$

therefore

$$\hat{T}_{\mathbf{R}}\psi_{n\mathbf{k}}(\mathbf{r}) = \psi_{n\mathbf{k}}(\mathbf{r}+\mathbf{R}) = e^{i\mathbf{k}\mathbf{R}}\psi_{n\mathbf{k}}(\mathbf{r}). \tag{1.121}$$

Alternatively, we can define a function $u_{n\mathbf{k}}(\mathbf{r})$

$$u_{n\mathbf{k}}(\mathbf{r}) = e^{-i\mathbf{k}\mathbf{r}}\psi_{n\mathbf{k}}(\mathbf{r}), \tag{1.122}$$

and immediately using Eq. (1.121) we can see $u_{n\mathbf{k}}(\mathbf{r})$ is a periodic function

$$u_{n\mathbf{k}}(\mathbf{r}) = u_{n\mathbf{k}}(\mathbf{r}+\mathbf{R}). \tag{1.123}$$

In another word, eigenstate $\psi_{n\mathbf{k}}(\mathbf{r})$ can be expressed as the product of phase modulation and a periodic function

$$\psi_{n\mathbf{k}}(\mathbf{r}) = e^{i\mathbf{k}\mathbf{r}}u_{n\mathbf{k}}(\mathbf{r}). \tag{1.124}$$

The above equation is the well-known Bloch theorem, which states that eigenstate $\psi_{n\mathbf{k}}$ of electron in periodic potential $U(\mathbf{r})$ with crystal momentum $\hbar\mathbf{k}$ is a periodic

wave $u_{n\mathbf{k}}$ modulated by a universal wave $e^{i\mathbf{kr}}$. With the Bloch form of wave functions, the Schrödinger equation for $u_{n\mathbf{k}}(\mathbf{r})$ is reformulated into the following equation

$$\left[-\frac{\hbar^2}{2m}\left(\nabla + i\mathbf{k}\right)^2 + U(\mathbf{r})\right]u_{n\mathbf{k}}(\mathbf{r}) = \varepsilon_{n\mathbf{k}}u_{n\mathbf{k}}(\mathbf{r}). \tag{1.125}$$

Bloch theorem further implies that

$$\psi_{n\mathbf{k}}(\mathbf{r}) = \psi_{n,\mathbf{k}+\mathbf{K}}(\mathbf{r}) \tag{1.126}$$

$$\varepsilon_{n\mathbf{k}} = \varepsilon_{n,\mathbf{k}+\mathbf{K}} \tag{1.127}$$

where $\mathbf{K}$ is reciprocal lattice vector and satisfies $e^{i\mathbf{KR}} = 1$. That means we only need to consider those $\mathbf{k}$ in the first Brillouin zone.

Bloch theorem [21, 22] has a significant impact on our realistic calculations since it demonstrates that it is not necessary to solve the Schrödinger equation for all atoms and electrons in the crystal. We only need to consider a small unit cell with limited number of particles as a result of translation symmetry of crystals. One typical boundary condition of the small cell is the Born-von Karman (BvK) boundary condition.

The BvK boundary condition for wave function $\psi_n(\mathbf{r})$ confined in a Bravais lattice is

$$\psi_{n\mathbf{k}}(\mathbf{r}) = \psi_{n\mathbf{k}}(\mathbf{r} + N_i\mathbf{R}_i), \tag{1.128}$$

where $i = 1, 2, 3$ for three different lattice vector directions and N_i is integer. With the aid of Bloch theorem, we have

$$\psi_{n\mathbf{k}}(\mathbf{r} + N_i\mathbf{R}_i) = e^{iN_i\mathbf{kR}_i}\psi_{n\mathbf{k}}(\mathbf{r}) = \psi_{n\mathbf{k}}(\mathbf{r}). \tag{1.129}$$

Then the allowed $\mathbf{k}$-points in the first Brillouin zone are

$$\mathbf{k} = \sum_{i=1}^{3}\frac{m_i}{N_i}\mathbf{K}_i \tag{1.130}$$

with reciprocal lattice vector $\mathbf{K} = 2\pi\mathbf{R}^{-1}$ and $m_i = 1, 2, \cdots, N_i$. The BvK boundary

condition simply says that after we obtain wave function $\psi_{n\mathbf{k}}(\mathbf{r})$ in one unit cell, we can build the corresponding wave function in total $N_1N_2N_3$ unit cells by different phase modulations in different unit cells. This enables us to think in the Bvk boundary condition while performing calculations in one unit cell for all allowed **k**-points in the first Brillouin zone.

Eq. (1.130) defines the well-known Monkhorst-Pack [23] **k**-point sampling in the first Brillouin zone and it has been extensively used in various density functional theory software packages. People often shift the center of the first Brillouin zone to the origin point, but it does not change any physics. All the DFT calculations in this thesis use Monkhorst-Pack **k**-point sampling.

1.4.2 General theory of pseudopotentials

Even with Bloch theorem, there still exist two issues with utmost importance when it comes to computational cost: choice of basis sets and pseudopotentials [24]. For ground-state DFT calculations that involve a significant number of metal atoms (e.g. surface catalysis), the method that tends to achieve the best cost-performance compromise is the ultrasoft pseudopotentials (USPP) [25, 26, 27] with planewave basis, and an independent and theoretically more rigorous formulation, the projector augmented-wave (PAW) [28] method.

The idea of pseudopotential [24] comes from two facts: (a) core electrons of an atom almost always tightly follow the motion of the nucleus; (b) the energy levels of core electrons are often well separated from those of valence electrons. Core electron band structure has almost negligible dispersion and very narrow band width. They are normally far away from valence bands by the order of 10 eV. It implies that core electrons usually do not precipitate in chemical bonding process and they are very localized around the nucleus. In another word, the effect of core electrons on valence electrons will be very similar to nucleus's Coulomb interaction except the opposite sign of charges. If all the electrons are included in the calculation, not only number of electrons will increase, but also the plane-wave cutoff will increase a lot due to the nodes in the radial part of wave functions. Therefore, we can separate an atom into

two parts: (a) its nucleus with core electrons and (b) valence electrons. This is so called *frozen-core approximation.* Under this approximation we can replace the effect of nucleus and core electrons with an effective core potential – *pseudopotential.*

The Schrödinger equation for an atom can be written as

$$H|\psi_c\rangle = \varepsilon_c|\psi_c\rangle, \tag{1.131}$$

$$H|\psi_v\rangle = \varepsilon_v|\psi_v\rangle, \tag{1.132}$$

where ψ_c and ψ_v are core and valence electron eigenstate respectively. We split valence state ψ_v into two parts

$$|\psi_v\rangle = |\tilde{\psi}_v\rangle + \sum_c a_{cv}|\psi_c\rangle, \tag{1.133}$$

in which $\tilde{\psi}_v$ is pseudo valence wave function without any node in its radial part. From the orthogonality condition between the core state and the valence state: $\langle\psi_c|\psi_v\rangle = 0$, we then have

$$a_{cv} = -\langle\psi_c|\tilde{\psi}_v\rangle \tag{1.134}$$

and

$$|\psi_v\rangle = |\tilde{\psi}_v\rangle - \sum_c |\psi_c\rangle\langle\psi_c|\tilde{\psi}_v\rangle = \Big(1 - \sum_c |\psi_c\rangle\langle\psi_c|\Big)|\tilde{\psi}_v\rangle. \tag{1.135}$$

Then the Schrödinger equation for valence state will change to

$$\left[H + \sum_c (\varepsilon_v - \varepsilon_c)|\psi_c\rangle\langle\psi_c|\right]|\tilde{\psi}_v\rangle = \varepsilon_v|\tilde{\psi}_v\rangle, \tag{1.136}$$

which means pseudo Hamiltonian for pseudo valence state $\tilde{\psi}_v$ is $\tilde{H} = H + \sum_c(\varepsilon_v - \varepsilon_c)|\psi_c\rangle\langle\psi_c|$. The eigen energy, however, is still the same as that of true valence state ψ_v. Correspondingly, the effective core potential $\tilde{V}$ for pseudo valence state $\tilde{\psi}_v$ is

$$\tilde{V} = \frac{Z}{r}\hat{\mathbf{r}} + \sum_c (\varepsilon_v - \varepsilon_c)|\psi_c\rangle\langle\psi_c|. \tag{1.137}$$

After the above transformation we obtain a smooth and nodeless pseudo valence wave function $\tilde{\psi}_v$ and the corresponding eigenvalue is still the true eigen energy. The

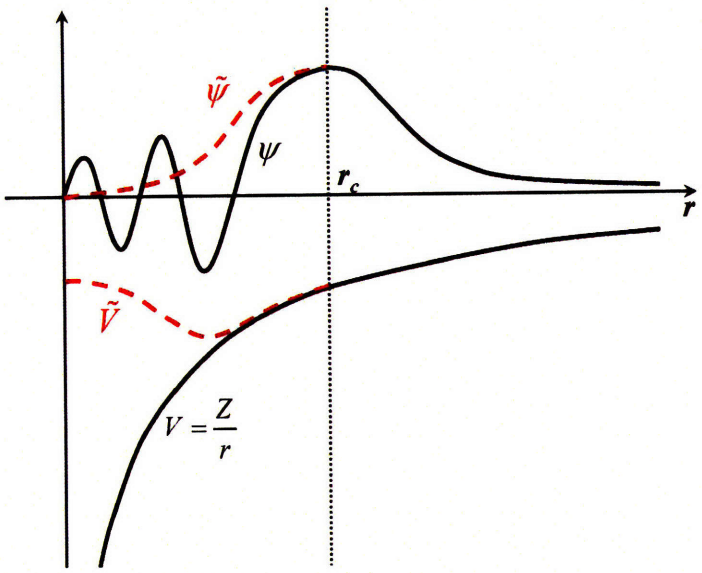

Figure 1-4: Pseudopotential concept for valence electrons

effective core potential $\tilde{V}$ obviously contains nonlocal component. It can be divided into local part V_L and nonlocal part V_{NL}, while V_{NL} can be further approximately expanded in the form of spherical harmonics $Y_{lm}(\theta, \phi)$ for angular dependence and $v_{\text{ps}}(r)$. That finally gives

$$\tilde{V}(\mathbf{r}, \mathbf{r}') = V_L(\mathbf{r})\delta(\mathbf{r} - \mathbf{r}') + \sum_{l=0}^{\infty} \sum_{m=-l}^{l} v_{ps}(r)|lm\rangle\langle lm|. \tag{1.138}$$

However, as illustrated in Fig. 1-4, norm-conserving pseudopotential(NCPP) [29, 30] has an additional requirement that the pseudo wave function $\tilde{\psi}_v$ of valence electron exactly matches the true wave function ψ_v outside a certain cutoff radius r_c. For computational convenience, the radial parts of local and nonlocal pseudo potential are usually fitted into some analytical functions.

1.4.3 Ultrasoft pseudopotentials

As we have mentioned before, the computational cost of planewave DFT calculations strongly depends on the selected type of pseudopotentials. Compared to traditional norm-conserving pseudopotentials (NCPP), Vanderbilt's USPP [25, 26, 27]

and Blöchl's PAW [28] method achieve dramatic savings for first-row elements ($2p$-elements like C,N,O, $3d$-transition metal elements and $4f$ rare-earth elements), with minimal loss of accuracy. USPP/PAW are the workhorses in popular codes such as VASP [31, 32] and DACAPO [33, 34, 35].

The key idea of USPP/PAW [25, 26, 27, 28] is a mapping of the true valence electron wavefunction $\tilde{\psi}(\mathbf{x})$ to a pseudo-wavefunction $\psi(\mathbf{x})$: $\tilde{\psi} \leftrightarrow \psi$, like in any pseudopotential scheme [1]. However, by discarding the requirement that $\psi(\mathbf{x})$ must be norm-conserved ($\langle\psi|\psi\rangle = 1$) while matching $\tilde{\psi}(\mathbf{x})$ outside the pseudopotential cutoff, a greater smoothness of $\psi(\mathbf{x})$ in the core region can be achieved; and therefore less planewaves are required to represent $\psi(\mathbf{x})$. In order for the physics to still work, one must define augmentation charges in the core region, and solve a generalized eigenvalue problem

$$\hat{H}|\psi_n\rangle = \varepsilon_n \hat{S}|\psi_n\rangle, \tag{1.139}$$

instead of the traditional eigenvalue problem, where $\hat{S}$ is a Hermitian and positive definite operator. $\hat{S}$ specifies the fundamental measure of the linear Hilbert space of pseudo-wavefunctions. Physically meaningful inner product between two pseudo-wavefunctions is always $\langle\psi|\hat{S}|\psi'\rangle$ instead of $\langle\psi|\psi'\rangle$. For instance, $\langle\psi_m|\psi_n\rangle \neq \delta_{mn}$ between the eigenfunctions of (1.139) because it is actually not physically meaningful, but $\langle\psi_m|\hat{S}|\psi_n\rangle \equiv \langle\tilde{\psi}_m|\tilde{\psi}_n\rangle = \delta_{mn}$ is.

$\hat{H}$ consists of the kinetic energy operator $\hat{T}$, ionic local pseudopotential $\hat{V}_{\mathrm{L}}$, ionic nonlocal pseudopotential $\hat{V}_{\mathrm{NL}}$, Hartree potential $\hat{V}_{\mathrm{H}}$, and exchange-correlation potential $\hat{V}_{\mathrm{XC}}$,

$$\hat{H} = \hat{T} + \hat{V}_{\mathrm{L}} + \hat{V}_{\mathrm{NL}} + \hat{V}_{\mathrm{H}} + \hat{V}_{\mathrm{XC}}. \tag{1.140}$$

The $\hat{S}$ operator is given by

$$\hat{S} = 1 + \sum_{i,j,I} q_{ij}^I |\beta_j^I\rangle\langle\beta_i^I|, \tag{1.141}$$

where $i \equiv (\tau lm)$ is the angular momentum channel number, and I labels the ions. $\hat{S}$

[1]For the convenience in the rest of this chapter, we will (a) use $\tilde{\psi}$ for true wave function and ψ for pseudo wave function and (b) set $\hbar = c = m = e = 1$

contains contributions from all ions in the supercell, just as the total pseudopotential operator $\hat{V}_{\rm L} + \hat{V}_{\rm NL}$, which is the sum of pseudopotential operators of all ions. In the above equation, the projector function $\beta_i^I(\mathbf{x}) \equiv \langle \mathbf{x}|\beta_i^I\rangle$ of atom I's channel i is

$$\beta_i^I(\mathbf{x}) = \beta_i(\mathbf{x} - \mathbf{X}_I), \tag{1.142}$$

where $\mathbf{X}_I$ is the ion position, and $\beta_i(\mathbf{x})$ vanishes outside the pseudopotential cutoff. These projector functions appear in the nonlocal pseudopotentials as well

$$\hat{V}_{\rm NL} = \sum_{i,j,I} D_{ji}^I |\beta_j^I\rangle\langle\beta_i^I|, \tag{1.143}$$

where

$$D_{ji}^I = D_{ji}^{I(0)} + \int d\mathbf{x}(V_{\rm L}(\mathbf{x}) + V_{\rm H}(\mathbf{x}) + V_{\rm XC}(\mathbf{x}))Q_{ji}^I(\mathbf{x}). \tag{1.144}$$

The coefficients $D_{ji}^{I(0)}$ are the unscreened scattering strengths, while the coefficients D_{ji}^I need to be self-consistently updated with the electron density

$$\rho(\mathbf{x}) = \sum_n \left\{ |\psi_n|^2 + \sum_{i,j,I} Q_{ji}^I(\mathbf{x})\langle\psi_n|\beta_j^I\rangle\langle\beta_i^I|\psi_n\rangle \right\} f(\varepsilon_n), \tag{1.145}$$

in which $f(\varepsilon_n)$ is the Fermi-Dirac distribution. $Q_{ji}^I(\mathbf{x})$ is the charge augmentation function, i.e., the difference between the true wavefunction charge (interference) and the pseudocharge for selected channels,

$$Q_{ji}^I(\mathbf{x}) \equiv \tilde{\psi}_j^{I*}(\mathbf{x})\tilde{\psi}_i^I(\mathbf{x}) - \psi_j^{I*}(\mathbf{x})\psi_i^I(\mathbf{x}), \tag{1.146}$$

which vanishes outside the cutoff. $Q_{ji}^I(\mathbf{x})$ is further expressed by pseudocounterparts,

$$Q_{ji}^I(\mathbf{x}) = \sum_{LM} c_{LM}^{ji} Q_{ji}^{I,\rm rad}(x) Y_{LM}(\hat{\mathbf{x}}), \tag{1.147}$$

where c_{LM}^{ji} are Clebsch-Gordan coefficients and $Q_{ji}^{I,\rm rad}(x)$ is the effective radial function

for charge augmentation function. There is also

$$q_{ij}^{I} \equiv \int d\mathbf{x} Q_{ji}^{I}(\mathbf{x}). \tag{1.148}$$

Thus the total energy is given by

$$E_{\text{tot}} = \sum_{n} \langle \psi_n | -\frac{\nabla^2}{2} + V_{\text{NL}}^{(0)} | \psi_n \rangle + \frac{1}{2} \int V_{\text{H}}(\mathbf{x}) \rho(\mathbf{x}) d\mathbf{x} + \int \varepsilon_{\text{xc}}(\mathbf{x}) \rho(\mathbf{x}) d\mathbf{x} + E_{\text{ion}}, \tag{1.149}$$

where the nonlocal operator is the *bare* nonlocal operator with

$$V_{\text{NL}}^{(0)} = \sum_{i,j,I} D_{ji}^{I(0)} |\beta_j^I\rangle \langle \beta_i^I|. \tag{1.150}$$

Terms in Eq. (1.145) are evaluated using two different grids, a sparse grid for the wavefunctions ψ_n and a dense grid for the augmentation functions $Q_{ji}^{I}(\mathbf{x})$. Ultrasoft pseudopotentials are thus fully specified by the functions $V_{\text{L}}(\mathbf{x})$, $\beta_i^I(\mathbf{x})$, $D_{ji}^{I(0)}$, and $Q_{ji}^{I}(\mathbf{x})$. Forces on ions and internal stress on the supercell can be derived analytically using linear response theory [27, 32].

1.4.4 Kohn-Sham equation in plane-wave basis-set

Kohn-Sham equation can be solved with various basis-sets such as Gaussian basis, wavelet basis, plane-wave basis and etc. Different basis may affect final results in calculations. Plane-wave basis is the most popular one since it has several advantages compared to other basis-sets:

- Both accuracy and convergence of plane-wave basis are controlled by single parameter E_{cut}– plane-wave energy cutoff. Therefore, they can be systematically improved by increasing energy cut off E_{cut}.

- It is very easy to implement plane-wave basis in density functional theory code. Meanwhile, fast Fourier transform(FFT) can speed up transformation of wave functions, local potentials and nonlocal potentials between real space and Fourier space.

- Any gradient operator will simply introduce an imaginary Fourier space vector $i(\mathbf{k}+\mathbf{G})$, therefore the kinetic energy has a very simple form.

- Different from Gaussian basis-set, plane-wave basis is independent of atom positions, therefore we do not need to change origin of basis-set with ionic motions.

In plane-wave basis the periodic part $u_{n\mathbf{k}}(\mathbf{x})$ of eigen wave function $\psi_{n\mathbf{k}}(\mathbf{x})$ is written as

$$u_{n\mathbf{k}}(\mathbf{x}) = \sum_{\mathbf{G}} C_{n,\mathbf{k}+\mathbf{G}} e^{i\mathbf{G}\mathbf{x}}, \tag{1.151}$$

and from Bloch theorem Eq (1.124) we have

$$\psi_{n\mathbf{k}}(\mathbf{x}) = \sum_{\mathbf{G}} C_{n,\mathbf{k}+\mathbf{G}} e^{i(\mathbf{k}+\mathbf{G})\mathbf{x}}. \tag{1.152}$$

Here $C_{n,\mathbf{k}+\mathbf{G}}$ is plane-wave coefficient. So the full plane-wave basis for Bloch wave function $\psi_{n\mathbf{k}}(\mathbf{x})$ is

$$\langle \mathbf{x}|\mathbf{k}+\mathbf{G}\rangle = \frac{1}{\sqrt{\Omega}} e^{i(\mathbf{k}+\mathbf{G})\mathbf{x}}, \tag{1.153}$$

and Bloch wave function in Dirac notation is

$$|\psi_{n\mathbf{k}}\rangle = \sum_{\mathbf{G}} C_{n,\mathbf{k}+\mathbf{G}} |\mathbf{k}+\mathbf{G}\rangle. \tag{1.154}$$

Now we can express Kohn-Sham equation with ultrasoft pseudopotentials in plane-wave basis

$$H_{\mathbf{k}+\mathbf{G},\mathbf{k}+\mathbf{G}'}\, C_{n,\mathbf{k}+\mathbf{G}'} = \varepsilon_{n\mathbf{k}}\, S_{\mathbf{k}+\mathbf{G},\mathbf{k}+\mathbf{G}'}\, C_{n,\mathbf{k}+\mathbf{G}'}, \tag{1.155}$$

where Hamiltonian element $H_{\mathbf{k}+\mathbf{G},\mathbf{k}+\mathbf{G}'}$ is

$$\begin{aligned} H_{\mathbf{k}+\mathbf{G},\mathbf{k}+\mathbf{G}'} &\equiv \langle \mathbf{k}+\mathbf{G}|H|\mathbf{k}+\mathbf{G}'\rangle & (1.156)\\ &= \frac{1}{2}\left|\mathbf{k}+\mathbf{G}\right|^2 \delta_{\mathbf{G}'\mathbf{G}} + V_{\mathrm{L}}(\mathbf{G}-\mathbf{G}') + V_{\mathrm{NL}}(\mathbf{k}+\mathbf{G},\mathbf{k}+\mathbf{G}') & (1.157)\\ &\quad + V_{\mathrm{H}}(\mathbf{G}-\mathbf{G}') + V_{\mathrm{XC}}(\mathbf{G}-\mathbf{G}'). & (1.158) \end{aligned}$$

$V_{\mathrm{L}}(\mathbf{G}-\mathbf{G}')$ is Fourier space representation of local pseudopotential

$$
\begin{aligned}
V_{\mathrm{L}}(\mathbf{G}-\mathbf{G}') &\equiv \langle \mathbf{k}+\mathbf{G}|V_{\mathrm{L}}|\mathbf{k}+\mathbf{G}'\rangle && (1.159)\\
&= \frac{1}{\Omega}\sum_I e^{-i(\mathbf{G}-\mathbf{G}')\mathbf{X}_I}\left(\int V^I_{\mathrm{loc}}(\mathbf{x}')e^{-i(\mathbf{G}-\mathbf{G}')\mathbf{x}'}d\mathbf{x}'\right) && (1.160)\\
&= \frac{1}{\Omega}\sum_I e^{-i(\mathbf{G}-\mathbf{G}')\mathbf{X}_I}V^I_{\mathrm{loc}}(\mathbf{G}-\mathbf{G}') && (1.161)
\end{aligned}
$$

and $V_{\mathrm{NL}}(\mathbf{k}+\mathbf{G},\mathbf{k}+\mathbf{G}')$ is Fourier space representation of nonlocal pseudopotential

$$
\begin{aligned}
V_{\mathrm{NL}}(\mathbf{k}+\mathbf{G},\mathbf{k}+\mathbf{G}') &\equiv \langle \mathbf{k}+\mathbf{G}|V_{\mathrm{NL}}|\mathbf{k}+\mathbf{G}'\rangle && (1.162)\\
&= \sum_{i,j,I} D^I_{ji}\langle \mathbf{k}+\mathbf{G}|\beta^I_j\rangle\langle\beta^I_i|\mathbf{k}+\mathbf{G}'\rangle && (1.163)\\
&= \sum_{i,j,I} D^I_{ji}\beta^I_j(\mathbf{k}+\mathbf{G})\beta^{*I}_i(\mathbf{k}+\mathbf{G}')e^{-i(\mathbf{G}-\mathbf{G}')\mathbf{X}_I}. && (1.164)
\end{aligned}
$$

Nonlocal projector β^I_i is a spherical harmonics multiplied by a radial function, $\beta^I_i(\mathbf{x}) = R^I_i(r)Y_{l_i m_i}(\theta,\phi)$. Similarly, the ultrasoft overlap element is

$$
\begin{aligned}
S_{\mathbf{k}+\mathbf{G},\mathbf{k}+\mathbf{G}'} &\equiv \langle \mathbf{k}+\mathbf{G}|S|\mathbf{k}+\mathbf{G}'\rangle && (1.165)\\
&= 1+\sum_{i,j,I} Q^I_{ji}\langle \mathbf{k}+\mathbf{G}|\beta^I_j\rangle\langle\beta^I_i|\mathbf{k}+\mathbf{G}'\rangle && (1.166)\\
&= 1+\sum_{i,j,I} Q^I_{ji}\beta^I_j(\mathbf{k}+\mathbf{G})\beta^{*I}_i(\mathbf{k}+\mathbf{G}')e^{-i(\mathbf{G}-\mathbf{G}')\mathbf{X}_I}. && (1.167)
\end{aligned}
$$

With total electron density in Fourier space

$$
\rho(\mathbf{G}) = \frac{1}{\Omega}\int_\Omega \rho(\mathbf{x})e^{-i\mathbf{G}\mathbf{x}} = \rho_{\mathrm{soft}}(\mathbf{G}) + \sum_{i,j,I,n} Q^I_{ji}(\mathbf{G})\langle\psi_{n\mathbf{k}}|\beta^I_j\rangle\langle\beta^I_i|\psi_{n\mathbf{k}}\rangle, \qquad (1.168)
$$

Hartree potential from electron-electron Coulomb interaction is given by

$$
V_{\mathrm{H}}(\mathbf{G}) = 4\pi\frac{\rho(\mathbf{G})}{|\mathbf{G}|^2}, \qquad (1.169)
$$

and exchange-correlation potential $V_{\mathrm{XC}}(\mathbf{G})$ is given by

$$
V_{\mathrm{XC}}(\mathbf{G}) = \frac{1}{\Omega}\int_\Omega V_{\mathrm{XC}}(\mathbf{x})e^{-i\mathbf{G}\mathbf{x}}. \qquad (1.170)
$$

The plane-wave cutoff E_{cut} is defined by maximum kinetic energy of for all the $\mathbf{G}$ vectors.

$$\frac{1}{2}|\mathbf{G}|^2 \leq E_{cut}, \tag{1.171}$$

which gives $G_{\max} = \sqrt{2E_{\text{cut}}}$. For ultrasoft pseudopotentials and PAW method, there is another dense grid $E_{\text{cut}}^{\text{aug}}$ for augmentation charge density beside the sparse wave function grid. It is often set to $E_{\text{cut}}^{\text{aug}} = 4E_{cut}$ and thus $G_{\text{max}}^{\text{aug}} = 2G_{\max}$, which means the total number of $\mathbf{G}$ vectors in the dense grid is about 8 times of that in the sparse grid in the three-dimensional space.

1.5 Time-dependent density functional theory

Density functional theory with the Kohn-Sham reference kinetic energy functional of a fictitious non-interacting electron system has become a leading method for treating many electrons in solids and molecules. While initially formulated to describe only the electronic ground state, it has been rigorously extended by Runge and Gross [36] to treat time-dependent, driven systems (excited states). TDDFT is therefore a natural theoretical platform for studying electron conduction at the nanoscale.

There are two flavors in which TDDFT is implemented. One is direct numerical integration [37, 38, 39, 40, 41, 42] of the time-dependent Kohn-Sham (TDKS) equations. The other is a *Gedanken experiment* of the former with an added assumption of infinitesimal time-dependent perturbation, so a linear response function may be first derived in closed form [43, 44, 45], which is then evaluated numerically. These two implementations should give exactly the same result when the external perturbation field is infinitesimal. The latter implementation can be computationally more efficient once the linear-response function has been analytically derived, while the former can treat non-infinitesimal perturbations and arbitrary initial states.

A key step of the TDDFT dynamics is updating of the Kohn-Sham effective potential by the present *excited-state* charge density $\rho(\mathbf{x}, t)$, $\hat{V}_{\text{KS}}(t) = \hat{V}_{\text{KS}}[\rho(\mathbf{x}, t), ...]$. This is what sets TDDFT apart from the ground-state DFT estimate of excitation energies, even when TDDFT is applied in its crudest, so-called adiabatic approximation,

[43] whereby the same exchange-correlation density functional form as the ground-state DFT calculation is used (for example, the so-called TDLDA approximation uses exactly the same Ceperley-Alder-Perdew-Zunger functional [8, 9] as the ground-state LDA calculation.) This difference in excitation energies comes out because in a ground-state DFT calculation, a virtual orbital such as LUMO (lowest unoccupied molecular orbital) experiences an effective potential due to N electrons occupying the lowest N orbitals; whereas in a TDDFT calculation, if one electron is excited to a LUMO-like orbital, it sees $N-1$ electrons occupying the lowest $N-1$ orbitals, plus its own charge density. Also, the excitation energy is defined by the collective reaction of this coupled dynamical system to time-dependent perturbation (pole in the response function) [46], rather than simple algebraic differences between present virtual and occupied orbital energies. For rather involved reasons beyond what is discussed here, TDDFT under the adiabatic approximation gives significantly improved excitation spectra [43, 44], although there are still much to be desired. Further systematic improvements to TDDFT such as current density functional [47] and self-interaction correction [48] have already made great strides.

The detailed derivations of time-dependent Kohn-Sham equation with ultrasoft pseudopotentials and PAW method will be presented in Chapter 5.

Chapter 2

Quantum transport

2.1 Introduction

The development of molecular scale electronic devices has attracted a great deal of interest in the past decade, although major experimental and theoretical challenges [49, 50, 51, 52, 53] still exist. To date precise experimental control of molecular conformation is lacking, resulting in large uncertainties in the measured electrical conductance. On the other hand, great effort has been made in the theoretical approaches such as nonequilibrium Green's function (NEGF) method within Landauer formalism for phase-coherent transport. Although NEGF has achieved many successes in describing electron transport at the meso [54, 55] and molecular [56, 57, 58, 59, 60, 61, 62, 63, 64] scales, issues such as dynamical electron correlation and large electron-phonon coupling effects [65, 66] are far from fully resolved.

In this chapter we will first introduce different characteristic length scales which determine various electron transport behaviors and point out the difference between classic and quantum transport. We then follow Meir's approach [67] to derive electric conductance for interacting many-electron systems. Finally we focus on phase-coherent approximation of Meir's general expression and recover multichannel Landauer formula [68, 69, 70, 71] with Green's function method [54, 72, 64], which will be combined with our non-orthogonal localized quasiatomic orbitals to calculate electrical conductance of nanowire, carbon nanotube and molecular junctions later.

2.2 Electrical conductance

Classic electron transport theory tells us that electrical resistance R of a macroscopic conductor with cross-sectional area A and length L is given by Ohm's law

$$R = \frac{L}{A}\rho, \tag{2.1}$$

where ρ is resistivity which depends on materials property only. Electrical conductance is the inverse of resistance

$$G = \frac{1}{R} = \frac{A}{L}\sigma \tag{2.2}$$

with electrical conductivity $\sigma = 1/\rho$. However the above formula will encounter serious problem when it is applied onto smaller and smaller electronic devices, where quantum nature of electrons becomes more and more important and electric conductance strongly depends on its environment such defects, impurities, phonons and other electrons along its wave propagation path through materials. In such small scale, the change of dimensionality due to confinement will also affect electron transport significantly.

Typical transport regimes can be classified by the relations among four important characteristic length scales: device length (L), Fermi wavelength (λ_{F}), momentum relaxation length (L_{m}) and phase-coherence length (L_{φ}). Fermi wavelength is the de Broglie wave length of electrons at Fermi energy and it is determined by the momentum of Fermi electrons through $\lambda_{\mathrm{F}} = 2\pi/k_{\mathrm{F}}$. Momentum relaxation length (L_{m}), also called mean free path, is the average traveling length of electrons through materials before collisions make their motion totally uncorrelated from initial momentum. Phase-coherence length (L_{φ}) is the length above which the phase of electron wave becomes incoherent and phase information is totally lost. The source of phase decoherence only comes from inelastic scattering with phonons, electrons and magnetic impurities, however both elastic (such as static ions) and inelastic scatterings will decrease momentum relaxation length (L_{m}). These characteristic length scales can be

changed by different materials or different experiment setups such as concentration of ionic and magnetic impurities, operating temperature, electric and magnetic fields.

With the above four length scales, we can characterize electron transport phenomena into the following four regimes:

- Classical transport regime ($L \gg L_{\mathrm{m}}, L_{\varphi}, \lambda_{\mathrm{F}}$). In this regime all quantum effects are negligible, therefore overall resistance can be viewed as the result of the particle-like collisions.

- Localization regime ($L > L_{\varphi} \gg L_{\mathrm{m}}$). In this regime, high concentrations of elastic scattering sources introduce a large amount of phase shifts of electron waves, therefore in the one-dimensional case electrical resistance is shown to increase exponentially with the increase of device length L.

- Diffusive transport regime ($L_{\varphi} > L > L_{\mathrm{m}}$). This is the region we will deal with by both Green's function method and time-dependent density functional method later. In this regime, quantum wave scattering inside the device and at the interface between the device and electron reservoirs dominates electron propagations, therefore reduces total conductance.

- Ballistic transport regime ($L_{\varphi}, L_{\mathrm{m}} \gg L$). In this regime like pure conductors and quantum point contacts, there is no momentum relaxation and phase-decoherence at all, thus electrons keep staying in its propagating wave state.

Here we will focus on the phase-coherent transport where phase-coherence length L_{φ} is much longer than the device length scale L.

2.3 Generalized Landauer formalism for interacting electrons

Pioneering work of Landauer [68] and Büttiker [73] leads to a simple formula of electrical conductance through two-terminal and four-terminal electronic devices in terms

of total transmission of electrons. They pointed out quantized conductance – conductance quantum $G_0 = 2e^2/h$ – of single conducting channel. Fisher and Lee [70] then related the multichannel conductance of the Landauer formula to the transmission matrix obtained from the standard Kubo's linear response theory of conductance. All those derivations, however, were based on non-interacting one-electron picture. Later Meir and Wingreen [67] extended the original Landauer formula into a more general one which considers the current through a conductor region of interacting electrons instead of non-interacting electrons. The general Landauer formula scales the original one by the self-energy correction to the conductor region due to electron-electron interactions. Recently Ferretti et al. [74, 75] and Thygesen et al. [76] use the above general formula and calculated the electrical conductance through one-dimensional small junctions with electron-electron interactions included. Some differences of electrical conductance between non-interacting and interacting systems are investigated in their work.

Let us consider a general conductor(C) sandwiched by left(L) and right(R) leads along one direction. Both leads are also connected to two reservoirs with chemical potential μ_L and μ_R respectively. Instead of using delocalized Bloch state characterized by momentum $\mathbf{k}$ in the case of Meir's derivation, we choose to express our system's total Hamiltonian in an orthonormal localized basis-set containing both orbital and spin degrees of freedom

$$\mathbf{H} = \mathbf{H}_L + \mathbf{H}_{CL} + \mathbf{H}_C + \mathbf{H}_{CR} + \mathbf{H}_R \tag{2.3}$$

where $\mathbf{H}_L$ ($\mathbf{H}_R$) is the Hamiltonian of left (right) lead given by

$$\mathbf{H}_b = \sum_{ij} \mathbf{H}_{bi,bj} c_{bi}^\dagger c_{bj}, \qquad b = \{L, R\} \tag{2.4}$$

and $\mathbf{H}_C$ is the conductor Hamiltonian given by

$$\mathbf{H}_C = \sum_{nm} H_{nm} d_n^\dagger d_m \qquad n, m \in C. \tag{2.5}$$

$c_{bi}^{\dagger}$ (c_{bi}) is the creation (annihilation) operator which creates (destroys) an electron in state i of the left or right lead. $d_n^{\dagger}$ and d_n are the similar operators for the conductor region. In addition to these Hamiltonian matrices of each part, $\mathbf{H}_{CL}$ ($\mathbf{H}_{CR}$) describes the interaction between conductor and left(right) lead

$$\mathbf{H}_{Cb} = \sum_{i,n} \left(H_{bi,n} c_{bi}^{\dagger} d_n + \text{H.c.} \right). \tag{2.6}$$

Then according to Heisenberg equation, the current traveling through the system is given by the current passing through left or right lead, or statistic average of the time derivative of the number operator $\mathbf{N}_b = \sum_i c_{bi}^{\dagger} c_{bi}$ for the left or right lead [72],

$$J \equiv J_L = -e\langle \dot{\mathbf{N}}_L \rangle = -\frac{ie}{\hbar} \langle [\mathbf{H}, \mathbf{N}_L] \rangle. \tag{2.7}$$

Since $\mathbf{H}_C$, $\mathbf{H}_L$ and $\mathbf{H}_R$ commute $\mathbf{N}_L$, one can find

$$\begin{aligned} J_L &= \frac{ie}{\hbar} \sum_{i,n} \left[H_{Li,n} \langle c_{Li}^{\dagger}(t) d_n(t) \rangle - H_{Li,n}^{*} \langle d_n^{\dagger}(t) c_{Li}(t) \rangle \right] && (2.8) \\ &= \frac{e}{\hbar} \sum_{i,n} \left[H_{Li,n}(t) G_{n,Li}^{<}(t,t) - H_{Li,n}^{*}(t) G_{Li,n}^{<}(t,t) \right], && (2.9) \end{aligned}$$

where we define the Keldysh Green's function [77, 72] $G_{n,Li}^{<}(t_1,t_2)$ and $G_{Li,n}^{<}(t_1,t_2)$

$$\begin{aligned} G_{n,Li}^{<}(t_1,t_2) &\equiv i\langle c_{Li}^{\dagger}(t_2) d_n(t_1) \rangle, && (2.10) \\ G_{Li,n}^{<}(t_1,t_2) &\equiv i\langle d_n^{\dagger}(t_2) c_{Li}(t_1) \rangle. && (2.11) \end{aligned}$$

It is easy to see that $G_{Li,n}^{<}(t,t) = -[G_{n,Li}^{<}(t,t)]^{*}$. A general relation for the contour-ordered Green's function $G_{n,Li}^{<}(t,t')$ is given by equation of motion technique [78]

$$G_{n,Li}(t,t') = \sum_{jm} \int dt_1 G_{nm}(t,t_1) H_{Lj,m}^{*}(t_1) g_{Lj,Li}(t_1,t'), \tag{2.12}$$

where $g_{Lj,Li}(t_1,t')$ is Green's function of left lead. Replacing $G_{n,Li}(t,t')$ in the J_L equation with the above expression and taking time-independent limit [67, 78], we

then have

$$J_L = \frac{ie}{\hbar}\int \frac{d\omega}{2\pi}\mathrm{Tr}\Big[f_L\mathbf{\Gamma}_L\big(\mathbf{G}_C^r - \mathbf{G}_C^a\big) + \mathbf{\Gamma}_L\mathbf{G}_C^<\Big]. \tag{2.13}$$

With the steady state condition of current $J = J_L = -J_R = (J_L - J_R)/2$, the final expression for the dc current at the steady state is given by

$$J = \frac{ie}{2\hbar}\int \frac{d\omega}{2\pi}\mathrm{Tr}\Big[\big(f_L\mathbf{\Gamma}_L - f_R\mathbf{\Gamma}_R\big)\big(\mathbf{G}_C^r - \mathbf{G}_C^a\big) + \big(\mathbf{\Gamma}_L - \mathbf{\Gamma}_R\big)\mathbf{G}_C^<\Big], \tag{2.14}$$

where coupling function $\mathbf{\Gamma}_{L,R}$ is defined through the retarded and advanced self-energy matrices of left and right leads – denoted by $\mathbf{\Sigma}_{L,R}^r$ and $\mathbf{\Sigma}_{L,R}^a$,

$$\mathbf{\Gamma}_b = i(\mathbf{\Sigma}_b^r - \mathbf{\Sigma}_b^a) \qquad b = L, R \tag{2.15}$$

$$\mathbf{\Sigma}_b^{r,a} = \mathbf{H}_{Cb}\,\mathbf{g}_b^{r,a}\,\mathbf{H}_{bC}. \tag{2.16}$$

Here $\mathbf{g}_b^{r,a}$ is the retarded or advanced Green's function of lead b in the equilibrium condition with electron occupation number $f_{L,R}$. Similarly $\mathbf{G}_C^{r,a}$ in Eq.(2.14) is the retarded or advanced Green's function of conductor region, while $\mathbf{G}_C^{<,>}$ is its lesser or greater Green's function. All these matrices including $\mathbf{G}_C^{r,a}, \mathbf{\Gamma}_{L,R}$ and $\mathbf{\Sigma}_{L,R}^{r,a}$ are frequency-dependent $N_C \times N_C$ matrices. In general $\mathbf{G}_C^{<,>}$ and $\mathbf{G}_C^{r,a}$ are determined by solving the Keldysh equation for lesser and advanced Green's functions and Dyson equations for retarded and advanced Green's function

$$\mathbf{G}_C^{<,>} = \mathbf{G}_C^r\,\mathbf{\Sigma}_C^{<,>}\,\mathbf{G}_C^a \tag{2.17}$$

$$\mathbf{G}_C^{r,a} = \mathbf{G}_{0,C}^{r,a} + \mathbf{G}_{0,C}^{r,a}\,\mathbf{\Sigma}_C^{r,a}\,\mathbf{G}_C^{r,a}, \tag{2.18}$$

where $\mathbf{G}_{0,C}^{r,a}$ is the retarded or advanced Green's function for the non-interacting case and $\mathbf{\Sigma}_C^{r,a}$ is the self-energy of conductor region due to the coupling with left lead, right lead and other interactions within conductor region

$$\mathbf{\Sigma}_C^{r,a} = \mathbf{\Sigma}_L^{r,a} + \mathbf{\Sigma}_R^{r,a} + \mathbf{\Sigma}_{\mathrm{corr}}^{r,a}. \tag{2.19}$$

$\mathbf{\Sigma}_{\mathrm{corr}}^{r,a}$ can be (a) electron-electron correlations, (b) electron-phonon interaction, (c)

electron-impurity interaction and etc. Meanwhile, since left and right leads are considered to be in equilibrium, the lesser and greater self-energy matrices due to the interactions between conductor and leads are given by

$$\mathbf{\Sigma}^{<}_{L,R} = i f_{L,R}\, \mathbf{\Gamma}_{L,R}, \tag{2.20}$$

$$\mathbf{\Sigma}^{>}_{L,R} = -i(1 - f_{L,R})\, \mathbf{\Gamma}_{L,R}, \tag{2.21}$$

where $f_{L,R}$ is Fermi occupation function for both leads $f_{L,R} = f(\omega - \mu_{L,R})$.

In summary, the above approach is very similar to Feynman diagram analysis of Hartree-Fock approximation in the first chapter. The general Landauer formula in Eq. (2.14) treats quasi-particle electron transport through two terminal devices by including carrier-carrier and carrier-environment interactions into quasi-particle Green's function and self-energy.

2.3.1 Landauer formalism for phase-coherent transport

In the non-interacting limit of the general Landauer formula, we do not consider the contribution of $\mathbf{\Sigma}^{r,a}_{\text{corr}}$. Therefore, lesser and greater Green's functions for conductor region are rewritten as

$$\mathbf{G}^{<}_{C} = \mathbf{G}^{r}_{C}\, (i f_L\, \mathbf{\Gamma}_L + i f_R\, \mathbf{\Gamma}_R)\, \mathbf{G}^{a}_{C}, \tag{2.22}$$

$$\mathbf{G}^{>}_{C} = \mathbf{G}^{r}_{C} \Big[-i(1 - f_{L,R})\, \mathbf{\Gamma}_L - i(1 - f_{L,R})\, \mathbf{\Gamma}_R \Big]\, \mathbf{G}^{a}_{C}. \tag{2.23}$$

Together with the relation $\mathbf{G}^{r}_{C} - \mathbf{G}^{a}_{C} = \mathbf{G}^{>}_{C} - \mathbf{G}^{<}_{C}$, we then have

$$\mathbf{G}^{r}_{C} - \mathbf{G}^{a}_{C} = -i \mathbf{G}^{r}_{C}\, (\mathbf{\Gamma}_L + \mathbf{\Gamma}_R)\, \mathbf{G}^{a}_{C}. \tag{2.24}$$

Then substituting $\mathbf{G}^{r}_{C} - \mathbf{G}^{a}_{C}$ and $\mathbf{G}^{<}_{C}$ in the general Landauer formula – Eq. (2.14) – with their expressions above, we will have

$$J = \frac{ie}{2\hbar} \int \frac{d\omega}{2\pi}\, \mathrm{Tr} \Big[\big(f_L \mathbf{\Gamma}_L - f_R \mathbf{\Gamma}_R \big) \big(-i \mathbf{G}^{r}_{C}\, (\mathbf{\Gamma}_L + \mathbf{\Gamma}_R)\, \mathbf{G}^{a}_{C} \big)$$

$$+ \quad \Big(\mathbf{\Gamma}_L - \mathbf{\Gamma}_R\Big)\mathbf{G}_C^r \left(if_L\,\mathbf{\Gamma}_L + if_R\,\mathbf{\Gamma}_R\right)\mathbf{G}_C^a\Big],$$

$$= \frac{e}{\hbar}\int \frac{d\omega}{2\pi}\left[f_L(\omega) - f_R(\omega)\right]\mathrm{Tr}\Big[\mathbf{\Gamma}_L\mathbf{G}_C^r\mathbf{\Gamma}_R\,\mathbf{G}_C^a\Big] \tag{2.25}$$

$$= \frac{e}{h}\int d\omega\left[f_L(\omega) - f_R(\omega)\right]T(\omega), \tag{2.26}$$

where $T(\omega)$ is the total transmission function

$$T(\omega) = \mathrm{Tr}\Big[\mathbf{\Gamma}_L\mathbf{G}_C^r\mathbf{\Gamma}_R\,\mathbf{G}_C^a\Big]. \tag{2.27}$$

It has been proved by Xue [79] that the original Landauer formula for orthonormal basis-set is still applicable to non-orthogonal localized basis-set.

If we take spin degeneracy into account, we finally obtain the original Landauer formula

$$J = \frac{2e}{h}\int d\omega[f_L(\omega) - f_R(\omega)]T(\omega). \tag{2.28}$$

with total electrical conductance G

$$G = \frac{2e^2}{h}T(\omega) = \frac{2e^2}{h}\mathrm{Tr}\Big[\mathbf{\Gamma}_L\mathbf{G}_C^r\mathbf{\Gamma}_R\,\mathbf{G}_C^a\Big]. \tag{2.29}$$

Conductance quantum G_0 for spin-degenerate single channel is defined as

$$G_0 = \frac{2e^2}{h} \approx 77.48\ \mu S. \tag{2.30}$$

Actually this conductance quantization in units of G_0 was first observed [80, 81] in 1988. We further define transmission matrix $\mathbf{t}$

$$\mathbf{t} = \mathbf{\Gamma}_R^{\frac{1}{2}}\mathbf{G}_C^a\mathbf{\Gamma}_L^{\frac{1}{2}}, \tag{2.31}$$

then

$$T(\omega) = \mathrm{Tr}\Big[\mathbf{t}^\dagger\mathbf{t}\Big]. \tag{2.32}$$

The above total transmission formula from transmission matrix $\mathbf{t}$ is first derived by Fisher and Lee [70] who related the multichannel conductance in Landauer formula

with transmission matrix from standard Kubo's linear response theory of conductance. It is worth to mention that here electrical conductance G is the conductance for multichannels between two reservoirs [71], which has included contact quantum conductance. If we try to measure the conductance $\tilde{G}$ of the conductor region between two leads without reservoirs, then it is

$$\tilde{G} = G_0 \frac{T}{1-T}, \tag{2.33}$$

which means $\tilde{G}$ will be infinite if there is no scattering within conductor and the corresponding resistance $\tilde{R}$ is 0.

In this thesis we will use the original Landauer formula for non-interacting electrons. However, we are not limited by this case. Since we have localized quasi-atomic orbitals which will be introduced in the next chapter, we can efficiently build electron-electron interaction matrix under this basis-set and use GW approach to calculate quasi-particle Green's function with all self-energy due to electron-electron and electron-phonon interactions included. Therefore, we can efficiently apply the Meir's generalized Landauer formula for interacting electrons to calculate electrical conductance.

2.4 Green's function method with non-orthogonal localized basis-set

2.4.1 Two-terminal device setup

Two-terminal device is usually represented by the standard structure [56, 79]: *left electron reservoir - left lead(L) - conductor(C) - right lead(R) - right electron reservoir* as shown in Fig. 2-1. The total Hamiltonian of the device region without reservoirs is

$$\mathbf{H} = \mathbf{H}_L + \mathbf{H}_{CL} + \mathbf{H}_C + \mathbf{H}_{CR} + \mathbf{H}_R. \tag{2.34}$$

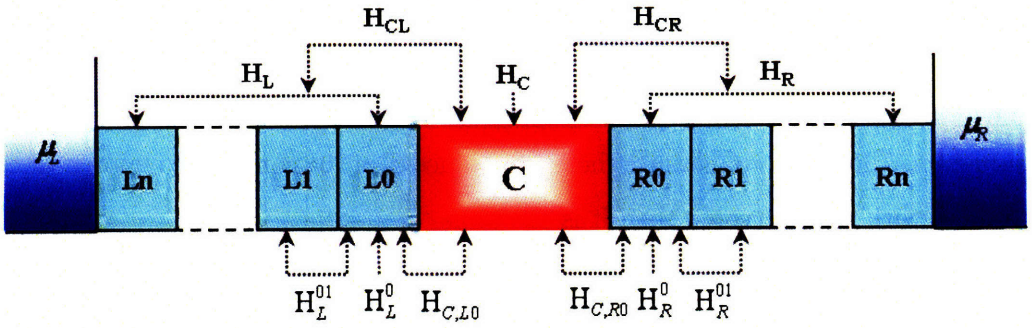

Figure 2-1: Standard two-terminal device: reservoir-lead-conductor-lead-reservoir

$\mathbf{H}_L$ and $\mathbf{H}_R$ are Hamiltonians for semi-infinite leads, and $\mathbf{H}_{CL}$ and $\mathbf{H}_{CR}$ are the coupling matrices between conductor and semi-infinite leads. Although the leads are semi-infinite, Hamiltonians in the non-orthogonal localized basis-set for both leads and conductor are localized. In another word, the non-zero off-diagonal terms of all the Hamiltonians are quite localized around the diagonal terms. Since usually left and right leads are extended systems, we may treat a number of unit cells as a principal layer $\mathbf{H}_L^i$ ($\mathbf{H}_R^i$) where $i = 0, 1, 2, \cdots$. The size of principal layer should be large enough so that in the localized basis-set the Hamiltonian $\mathbf{H}_L^{i,i\pm n}$ ($\mathbf{H}_R^{i,i\pm n}$) between the i-th principal layer and the $[i \pm n]$-th principal layer is negligible for $n \geq 2$, and thus only $\mathbf{H}_L^{i,i\pm 1}$ ($\mathbf{H}_R^{i,i\pm 1}$) needs to be considered. That should also apply for the interaction between the conductor and principal layers so that $\mathbf{H}_{C,Li}$ and $\mathbf{H}_{C,Ri}$ will be non-zero for $i = 0$ only. Several issues should be emphasized:

- Since we will use non-orthogonal localized basis-set, there will be a corresponding orbital overlap matrix for each Hamiltonian shown in Fig. 2-1.

- The localization and total number of basis-set is very crucial for computational cost since more delocalized basis will give larger principal layer and require more computation power for Green's function calculations.

- The choice of basis-set will strongly affect the accuracy of conductance calculations.

- The conductor region should be defined large enough so that there is no coupling between left and right leads.

For realistic calculations, we need to further simplify the total Hamiltonian and its Green's function. We first explicitly write the total Hamiltonian H and overlap matrix S in terms of each part of the device

$$\mathbf{H} = \begin{pmatrix} \mathbf{H}_L & \mathbf{H}_{CL}^+ & 0 \\ \mathbf{H}_{CL} & \mathbf{H}_C & \mathbf{H}_{CR} \\ 0 & \mathbf{H}_{CR}^+ & \mathbf{H}_R \end{pmatrix}, \qquad \mathbf{S} = \begin{pmatrix} \mathbf{S}_L & \mathbf{S}_{CL}^+ & 0 \\ \mathbf{S}_{CL} & \mathbf{S}_C & \mathbf{S}_{CR} \\ 0 & \mathbf{S}_{CR}^+ & \mathbf{S}_R \end{pmatrix}.$$

Retarded Green's function of Hamiltonian is defined as $(z\mathbf{S}-\mathbf{H})\mathbf{G}^r = \mathbf{I}$ with $z = \omega + i\eta$ and η is an infinitesimal positive number. Its corresponding expanded form is written as

$$\begin{pmatrix} z\mathbf{S}_L - \mathbf{H}_L & z\mathbf{S}_{CL}^+ - \mathbf{H}_{CL}^+ & 0 \\ z\mathbf{S}_{CL} - \mathbf{H}_{CL} & z\mathbf{S}_C - \mathbf{H}_C & z\mathbf{S}_{CR} - \mathbf{H}_{CR} \\ 0 & z\mathbf{S}_{CR}^+ - \mathbf{H}_{CR}^+ & z\mathbf{S}_R - \mathbf{H}_R \end{pmatrix} \begin{pmatrix} \mathbf{G}_L^r & \mathbf{G}_{LC}^r & \mathbf{G}_{LR}^r \\ \mathbf{G}_{CL}^r & \mathbf{G}_C^r & \mathbf{G}_{CR}^r \\ \mathbf{G}_{RL}^r & \mathbf{G}_{RC}^r & \mathbf{G}_R^r \end{pmatrix} = \begin{pmatrix} \mathbf{I}_L & 0 & 0 \\ 0 & \mathbf{I}_C & 0 \\ 0 & 0 & \mathbf{I}_R \end{pmatrix}. \quad (2.35)$$

Since we have short-ranged Hamiltonian and overlap matrices, $\mathbf{G}_{LR}^r$ and $\mathbf{G}_{RL}^r$ of direct couplings are negligible. Thus we have the following solution for the retarded Green's function of the conductor

$$\mathbf{G}_C^r = \left(z\mathbf{S}_C - \mathbf{H}_C - \mathbf{\Sigma}_L - \mathbf{\Sigma}_R\right)^{-1}, \quad (2.36)$$

$$\mathbf{\Sigma}_L = \left(z\mathbf{S}_{CL} - \mathbf{H}_{CL}\right)\mathbf{g}_L^r\left(z\mathbf{S}_{CL}^+ - \mathbf{H}_{CL}^+\right), \quad (2.37)$$

$$\mathbf{\Sigma}_R = \left(z\mathbf{S}_{CR} - \mathbf{H}_{CR}\right)\mathbf{g}_R^r\left(z\mathbf{S}_{CR}^+ - \mathbf{H}_{CR}^+\right), \quad (2.38)$$

$$\mathbf{g}_L^r = \left(z\mathbf{S}_L - \mathbf{H}_L\right)^{-1}, \quad (2.39)$$

$$\mathbf{g}_R^r = \left(z\mathbf{S}_R - \mathbf{H}_R\right)^{-1}. \quad (2.40)$$

$\mathbf{\Sigma}_{L,R}$ is the self-energy due to the coupling between conductor and leads, and $\mathbf{g}^r_{L,R}$ is the retarded Green's function of left and right leads, which are expanded in terms of principal layer Hamiltonians. Here we take $\mathbf{\Sigma}_L$ as an example,

$$
\begin{aligned}
\mathbf{\Sigma}_L &= \begin{pmatrix} \cdots & 0 & 0 & z\mathbf{S}_{C,L0} - \mathbf{H}_{C,L0} \end{pmatrix} \times \\
&\quad \begin{pmatrix} \ddots & \vdots & \vdots & \vdots \\ \cdots & z\mathbf{S}^0_L - \mathbf{H}^0_L & z\mathbf{S}^{10}_L - \mathbf{H}^{10}_L & 0 \\ \cdots & z\mathbf{S}^{01}_L - \mathbf{H}^{01}_L & z\mathbf{S}^0_L - \mathbf{H}^0_L & z\mathbf{S}^{10}_L - \mathbf{H}^{10}_L \\ \cdots & 0 & z\mathbf{S}^{01}_L - \mathbf{H}^{01}_L & z\mathbf{S}^0_L - \mathbf{H}^0_L \end{pmatrix}^{-1} \begin{pmatrix} \vdots \\ 0 \\ 0 \\ z\mathbf{S}^+_{C,L0} - \mathbf{H}^+_{C,L0} \end{pmatrix} \\
&= \begin{pmatrix} \cdots & 0 & 0 & z\mathbf{S}_{C,L0} - \mathbf{H}_{C,L0} \end{pmatrix} \begin{pmatrix} \ddots & \vdots & \vdots & \vdots \\ \cdots & \mathbf{g}^2_L & \mathbf{g}^{21}_L & \mathbf{g}^{20}_L \\ \cdots & \mathbf{g}^{12}_L & \mathbf{g}^1_L & \mathbf{g}^{10}_L \\ \cdots & \mathbf{g}^{02}_L & \mathbf{g}^{01}_L & \mathbf{g}^0_L \end{pmatrix} \begin{pmatrix} \vdots \\ 0 \\ 0 \\ z\mathbf{S}^+_{C,L0} - \mathbf{H}^+_{C,L0} \end{pmatrix} \\
&= \left(z\mathbf{S}_{C,L0} - \mathbf{H}_{C,L0}\right) \mathbf{g}^0_L \left(z\mathbf{S}_{C,L0} - \mathbf{H}^+_{C,L0}\right). \qquad (2.41)
\end{aligned}
$$

$\mathbf{g}^0_L$ is the self-energy of the first principal layer near the conductor C. The similar expression for $\mathbf{g}^0_R$ can be directly obtained by changing "L" to "R" in the above formula. With the various quantities listed above, we can calculate electrical conductance using Landauer formula

$$G = \frac{2e^2}{h} T(\omega) = \frac{2e^2}{h} \mathrm{Tr}\Big[\mathbf{\Gamma}_L \mathbf{G}^r_C \mathbf{\Gamma}_R \, \mathbf{G}^a_C\Big], \qquad (2.42)$$

and total density of states $N_C(\omega)$ for the conductor region is given by

$$N_C(\omega) = -\frac{1}{\pi} \mathrm{Im}\Big\{ \mathrm{Tr}\Big[\mathbf{G}^r_C \mathbf{S}_C\Big] \Big\}. \qquad (2.43)$$

The corresponding local density of states $N(\mathbf{r}, \omega)$ is also easy to compute for any localized basis-set $\phi_m(\mathbf{r})$

$$N_C(\mathbf{r}, \omega) = -\frac{1}{\pi} \lim_{\eta \to 0} \sum_{mn} \mathrm{Im}\Big[\mathbf{G}^r_C(\omega + i\eta)\Big] \, \phi^*_m(\mathbf{r}) \, \phi_n(\mathbf{r}). \qquad (2.44)$$

2.4.2 Surface Green's function

The most difficult task is to evaluate $\mathbf{g}_L^0$ and $\mathbf{g}_R^0$. If we continue to iteratively evaluate $\mathbf{g}_L^0$, $\mathbf{g}_L^1$, $\cdots$, we will easily obtain the following recursion relation for the n-th principal layer

$$\mathbf{g}_L^n = \frac{1}{z\mathbf{S}_L^n - \mathbf{H}_L^n - \left(z\mathbf{S}_L^{n,n+1} - \mathbf{H}_L^{n,n+1}\right)\mathbf{g}_L^{n+1}\left(z\mathbf{S}_L^{n+1,n} - \mathbf{H}_L^{n+1,n}\right)}. \tag{2.45}$$

The above equation can be directly solved by iterative calculations until $\mathbf{g}_L^0$ converges. However, another method by Sancho and *et al.* [82, 83, 84] can evaluate the surface Green's function $\mathbf{g}_L^0$ much more efficiently.

We follow Sancho's method [82] by expanding the Hamiltonian and retarded Green's function explicitly

$$\begin{pmatrix} \ddots & \vdots & \vdots & \vdots \\ \cdots & z\mathbf{S}_L^0 - \mathbf{H}_L^0 & z\mathbf{S}_L^{10} - \mathbf{H}_L^{10} & 0 \\ \cdots & z\mathbf{S}_L^{01} - \mathbf{H}_L^{01} & z\mathbf{S}_L^0 - \mathbf{H}_L^0 & z\mathbf{S}_L^{10} - \mathbf{H}_L^{10} \\ \cdots & 0 & z\mathbf{S}_L^{01} - \mathbf{H}_L^{01} & z\mathbf{S}_L^0 - \mathbf{H}_L^0 \end{pmatrix} \begin{pmatrix} \ddots & \vdots & \vdots & \vdots \\ \cdots & \mathbf{g}_L^2 & \mathbf{g}_L^{21} & \mathbf{g}_L^{20} \\ \cdots & \mathbf{g}_L^{12} & \mathbf{g}_L^1 & \mathbf{g}_L^{10} \\ \cdots & \mathbf{g}_L^{02} & \mathbf{g}_L^{01} & \mathbf{g}_L^0 \end{pmatrix} = \mathbf{I}. \tag{2.46}$$

It is easy to see from the above equation that

$$\mathbf{g}_L^{n,0} = \left(z\mathbf{S}_L^0 - \mathbf{H}_L^0\right)^{-1}\left[\left(\mathbf{H}_L^{10} - z\mathbf{S}_L^{10}\right)\mathbf{g}_L^{n-1,0} + \left(\mathbf{H}_L^{01} - z\mathbf{S}_L^{01}\right)\mathbf{g}_L^{n+1,0}\right], \tag{2.47}$$

from which we can define

$$\mathbf{t}_L^0 = \left(z\mathbf{S}_L^0 - \mathbf{H}_L^0\right)^{-1}\left(\mathbf{H}_L^{10} - z\mathbf{S}_L^{10}\right) \tag{2.48}$$

$$\tilde{\mathbf{t}}_L^0 = \left(z\mathbf{S}_L^0 - \mathbf{H}_L^0\right)^{-1}\left(\mathbf{H}_L^{01} - z\mathbf{S}_L^{01}\right). \tag{2.49}$$

Then we get the following simple expression

$$\mathbf{g}_L^{n,0} = \mathbf{t}_L^0\,\mathbf{g}_L^{n-1,0} + \tilde{\mathbf{t}}_L^0\,\mathbf{g}_L^{n+1,0}, \tag{2.50}$$

which can be repeated iteratively. After i iterations

$$\mathbf{g}_L^{n,0} = \mathbf{t}_L^i \, \mathbf{g}_L^{n-2^i,0} + \tilde{\mathbf{t}}_L^i \, \mathbf{g}_L^{n+2^i,0}, \tag{2.51}$$

where $\mathbf{t}_L^i$ and $\tilde{\mathbf{t}}_L^i$ are

$$\mathbf{t}_L^i = \left(I - \mathbf{t}_L^{i-1}\tilde{\mathbf{t}}_L^{i-1} - \tilde{\mathbf{t}}_L^{i-1}\mathbf{t}_L^{i-1}\right)^{-1}(\mathbf{t}_L^{i-1})^2 \tag{2.52}$$

$$\tilde{\mathbf{t}}_L^i = \left(I - \mathbf{t}_L^{i-1}\tilde{\mathbf{t}}_L^{i-1} - \tilde{\mathbf{t}}_L^{i-1}\mathbf{t}_L^{i-1}\right)^{-1}(\tilde{\mathbf{t}}_L^{i-1})^2. \tag{2.53}$$

It should be mentioned that $\mathbf{t}_L^i$ and $\tilde{\mathbf{t}}_L^i$ are not the transmission matrix defined in the previous section. Assuming that $n = 2^i$, we then obtain the following expression for $\mathbf{g}_L^{n,0}$

$$\mathbf{g}_L^{1,0} = \left(\mathbf{t}_L^0 + \tilde{\mathbf{t}}_L^0\mathbf{t}_L^1 + \cdots + \tilde{\mathbf{t}}_L^0 \cdots \tilde{\mathbf{t}}_L^{i-1}\mathbf{t}_L^i\right) \mathbf{g}_L^0 + \tilde{\mathbf{t}}_L^i \, \mathbf{g}_L^{2^{i+1},0}. \tag{2.54}$$

We should run enough iterations until the norm of $\mathbf{t}_L^i$ and $\tilde{\mathbf{t}}_L^i$ is less than certain threshold, thus

$$\mathbf{g}_L^{1,0} = \left(\mathbf{t}_L^0 + \tilde{\mathbf{t}}_L^0\mathbf{t}_L^1 + \cdots + \tilde{\mathbf{t}}_L^0 \cdots \tilde{\mathbf{t}}_L^{i-1}\mathbf{t}_L^i\right) \mathbf{g}_L^0 = \bar{\mathbf{T}}\mathbf{g}_L^0, \tag{2.55}$$

where

$$\bar{\mathbf{T}} = \mathbf{t}_L^0 + \tilde{\mathbf{t}}_L^0\mathbf{t}_L^1 + \cdots + \tilde{\mathbf{t}}_L^0 \cdots \tilde{\mathbf{t}}_L^{i-1}\mathbf{t}_L^i. \tag{2.56}$$

Replacing $\mathbf{g}_L^{1,0}$ in Eq. (2.47) with the above expression for $n = 0$, we finally have

$$\mathbf{g}_L^0 = \left[z\mathbf{S}_L^0 - \mathbf{H}_L^0 - \left(\mathbf{H}_L^{01} - z\mathbf{S}_L^{01}\right)\bar{\mathbf{T}}\right]^{-1}. \tag{2.57}$$

Compared to Eq. (2.45), the above Eq. (2.57) is much more efficient since for each i-th iteration the latter one includes 2^i layers. In the former method the full convergence will be achieved after several hundred steps, however with Sancho's algorithm only 10 to 20 iterations are required to reach the same convergence criteria. This efficient algorithm is implemented in our code for electrical conductance calculations.

2.4.3 Nonequilibrium Green's function method

Although currently we have not implemented self-consistent nonequilibrium Green's function(NEGF) method to include the effect of bias voltage, I would like to briefly summarize the crucial steps toward NEGF implementation with our localized quasi-atomic orbitals in future. The most important step of the NEGF method is to iteratively evaluate non-equilibrium charge density under finite bias, thus obtain new Kohn-Sham potentials and its new eigenvalues and eigenstates, then construct localized quasi-atomic orbitals and its tight-binding Hamiltonian and overlap matrices until final convergence of total charge density or Kohn-Sham potential is achieved. The density matrix in a localized orbital basis is

$$\mathbf{D}_C = \int \frac{d\omega}{2\pi i} \mathbf{G}_C^<(\omega) \tag{2.58}$$

From Eq. (2.15) and Eq. (2.22), density matrix is rewritten as

$$\begin{aligned}
\mathbf{D}_C &= \int_{-\infty}^{+\infty} \frac{d\omega}{2\pi i} \left[\mathbf{G}_C^r \left(i f_L \, \mathbf{\Gamma}_L + i f_R \, \mathbf{\Gamma}_R \right) \mathbf{G}_C^a \right] && (2.59) \\
&= \int_{-\infty}^{+\infty} \frac{d\omega}{2\pi} \mathbf{G}_C^r \left[f_L \left(\mathbf{\Gamma}_L + \mathbf{\Gamma}_R \right) + \left(f_R - f_L \right) \mathbf{\Gamma}_R \right] \mathbf{G}_C^a && (2.60) \\
&= \int_{-\infty}^{+\infty} \frac{d\omega}{2\pi} i f_L \left(\mathbf{G}_C^r - \mathbf{G}_C^a \right) + \int_{-\infty}^{+\infty} \frac{d\omega}{2\pi} \mathbf{G}_C^r \left[\left(f_R - f_L \right) \mathbf{\Gamma}_R \right] \mathbf{G}_C^a, && (2.61)
\end{aligned}$$

where we have also used the identity $i(\mathbf{G}_C^r - \mathbf{G}_C^a) = \mathbf{G}_C^r(\mathbf{\Gamma}_L + \mathbf{\Gamma}_R)\mathbf{G}_C^a$. Then finally we have

$$\mathbf{D}_C = -\int_{-\infty}^{+\infty} \frac{d\omega}{\pi} \mathrm{Im}(\mathbf{G}_C^r) \, f_L + \int_{-\infty}^{+\infty} \frac{d\omega}{2\pi} \mathbf{G}_C^r \, \mathbf{\Gamma}_R \, \mathbf{G}_C^a \, (f_R - f_L). \tag{2.62}$$

At the equilibrium, $\mu_L = \mu_R$, thus $f_L = f_R$ and the second term will be zero. The first integration contains the charge density contribution from the equilibrium condition, while the second one contains density correction due to the nonequilibrium condition at finite bias. Since the first term is analytic and smooth, it can be computed from contour integration on the complex plane. The second term only needs to be calculated in a small energy window from $\mu_{\min}$ to $\mu_{\max}$ using a fine grid close to real

axis, where $\mu_{\min} = \min\{\mu_L, \mu_R\}$ and $\mu_{\max} = \max\{\mu_L, \mu_R\}$. The charge density in real space $\rho_C(\mathbf{r})$ corresponding to density matrix $\mathbf{D}_C$ of conductor is given by

$$\rho_C(\mathbf{r}) = \sum_{mn} (\mathbf{D}_C)_{mn}\, \phi_m^*(\mathbf{r})\phi_n(\mathbf{r}). \tag{2.63}$$

The new charge density is treated as new input for DFT calculations where we obtain updated eigenvalues and Bloch eigenstates from either traditional DFT electronic minimization or non-self-consistent Harris-Foulkes functional [85, 86]. During the above step, the charge density is always fixed. Then new *ab initio* localized quasi-atomic orbitals and their tight-binding Hamiltonian are constructed from the DFT results and then the new iteration is performed to calculate new electrical conductance and charge density. The above steps are iteratively repeated until the input and output charge density converge within a certain small threshold at finite bias.

2.4.4 Conducting eigenchannel

Conducting eigenchannel analysis [54, 87] is very useful to understand the microscopic electron transport mechanism. There are at least two ways to obtain conducting eigenchannels with different normalization criteria based on Green's function method.

One simplest way is to diagonalize the total transmission matrix $\mathbf{t}^\dagger\mathbf{t} = \mathbf{\Gamma}_L\mathbf{G}_C^r\mathbf{\Gamma}_R\,\mathbf{G}_C^a$ in Landauer formula so that

$$\mathbf{U}^\dagger\mathbf{t}^\dagger\mathbf{t}\mathbf{U} = \mathbf{T}, \tag{2.64}$$

where $\mathbf{U}$ is the unitary transformation matrix to diagonalize $\mathbf{t}^\dagger\mathbf{t}$ and $\mathbf{T}$ is the diagonal matrix which contains transmission coefficients for the corresponding eigenchannels. Thus, we can find out those eigenchannels with non-zero transmission coefficients.

However, the above approach does not directly embed the transmission coefficient information into eigenchannel wavefunction. Paulsson and Brandbyge proposed a better approach with non-orthogonal basis-set. See Ref. [87] for the details of that approach.

2.4.5 Local current and induced orbital magnetic moment

By taking the trace of $\mathbf{t}^\dagger\mathbf{t}$ we can obtain electrical conductance G and net terminal current J. However, beside the net terminal current there exists quantum internal current [88, 89, 90] in various nanoscale materials such as graphene, fullerene, nanotubes and molecular bridges. The internal loop current is naturally associated with induced magnetic momentum at local region. A direct way to study those loop current is to calculate and visualize local current distribution [54, 88, 89, 90, 79] inside electronic devices. The simple form of bond current between atom i and atom j is expressed as

$$J_{ij} = \frac{4e}{h}\mathrm{Im}\big[G^n_{ij}H^C_{ij}\big], \tag{2.65}$$

where $\mathbf{G}^n$ is correlation Green's function determined by

$$\mathbf{G}^n(E) = \mathbf{G}^r_C\mathbf{\Gamma}_L\mathbf{G}^a_C. \tag{2.66}$$

Then the induced orbital magnetic moment $\mathbf{M}$ is

$$\mathbf{M} = \frac{1}{2}\int d\mathbf{r}\ \mathbf{r}\times\mathbf{j}(\mathbf{r}) = \frac{1}{2}J_{ij}\mathbf{r}_i\times\mathbf{r}_j. \tag{2.67}$$

2.4.6 Landauer formalism extended to multi-terminal devices

The original Landauer formalism for two-terminal devices has been extended to four-terminal electronic devices by Büttiker [73]. Within the same frame work, we can derive the Green's function formula of electrical conductance $G_{pq}(E)$ for any two leads in an n-terminal device,

$$G_{pq}(E) = \mathbf{\Gamma}_p\mathbf{G}^r_C\mathbf{\Gamma}_q\ \mathbf{G}^a_C, \tag{2.68}$$

where retarded Green's function $\mathbf{G}^r_C$ includes all the self-energies from n leads,

$$\mathbf{G}^r_C = \Big(z\mathbf{S}_C - \mathbf{H}_C - \sum_p \mathbf{\Sigma}_p\Big)^{-1}. \tag{2.69}$$

2.5 Summary

The above eigenchannel decomposition and local current mapping are useful tools to investigate electron transport mechanism and chemical bonding nature in molecular and nanoscale electronics. Three important steps to be carried out in future are to include transverse **k**-point sampling, to include full electron-electron correlation and electron-phonon coupling, and to take electromagnetic field into account.

The efficiency of Green's function method based on Landauer formalism relies on the localization of basis-set of Hamiltonian while the accuracy depends on the ground-state DFT calculation under zero-bias voltage or the self-consistent DFT calculation in the non-equilibrium situation. Both efficiency and accuracy can be achieved at the same time if we can start from plane-wave DFT results and construct a set of *ab initio* localized orbitals, such as Wannier functions, quasiatomic minimal basis-set or our quasiatomic orbitals (which will be introduced in the next chapter), and their corresponding tight-binding Hamiltonian and overlap matrix (if nonorthogonal) to exactly represent all the Bloch states in the range that we are interested in.

Chapter 3

Quasiatomic orbitals and their applications

The ground-state electronic structure of solids within single-particle approximation is often represented by extended Bloch eigenstates and their eigen energies. These delocalized Bloch states usually can not be directly used for further analysis and development. Meanwhile, chemical analysis, linear scaling (order-N) methods [91, 92, 93, 94], transport [95, 96, 97], modern theory of polarization [98] and magnetization [99], LDA+U [100, 101, 102] and self-interaction correction [103], etc. rely on high-quality localized basis-set. To achieve both efficiency and accuracy of various DFT applications, especially electrical conductance of nanoscale electronics described in the previous chapter, we have developed a new scheme based on Wannier functions [104, 105, 106], quasiatomic minimal basis orbitals (QUAMBO) [107, 108, 109, 110, 111], and projected-atomic-orbitals (PAO) [112, 113, 114] to construct a set of non-orthogonal localized quasiatomic orbitals (QO) and their *ab initio* tight-binding Hamiltonian and overlap matrix with density functional theory calculations.

This chapter is organized as follows. In Sec. 3.1 we will discuss *ab initio* tight-binding method including Wannier function, QUAMBO and our QO. In Sec. 3.2 we review USPP and PAW formalisms required for properly defining projection. In Sec. 3.3 quasiatomic orbitals within USPP and PAW formalisms are derived for extended systems. Improved subspace optimization method is also discussed in this section.

The corresponding tight-binding Hamiltonian and overlap matrices, Mülliken charge matrix and bond order based on QO are derived in Sec. 3.4. Our QO validates the general applicability of Slater's linear combinations of atomic orbitals (LCAO) idea, and points to future *ab initio* tight-binding parametrizations. To demonstrate the efficiency and robustness of this method, in Sec. 3.5 band structure, QO-projected band structure, total density of states, QO-projected density of states, Mülliken charge, bond order, Fermi surface and velocity/QO-projected Fermi surface [115, 116, 117] are calculated and compared with planewave DFT results for various extended systems. Mülliken charges for atoms in silane (SiH_4), methane (CH_4), beta phase silicon carbide (β-SiC) crystal, and other systems are analyzed. QOs are, therefore, demonstrated to be a good candidate for quantitatively measuring charge transfer. In Sec. 3.6, 3.7, and 3.8 we will discuss the similarity and difference among QO, maximal localized Wannier function (MLWF), QUAMBO, and PAO. In Sec. 3.9 we summarize our work and discuss some future applications of QO.

3.1 Introduction to *ab initio* tight-binging method

Density functional theory (DFT) has been extensively developed in the past decades. For condensed-matter systems, efficient supercell calculations using planewave basis and ultrasoft pseudopotential (USPP) or projector augmented-wave (PAW) are now mainstream. Planewave basis is easy to implement. Its quality is continuously tunable and spatially homogeneous. The drawback is that this "rich basis" can sometimes mask the physical ingredients of a problem, making their detection and distillation difficult. This becomes particularly clear when one wants to develop a parametrized tight-binding (TB) potential [118, 119, 120] or classical empirical potential [121] based on planewave DFT results, often a crucial step in multiscale modeling [122]. For developing TB potentials, one usually fits to the DFT total energy, forces and quasiparticle energies $\{\varepsilon_n\}$ (band diagram). However the planewave electronic-structure information is still vastly under-utilized in the potential development process.

Modern TB approach assumes the existence of a minimal basis of dimension sN,

where N is the number of atoms and s is a small prefactor (4 for Si), without explicitly stating what these basis orbitals are. Under this minimal basis, the electronic Hamiltonian is represented by a small matrix $\mathbf{H}^{\mathrm{TB}}_{sN\times sN}$, which is parametrized[123], and then explicitly diagonalized at runtime to get $\{\varepsilon_n^{\mathrm{TB}}\}$. In contrast, under planewave basis the basis-space dimension is pN, where p is a large number, usually $10^2 - 10^3$. The Kohn-Sham Hamiltonian represented under the planewave basis, $\mathbf{H}^{\mathrm{KS}}_{pN\times pN}$, is often so large that it cannot be stored in computer memory. So instead of direct diagonalization which yields the entire eigenspectrum, matrix-free algorithms that only call upon matrix-vector products are employed to find just a small portion of the eigenspectrum $\{\varepsilon_n\}$ on the low-energy end [124]. This is wise because the ground-state total energy and a great majority of the system's physical properties depend only on a small portion of the electronic eigenstates with ε_n below or near the Fermi energy ε_{F}.

Unlike many *ab initio* approaches that adopt explicit, spatially localized basis sets such as Slater-type orbitals (STO) and Gaussian-type orbitals (GTO) [125], the defining characteristic of the *empirical* TB approach is the unavailability of the minimal-basis orbitals, which are declared to exist but never shown explicitly. This leads to the following conundrum. In constructing material-specific TB potentials [118, 119, 120], the $\mathbf{H}^{\mathrm{TB}}_{sN\times sN}$ matrix is parametrized, but the $sN(sN+1)/2$ matrix elements are not targets of fitting themselves because one does not have access to their values, since one never knows the minimal-basis orbitals to start with. Instead, the fitting targets are the eigenvalues of $\mathbf{H}^{\mathrm{TB}}_{sN\times sN}$, $\{\varepsilon_n^{\mathrm{TB}}\}$, which are demanded to match the occupied eigenvalues $\{\varepsilon_n\}_{\mathrm{occ}}$ of $\mathbf{H}^{\mathrm{KS}}_{pN\times pN}$ from planewave DFT calculation, and perhaps a few unoccupied $\{\varepsilon_n\}$ as well. A transferable TB potential should have the correct physical ingredients; but a great difficulty arises here because $\{\varepsilon_n\}$ in fact contain much less information than the $\mathbf{H}^{\mathrm{TB}}_{sN\times sN}$ matrix elements. From $\mathbf{H}^{\mathrm{TB}}_{sN\times sN}$ matrix we can get $\{\varepsilon_n^{\mathrm{TB}}\}$, but not vice versa. As fitting targets, not only are the $\{\varepsilon_n^{\mathrm{TB}}\}$ much fewer in number than the matrix elements (sN versus $sN(sN+1)/2$), but they are also much less physically transparent. The TB matrix elements must convey clear spatial (both position and orientation) information, as is evident from the analytic angular func-

tions of the original Slater-Koster LCAO [126] scheme based on $pp\pi$, $pd\sigma$, $dd\delta$, etc. Physi-chemical effects such as charge transfer, saturation and screening [118, 119, 120] should manifest more directly in the matrix elements, but such information gets garbled after diagonalization. For example, if the 5th eigenvalue $\varepsilon^{\rm TB}_{n=5}$ at $\mathbf{k} = [111]\pi/3a$ in β-SiC crystal is lower than that of planewave DFT by 0.2 eV, should one increase the screening term [118, 119, 120] in the TB model to get a better fit, or not? The answer will not be at all obvious, since (a) the $\mathbf{k}$-space result masks the real-space physics, and (b) the eigenvalue reflects nothing about the spatial features of the eigenfunction $|\psi_{n\mathbf{k}}\rangle$. The information necessary for answering the question is hidden in the wavefunctions $\{|\psi_n\rangle\}$ (now expanded in planewaves), and the electronic Hamiltonian $\mathbf{H}^{\rm KS}_{pN\times pN}$ (now a huge matrix). But the clues are simply not sufficiently embedded in $\{\varepsilon_n\}$, which do not contain any spatial information [98]. Thus, the present empirical TB approach is like "shooting in the dark".

It is thus desirable to come up with a systematic and numerically robust method to distill information from planewave DFT calculation into a TB representation. Philosophically this is the same as the "downfolding" procedure of Andersen et al.[127] Namely, can we construct the minimal basis functions from $\{|\psi_n\rangle\}$ explicitly? can we get $\mathbf{H}^{\rm TB}_{sN\times sN}$ from $\mathbf{H}^{\rm KS}_{pN\times pN}$? This $\mathbf{H}^{\rm KS}_{pN\times pN} \rightarrow \mathbf{H}^{\rm TB}_{sN\times sN}$ mapping would work like computer file compression, because $\mathbf{H}^{\rm KS}_{pN\times pN}$ is a huge matrix and $\mathbf{H}^{\rm TB}_{sN\times sN}$ is small. Can then the compression be lossless? i.e. can we retain exactly the occupied eigenspectrum $\{\varepsilon_n\}_{\rm occ}$ of $\mathbf{H}^{\rm KS}_{pN\times pN}$, and perhaps a few unoccupied $\{\varepsilon_n\}$ as well? For modeling the total energy of the system, only the occupied bands are important. But if one is interested in transport properties [128], the low-energy portion of the unoccupied bands will be important as well.

In this chapter we present an explicit *ab initio* TB matrix construction scheme based on planewave DFT calculations. The present scheme is significantly improved over previous developments of QUAMBO [107, 108, 109, 110, 111] in efficiency and stability, and now extended to work with USPP/PAW formalisms and popular DFT programs such as VASP [31, 32, 129] and DACAPO [33, 35]. The improved scheme no longer requires the computation and storage of the wavefunctions of hundreds

of unoccupied DFT bands, reducing disk/memory/CPU time requirements by order of magnitude. But one also obtains converged quasiatomic orbitals of the previous scheme [107, 108, 109, 110, 111] as if infinite number of unoccupied bands were taken - the so-called "infiniband" limit that completely eliminates unoccupied bands truncation error (UBTE). We will demonstrate through a large number of examples that an "atomic orbital (AO) like" minimal basis can generally be constructed, and are sufficiently localized for both insulators and metals. These examples [130] demonstrate the physical soundness underlying the environment-dependent TB approach[118]. While we stop short of giving material-specific parametrizations for the $\mathbf{H}^{\mathrm{TB}}_{sN\times sN}$ matrix elements, their physical properties will be discussed with view towards explicit parametrizations [118, 119, 120] later.

Our method follows the general approach of Wannier function (WF) [104, 131, 132, 133, 105, 134, 106, 135, 136, 137, 138, 139, 140, 141], which combines Bloch eigenstates obtained from periodic cell calculation in $\mathbf{k}$-space to achieve good localization in real space. Other than chemical analysis, linear scaling (order-N) methods [91, 92, 93, 94], transport [95, 96, 97], modern theory of polarization [98] and magnetization [99], LDA+U [100, 101, 102] and self-interaction correction [103] etc. also rely on high-quality localized basis set. The WF approach guarantees exact reproducibility of the occupied subspace, and exponential localization in the case of a single band [142] and insulators [141].

There is some indeterminacy ("gauge" freedom [143, 144]) in the WF approach. One could multiply a smooth phase function on the Bloch band states and they would still be smooth Bloch bands. One could also mix different band branches and still maintain unitarity of the WF transform. Marzari and Vanderbilt proposed the concept of maximally localized Wannier functions (MLWF) [105] for an isolated group of bands, using the quadratic spread localization measure originally proposed by Foster and Boys [145] for molecular systems. Later Souza, Marzari and Vanderbilt [106] extended this scheme for entangled bands by selecting a subspace from a larger Hilbert space within a certain energy window. Choosing the MLWF gauge for a given energy window removes all indeterminacy in the WF transform. Unfortunately,

there is no closed-form solution for MLWF, so iterative numerical procedures must be adopted, associated with which is the problem of finding global minima. Despite the tremendous success of the MLWF approach [105, 106], there are still something to be desired of in the way of a robust and physically transparent algorithm, resulting in a great deal of recent activities [135, 136, 107, 108, 109, 110, 137, 138, 139, 140, 111].

Here we take a different strategy [112, 113, 114, 107, 108, 109, 110, 111] which eventually combines both Lu's QUAMBO and Pulay's PAO. While maximal localization is a worthy goal, if there is no analytical solution its attainment is perhaps uncertain. The question is, does one really need *maximal* localization? May one be satisfied if a set of WF orbitals can be constructed robustly, and they are "localized enough"? Both the projected atomic orbitals [112, 113, 114] and the quasiatomic minimal basis orbitals [107, 108, 109, 110, 111] are constructed based on the projection operation, where one demands maximal similarity between the minimal basis orbitals with preselected atomic orbitals with angular momentum quantum numbers. Since "maximal similarity" is a quadratic problem, it has exact solution and the numerical procedure is non-iterative and relatively straightforward. However briefly speaking QUAMBO and PAO use two different strategies to obtain the unoccupied Bloch space. On the other hand, whether these maximally similar WF orbitals are localized enough for the practical purpose of *ab initio* TB analysis and constructing *ab initio* TB potentials needs to be demonstrated, through a large number of examples. Preliminary results are encouraging. We note that philosophically, these minimal basis orbitals "maximally similar" to atomic orbitals are probably the closest to the original idea of Slater and Koster of linear combinations of atomic orbitals, since using true atomic orbital basis leads to very poor accuracy in present empirical TB standard.

3.2 Projection operation in USPP / PAW

Previous work [107, 108, 109, 110, 111] was based on norm-conserving pseudopotentials. We extend the method to USPP and PAW calculations, which are implemented in popular DFT codes such as VASP [32, 129], DACAPO [35], PWscf [146], CPMD

[147], CP-PAW [148] and ABINIT [149]. We have implemented interfaces to VASP and DACAPO [130]. The formalisms of USPP / PAW have been carefully reviewed in the first chapter and Ref. [128]. Here we just highlight the part important to quasiatomic orbitals, which is the metric operator $\hat{S}$.

The key idea behind USPP and PAW is a mapping of the true valence electron wavefunction $\tilde{\psi}(\mathbf{x})$ to a pseudowavefunction $\psi(\mathbf{x})$: $\tilde{\psi} \leftrightarrow \psi$, just as in any pseudopotential scheme. However, by discarding the requirement that $\psi(\mathbf{x})$ must be norm-conserved ($\langle\psi|\psi\rangle = 1$) while matching $\tilde{\psi}(\mathbf{x})$ outside the pseudopotential cutoff, a greater smoothness of $\psi(\mathbf{x})$ in the core region can be achieved; and therefore less planewaves are required to represent3 $\psi(\mathbf{x})$. In order for the physics to still work, in USPP and PAW schemes one must define augmentation charges in the core region, and solve a generalized eigenvalue problem

$$\hat{H}|\psi_n\rangle = \varepsilon_n \hat{S}|\psi_n\rangle, \tag{3.1}$$

where $\hat{S}$ is a Hermitian and positive definite operator. $\hat{S}$ defines the fundamental metric of the linear Hilbert space of pseudowavefunctions. Physically meaningful inner product (ψ, ψ') between two pseudowavefunctions is always $\langle\psi|\hat{S}|\psi'\rangle$ instead of $\langle\psi|\psi'\rangle$. For instance, $\langle\psi_m|\psi_n\rangle \neq \delta_{mn}$ between the eigenfunctions of (3.1) because it is not actually physically meaningful, but $\langle\psi_m|\hat{S}|\psi_n\rangle \equiv \langle\tilde{\psi}_m|\tilde{\psi}_n\rangle = \delta_{mn}$ is. The $\hat{S}$ operator is given by

$$\hat{S} = 1 + \sum_{i,j,I} q_{ij}^I |\beta_j^I\rangle\langle\beta_i^I|, \tag{3.2}$$

where $i \equiv \{\varepsilon_i lm\}$ is the angular momentum channel number [25], and I labels the ions. In above, the projector function $\beta_i^I(\mathbf{x}) \equiv \langle\mathbf{x}|\beta_i^I\rangle$ of atom I's channel i is

$$\beta_i^I(\mathbf{x}) = \beta_i(\mathbf{x} - \mathbf{X}_I), \tag{3.3}$$

where $\mathbf{X}_I$ is the ion position, and $\beta_i(\mathbf{x})$ vanishes outside the pseudopotential cutoff.

Just like $\hat{H}$, $\hat{S}$ contains contributions from all ions. Consider a parallelepiped computational supercell of volume Ω, with N ions inside. One usually will perform

$l_1 \times l_2 \times l_3$ **k**-sampling in the supercell's first Brillouin zone in a ground-state total energy calculation. For the sake of clarity, let us define a Born-von Kármán (Bv) universe, which is a $l_1 \times l_2 \times l_3$ replica of the computational supercell, periodically wrapped around. So the Bv universe has finite volume $l_1 l_2 l_3 \Omega$, with total of $l_1 l_2 l_3 N$ ions. Using Bloch's theorem, it is easy to show that the eigenstates of the Bv universe can be labeled by the $l_1 l_2 l_3$ **k**'s of the **k**-mesh. Computationally, the $l_1 \times l_2 \times l_3$ **k**-sampling is a cost-saving measure. But the basic metric of function length and inner product should be defined in the Bv universe:

$$(\psi, \psi') \equiv \langle \psi | \hat{S} | \psi' \rangle = \int_{\text{Bv}} d^3\mathbf{x} \psi^*(\mathbf{x}) (\hat{S}|\psi'\rangle)(\mathbf{x}). \tag{3.4}$$

$\hat{S}$ above contains contributions from all $l_1 l_2 l_3 N$ ions.

Suppose ψ and ψ' both satisfy Bloch's theorem, but with different **k** labels in the $l_1 \times l_2 \times l_3$ **k**-mesh:

$$\psi(\mathbf{x} - \mathbf{a}) = \psi(\mathbf{x}) e^{-i\mathbf{k}\cdot\mathbf{a}}, \quad \psi'(\mathbf{x} - \mathbf{a}) = \psi'(\mathbf{x}) e^{-i\mathbf{k}'\cdot\mathbf{a}}, \quad \mathbf{k} \neq \mathbf{k}', \tag{3.5}$$

where **a** is an arbitrary combination of supercell edge vectors, then ψ and ψ' will obviously be orthogonal in (3.4). This is because the $\hat{S}$ metric in (3.2), being a simple sum, commutes with the supercell translation operator $\hat{T}(\mathbf{a})$: $[\hat{S}, \hat{T}(\mathbf{a})] = 0$. So it is easy to show that $(\hat{S}|\psi'\rangle)(\mathbf{x})$ is also a Bloch state labeled by $\mathbf{k}'$:

$$(\hat{S}|\psi'\rangle)(\mathbf{x} - \mathbf{a}) = e^{-i\mathbf{k}'\cdot\mathbf{a}} (\hat{S}|\psi'\rangle)(\mathbf{x}). \tag{3.6}$$

So the integral (3.4) can be decomposed into a sum, which is always zero no matter how ψ and ψ' overlap in Ω, due to the $e^{i(\mathbf{k}-\mathbf{k}')\cdot\mathbf{a}}$ phase factor when going around the Bv universe. On the other hand, if $\mathbf{k} = \mathbf{k}'$, then the two phase factors cancel out, and it is easy to show that:

$$(\psi, \psi') = \int_{\text{Bv}} d^3\mathbf{x} \psi^*(\mathbf{x}) (\hat{S}|\psi'\rangle)(\mathbf{x}) = l_1 l_2 l_3 \int_{\Omega} d^3\mathbf{x} \psi^*(\mathbf{x}) (\hat{S}|\psi'\rangle)(\mathbf{x}). \tag{3.7}$$

From above we see it is always advantageous to "think" in the Bv universe, but by employing Bloch's theorem we often only need to "compute" in the Ω-supercell.

With the inner product defined in (3.4), the projection of any state $|\phi\rangle$ on $|\psi\rangle$ is straightforward:

$$\hat{P}_\psi|\phi\rangle \equiv \frac{(\psi,\phi)}{(\psi,\psi)}|\psi\rangle = \frac{\langle\psi|\hat{S}|\phi\rangle}{\langle\psi|\hat{S}|\psi\rangle}|\psi\rangle. \tag{3.8}$$

Note that all functions discussed here must be periodic in the Bv universe. $|\phi\rangle$ could be atomic orbital (AO) like. Even though real AOs are often obtained and represented in infinite space, this is not a problem numerically so long as the AO extent is much smaller than the size of the Bv universe. The AO extent does not have to be smaller than the computational supercell Ω, however.

3.3 Quasiatomic orbital

3.3.1 Introduction to QO algorithm

From a planewave calculation using USPP or PAW potential, we obtain Bloch eigenstates labeled by supercell $\mathbf{k}$ and band index n (occupied) or $\bar{n}$ (unoccupied; we always use index with bar on top to label unoccupied states). These supercell Bloch states $\{\psi_{n\mathbf{k}}\}$, $\{\psi_{\bar{n}\mathbf{k}}\}$ are often delocalized, making them hard to visualize and interpret. An alternative representation of electronic wavefunction and bonding is often needed in the flavor of the LCAO[126] or tight-binding [118, 119, 120] approach. Ideally, this representation should have features such as exponential localization of the basis orbitals [142], should be "AO-like", and should retain all the information of the original Bloch eigenstates expressed in planewaves, at least of all the *occupied* Bloch states $\{\psi_{n\mathbf{k}}\}$, so they can be losslessly reconstructed.

Quasiatomic minimal basis-set orbital (QUAMBO) is a projection-based non-iterative approach. It was first implemented by Lu *et al.* [107, 108, 109, 110, 111], after the previous work of Ruedenberg et al. [150] on molecular systems. The basic idea is illustrated in Fig. 3-1. The objective is to seek an optimized subspace $\mathcal{S}$, containing the occupied $\{\psi_{n\mathbf{k}}\}$ in its entirety plus a limited set of combined unoccupied

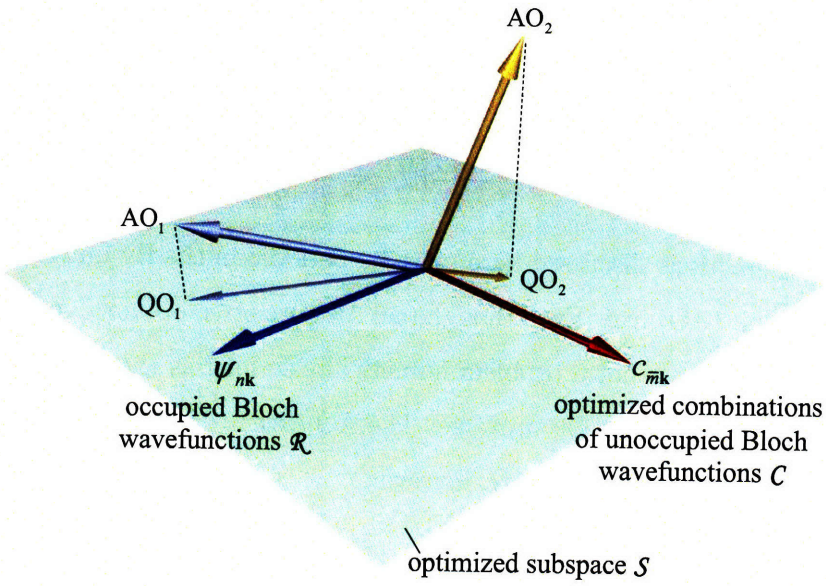

Figure 3-1: Illustration of QO construction. We seek a reduced optimized subspace, spanned by the occupied Bloch wavefunctions $\{\psi_{n\mathbf{k}}\}$, plus a limited number of $\{c_{\bar{m}\mathbf{k}}\}$ wavefunctions to be determined, such that the atomic orbitals (AO) have maximal projection onto the subspace. Once this optimized subspace is determined, the QOs which are the "shadows" of the AOs onto the subspace, form a non-orthogonal but complete basis for this subspace. The QOs can then be used to reconstruct all the occupied Bloch wavefunctions $\{\psi_{n\mathbf{k}}\}$ without loss. This means in a variational calculation, using the QO basis for this particular configuration would achieve the same total energy minimum as the full planewave basis. Furthermore since the QOs are maximally similar to the AOs, they inherit most of the AO characters.

$\{c_{\bar{m}\mathbf{k}}\}$ wavefunctions to be determined, such that the atomic orbitals have maximal projection onto this subspace. The dimension of this "optimized Bloch subspace" is constrained to be that of the minimal (tight-binding) basis, and $\{\psi_{n\mathbf{k}}\}$, $\{c_{\bar{m}\mathbf{k}}\}$ form an orthonormal basis for it. But the "shadows" of the AOs projected onto this subspace, which are the QOs, can represent the subspace equally well, forming a non-orthogonal but also complete basis for it. Furthermore, since the QOs are maximally similar to the AOs (under the constraint that they contain $\{\psi_{n\mathbf{k}}\}$ exactly), their localization properties should be "good".

It is important to realize that here we are doing dimension reduction, the optimized

subspace is a small part of the entire function space, which is infinite dimensional. Since each AO makes one shadow, and we use all shadows collected on the plane as non-orthogonal complete basis for the subspace, the dimension of the subspace has to be $sl_1l_2l_3N$, where s is the average number of AOs per atom. With the minimal basis scheme, s should be 4 for Si and C, and the AOs are $\{s, p_x, p_y, p_z\}$. If we take the smallest supercell admissible for diamond cubic Si, for instance, then $N = 2$ and the dimension of the optimized subspace has to be $8l_1l_2l_3$, which is equal to the total number of AOs in the Bv universe. Since we have $l_1l_2l_3$ **k**-points, this comes down to 8 $\psi_{n\mathbf{k}}$,$c_{\bar{m}\mathbf{k}}$'s per **k**. Because there are 4 (in general rN where $2r$ is the average valence number of atoms) occupied $\psi_{n\mathbf{k}}$'s at each **k**-point, we need to choose 4 complementary $c_{\bar{m}\mathbf{k}}$'s per **k**. These 4 $c_{\bar{m}\mathbf{k}}$'s will be chosen from the unoccupied $\{\psi_{\bar{n}\mathbf{k}}\}$ subspace, which is infinite dimensional. The whole process can be visualized as rotating the plane around the $\psi_{n\mathbf{k}}$ axis in Fig. 3-1, seeking the orientation where the longest shadows fall onto the plane (subspace $\mathcal{S}$).

Two remarks are in order. First, the label "occupied" can be replaced by "desired" Bloch wavefunctions in Fig. 3-1. While many problems such as fitting TB potentials are mainly concerned with reproducing the occupied bands and the total energy with a minimal basis, problems like excited-state calculations require more bands to be reproduced. Then, one just need to generalize the meaning of $\psi_{n\mathbf{k}}$ in Fig. 3-1 from "occupied" bands to "desired" bands. To be able to do this and still retain AO-like characters, the size of the subspace may necessarily be expanded, for example from $\{3s, 3p\}$ $(s = 4)$ to $\{3s, 3p, 4s, 3d\}$ $(s = 10)$ for Si, and then the "minimal basis" is taken to mean the minimal set of AO-like orbitals to reproduce the desired bands, whatever they may be, instead of just the occupied bands. Indeed, a novel utility of the present QO scheme is to quantitatively guide the user in deciding (a) when to expand, (b) how to expand, and (c) the effectiveness of representing the *desired* part of the electronic structure in AO-like orbitals with pseudo angular-momentum quantum numbers. Formally, denote the subspace we want to reproduce at each **k** by $\mathcal{R}(\mathbf{k}) \equiv \{\psi_{n\mathbf{k}}\}$. Then, the wavefunctions we do not desire to reproduce at each **k** form a complementary subspace $\bar{\mathcal{R}}(\mathbf{k}) \equiv \{\psi_{\bar{n}\mathbf{k}}\}$, which is infinite dimensional. We note that

$\langle \dim \mathcal{R}(\mathbf{k}) \rangle = rN$, but $\dim \mathcal{R}(\mathbf{k})$ or $\mathcal{R}(\mathbf{k})$ generally may not be a continuous function of $\mathbf{k}$. For instance in metals, the Fermi energy ε_{F} cuts across continuous bands, and the set of occupied bands is not a continuous function of $\mathbf{k}$. We shall call any mathematical or numerical feature caused by a discontinuity in $\mathcal{R}(\mathbf{k})$ as being caused by "type-I" discontinuity.

Second, note that the subspace $\mathcal{S}$ we seek in Fig. 3-1 in the Bv universe can be decomposed into smaller subspaces labeled by the Bloch $\mathbf{k}$'s, that are mutually orthogonal:

$$\mathcal{S} \;=\; \mathcal{S}(\mathbf{k}_1) \cup \mathcal{S}(\mathbf{k}_2) \cup ... \cup \mathcal{S}(\mathbf{k}_{l_1 l_2 l_3}) \tag{3.9}$$

Therefore, the length squared of an AO's shadow in $\mathcal{S}$ is exactly the sum of the projected length squared onto every $\mathcal{S}(\mathbf{k})$. If without any other considerations, the choice of the best rotation can be made independently for each $\mathbf{k}$:

$$\mathcal{S}(\mathbf{k}) \;=\; \mathcal{R}(\mathbf{k}) \cup \mathcal{C}(\mathbf{k}), \quad \mathcal{C}(\mathbf{k}) \;\subset\; \bar{\mathcal{R}}(\mathbf{k}), \tag{3.10}$$

with

$$\dim \mathcal{S}(\mathbf{k}) = sN, \;\; \dim \mathcal{C}(\mathbf{k}) = sN - \dim \mathcal{R}(\mathbf{k}), \;\; \langle \dim \mathcal{R}(\mathbf{k}) \rangle = rN, \tag{3.11}$$

where $\mathcal{C}(\mathbf{k}) \equiv \{c_{\bar{m}\mathbf{k}}\}$ is the *choice* of $\psi_{\bar{n}\mathbf{k}}$ combinations:

$$c_{\bar{m}\mathbf{k}} \;=\; \sum_{\bar{n}} C_{\bar{m}\bar{n}}(\mathbf{k}) \psi_{\bar{n}\mathbf{k}}. \tag{3.12}$$

Here, $\mathbf{C}(\mathbf{k}) \equiv \{C_{\bar{m}\bar{n}}(\mathbf{k})\}$ is theoretically a $\dim \mathcal{C}(\mathbf{k}) \times \infty$ matrix. We note that in (3.10), only the total function content belonging to subspace $\mathcal{C}(\mathbf{k})$ is important, so any unitary transformation $\mathbf{U}\mathbf{C}(\mathbf{k})$ is equivalent to to the original choice $\mathbf{C}(\mathbf{k})$, where $\mathbf{U}$ is $\dim \mathcal{C}(\mathbf{k}) \times \dim \mathcal{C}(\mathbf{k})$ matrix and $\mathbf{U}^T\mathbf{U} = \mathbf{I}$. Also, even if $\mathcal{R}(\mathbf{k})$ and $\bar{\mathcal{R}}(\mathbf{k})$ are continuous, $\mathcal{C}(\mathbf{k})$ does not have to be continuous in $\mathbf{k}$, in the same way that the minimum eigenvalue of a continuous matrix function $\mathbf{A}(\mathbf{k})$ may not be continuous in $\mathbf{k}$ due to eigenvalue crossings. We call such discontinuity in $\mathcal{C}(\mathbf{k})$, which is not caused

by discontinuity in $\mathcal{R}(\mathbf{k})$, "type-II" discontinuity. Both type-I and type-II discontinuities could negatively influence the localization properties of QOs, in the same way that the Fourier transform of a step function or functions containing higher-order discontinuities causes algebraic tails in the transformed function [142]. Algebraic decay, however, is not necessarily a show-stopper.

In the previous development [107, 108, 109, 110, 111], the "rotation" in Fig. 3-1 was formulated as a matrix problem with explicit $\{\psi_{\bar{n}\mathbf{k}}\}$ wavefunctions as the corresponding basis. While formally exact, in practice it requires the computation and storage of a large number of $\psi_{\bar{n}\mathbf{k}}$'s, which are then loaded into the post-processing program to be taken inner product with the AOs. The disk space required to store the $\psi_{\bar{n}\mathbf{k}}$'s can run up to tens of gigabytes. Still, one has finite unoccupied bands truncation error (UBTE), which can severely impact the stability of the program. For instance, it was found that when $\{s,p,d\}$ AOs ($s=9$) are used for each Mo atom in bcc Mo, the condition number of the constructed QO overlap matrix is so bad that the numerically calculated TB bands turn singular at some $\mathbf{k}$-points, unless exorbitant numbers of unoccupied bands are kept. The bad condition number problem can be temporarily avoided if $\{s,d\}$ AOs ($s=6$) are used instead of $\{s,p,d\}$ [111]. But such solutions are fundamentally unsatisfactory because it is the user's prerogative to decide what is the proper "minimal" basis for the physics one wants to represent, and be able to use a richer QO basis if one desires.

It was discovered recently that a great majority of the bad condition number problems of the previous scheme [107, 108, 109, 110, 111] were associated with UBTE. In our method, by resorting to the resolution of identity property of the unoccupied subspace $\bar{\mathcal{R}}(\mathbf{k})$, we avoid the Eq. (3.12) representation all together. This not only eliminates the requirement to save a large number of $\psi_{\bar{n}\mathbf{k}}$'s, reducing disk/memory/CPU time requirements by order of magnitude, but also eliminates UBTE as a source of bad condition number. This allows one to construct arbitrarily rich QO basis for bcc Mo ($\{s,d\}$, $\{s,p,d\}$ or $\{s,p,d,f\}$) without numerical problem, all within reasonable computational cost.

Before we move onto the algorithmic details, it is instructive to define qualitatively

what we expect at the end. Let us use

$$\langle \mathbf{x}|\mathrm{A}_i^I\rangle = \mathrm{A}_i^I(\mathbf{x}) = \mathrm{A}_i(\mathbf{x}-\mathbf{X}_I) \tag{3.13}$$

to denote the AOs, where I labels the ions and $\mathbf{X}_I$ the ion center, $i \equiv \{lm\}$ is the angular momentum channel number. The AO themselves (e.g. s, p_x, p_y, p_z) are highly distinct from each other. Indeed, if there were just one isolated atom in a big supercell, AOs of different angular momentum are orthogonal to each other. When there are multiple atoms in the supercell and the metric $\hat{S}$ contains projectors from all ion centers, this orthogonality between AO pseudowavefunctions on the same site is no longer true rigorously, since two orbitals both centered at $\mathbf{X}_I$ could still overlap in regions covered by other projectors $|\beta_j^J\rangle\langle\beta_i^J|$. (The AO pseudowavefunctions are spherical harmonics representing full rotation group, whereas $\hat{S}$ has crystal group symmetry.) Nonetheless, AOs of different angular momentum should be nearly orthogonal, and should be highly distinguishable from each other. The same can be said for two AOs $\mathrm{A}_i(\mathbf{x}-\mathbf{X}_I)$, $\mathrm{A}_j(\mathbf{x}-\mathbf{X}_J)$ centered on two different ions. While this is obviously not true if $|\mathbf{X}_J-\mathbf{X}_I| \to 0$, in most systems $\mathbf{X}_I$ and $\mathbf{X}_J$ are well separated, by 1 Å or more between non-hydrogen elements [151]. The full-rankness of the AO basis in Bv universe guarantees the well-behaving (not to be confused with the accuracy) of the numerical LCAO energy bands in the entire Brillouin zone. For if this is not the case, in particular if the AO overlap matrix is rank-deficient when projected onto some $\mathbf{k}$-point, then the band eigenvalues cannot be obtained in a well-posed manner, and it would manifest as numerical singularities at that $\mathbf{k}$-point in the LCAO energy band diagram due to bad condition number.

Corresponding to each AO, there is a shadow in the optimized subspace, the QO

$$\langle \mathbf{x}|\mathrm{Q}_i^I\rangle = \mathrm{Q}_i^I(\mathbf{x}) = \mathrm{Q}_i(\mathbf{x}-\mathbf{X}_I). \tag{3.14}$$

Even though $\mathrm{Q}_i^I(\mathbf{x})$ is no longer rigorously spherical harmonic, in the spirit of LCAO $\{\mathrm{Q}_i^I\}$ should inherit the main characters of $\{\mathrm{A}_i^I\}$, and therefore should also be *highly distinct.* In other words, when presented with 3D rendering of the QO orbitals, one

should be able to recognize that this a "p_x-like" QO on atom I, that is a "$d_{x^2-y^2}$-like" QO on atom J, etc. If this is not possible, the results would not be considered satisfactory, even if these orbitals are localized.

Mathematically the above translates to the following. If the Q_i^I's are individually normalized, and so are the $\{\psi_{n\mathbf{k}}\}$, $\{c_{\bar{m}\mathbf{k}}\}$, then the linear transformation matrix $\mathbf{\Omega}$ connecting $\{\mathrm{Q}_i^I\}$ to $\{\psi_{n\mathbf{k}}, c_{\bar{m}\mathbf{k}}\}$ must have a reasonable condition number κ, defined here as the ratio of the maximum to minimum eigenvalues of $\mathbf{\Omega}^\dagger\mathbf{\Omega}$. The following pathology can be identified by a large κ, which is that one QO orbital can be expressed as, or well-approximated by a linear combination of other QO orbitals. The QOs are supposedly highly distinct from each other and linearly independent. A large condition number would mean this is close to becoming false. This pathology happened in reality, for example, when we attempted to use $\{s, p, d\}$ AOs for each Mo atom ($s = 9$) in extracting QOs for bcc Mo with the previous scheme [111]. The bad condition number (due to UBTE) corresponds to nearly linearly dependent QO orbitals when projected onto some $\mathbf{k}$-point, which means that some of the QOs have lost their distinct character. Once we switch to a smaller basis set using only the $\{s, d\}$ AOs ($s = 6$), this problem went away.

This good condition number (GCN) criterion provides a quantitative measure of what constitutes a good minimal basis for solid-state systems. While it has not been proved that AO-like minimal basis can be found for all molecular [150] and solid-state systems, experiences with QO show that for the vast majority of systems, a very satisfactory minimal basis can be found (good condition number and good localization) with a little care. Indeed, by changing the AOs "as little as possible" while maintaining the $\{\psi_{n\mathbf{k}}\}$ band structure, we believe QO fulfills the true spirit of LCAO [126].

3.3.2 Subspace optimization

From planewave calculation we obtain the occupied Bloch states,

$$\hat{H}|\psi_{n\mathbf{k}}\rangle = \varepsilon_{n\mathbf{k}}\hat{S}|\psi_{n\mathbf{k}}\rangle, \quad n = 1..O_{\mathbf{k}}, \tag{3.15}$$

where $O_{\mathbf{k}}$ is the number of occupied eigenvalues at $\mathbf{k}$ and $\varepsilon_{n\mathbf{k}}$ is Kohn-Sham eigen energy of band $n\mathbf{k}$ (for simplicity we assume a spin-unpolarized system), as well as the unoccupied Bloch states:

$$\hat{H}|\psi_{\bar{n}\mathbf{k}}\rangle = \varepsilon_{\bar{n}\mathbf{k}}\hat{S}|\psi_{\bar{n}\mathbf{k}}\rangle, \quad \bar{n} = 1..U_{\mathbf{k}}. \tag{3.16}$$

Kohn-Sham Hamiltonian $\hat{H}$ for USPP and PAW potential consists of kinetic energy operator $\hat{T}$, ionic local pseudopotential $\hat{V}_{\mathrm{L}}$, ionic nonlocal pseudopotential $\hat{V}_{\mathrm{NL}}$, Hartree potential $\hat{V}_{\mathrm{H}}$ and exchange-correlation potential $\hat{V}_{\mathrm{XC}}$,

$$\hat{H} = \hat{T} + \hat{V}_{\mathrm{L}} + \hat{V}_{\mathrm{NL}} + \hat{V}_{\mathrm{H}} + \hat{V}_{\mathrm{XC}}. \tag{3.17}$$

When averaged over the supercell's Brillouin zone, we have $O_{\mathbf{k}} = Nq/2$, but $O_{\mathbf{k}}$ and $U_{\mathbf{k}}$ can vary with $\mathbf{k}$ for metals. N is total number of atoms and q is averaged number of valence electrons on each atom. Different Bloch states, either of different $\mathbf{k}$ or of the same $\mathbf{k}$ but different n or $\bar{n}$, are orthogonal to each other in the sense of (3.4) (over the Bv universe). Let us choose normalization (over the Bv universe as well)

$$\begin{aligned} \| \psi_{n\mathbf{k}} \|^2 &= (\psi_{n\mathbf{k}}, \psi_{n\mathbf{k}}) = \langle\psi_{n\mathbf{k}}|\hat{S}|\psi_{n\mathbf{k}}\rangle = 1, \\ \| \psi_{\bar{n}\mathbf{k}} \|^2 &= (\psi_{\bar{n}\mathbf{k}}, \psi_{\bar{n}\mathbf{k}}) = \langle\psi_{\bar{n}\mathbf{k}}|\hat{S}|\psi_{\bar{n}\mathbf{k}}\rangle = 1. \end{aligned} \tag{3.18}$$

The original QUAMBO scheme is to optimize true unoccupied Bloch space $\{\psi_{\bar{n}\mathbf{k}}\}$ to obtain maximal atomic orbital projection. In our QO scheme, we use the same criteria but optimize the virtual Bloch space formed by atomic orbitals.

Assuming that we have another set of virtual unoccupied Bloch states $\{c_{m\mathbf{k}}\}$, we choose to maximize the "sum-over-square" measure

$$\max \sum_{Ii} \| \Big(\sum_{n\mathbf{k}} \hat{P}_{\psi_{n\mathbf{k}}} + \sum_{m\mathbf{k}} \hat{P}_{c_{m\mathbf{k}}} \Big) |\mathrm{A}_i^I\rangle \|^2 \tag{3.19}$$

by optimizing $\{c_{m\mathbf{k}}\}$. As shown in Fig. 3-1, QOs in real space are defined as a set of valence quasiatomic orbitals $\{\mathrm{Q}_i(\mathbf{x}-\mathbf{X}_I)\}$, labeled by atomic position $\mathbf{X}_I$ and orbital

type i (e.g., s or p_x, p_y, p_z, etc.), which can be expressed as unitary transformation of occupied true Bloch states $\{\psi_{n\mathbf{k}}(\mathbf{x})\}$ and unoccupied virtual Bloch states $\{c_{m\mathbf{k}}(\mathbf{x})\}$ with $n = 1, 2, ..., O_{\mathbf{k}}$ and $m = 1, 2, ..., P_{\mathbf{k}}$. Due to the unitary transformation, for any $\mathbf{k}$ point, $P_{\mathbf{k}} = N(d - q/2)$ and Nd is the total number of QOs in the unit cell, $Nd = \sum_{Ii}$. Therefore, the i-th QO of atom I, $|\mathrm{Q}_i^I\rangle$, can be defined as two parts: parallel part $|\mathrm{Q}_{Ii}^{\parallel}\rangle$ and perpendicular part $|\mathrm{Q}_{Ii}^{\perp}\rangle$. The parallel part is the projection of atomic orbital $|\mathrm{A}_i^I\rangle$ on occupied Bloch space $|\psi_{n\mathbf{k}}\rangle$ while the perpendicular part contains the projection of atomic orbital $|\mathrm{A}_i^I\rangle$ on unoccupied virtual Bloch space $|c_{m\mathbf{k}}\rangle$,

$$|\mathrm{Q}_i^I\rangle = |\mathrm{Q}_{Ii}^{\parallel}\rangle + |\mathrm{Q}_{Ii}^{\perp}\rangle = \lambda_{Ii}\Big(\sum_{n\mathbf{k}} \hat{P}_{\psi_{n\mathbf{k}}} |\mathrm{A}_i^I\rangle + \sum_{m\mathbf{k}} \hat{P}_{c_{m\mathbf{k}}} |\mathrm{A}_i^I\rangle\Big), \tag{3.20}$$

where λ_{Ii} is a normalization constant so that

$$\langle \mathrm{Q}_i^I | \hat{S} | \mathrm{Q}_i^I \rangle = 1. \tag{3.21}$$

Eq. (3.19) indicates that once the occupied Bloch space is selected, the measure will be affected by the virtual unoccupied Bloch space $\{c_{m\mathbf{k}}\}$ only. Therefore, the key of QO construction is to find an optimized set of virtual unoccupied Bloch states. Instead of extracting and optimizing a subspace from the unoccupied true Bloch space $\{\psi_{\bar{n}\mathbf{k}}\}$ in both MLWF and the original Lu's QUAMBO scheme, we *directly* construct $\{c_{m\mathbf{k}}\}$, similar to Pulay and Sæbø's PAO [112, 113, 114], which will be described below.

To achieve $\{c_{m\mathbf{k}}\}$, first we define the perpendicular part of atomic orbital $|\mathrm{A}_{Ii,\mathbf{k}}^{\perp}\rangle$ at particular $\mathbf{k}$ point as

$$|\mathrm{A}_{Ii,\mathbf{k}}^{\perp}\rangle = \Big(\hat{1} - \sum_{n} \hat{P}_{\psi_{n\mathbf{k}}}\Big) |\mathrm{A}_i^I\rangle, \tag{3.22}$$

and the corresponding overlap matrix of all atomic orbitals $\{|\mathrm{A}_{Ii}^{\perp}\rangle\}$ is defined as

$$(\mathbf{W}_{\mathbf{k}})_{Ii,Jj} = (\mathrm{A}_{Ii,\mathbf{k}}^{\perp}\ ,\ \mathrm{A}_{Jj,\mathbf{k}}^{\perp}) = \langle \mathrm{A}_{Ii,\mathbf{k}}^{\perp} | \hat{S} | \mathrm{A}_{Jj,\mathbf{k}}^{\perp} \rangle. \tag{3.23}$$

By diagonalizing Hermitian matrix $\mathbf{W_k}$, we can obtain the largest $P_\mathbf{k}$ number of real eigenvalues D_m and their corresponding eigenvectors $(\mathbf{V_k})_{m,Ii}$. Finally $|c_{m\mathbf{k}}\rangle$ is defined as

$$|c_{m\mathbf{k}}\rangle = \sum_{Ii} (\mathbf{V_k})_{m,Ii} |\mathrm{A}^{\perp}_{Ii,\mathbf{k}}\rangle. \tag{3.24}$$

It is easy to prove that $|c_{m\mathbf{k}}\rangle$ is perpendicular to $|\mathrm{A}^{\perp}_{Ii,\mathbf{k}}\rangle$,

$$\begin{aligned} \langle \psi_{n\mathbf{k}} | \hat{S} | \mathrm{A}^{\perp}_{Ii,\mathbf{k}} \rangle &= \langle \psi_{n\mathbf{k}} | \hat{S} | \Big(\hat{1} - \sum_l \hat{P}_{\psi_{l\mathbf{k}}} \Big) | \mathrm{A}^I_i \rangle \\ &= \langle \psi_{n\mathbf{k}} | \hat{S} | \mathrm{A}^I_i \rangle - \delta_{nl} \langle \psi_{l\mathbf{k}} | \hat{S} | \mathrm{A}^I_i \rangle \\ &= 0. \end{aligned} \tag{3.25}$$

Therefore $|c_{m\mathbf{k}}\rangle$ is also perpendicular to $|\psi_{n\mathbf{k}}\rangle$,

$$\langle \psi_{n\mathbf{k}} | \hat{S} | c_{m\mathbf{k}} \rangle = \sum_{Ii} (\mathbf{V_k})_{m,Ii} \langle \psi_{n\mathbf{k}} | \hat{S} | \mathrm{A}^{\perp}_{Ii,\mathbf{k}} \rangle = 0. \tag{3.26}$$

Furthermore, it can be shown that $|c_{m\mathbf{k}}\rangle$ is orthogonal to each other. For each $\mathbf{k}$, $\mathbf{V_k}$ is rescaled by a constant so that unoccupied virtual Bloch state $|c_{m\mathbf{k}}\rangle$ satisfies the normalization condition as a true Bloch state does. Then we have the following expression of normalization,

$$\langle c_{m\mathbf{k}} | \hat{S} | c_{m'\mathbf{k}} \rangle = \delta_{mm'}. \tag{3.27}$$

Beside this rescaling procedure, to obtain full electronic structure information we need to evaluate the energies of these virtual Bloch states. This can be done by using the Kohn-Sham Hamiltonian from DFT,

$$\hat{H} | c_{m\mathbf{k}} \rangle = \varepsilon_{m\mathbf{k}} \hat{S} | c_{m\mathbf{k}} \rangle, \quad m = 1..P_\mathbf{k}. \tag{3.28}$$

It should be mentioned that $\varepsilon_{m\mathbf{k}}$ is still real value since $|c_{m\mathbf{k}}\rangle$ is eigenstate of the translation operator and thus eigenstate of $\hat{H}$. Since the number of virtual unoccupied Bloch states, $P_\mathbf{k}$, is no more than the total number of atomic orbitals, the

computational cost of energy calculation is small. To keep the normalization condition for $|\mathrm{Q}_i^I\rangle$, we have

$$\begin{aligned} 1 &= \langle \mathrm{Q}_i^I|\hat{S}|\mathrm{Q}_i^I\rangle \\ &= \lambda_{Ii}^2\Big(\sum_{n\mathbf{k}}\langle \mathrm{A}_i^I|\hat{P}_{\psi_{n\mathbf{k}}} + \sum_{m\mathbf{k}}\langle \mathrm{A}_i^I|\hat{P}_{c_{m\mathbf{k}}}\Big)|\hat{S}|\Big(\sum_{n\mathbf{k}}\hat{P}_{\psi_{n\mathbf{k}}}|\mathrm{A}_i^I\rangle + \sum_{m\mathbf{k}}\hat{P}_{c_{m\mathbf{k}}}|\mathrm{A}_i^I\rangle\Big) \\ &= \lambda_{Ii}^2\Big(\sum_{n\mathbf{k}}\langle \mathrm{A}_i^I|\hat{P}_{\psi_{n\mathbf{k}}}|\mathrm{A}_i^I\rangle + \sum_{m\mathbf{k}}\langle \mathrm{A}_i^I|\hat{P}_{c_{m\mathbf{k}}}|\mathrm{A}_i^I\rangle\Big), \end{aligned} \tag{3.29}$$

where we use the following identities that

$$\begin{aligned} \hat{P}_{c_{m\mathbf{k}}}\hat{S}\hat{P}_{c_{m'\mathbf{k}}} &= \delta_{mm'}\hat{P}_{c_{m\mathbf{k}}}, \\ \hat{P}_{\psi_{n\mathbf{k}}}\hat{S}\hat{P}_{\psi_{n'\mathbf{k}}} &= \delta_{nn'}\hat{P}_{\psi_{n\mathbf{k}}}, \\ \hat{P}_{\psi_{n\mathbf{k}}}\hat{S}\hat{P}_{c_{m\mathbf{k}}} &= 0. \end{aligned} \tag{3.30}$$

Therefore, λ_{Ii} can be expressed as

$$\lambda_{Ii} = \Big(\sum_{n\mathbf{k}}\langle \mathrm{A}_i^I|\hat{P}_{\psi_{n\mathbf{k}}}|\mathrm{A}_i^I\rangle + \sum_{m\mathbf{k}}\langle \mathrm{A}_i^I|\hat{P}_{c_{m\mathbf{k}}}|\mathrm{A}_i^I\rangle\Big)^{-\frac{1}{2}}. \tag{3.31}$$

Finally, for optimized $|\mathrm{Q}_i^I\rangle$, the total mean-square deviation from atomic orbitals $|\mathrm{A}_i^I\rangle$ is

$$\begin{aligned} \Delta^2 &= \sum_{Ii}\langle \mathrm{Q}_i^I - \mathrm{A}_i^I|\hat{S}|\mathrm{Q}_i^I - \mathrm{A}_i^I\rangle \\ &= \sum_{Ii}\Big[1 + \langle \mathrm{A}_i^I|\hat{S}|\mathrm{A}_i^I\rangle - 2\,\lambda_{Ii}\Big(\sum_{n\mathbf{k}}\langle \mathrm{A}_i^I|\hat{P}_{\psi_{n\mathbf{k}}}|\mathrm{A}_i^I\rangle + \sum_{m\mathbf{k}}\langle \mathrm{A}_i^I|\hat{P}_{c_{m\mathbf{k}}}|\mathrm{A}_i^I\rangle\Big)\Big] \qquad (3.32) \\ &= \sum_{Ii}\Big(1 + \langle \mathrm{A}_i^I|\hat{S}|\mathrm{A}_i^I\rangle - 2\lambda_{Ii}^{-1}\Big) \qquad (3.33) \end{aligned}$$

It should be emphasized that $\langle \mathrm{A}_i^I|\hat{S}|\mathrm{A}_i^I\rangle$ may not be equal to 1 since within USPP and PAW formalism the overlap operator $\hat{S}$ includes contributions from all atoms while for NCPP $\hat{S} = 1$ and hence $\langle \mathrm{A}_i^I|\hat{S}|\mathrm{A}_i^I\rangle = 1$. It is clear that the smaller Δ^2 means less deviation from atomic orbitals and better localization.

Mathematically there is no difference between $\psi_{n\mathbf{k}}$ and $c_{m\mathbf{k}}$ except that one is true Bloch state and the other is virtual Bloch state constructed by ourselves. Therefore,

to keep simplicity we only use one symbol $\psi_{n\mathbf{k}}$ to represent both the original occupied true Bloch states $\psi_{n\mathbf{k}}$ and newly-constructed unoccupied virtual Bloch states $c_{m\mathbf{k}}$. Then QO formula, Eq. (3.20), is rewritten as

$$\begin{aligned} |\mathrm{Q}_i^I\rangle &= \lambda_{Ii} \sum_{n\mathbf{k}} \hat{P}_{\psi_{n\mathbf{k}}} |\mathrm{A}_i^I\rangle \\ &= \sum_{n\mathbf{k}} \lambda_{Ii} \langle \psi_{n\mathbf{k}} | \hat{S} | \mathrm{A}_i^I \rangle \ |\psi_{n\mathbf{k}}\rangle \\ &= \sum_{n\mathbf{k}} (\mathbf{\Omega}_{\mathbf{k}})_{n,Ii} \ |\psi_{n\mathbf{k}}\rangle \end{aligned} \tag{3.34}$$

where now $n = O_{\mathbf{k}} + P_{\mathbf{k}} = C$ and $(\mathbf{\Omega}_{\mathbf{k}})_{n,Ii} = \lambda_{Ii} \langle \psi_{n\mathbf{k}} | \hat{S} | \mathrm{A}_i^I \rangle$. Matrix $\mathbf{\Omega}_{\mathbf{k}}$ with the size of $C \times C$ is transformation matrix between new Bloch space $\{\psi_{n\mathbf{k}}\}$ and QO representation$\{\mathrm{Q}_i^I\}$.

3.3.3 Pseudoatomic orbitals

In the original Lu's QUAMBO construction scheme, pseudoatomic orbitals $\mathrm{A}_i^I(\mathbf{x})$ from pseudopotential generators are used as projection objects. However in NCPP, USPP and PAW method some elements' pseudoatomic orbitals have very long tails, extending to 10 Å. Then to use this long-tailed orbitals as projection objects is not very reasonable since these relatively delocalized orbitals are often changed a lot in chemical bonding environment. One simple strategy is to rescale the radial part of pseudoatomic orbitals by multiplying an exponentially decaying function,

$$\bar{\mathrm{A}}_i^I(\mathbf{x}) = \xi \mathrm{A}_i^I(\mathbf{x}) \ e^{-\eta|\mathbf{x}|}, \tag{3.35}$$

where η is a positive real number and ξ is a positive normalization factor. We find that it improves localization of QO and localization of the corresponding tight-binding Hamiltonian and overlap matrices.

3.3.4 "Occupied" states

As shown in Eq. (3.20) all the Bloch states below Fermi level are defined as occupied Bloch states, which are kept lossless by unitary transformation. However in practice the states we want to preserve under the QO reconstruction can be up to several electron volts above Fermi level in order to capture more electronic structure information accurately near the Fermi level. For example, electron transport in molecular electronics usually needs exact *ab initio* information near Fermi level since left and right semi-infinite electrodes have different chemical potentials to build potential difference. This requirement can be satisfied by defining an artificial "Fermi level" several eV above the true Fermi level (defined as E_{shift} in Table 3.1) in our QO scheme where one can setup an energy window to capture the region of interest exactly.

3.4 *Ab initio* tight-binding method based on quasi-atomic orbitals

3.4.1 *Ab initio* tight-binding method

Hopping Hamiltonian H and overlap matrix S under QO basis set can be easily obtained by using eigen energies of Bloch states. Computationally it is much more efficient than direct planewave DFT calculations. Therefore with smaller H and S matrices several useful applications can be easily implemented, including band structure, density of states, and Fermi surface.

Under the QO basis set, tight-binding hopping Hamiltonian $H_{Ii,Jj}(\mathbf{X}_n)$ between Q_i^{In} and Q_j^{J0} in two unit cells is written as

$$H_{Ii,Jj}(\mathbf{X}_n) = \int d^3\mathbf{x}\, \mathrm{Q}_i^*(\mathbf{x}-\mathbf{X}_I-\mathbf{X}_n)\hat{H}\mathrm{Q}_j(\mathbf{x}-\mathbf{X}_J) \tag{3.36}$$

$$= \langle \mathrm{Q}_i^{In}|\hat{H}|\mathrm{Q}_j^{J0}\rangle, \tag{3.37}$$

where $\mathbf{X}_n$ represents the difference of lattice vectors between two different unit cells.

With Eq. (3.34) and properties of Bloch states, we have

$$\begin{aligned} \mathrm{Q}_i(\mathbf{x}-\mathbf{X}_I-\mathbf{X}_n) &= \sum_{t\mathbf{k}} (\mathbf{\Omega}_{\mathbf{k}})_{t,Ii}\, \psi_{t\mathbf{k}}(\mathbf{x}-\mathbf{X}_n) && (3.38)\\ &= \sum_{t\mathbf{k}} (\mathbf{\Omega}_{\mathbf{k}})_{t,Ii}\, e^{-i\mathbf{k}\cdot\mathbf{X}_n} \psi_{t\mathbf{k}}(\mathbf{x}), && (3.39) \end{aligned}$$

then tight-binding Hamiltonian $H_{Ii,Jj}(\mathbf{X}_n)$ is further derived as,

$$\begin{aligned} H_{Ii,Jj}(\mathbf{X}_n) &= \sum_{t\mathbf{k}}\sum_{m\mathbf{k}'} e^{i\mathbf{k}\cdot\mathbf{X}_n} (\mathbf{\Omega}_{\mathbf{k}})^*_{t,Ii} (\mathbf{\Omega}_{\mathbf{k}'})_{m,Jj} \langle \psi_{t\mathbf{k}}|\hat{H}|\psi_{m\mathbf{k}'}\rangle && (3.40)\\ &= \sum_{m\mathbf{k}} e^{i\mathbf{k}\cdot\mathbf{X}_n} (\mathbf{\Omega}_{\mathbf{k}})^*_{m,Ii} (\mathbf{\Omega}_{\mathbf{k}})_{m,Jj} E_{m\mathbf{k}}, && (3.41) \end{aligned}$$

where $E_{m\mathbf{k}}$ is the corresponding eigen energy for Bloch state $\psi_{m\mathbf{k}}$. Following the same procedure we can easily find tight-binding overlap matrix $S_{Ii,Jj}(\mathbf{X}_n)$

$$\begin{aligned} S_{Ii,Jj}(\mathbf{X}_n) &= \int d^3\mathbf{x}\; \mathrm{Q}^*_i(\mathbf{x}-\mathbf{X}_I-\mathbf{X}_n)\hat{S}\mathrm{Q}_j(\mathbf{x}-\mathbf{X}_J) && (3.42)\\ &= \langle \mathrm{Q}^{In}_i|\hat{H}|\mathrm{Q}^{J0}_j\rangle && (3.43)\\ &= \sum_{m\mathbf{k}} e^{i\mathbf{k}\cdot\mathbf{X}_n} (\mathbf{\Omega}_{\mathbf{k}})^*_{m,Ii} (\mathbf{\Omega}_{\mathbf{k}})_{m,Jj}\,. && (3.44) \end{aligned}$$

Then based on matrix $H_{Ii,Jj}(\mathbf{X}_n)$ and $S_{Ii,Jj}(\mathbf{X}_n)$, we can exactly and efficiently reproduce eigenvalues below Fermi level. This is achieved by forming Hamiltonian $\tilde{H}_{Ii,Jj}(\mathbf{k})$ and overlap matrix $\tilde{S}_{Ii,Jj}(\mathbf{k})$ at each $\mathbf{k}$ point,

$$\begin{aligned} \tilde{H}_{Ii,Jj}(\mathbf{k}) &= \sum_n e^{i\mathbf{k}\cdot\mathbf{X}_n} H_{Ii,Jj}(\mathbf{X}_n), && (3.45)\\ \tilde{S}_{Ii,Jj}(\mathbf{k}) &= \sum_n e^{i\mathbf{k}\cdot\mathbf{X}_n} S_{Ii,Jj}(\mathbf{X}_n). && (3.46) \end{aligned}$$

Then by solving the following linear equation,

$$\tilde{\mathbf{H}}(\mathbf{k})\tilde{\Psi}(\mathbf{k}) = \tilde{\mathbf{E}}(\mathbf{k})\tilde{\mathbf{S}}(\mathbf{k})\tilde{\Psi}(\mathbf{k}), \tag{3.47}$$

we can get C eigen energies $\tilde{\mathbf{E}}(\mathbf{k})$ at this $\mathbf{k}$ point with $C = O_{\mathbf{k}} + P_{\mathbf{k}} = Nd$. It is expected that all the $O_{\mathbf{k}}$ energies lower than E_{Fermi} are exactly the same as the result

from DFT calculation with the same **k**-point sampling. The rest $P_{\mathbf{k}}$ eigen energies belong to virtual unoccupied Bloch states $\{c_{m\mathbf{k}}\}$.

3.4.2 Mülliken charge and bond order

Since QOs are environment-dependent quasiatomic orbitals, they can directly reflect bonding environment in vision which differ from those free-atomic orbitals with pure spherical harmonic characters such as s, p and *etc.* At the same time, they fully reproduce all the information under Fermi level. Therefore QO can be a good candidate for charge transfer and bond analysis, such as Mülliken population analysis and bond order analysis. Mülliken's overlap matrix analysis is one popular definition of electron charge associated with each atom. Since QO can be directly expressed as Bloch states (3.34), we can construct the Bloch sum of QOs

$$\begin{aligned}
\tilde{\mathrm{Q}}^I_{i,\mathbf{k}}(\mathbf{x}) &= \tilde{\mathrm{Q}}_i(\mathbf{k}, \mathbf{x} - \mathbf{X}_I) && (3.48)\\
&= \frac{1}{\sqrt{N}} \sum_n e^{i\mathbf{k}\cdot\mathbf{X}_n} \mathrm{Q}_i(\mathbf{x} - \mathbf{X}_I - \mathbf{X}_n) && (3.49)\\
&= \sqrt{N} \sum_m (\mathbf{\Omega}_{\mathbf{k}})_{m,Ii}\, \psi_{m\mathbf{k}}(\mathbf{x}). && (3.50)
\end{aligned}$$

On the other hand we express the Bloch states in terms of Bloch sum of QOs,

$$\begin{aligned}
\psi_{n\mathbf{k}}(\mathbf{x}) &= \sum_{Ii} c_{Ii,n\mathbf{k}} \tilde{\mathrm{Q}}_i(\mathbf{k}, \mathbf{x} - \mathbf{X}_I) && (3.51)\\
&= \sum_{Ii} c_{Ii,n\mathbf{k}} \frac{1}{\sqrt{N}} \sum_m e^{i\mathbf{k}\cdot\mathbf{X}_m} \mathrm{Q}_i(\mathbf{x} - \mathbf{X}_I - \mathbf{X}_m). && (3.52)
\end{aligned}$$

By multiplying $(\langle \tilde{\mathrm{Q}}^J_{j,\mathbf{k}'} | \hat{S})$ on the left hand side of Eq. (3.50), we obtain

$$\begin{aligned}
\langle \tilde{\mathrm{Q}}^J_{j,\mathbf{k}'} | \hat{S} | \tilde{\mathrm{Q}}^I_{i,\mathbf{k}} \rangle &= N \sum_{nm} (\mathbf{\Omega}_{\mathbf{k}'})^*_{n,Jj} (\mathbf{\Omega}_{\mathbf{k}})_{m,Ii} \langle \psi_{n\mathbf{k}'} | \hat{S} | \psi_{m\mathbf{k}} \rangle && (3.53)\\
&= N \delta_{\mathbf{k}'\mathbf{k}} \sum_n (\mathbf{\Omega}_{\mathbf{k}})^*_{n,Jj} (\mathbf{\Omega}_{\mathbf{k}})_{n,Ii}\,. && (3.54)
\end{aligned}$$

Again by multiplying $(\langle\tilde{Q}^J_{j,\mathbf{k}}|\hat{S})$ on the left hand side of Eq. (3.51), we obtain

$$\langle\tilde{Q}^J_{j,\mathbf{k}}|\hat{S}|\psi_{n\mathbf{k}}\rangle = \sum_{Ii} c_{Ii,n\mathbf{k}}\langle\tilde{Q}^J_{j,\mathbf{k}}|\hat{S}|\tilde{Q}^I_{i,\mathbf{k}}\rangle \tag{3.55}$$

$$= N\sum_{Ii} c_{Ii,n\mathbf{k}}\sum_m (\mathbf{\Omega_k})^*_{m,Jj}\,(\mathbf{\Omega_k})_{m,Ii}\,, \tag{3.56}$$

while from Eq. (3.50) we also have

$$\langle\tilde{Q}^J_{j,\mathbf{k}}|\hat{S}|\psi_{n\mathbf{k}}\rangle = \sqrt{N}\sum_m (\mathbf{\Omega_k})^*_{m,Jj}\,\langle\psi_{m\mathbf{k}}|\hat{S}|\psi_{n\mathbf{k}}\rangle \tag{3.57}$$

$$= \sqrt{N}\,(\mathbf{\Omega_k})^*_{n,Jj}\,. \tag{3.58}$$

By the equity of Eq. (3.56) and Eq. (3.58), we have the following expression

$$\sum_{Ii} c_{Ii,n\mathbf{k}}\sum_m (\mathbf{\Omega_k})^*_{m,Jj}\,(\mathbf{\Omega_k})_{m,Ii} = \frac{1}{\sqrt{N}}\,(\mathbf{\Omega_k})^*_{n,Jj} \tag{3.59}$$

We can define square matrix $\mathbf{G}(\mathbf{k})$ with element $G_{Jj,Ii}(\mathbf{k}) = \sum_m (\mathbf{\Omega_k})^*_{m,Jj}\,(\mathbf{\Omega_k})_{m,Ii}$, vector $\mathbf{c}(n\mathbf{k})$ with element $c_{Ii,n\mathbf{k}}$ and vector $\mathbf{a}(n\mathbf{k})$ with element $(\mathbf{\Omega_k})^*_{n,Jj}/\sqrt{N}$ for each n and $\mathbf{k}$, then the problem is just to solve a linear matrix equation for particular n and $\mathbf{k}$,

$$\mathbf{G}(\mathbf{k})\mathbf{c}(n\mathbf{k}) = \mathbf{a}(n\mathbf{k}), \tag{3.60}$$

therefore by inversion of matrix $\mathbf{G}(\mathbf{k})$, finally we get the expression for $\mathbf{c}(n\mathbf{k})$,

$$\mathbf{c}(n\mathbf{k}) = \mathbf{G}(\mathbf{k})^{-1}\mathbf{a}(n\mathbf{k}). \tag{3.61}$$

To split charge density onto different orbitals at each atom, we first need to define density operator in terms of true Bloch states $|\tilde{\psi}_{n\mathbf{k}}\rangle$

$$\hat{\rho} = \sum_{n\mathbf{k}} f_{n\mathbf{k}}|\tilde{\psi}_{n\mathbf{k}}\rangle\langle\tilde{\psi}_{n\mathbf{k}}|, \tag{3.62}$$

where $f_{n\mathbf{k}}$ is the occupation number of electrons in the corresponding true Bloch state $|\tilde{\psi}_{n\mathbf{k}}\rangle$. And we know from PAW formalism that PAW transformation operator

$\hat{T}$ defined by

$$|\tilde{\psi}_{n\mathbf{k}}\rangle = \hat{T}|\psi_{n\mathbf{k}}\rangle \tag{3.63}$$

and operator $\hat{S}$ in USPP are related by $\hat{S} = \hat{T}^{\dagger}\hat{T}$. Then it is easy to see that

$$\hat{\rho} = \sum_{n\mathbf{k}} f_{n\mathbf{k}} \hat{T}|\psi_{n\mathbf{k}}\rangle\langle\psi_{n\mathbf{k}}|\hat{T}^{\dagger}. \tag{3.64}$$

From inverse Fourier transformation of Eq. (3.49) we get

$$\mathrm{Q}_i(\mathbf{x} - \mathbf{X}_I - \mathbf{X}_n) = \frac{1}{\sqrt{N}} \sum_{\mathbf{k}} e^{-i\mathbf{k}\cdot\mathbf{X}_n} \tilde{\mathrm{Q}}_i(\mathbf{k}, \mathbf{x} - \mathbf{X}_I). \tag{3.65}$$

Then under QO basis set, the density matrix is expressed as

$$\begin{aligned}
& \hat{\rho}\left(\hat{T}|\mathrm{Q}_i^{I0}\rangle\right) && (3.66)\\
= \; & \frac{1}{N} \sum_{\mathbf{k}} f_{\mu\mathbf{k}} \sum_{Jj} \sum_{Ll} \left(\sum_{\mu} c_{Jj,\mu\mathbf{k}} c^{*}_{Ll,\mu\mathbf{k}} \right) \left(\sum_{\mathbf{X}_m} e^{-i\mathbf{k}\cdot\mathbf{X}_m} \langle \mathrm{Q}_l^{Lm}|\hat{S}|\mathrm{Q}_i^{I0}\rangle \right) \times \\
& \sum_{\mathbf{X}_n} e^{i\mathbf{k}\cdot\mathbf{X}_n} \hat{T}|\mathrm{Q}_j^{Jn}\rangle && (3.67)\\
= \; & \sum_{Jj} \sum_{\mathbf{X}_n} (\mathbf{PS})_{ji}^{Jn,I0} \left(\hat{T}|\mathrm{Q}_j^{Jn}\rangle\right), && (3.68)
\end{aligned}$$

where matrices $P_{ij}^{I,J}(\mathbf{k})$ and $S_{j,i}^{Jn,I0}(\mathbf{k})$ are defined by

$$\begin{aligned}
P_{jl}^{J,L}(\mathbf{k}) &= \sum_{\mu} f_{\mu\mathbf{k}} c_{Jj,\mu\mathbf{k}} c^{*}_{Ll,\mu\mathbf{k}}, && (3.69)\\
S_{li}^{L,I}(\mathbf{k}) &= \sum_{\mathbf{X}_m} e^{-i\mathbf{k}\cdot\mathbf{X}_m} \langle \mathrm{Q}_l^{Lm}|\hat{S}|\mathrm{Q}_i^{I0}\rangle, && (3.70)
\end{aligned}$$

and $(\mathbf{PS})_{ji}^{Jn,I0}$ is defined by

$$(\mathbf{PS})_{ji}^{Jn,I0} = \frac{1}{N} \sum_{\mathbf{k}} \sum_{Ll} P_{jl}^{J,L}(\mathbf{k}) S_{li}^{L,I}(\mathbf{k}) e^{i\mathbf{k}\cdot\mathbf{X}_n}. \tag{3.71}$$

It is noticed that density matrix $\hat{\rho}$ has the following property,

$$\mathrm{Tr}(\hat{\rho}) = N_e, \tag{3.72}$$

where N_e represents total valence electrons within one unit cell, therefore under QO basis set $\{Q_i^I\}$ we have

$$N_e = \sum_I \sum_i (\mathbf{PS})_{ii}^{I0,I0} = \sum_I N_I^0, \tag{3.73}$$

where N_I^0 is number of electrons associated with atom I. N_I^0 can be decomposed into Mülliken overlap population matrix $M_{I0,Jn}$ between the I-th atom of the origin cell $\mathbf{X}_0$ and the J-th atom of cell $\mathbf{X}_n$ by the following derivation

$$\begin{aligned} N_I^0 &= \sum_i (\mathbf{PS})_{ii}^{I0,I0} \\ &= \sum_{\mathbf{X}_n} \sum_J \left[\frac{1}{N} \sum_{\mathbf{k}} \sum_{ij} P_{ij}^{I,J}(\mathbf{k}) \left(e^{-i\mathbf{k}\cdot\mathbf{X}_n} \langle Q_j^{Jn} | \hat{S} | Q_i^{I0} \rangle \right) \right] \\ &= \sum_{\mathbf{X}_n} \sum_J \left[\frac{1}{N} \sum_{\mathbf{k}} \sum_{ij} P_{ij}^{I,J}(\mathbf{k}) S_{ij}^{I0,Jn}(\mathbf{k}) \right] \\ &= \sum_{\mathbf{X}_n} \sum_J M_{I0,Jn}, \end{aligned} \tag{3.74}$$

where

$$S_{ij}^{I0,Jn}(\mathbf{k}) = e^{-i\mathbf{k}\cdot\mathbf{X}_n} \langle Q_j^{Jn} | \hat{S} | Q_i^{I0} \rangle \tag{3.75}$$

and

$$M_{I0,Jn} = \frac{1}{N} \sum_{\mathbf{k}} \sum_{ij} P_{ij}^{I,J}(\mathbf{k}) S_{ij}^{I0,Jn}(\mathbf{k}). \tag{3.76}$$

For spin-polarized calculations, since $P_{ij}^{I,J}(\sigma, \mathbf{k})$ depends on spin degree of freedom σ, Mülliken overlap population matrix $M_{I0,Jn}^{\sigma}$ also depends on σ. Then Eq. (3.76) becomes

$$M_{I0,Jn}^{\sigma} = \frac{1}{N} \sum_{\mathbf{k}} \sum_{ij} P_{ij}^{I,J}(\sigma, \mathbf{k}) S_{ij}^{I0,Jn}(\sigma, \mathbf{k}). \tag{3.77}$$

Similarly, bond order between two atoms can be derived in the same procedure with spin degree of freedom included. The square of density matrix is defined as,

$$\hat{\rho}^2 = \sum_{\sigma} \hat{\rho}_{\sigma}^2 = \sum_{\mu,\mathbf{k},\sigma} (f_{\mu\mathbf{k}}^{\sigma})^2 \hat{T} |\psi_{\mu\mathbf{k}}^{\sigma}\rangle \langle \psi_{\mu\mathbf{k}}^{\sigma}| \hat{T}^{\dagger}. \tag{3.78}$$

Then, the trace of $\hat{\rho}^2$ is

$$\begin{aligned}\sum_{\sigma}\mathrm{Tr}\left(\hat{\rho}_{\sigma}^{2}\right) &= \sum_{\mu,\mathbf{k},\sigma}(f_{\mu\mathbf{k}}^{\sigma})^{2}=\sum_{\sigma}\sum_{I,i}\left[\sum_{\mathbf{X}_n}\sum_{J,j}\left(\mathbf{PS}(\sigma)\right)_{ij}^{I0,Jn}\left(\mathbf{PS}(\sigma)\right)_{ji}^{Jn,I0}\right] \\ &= \sum_{\mathbf{X}_n}\sum_{I,J}\mathrm{BO}_{I0,Jn} \end{aligned} \tag{3.79}$$

where $\mathrm{BO}_{I0,Jn}$ is defined as bond order between the Ith atom of the origin cell $\mathbf{X}_0$ and the Jth atom of cell $\mathbf{X}_N$,

$$\mathrm{BO}_{I0,Jn}=\sum_{\sigma ij}\left(\mathbf{PS}(\sigma)\right)_{ij}^{I0,Jn}\left(\mathbf{PS}(\sigma)\right)_{ji}^{Jn,I0}. \tag{3.80}$$

It is obvious that the bond order matrix should satisfy the general sum rule

$$\sum_{\mathbf{X}_n}\sum_{I,J}\mathrm{BO}_{I0,Jn}=\sum_{\mu,\mathbf{k},\sigma}(f_{\mu\mathbf{k}}^{\sigma})^{2}. \tag{3.81}$$

From the above formula, we can easily see for spin-unpolarized nonmetallic systems without Fermi broadening, it exactly satisfies

$$\sum_{\mathbf{X}_n}\sum_{I,J}\mathrm{BO}_{I0,Jn}=2N_e. \tag{3.82}$$

and for spin-polarized nonmetallic systems without Fermi broadening, it satisfies

$$\sum_{\mathbf{X}_n}\sum_{I,J}\mathrm{BO}_{I0,Jn}=N_e. \tag{3.83}$$

Therefore, for metallic systems with Fermi broadening it is better to include the unoccupied Bloch space several eV above Fermi level so that total Mülliken charge and bond order can satisfy the above sum rules exactly.

3.5 Applications of quasiatomic orbitals

Some typical materials are selected to demonstrate construction of QOs and their applications with USPP, including semiconductor, simple metal, ferromagnetic mate-

rial, transition metal oxide, high temperature superconductor and quasi-one dimensional material. The ground-state electronic configurations are calculated by the free USPP-DFT DACAPO package [33, 34, 35] with Vanderbilt USPP [25, 26, 27], where Monkhorst-Pack [23] **k**-point sampling is used and generalized gradient approximation(GGA) of exchange-correlation functionals, such as PW91 [12], is applied. Parameters for the corresponding DFT calculations are included in Table 3.1.

Table 3.1: Parameters for DFT calculations and QO constructions in various systems. E_{shift} is defined as the difference between the artificial Fermi level used in the QO construction and the true Fermi level of the system.

Material	# atoms	structure	a_0, c_0[Å]	E_{cut}[eV]	# $\boldsymbol{k}$-points	# bands	XC	R_{cut}[Å]	E_{shift}[eV]
Si	2	FCC	5.430	300	7×7×7	60	PW91	12.0	0
β-SiC	2	FCC	4.32	350	7×7×7	40	PW91	12.0	0
CH_4	5		1.1	350	Γ-point	60	PW91	8.0	0
SiH_4	5		1.48	350	Γ-point	40	PW91	8.0	0
Al	1	FCC	4.030	300	9×9×9	60	PW91	8.0	1.0
Fe[1]	1	BCC	2.843	400	9×9×9	40	PW91	10.0	3.0
MgB_2	3	HCP	3.067, 3.515	300	7×7×7	40	PW91	10.0	3.0
TiO_2(rutile)	6	Tetragonal	4.584, 2.961	400	7×7×7	100	PW91	10.0	0
CNT(5,5)	20		1.415	300	2×1×9	80	PW91	10.0	1.0

[a]Ferromagnetic

3.5.1 Semiconductor: diamond Si crystal

Semiconductors with a small band gap less than 2 eV have been widely used in various electronic systems. It is well known that as temperature goes up the density of carriers in semiconductors increases dramatically, and therefore the electrical conductivity also increases rapidly, although the relaxation time of electrons decreases due to the stronger electron-phonon coupling. Therefore, they can be easily changed to conductors by thermal excitations. Band theory and three dimensional energy surface are often used to analyze characteristics of semiconductors, such as energy band gap, light and heavy holes.

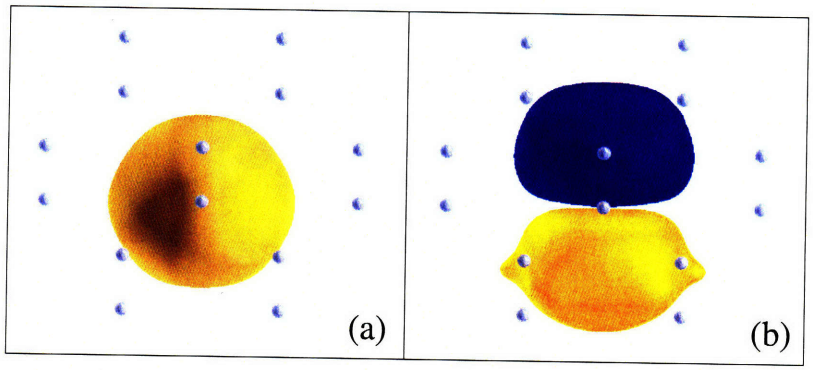

Figure 3-2: QO in diamond Si crystal: (a) s-like and (b) p_z-like with absolute isosurface value of 0.03 $Å^{-3}$. (Yellow or light gray for positive values; blue or dark gray for negative values.)

Silicon is one of important semiconductor materials. The cubic diamond Si crystal is one typical semiconductor with an indirect band gap of 1.17 eV at 0 K. Fig. 3-2 shows two of total eight QOs: s-like QO and p_z-like QO. Pure free atomic s and p_z orbitals are strongly "squeezed" due to the interaction with their nearest neighbor atoms while the overall shapes of s and p_z are kept. This fact reflects that chemical bonding in diamond Si crystal does not change the electrons' angular momentum characteristics and therefore it leads to the success of linear combination of atomic orbitals(LCAO) method in describing the electronic structure of diamond Si crystal and other similar systems. Fig. 3-3(a) compares the band structure between planewave DFT calculation and tight-binding calculation based on eight QOs of two Si atoms described in Sec. 3.4.1. It is observed that four valence energy bands below Fermi

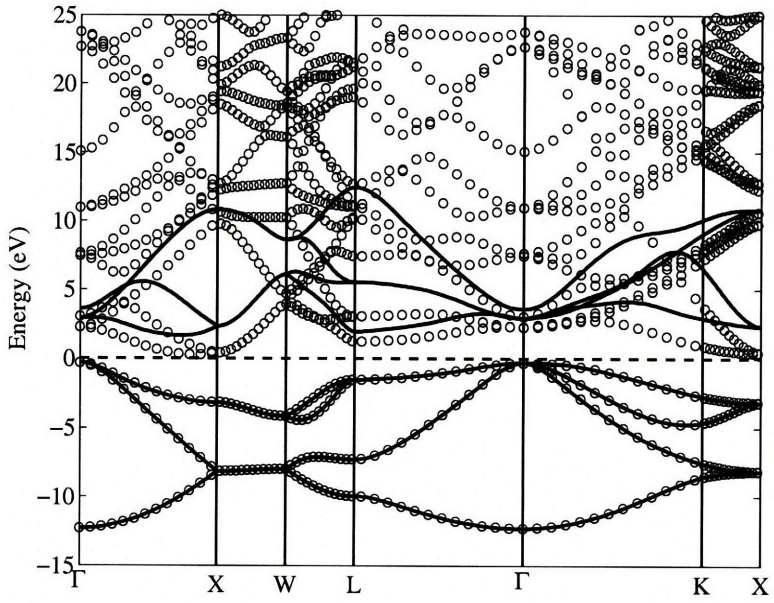

(a)

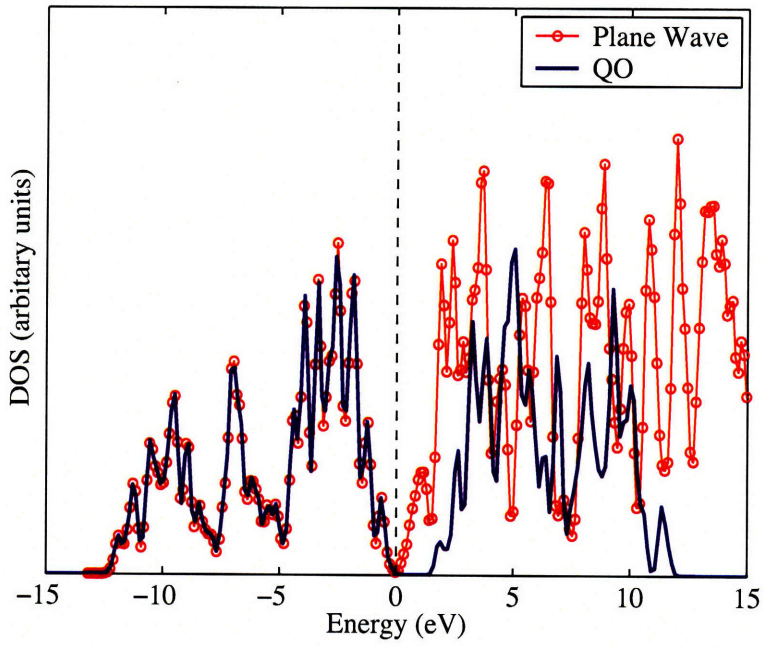

(b)

Figure 3-3: Diamond Si crystal: (a) band structure (circle dot: planewave DFT calculation; solid line: tight-binding calculation based on eight QOs of two Si atoms; dashed line: Fermi level.) (b) density of states. (circle-dot line: planewave DFT calculation; solid line: tight-binding calculation; dashed line: Fermi level.)

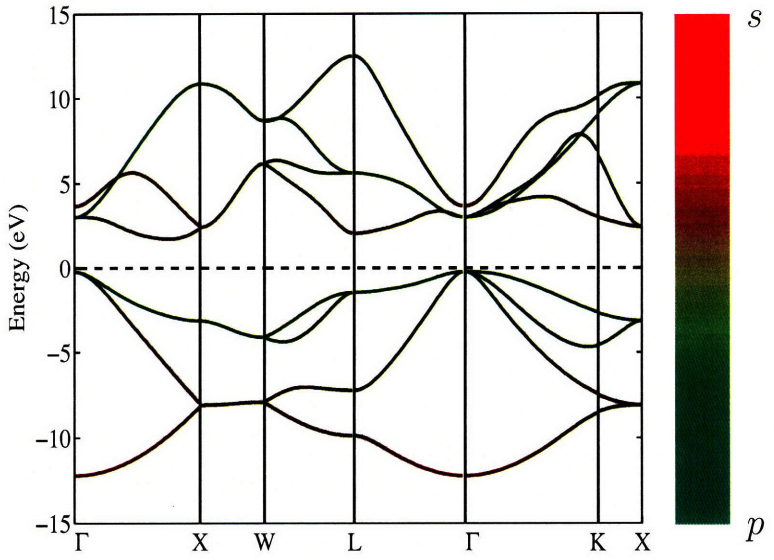

Figure 3-4: QO-projected band structure of diamond Si crystal with red for the s-like QO and green for all three p-like QOs.

level are exactly reproduced with each band doubly occupied. The indirect band gap from DFT calculation is around 0.7 eV and smaller than 1.17 eV from experiments, which is a common problem of DFT due to inaccurate exchange-correlation functional and the discontinuity of the functional. However QO-based tight-binding calculation gives a band gap of around 2.0 eV and the position of this indirect band gap shifts along XΓ direction. It is also noted that overall conduction bands from tight-binding calculation are higher than planewave DFT result. These higher Bloch states in the conduction bands are anti-bonding states while the corresponding bonding states are in the valence bands. The above mismatch between plane-wave DFT result and QO-based tight-binding result are simply because *virtual* unoccupied Bloch states are *manually* constructed and they are not true unoccupied low-lying Bloch states. These *virtual* unoccupied Bloch states in $\mathcal{C}(\mathbf{k})$ can be represented by a linear combination of the infinite *true* unoccupied Bloch states in $\bar{\mathcal{R}}(\mathbf{k})$. Therefore the energies above Fermi level obtained from QO-based tight-binding calculation are always higher than Kohn-Sham eigen energies. Density of states (DOS) in Fig. 3-3(b) also shows the similar change in the conduction bands while DOS below Fermi level is exactly the same in both calculations. Fig. 3-4 is the QO-projected band structure color-coded

by the weight of s-like and p-like QO components. It clearly shows that one s-like QO has more weight at the bottom of occupied bands while three p-like QOs dominate the top of occupied bands.

It is worth to mention that in this case band structure is only kept exactly under Fermi level with $E_{\text{shift}} = 0$ eV in Table 3.1, however, Fermi level can be shifted since the energy window is defined by users for their interests.

3.5.2 Covalent compound: β-SiC crystal

Silicon carbide is a typical example of covalent compounds and it has been extensively studied and used because of its chemical inertness, high thermal conductivity, high electron mobility, high hardness and high melting point. SiC has two solid phases: α-SiC and β-SiC. The former is an intrinsic semiconductor in hexagonal crystal structure and the latter has an indirect band gap of 2.2 eV in zincblende-type structure.

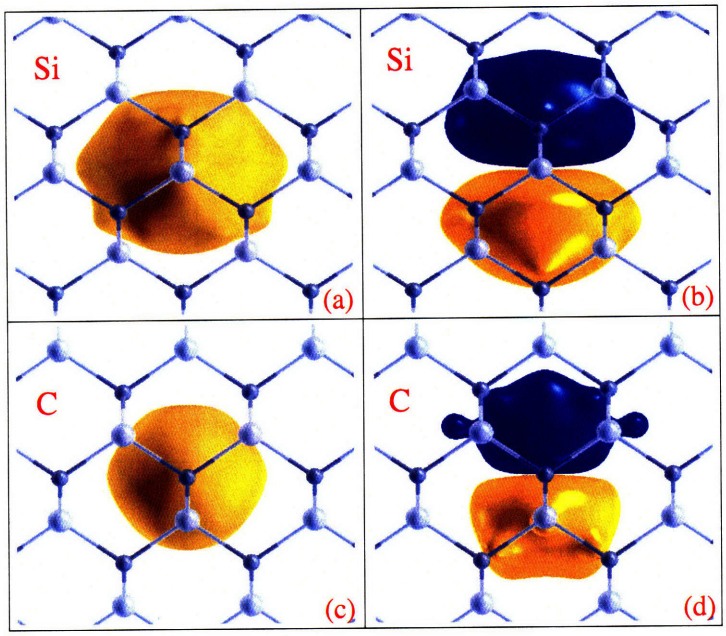

Figure 3-5: QO in β-SiC crystal. (a) Si: s-like (b) Si: p_z-like (c) C: s-like (d) C: p_z-like (absolute isosurface value: 0.03 Å^{-3})

Conduction bands in tight-binding band structure plot (Fig. 3-6) and DOS plot

(Fig. 3-8(a)) shift up due to the same reason as the situation in diamond Si crystal case. From DFT calculation a band gap of around 1.0 eV is obtained while from tight-binding calculation it is around 3.0 eV. It is seen from Fig. 3-5 that both s-like and p-like QO of Si atom are more delocalized than those of C atom, which means Si has less capability to attract electrons than C in β-SiC crystal. It is indeed shown by the QO-projected density of states plot in Fig. 3-8(b) where total density of states on C atom below Fermi level has much more weight than that on Si atom. That further indicates more charges are localized at C atom. It can be checked that the sum of QO-projected density of states is equal the tight-binding total density of states. However, it is not true for simple atomic-orbital-projected density of states in standard DFT calculations.

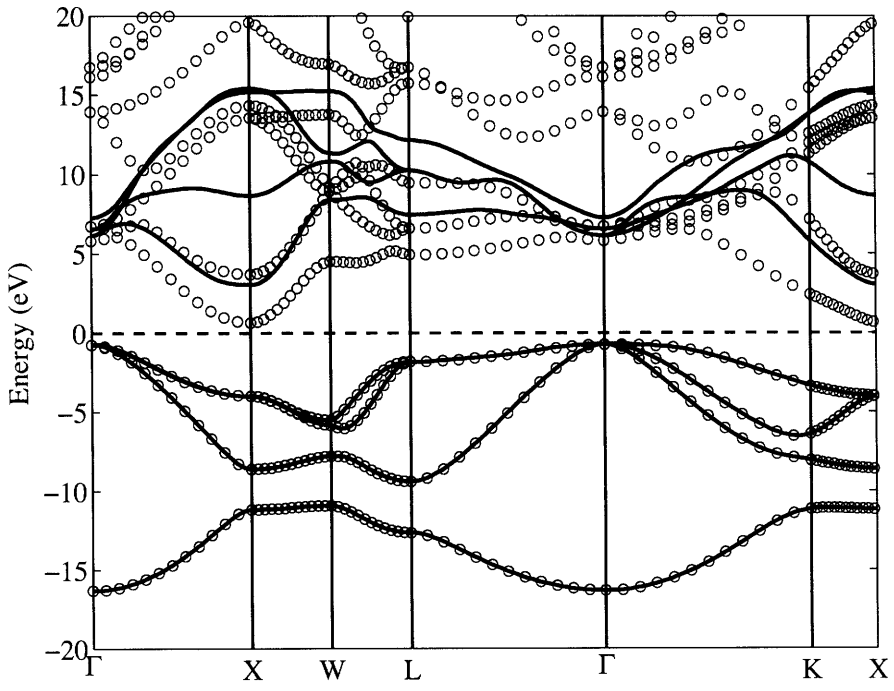

Figure 3-6: Band structure of β-SiC. (circle dot: planewave DFT calculation; solid line: tight-binding calculation based on 8 QOs; dashed line: Fermi level)

Compared to Fig. 3-3(a) in the diamond Si crystal, there is a large splitting between two bottom bands along the X-W line in Fig. 3-6 in the SiC crystal. Four higher peaks of DOS, shown in Fig. 3-8(b), are useful to explain this splitting. Two

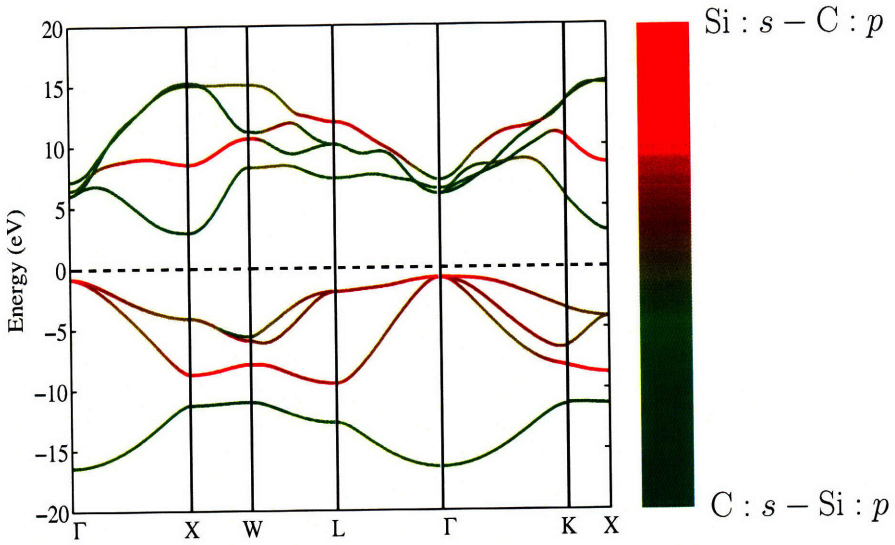

Figure 3-7: QO-projected band structure of SiC crystal with red for Si-s and C-p and green for C-s and Si-p

peaks around -12.0 eV (C's s peak on the bottom panel and Si's p peak on the top panel) and another two peaks around -8.0 eV(C's p peak on the bottom panel and Si's s peak on the top panel) lead to two non-symmetric types of s-p bonding. One is the bond between Si's s-like QO and C's p-like QO and the other is the bond between Si's s-like QO and C's p-like QO. In diamond Si crystal the above two types are degenerate bonds, which give two degenerate bands at the bottom of band structure between X and W. This splitting is much clearly reflected in QO-projected band structure shown in Fig. 3-7, where the bonding between silicon's s-like QO and carbon's three p-like QOs is dominant at the higher energy band while the bonding between carbon's s-like QO and silicon's three p-like QOs is dominant at the lower energy band.

To further study electron transfer we investigate Mülliken charges in three different compounds in Table 3.2, including CH_4 molecule, SiH_4 molecule and β-SiC crystal. It is seen that the capability of three different elements to attract electrons is in the following order: C > H > Si. Table 3.3 lists the bond order between atoms and their first and 2nd nearest neighbors in various systems. It is expected that bond order between the atom and their 2nd nearest neighbor is almost zero and much less than bond order between the atom and their 1st nearest neighbor, which is a characteristics

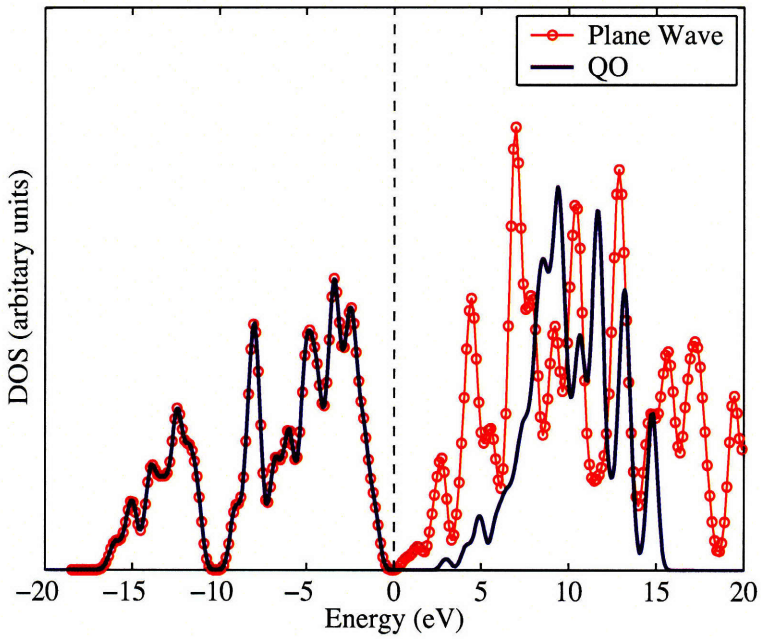

(a)

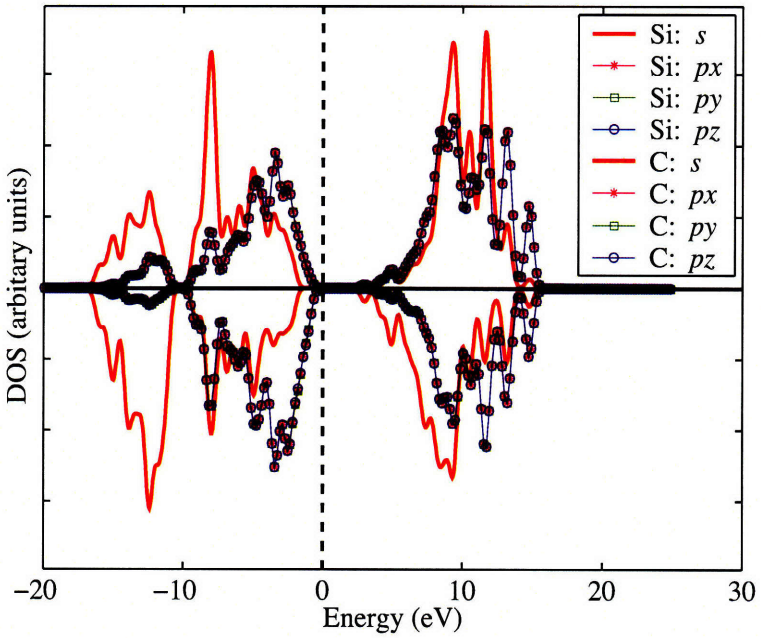

(b)

Figure 3-8: (a) Density of states of β-SiC. (circle-dot line: planewave DFT calculation; solid line: tight-binding calculation; dashed line: Fermi level.) (b) Projected density of states of β-SiC. (Top panel: Si; bottom panel: C; dashed line: Fermi level.)

Table 3.2: Mülliken charge comparison in CH_4, SiH_4 and β-SiC

Material	Mülliken Charge		total charge
CH_4	C: 5.160	H: 0.710	8.0
SiH_4	Si: 3.300	H: 1.175	8.0
β-SiC	Si: 2.729	C: 5.271	8.0

of covalent-bonding systems. Unlike the covalent system, FCC aluminum and BCC iron have small bond orders for both the 1st and 2nd nearest neighbors. In the case of MgB_2 crystal, it has very strong covalent bonding on the boron plane and large bond order between boron and magnesium, but very small bond order between magnesium atoms. Here again, total Mülliken charge and total bond order satisfy their sum rules, which is not the case for the traditional charge analysis used in DFT calculations by setting a radius cutoff and integrating valence electron density within that radius for one atom. This good property will be very useful for tight-binding parameter fitting in future.

Table 3.3: Bond order for 1st and 2nd nearest neighbors in various materials

Material	BO		$\frac{1}{2}$(total BO)/sum rule
CH_4	C-H: 0.882	H-H: 0.012	8.0 / 8.0
SiH_4	Si-H: 0.866	H-H: 0.033	8.0 / 8.0
β-SiC	Si-C: 0.823	Si-Si: 0.009	8.0 / 8.0
	C-C: 0.015		
Si-diamond	Si-Si: 0.874	Si-Si: 0.009	8.0 / 8.0
Al-FCC	Al-Al(1): 0.213	Al-Al(2): 0.015	2.898 / 2.896
Fe-BCC(majority)	Fe-Fe(1): 0.092	Fe-Fe(2): 0.035	4.967 / 4.967
Fe-BCC(minority)	Fe-Fe(1): 0.164	Fe-Fe(2): 0.057	2.842 / 2.843
MgB_2	B-B: 0.698	Mg-B: 0.206	13.868 / 13.868
	Mg-Mg: 0.085		

3.5.3 Simple metal: FCC Al

Aluminum is one of trivalent simple metals with a lot of applications. It is, therefore, natural for us to study FCC aluminum as well. In this case one s and three p pseudoatomic orbitals are used as free atomic basis set. These orbitals are rescaled by $e^{-\eta|\mathbf{x}|}$ with $\eta = 0.5$ and renormalized to get better localization. Total four corre-

sponding QOs are obtained, some of which are shown in Fig. 3-9. Based on this QO basis set, band structure, projected band structure, density of states and Fermi surface are efficiently calculated as presented in Fig. 3-10(a), Fig. 3-10(b), Fig. 3-11(a) and Fig. 3-11(b). Density of states $n(E)$ in Fig. 3-11(a) is nearly proportional to $\sqrt{E}$, which is very similar to free electron model. This nearly free electron behavior is also observed on Fermi surface within first Brillouin zone shown in Fig. 3-11(b). The concave surface in the center encloses holes folded from Fermi surface in the second Brillouin zone. The other small surfaces around the edges of the zone enclose the electrons translated from Fermi surface in the third zone. However, FCC Al does not have the third type of tiny surface around corners of the zone as free electron's Fermi surface does. It is well known that this disappearance is due to FCC Al's periodic potential, which does not exist in free electron model and it was confirmed by de Haas-van Alphen experiment data. In addition, Fig. 3-12 shows the Fermi surfaces for band 3 and 4 which are colored by velocity magnitude while Fig. 3-13 presents both surfaces colored by QO components. The magnitude of our Fermi velocity agrees with the experimental data [21] and it is also the key quantity to determine the electrical conductivity of bulk materials. QO-encoded Fermi surface in Fig. 3-13 demonstrates that p orbitals are the major angular momentum component on the large Fermi surface sheet while the small Fermi surface around the zone edges are dominated by both s and p angular momenta. QO-projected band structure in Fig. 3-10(b) also supports the above conclusion.

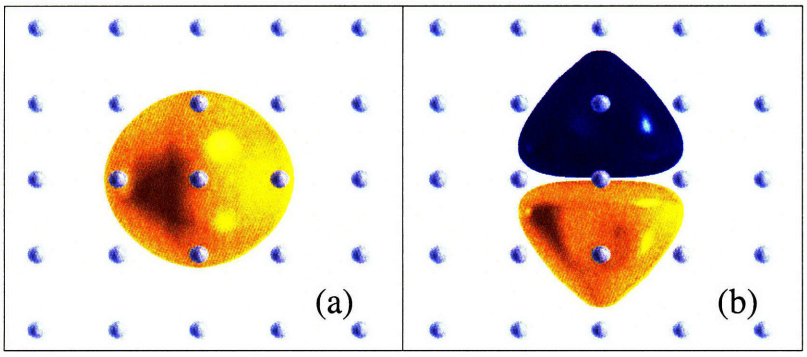

Figure 3-9: QO in FCC Al: (a) s-like (b) p_z-like (absolute isosurface value: 0.03 $Å^{-3}$)

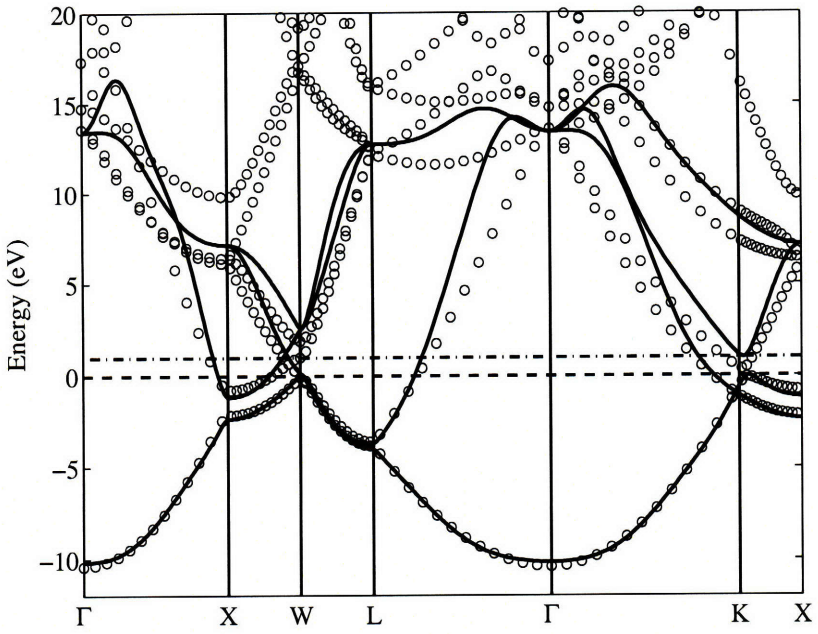

(a) Band structure

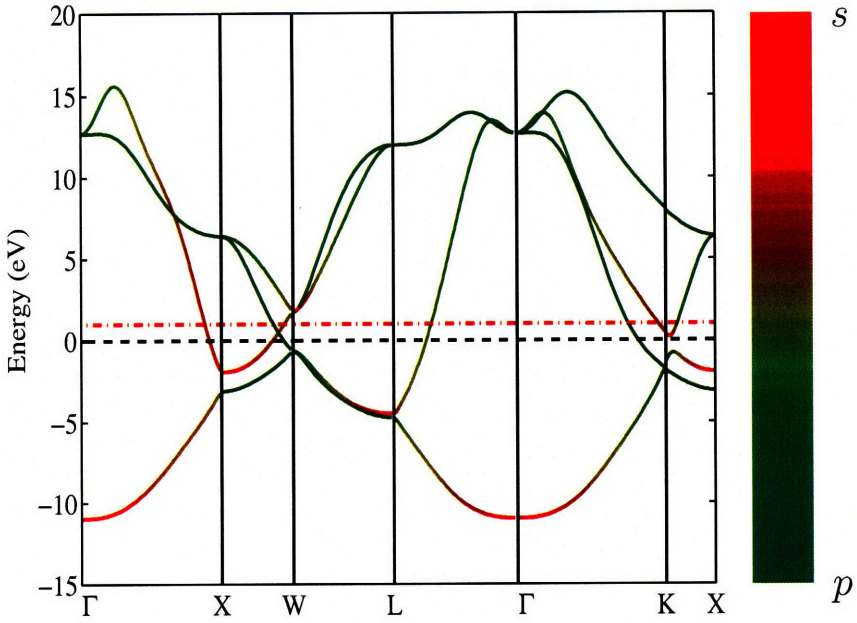

(b) QO-projected band structure

Figure 3-10: (a) DFT and tight-binding band structures of FCC Al. (b) Color-coded band structure of FCC Al with red for s-like QO and green for p-like QOs. (circle dot: planewave DFT calculation; solid line: tight-binding calculation based on four QOs; dashed line: Fermi level; dash-dot line: shifted Fermi level with $E_{\text{shift}} = 1$ eV.)

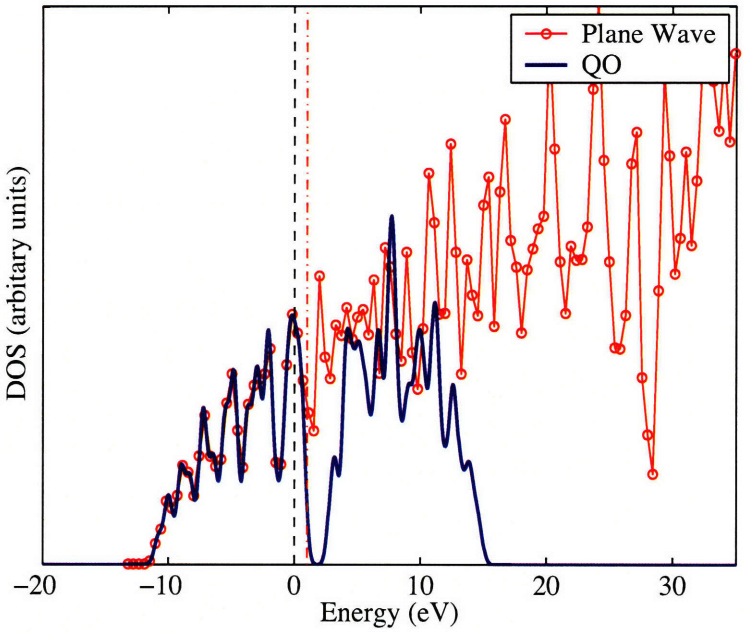

(a) Density of states

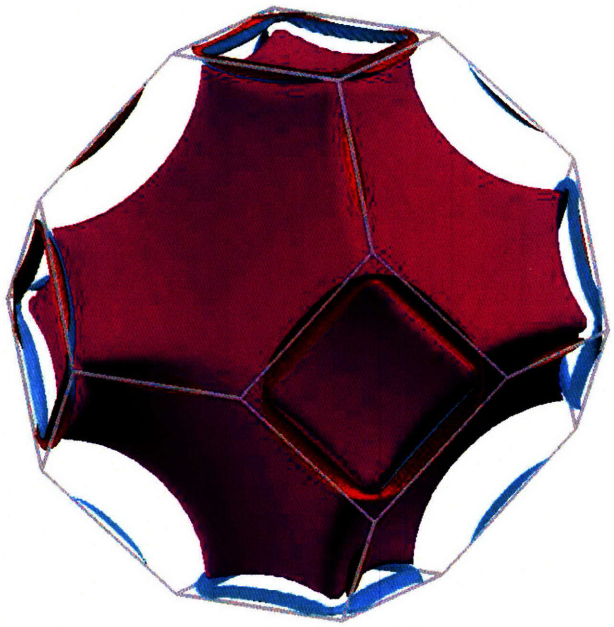

(b) Fermi surface

Figure 3-11: (a) Density of states of FCC Al. (circle-dot line: planewave DFT calculation; solid line: tight-binding calculation; dashed line: Fermi level; dash-dot line: shifted Fermi level with $E_{\text{shift}} = 1$ eV.) (b) Fermi surface of FCC Al.

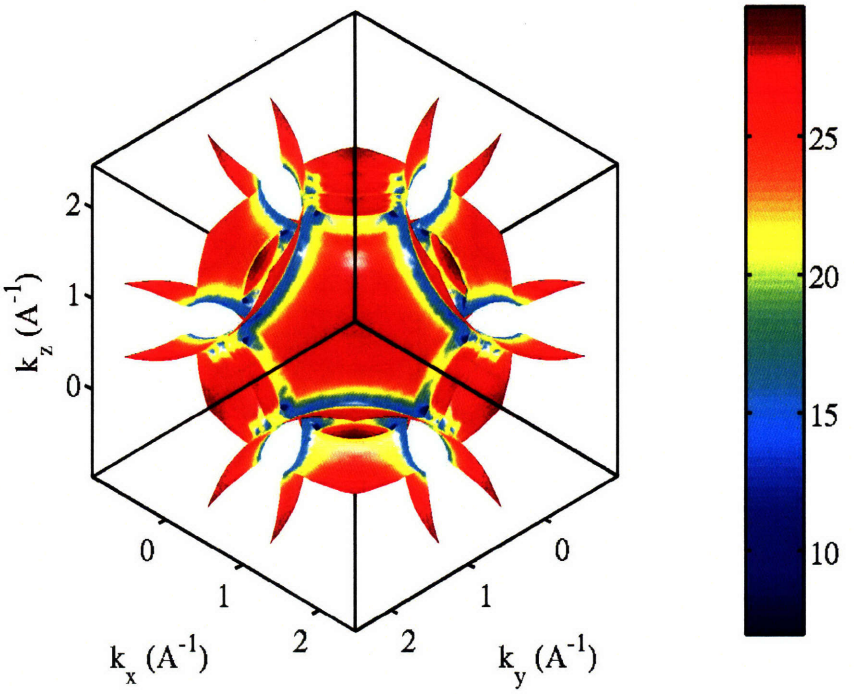

(a) band 2

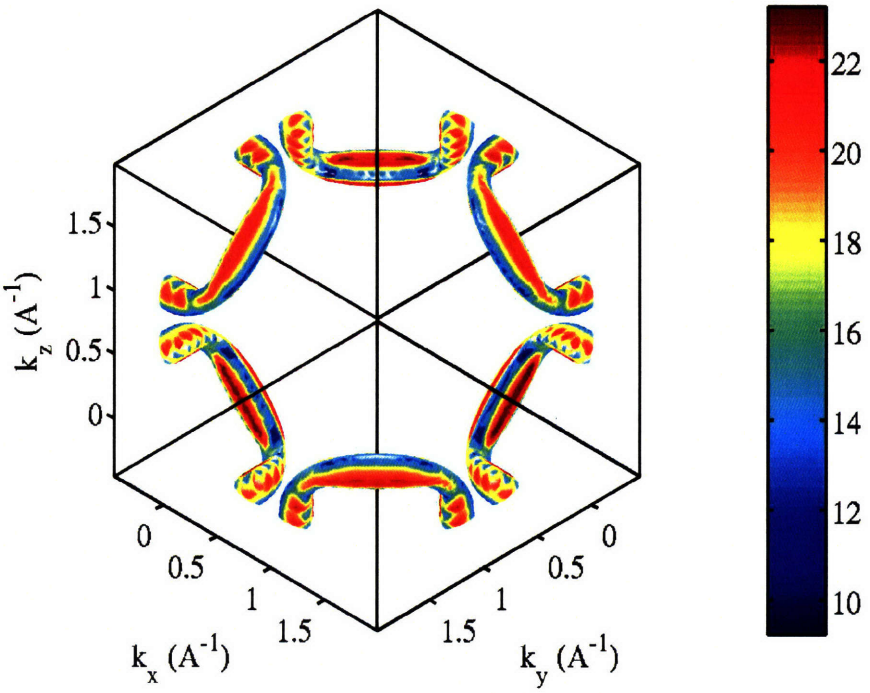

(b) band 3

Figure 3-12: Fermi surface of FCC Al color-coded by Fermi velocity (velocity units: Å/fs).

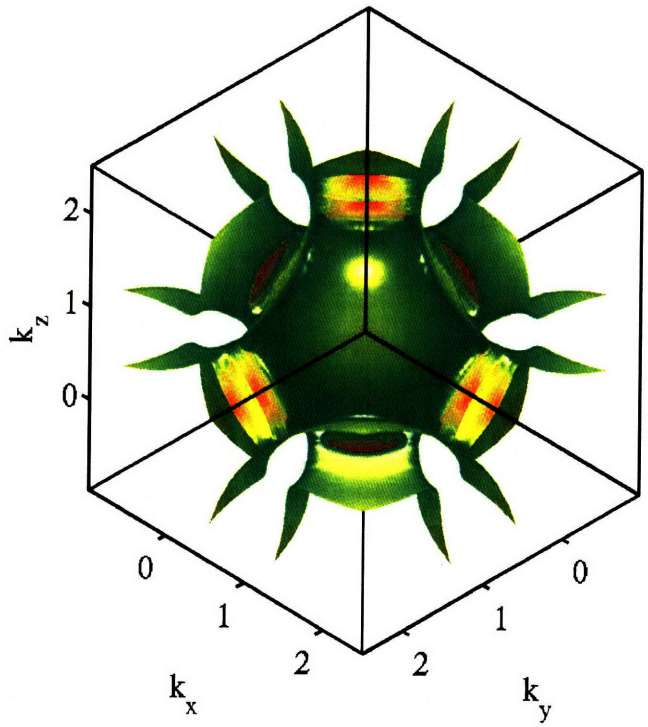

(a) band 2

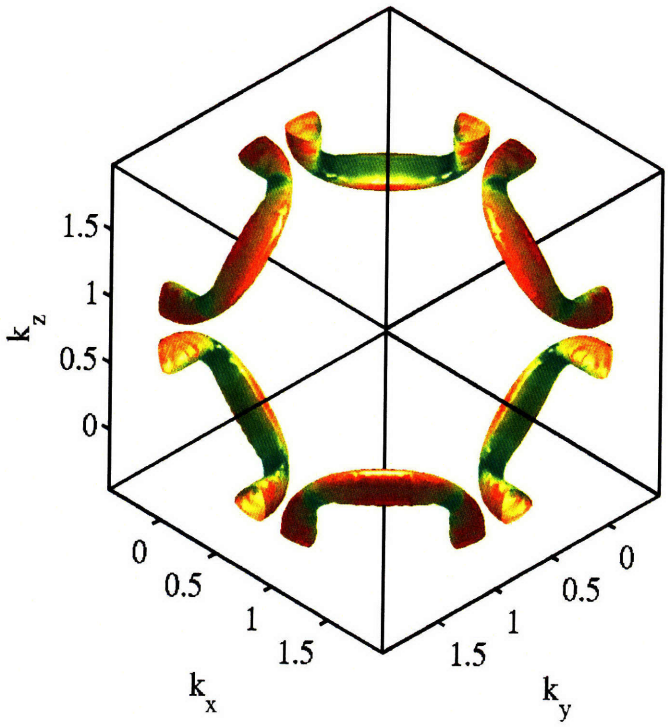

(b) band 3

Figure 3-13: QO-projected Fermi surface of FCC Al color-coded by angular momentum components of QOs. (The color map is the same as that of Fig. 3-10(b).)

3.5.4 Ferromagnetic material: BCC Fe

One of ferromagnetic materials — BCC iron — is investigated, in which we expect some differences between the QOs with majority spin and those with minority spin. Here the Fermi level is shifted up by 3 eV to keep electronic structure near the original Fermi level to be exact. Pseudoatomic orbitals $4s$ and $4p$ are rescaled by $e^{-\eta|\mathbf{x}|}$ with $\eta = 0.5$ and then renormalized. Fig. 3-14 displays five of total 9 QOs. The QOs for both majority spin and minority spin, on the left and middle columns respectively, look very similar. However the difference between these QOs shown in the right column is very clear and the isosurfaces of the orbital difference have the same symmetry as the corresponding QOs. Fig. 3-15(a) and Fig. 3-15(b) present two different band structures with majority spin and minority spin respectively and both of them have excellent agreement with those from DFT calculations. Density of states plotted in Fig. 3-17 shows the dramatic difference of electronic structure between majority spin and minority spin in BCC Fe.

Fig. 3-18(a) and Fig. 3-18(b) are two corresponding Fermi surface plots. In Fig. 3-18(a) for the majority spin case, the closed surface around Γ point holds electrons while the open surfaces on the zone faces and another two types of small surfaces an the corners enclose holes. These open surfaces are connected to other surfaces of the same type in the second Brillouin zone and thus form open orbits along certain directions. In Fig. 3-18(b) for the minority spin case, the surfaces around H point at the corners and those around N point on the zone faces form hole pockets while one octahedral closed surface around Γ point and six spherical balls form electron pockets. Moreover, Fig. 3-19 and Fig. 3-20 show Fermi surfaces color-coded by the amplitude of Fermi velocity: Fig. 3-19(a, b) for band 5 and 6 of majority spin and Fig. 3-20(a, b) for band 3 and 4 of minority spin respectively. Fig. 3-21 and Fig. 3-22 are Fermi surfaces color-coded by QO components: Fig. 3-21(a, b) for band 5 and 6 of majority spin and Fig. 3-22(a, b) for band 3 and 4 of minority spin respectively. Those plots reflect that Fermi electrons of both spins mostly contain d characters. However compared to the FCC Al case, averaged Fermi velocity of BCC Fe is smaller.

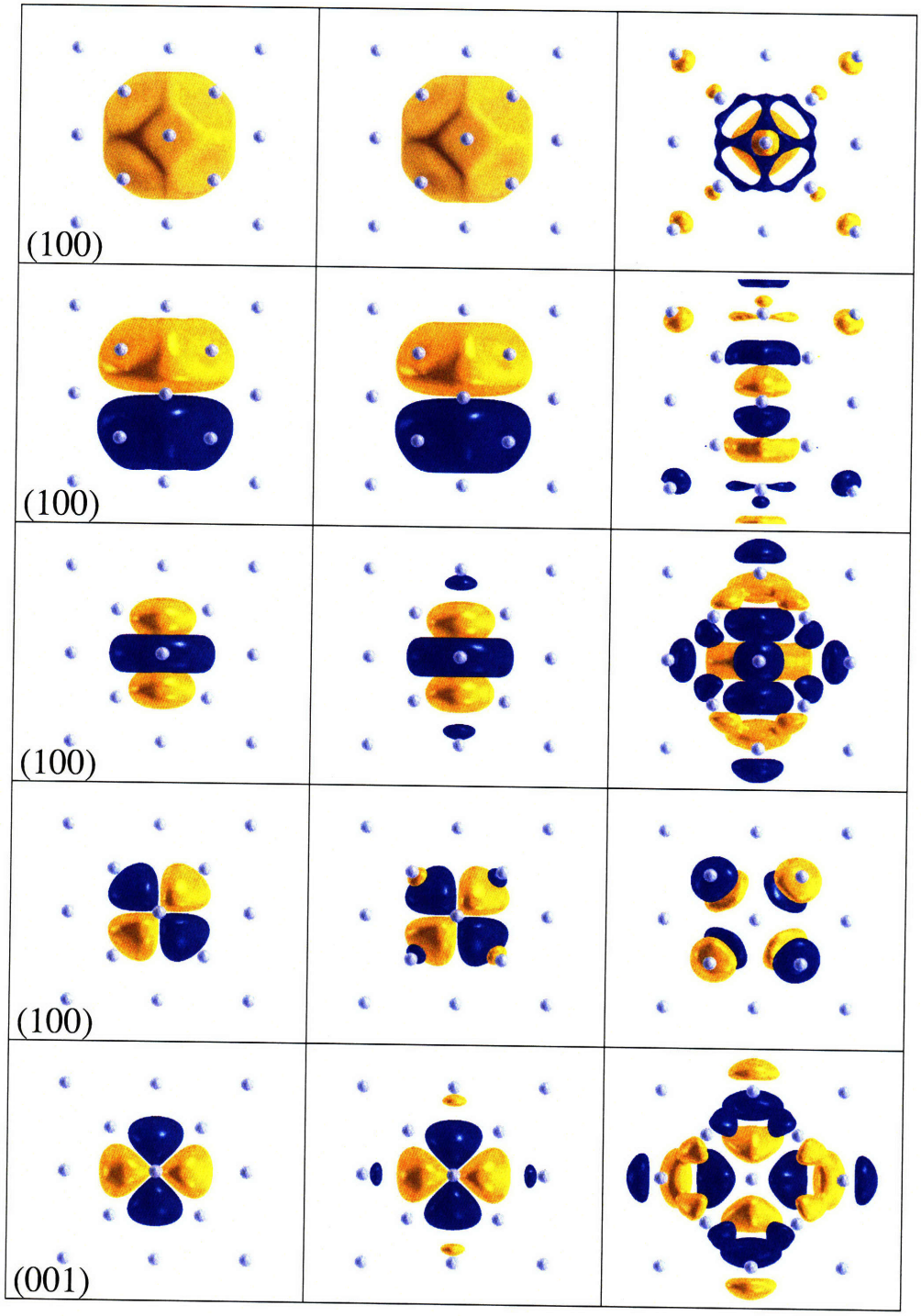

Figure 3-14: QO in BCC Fe. From top to bottom they are: s-like, p_z-like, d_{z^2}-like, d_{yz}-like and $d_{x^2-y^2}$-like QOs. Left column: QOs with majority spin (absolute isosurface value: 0.03 Å^{-3}). Middle column: QOs with minority spin (absolute isosurface value: 0.03 Å^{-3}). Right column: difference between QOs with majority spin and QOs with minority spin (absolute isosurface value: 0.003 Å^{-3})

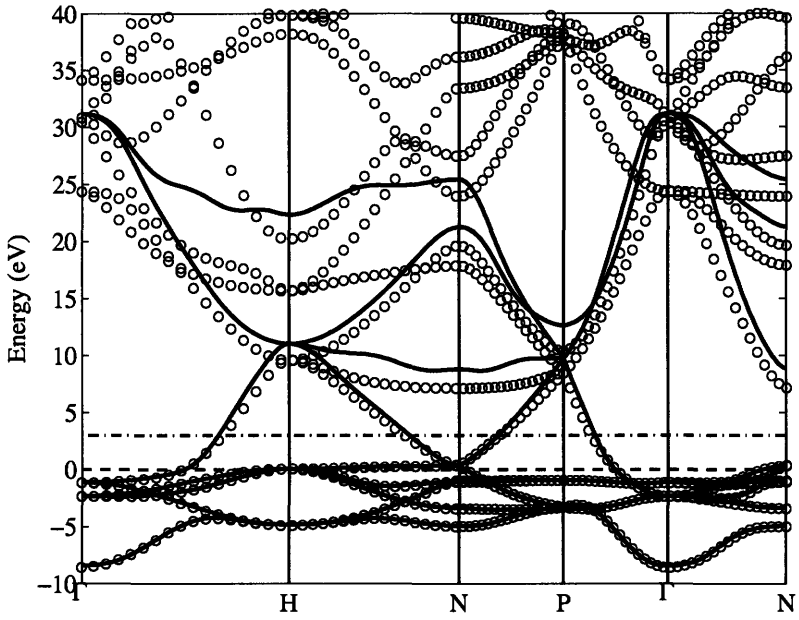

(a) majority spin

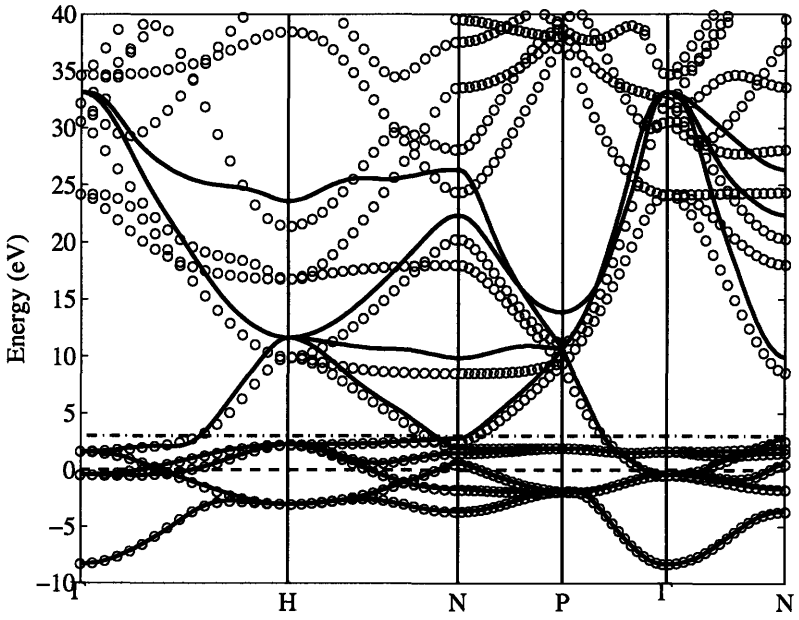

(b) minority spin

Figure 3-15: Band structure of BCC Fe with (a) majority spin and (b) minority spin. (circle dot: planewave DFT calculation; solid line: tight-binding calculation based on 9 QOs; dashed line: Fermi level; dash-dot line: shifted Fermi level with $E_{\text{shift}} = 3$ eV.)

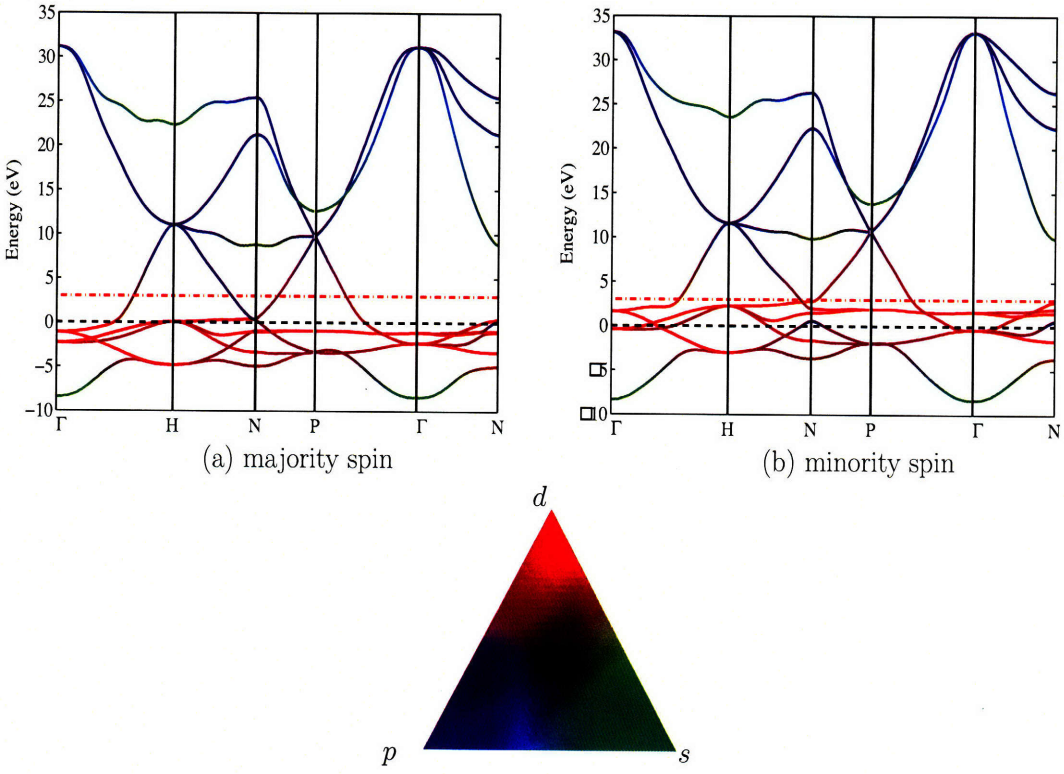

Figure 3-16: QO-projected band structure of BCC Fe with (a) majority spin and (b) minority spin. They are color-coded by (c) color triangle with red for five d-like QOs, green for one s-like QO, and blue for three p-like QOs. (dashed line: Fermi level; dash-dot line: shifted Fermi level with $E_{\text{shift}} = 3$ eV.)

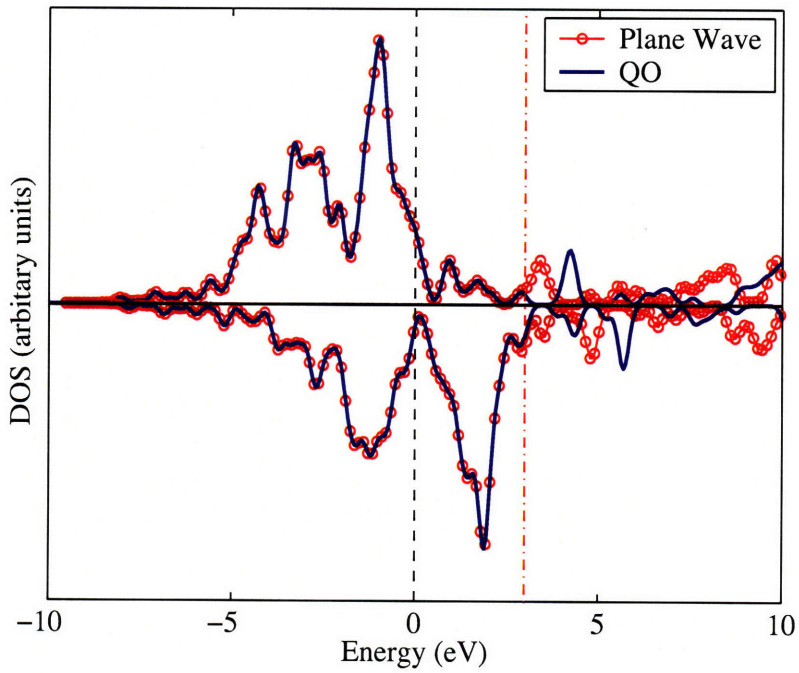

Figure 3-17: Density of states of BCC Fe. Top panel: majority spin; bottom panel:minority spin. (circle-dot line: planewave DFT calculation; solid line: tight-binding calculation; dashed line: Fermi level; dash-dot line: shifted Fermi level with $E_{\text{shift}} = 3$ eV.)

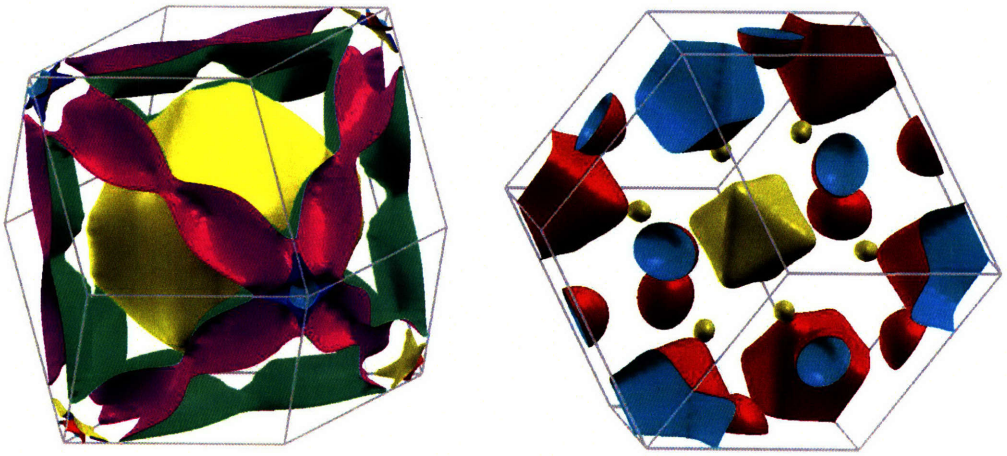

(a) majority spin

(b) minority spin

Figure 3-18: Fermi surface of BCC Fe with (a) majority spin and (b) minority spin.

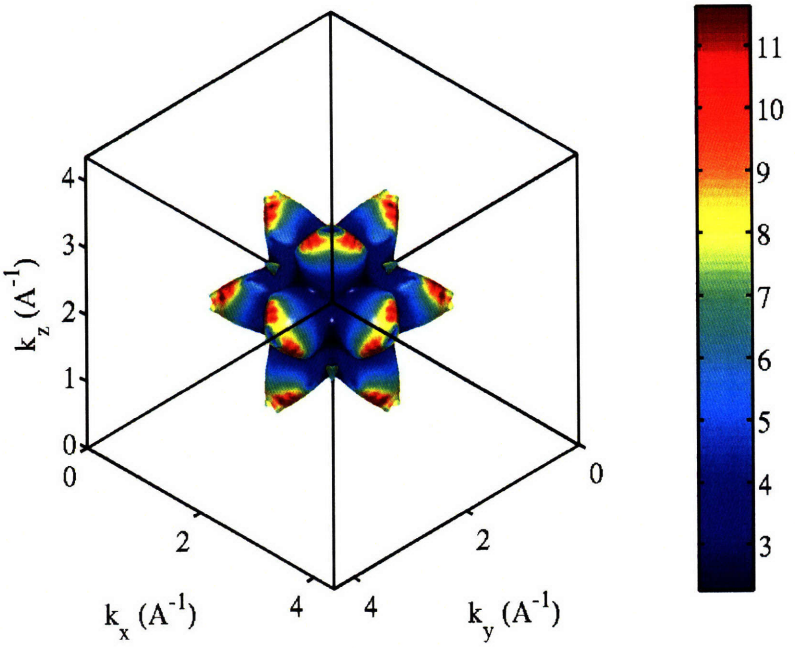

(a) band 5

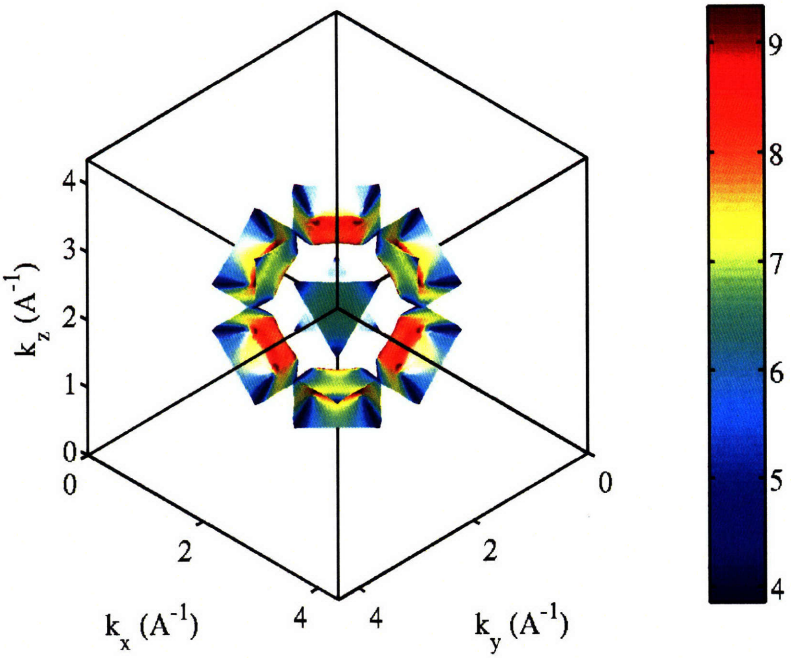

(b) band 6

Figure 3-19: Fermi surface of BCC Fe with majority spin color-coded by Fermi velocity: (a) band 5 (b) band 6 (velocity units: Å/fs).

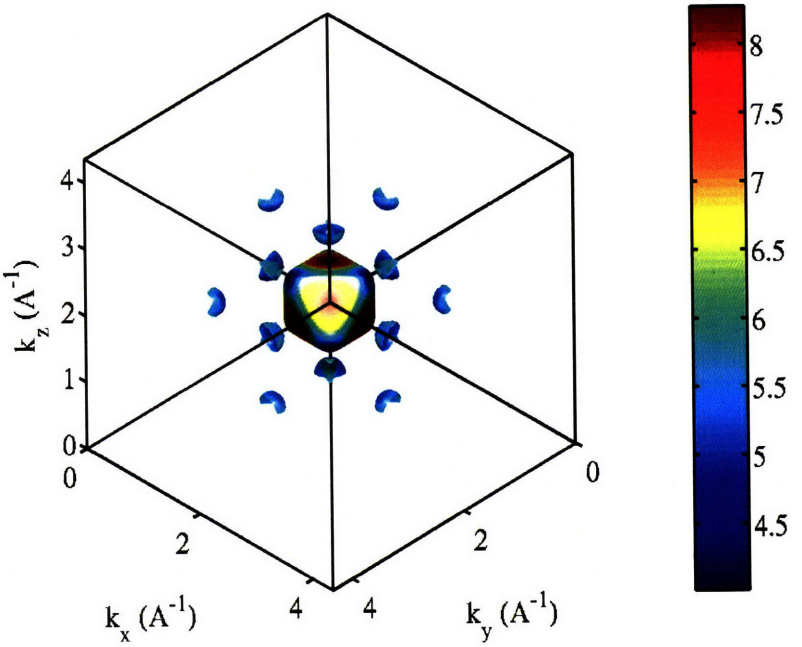

(a) band 3

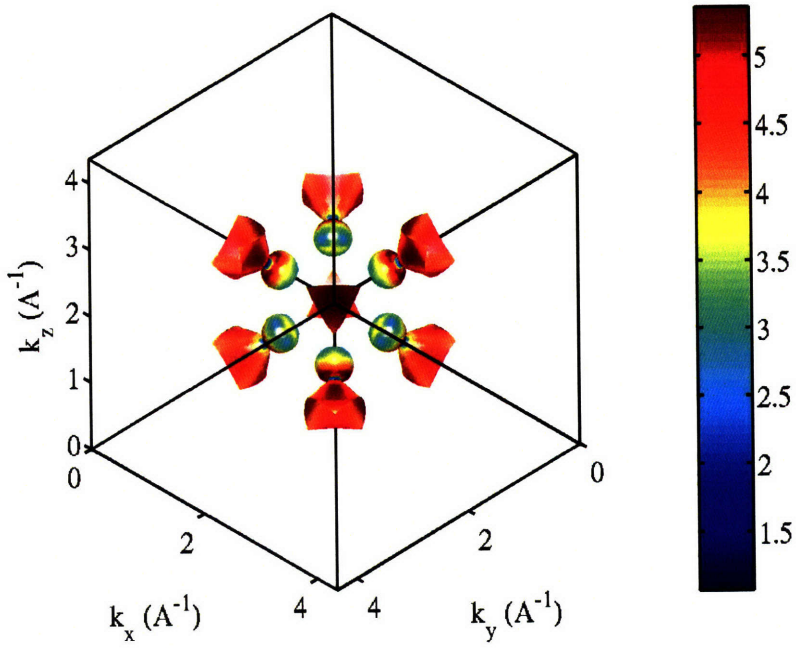

(b) band 4

Figure 3-20: Fermi surface of BCC Fe with minority spin color-coded by Fermi velocity: (a) band 3 (b) band 4 (velocity units: Å/fs).

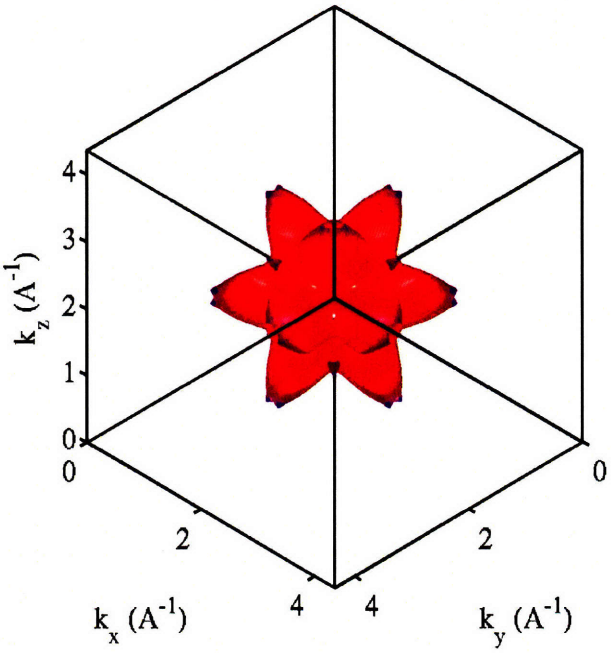

(a) band 5

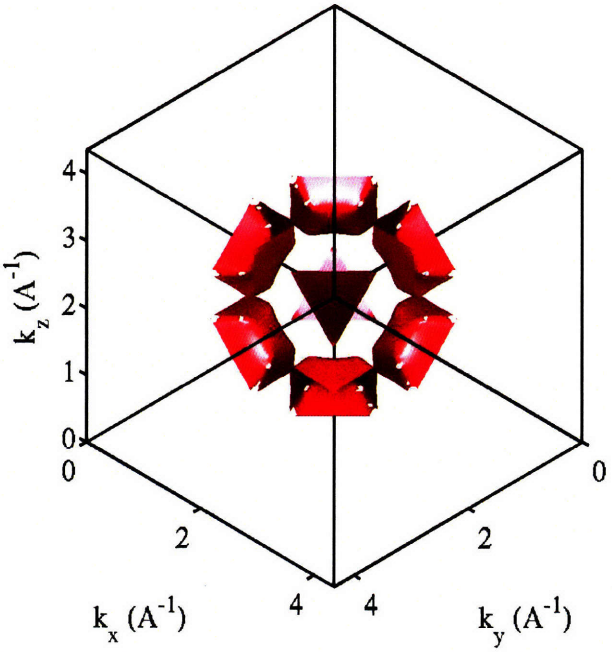

(b) band 6

Figure 3-21: QO-projected Fermi surface of BCC Fe with majority spin color-coded by angular momentum components of QOs: (a) band 5 (b) band 6. (The color map is the same as Fig. 3-16(c).)

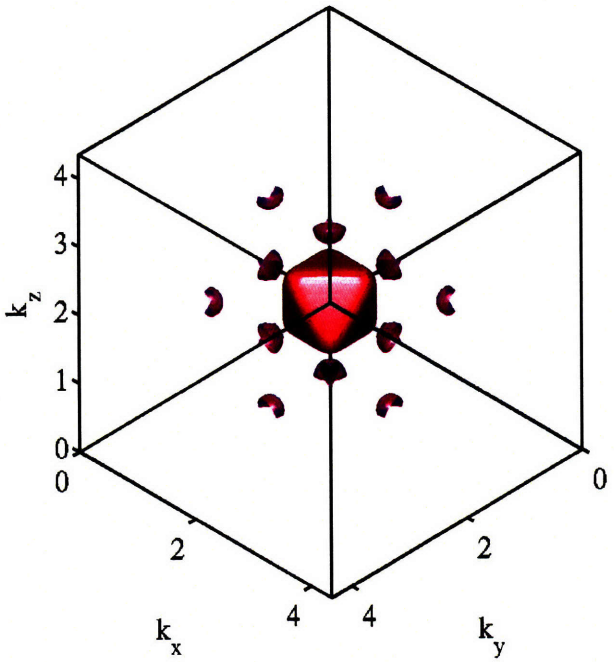

(a) band 3

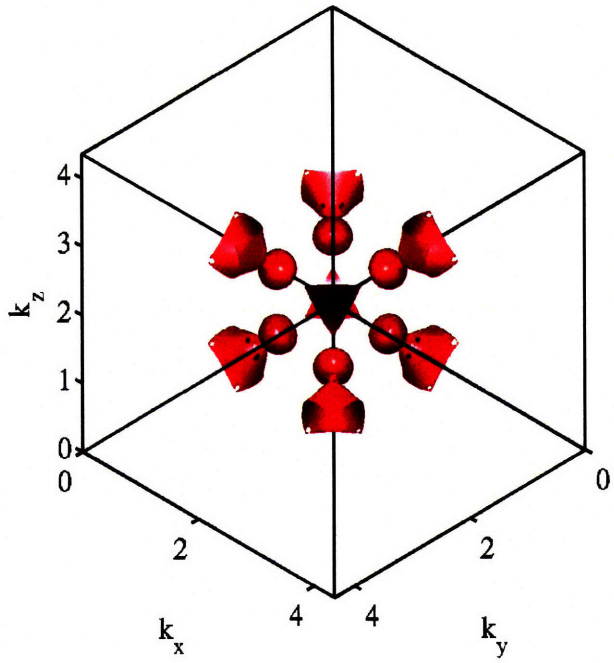

(b) band 4

Figure 3-22: QO-projected Fermi surface of BCC Fe with minority spin color-coded by angular momentum components of QOs: (a) band 3 (b) band 4 (The color map is the same as Fig. 3-16(c).)

3.5.5 Transition metal oxide: rutile TiO_2 crystal

QO can also be constructed in transition metal oxides such as rutile-phase titanium dioxide(TiO_2) crystal. It is seen from Fig. 3-23(a) that TiO_2 has a wide band gap — about 2 eV. Fig. 3-23(b) presents the corresponding density of states from both DFT calculation and QO-based tight-binding calculation. Again both band structure and density of states show the perfect match between plane-wave DFT result and *ab initio* tight-binding result below Fermi level. If we examine the DOS plot carefully, we can see even DOS above Fermi level but below 7.5 eV is very similar to each other in both calculations. That is further confirmed by the comparison between the band structures from DFT and tight-binding calculations. The manifold of the DFT band structure is almost fully represented by the *manually-constructed* unoccupied Bloch subspace.

3.5.6 High temperature superconductor: HCP MgB_2

It is well known that magnesium diboride (MgB_2) crystal in hexagonal close packed structure, shown in Fig. 3-24(a), is a superconductor material. Here pseudoatomic atomic orbitals include magnesium's $2p$, $3s$, $3p$ and $3d$ orbitals and boron's $2s$ and $2p$ orbitals, and the corresponding 20 QOs are constructed with the Fermi level shifted up by 3 eV. During the construction we rescale $2p$, $3s$, $3p$, and $3d$ pseudoatomic orbitals by $e^{-\eta|\mathbf{x}|}$ with $\eta = 0.5$, 0.5, 0.5, and 1.0 respectively and then renormalize them. As shown in Fig. 3-24(b), below the shifted Fermi level ($E_{\text{shift}} = 3$ eV) two band structures obtained from planewave DFT calculation and QO-based tight-binding calculation are exactly the same as each other. The density of states also shows the similar exact match, demonstrated in Fig. 3-25(a).

Fermi surface plotted in Fig. 3-25(b) provides a visual tool to understand the contribution of Fermi electrons. One type of the Fermi surfaces is σ-type band from σ-bonding on the boron $x-y$ plane and it is seen from Fig. 3-25(b) that around Γ point there are two cylindrical sheets of Fermi surface which enclose holes. Two sheets are open surfaces along Γ-A direction in momentum space and form open hole orbits in the

same direction. Since velocity direction of charge carriers in real space is perpendicular to Fermi surface in momentum space, these two bands corresponds to two σ bands of p_x and p_y orbitals on boron plane. The other type of the Fermi surfaces comes from π bonding orbital of boron plane. Two ring-shaped sheets (purple/green) of Fermi surface around the zone's top and bottom edges enclose electrons from p_z antibonding orbitals (π^*) of boron plane while another ring-shaped sheet (yellow/blue) around the center of zone faces encloses holes from p_z bonding orbitals (π). The above conclusion can also be found in QO-projected band structure (Fig. 3-26), where two distinct types of bands are around Fermi level. Especially green bands with boron's s-like, p_x-like and p_y-like QO characters are not only the major components around A and Γ points, but also dominate most of occupied bands except two dark bands formed by boron's p_z-like QOs and magnesium's s-like and p-like QOs. Our results are very similar to the conclusions of Choi and et al. [153]. However, the difference is that the π Fermi sheets also contain some contributions from magnesium's s-like and p-like QOs beside boron's p_z-like QOs. Similar to the BCC iron case, Fig. 3-27 shows Fermi surfaces color-coded by Fermi velocity (a,c,e) and QO components (b,d,f). From these surface plots, we see that most of Fermi surfaces are dominated by boron's s-like, p_x-like and p_y-like QOs while Fermi velocity distribution changes a lot in all the surface sheets.

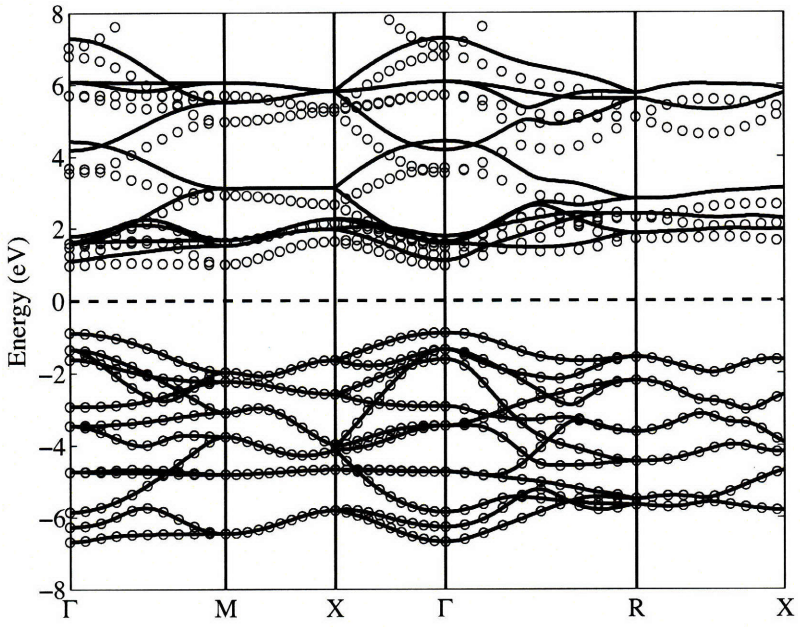

(a)

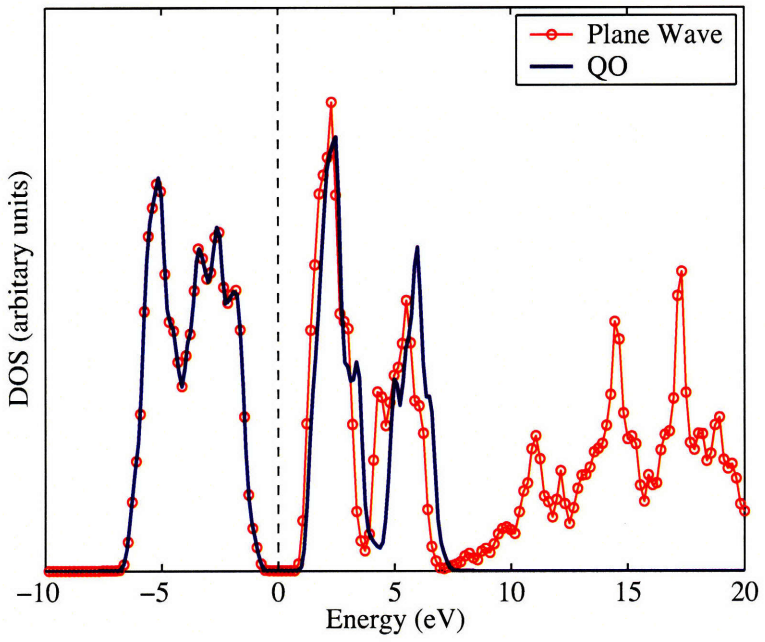

(b)

Figure 3-23: (a) Band structure of rutile TiO_2. (circle dot: planewave DFT calculation; solid line: tight-binding calculation; dashed line: Fermi level.) (b) Density of states of rutile TiO_2. (circle-dot line: planewave DFT calculation; solid line: tight-binding calculation; dashed line: Fermi level.)

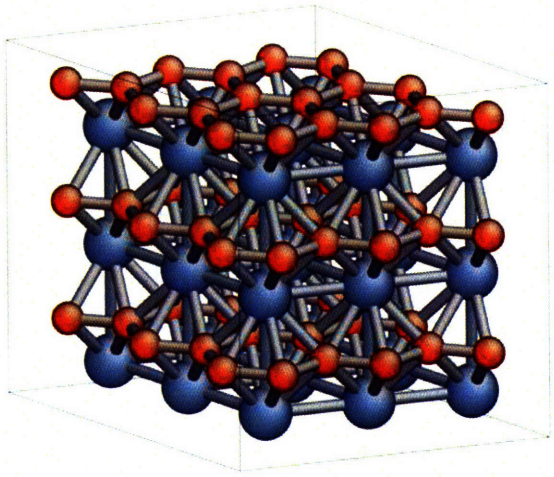

(a)

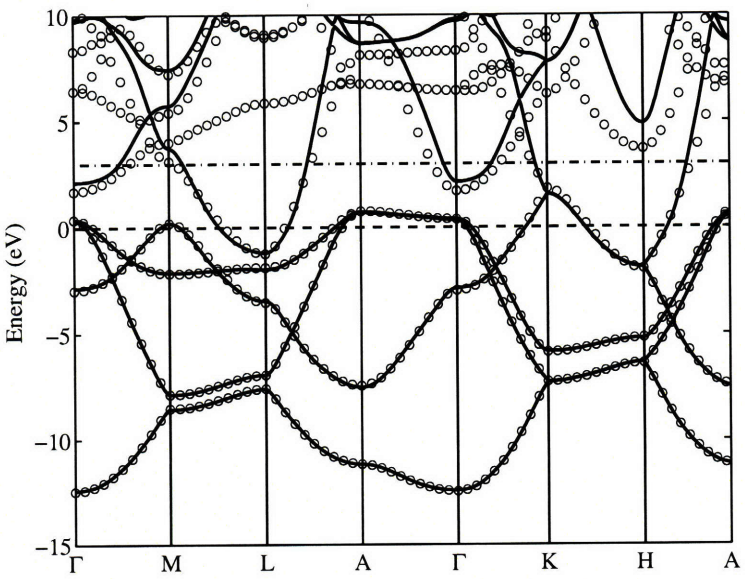

(b)

Figure 3-24: (a) Atomistic structure of HCP MgB_2 visualized by AtomEye [152].(Gray: Mg; Orange: B) and (b) band structure of HCP MgB_2. (circle dot: planewave DFT calculation; solid line: tight-binding calculation based on 20 QOs; dashed line: Fermi level; dash-dot line: shifted Fermi level with $E_{\text{shift}} = 3$ eV.)

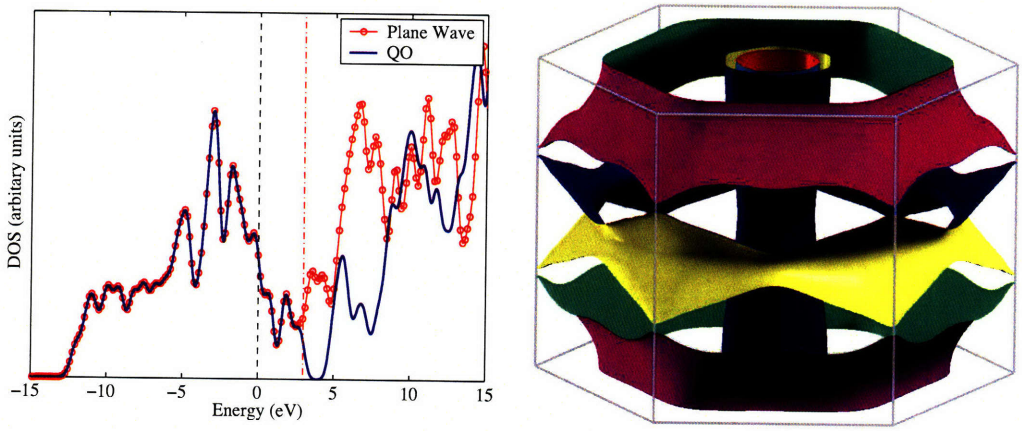

(a) (b)

Figure 3-25: (a) Density of states of HCP MgB_2. (circle-dot line: planewave DFT calculation; solid line: tight-binding calculation; dashed line: Fermi level; dash-dot line: shifted Fermi level with $E_{\text{shift}} = 3$ eV.) (b) Fermi surface of HCP MgB_2.

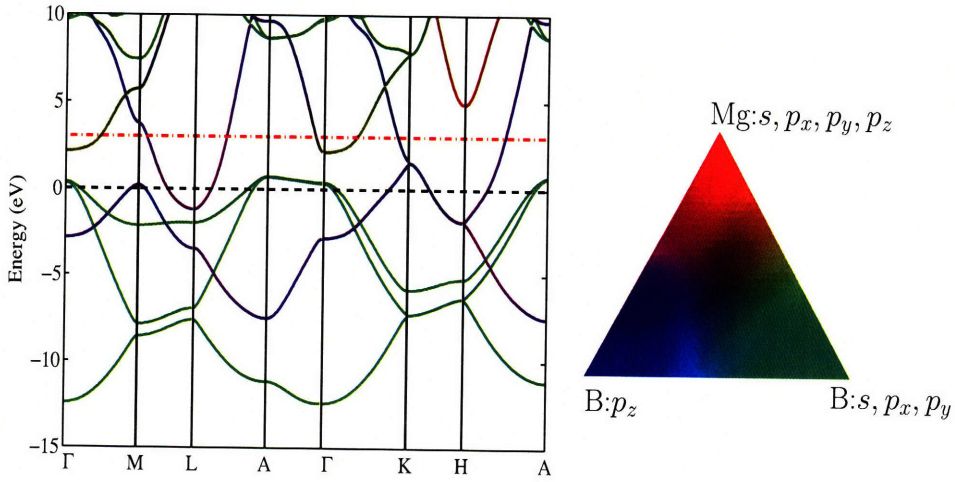

Figure 3-26: QO-projected band structure of HCP MgB_2 colored by three components with red for Mg's s-like and p-like QOs, green for B's s, p_x-like and p_y-like QOs, and blue for B's p_z-like QO. (dashed line: Fermi level; dash-dot line: shifted Fermi level with $E_{\text{shift}} = 3$ eV.)

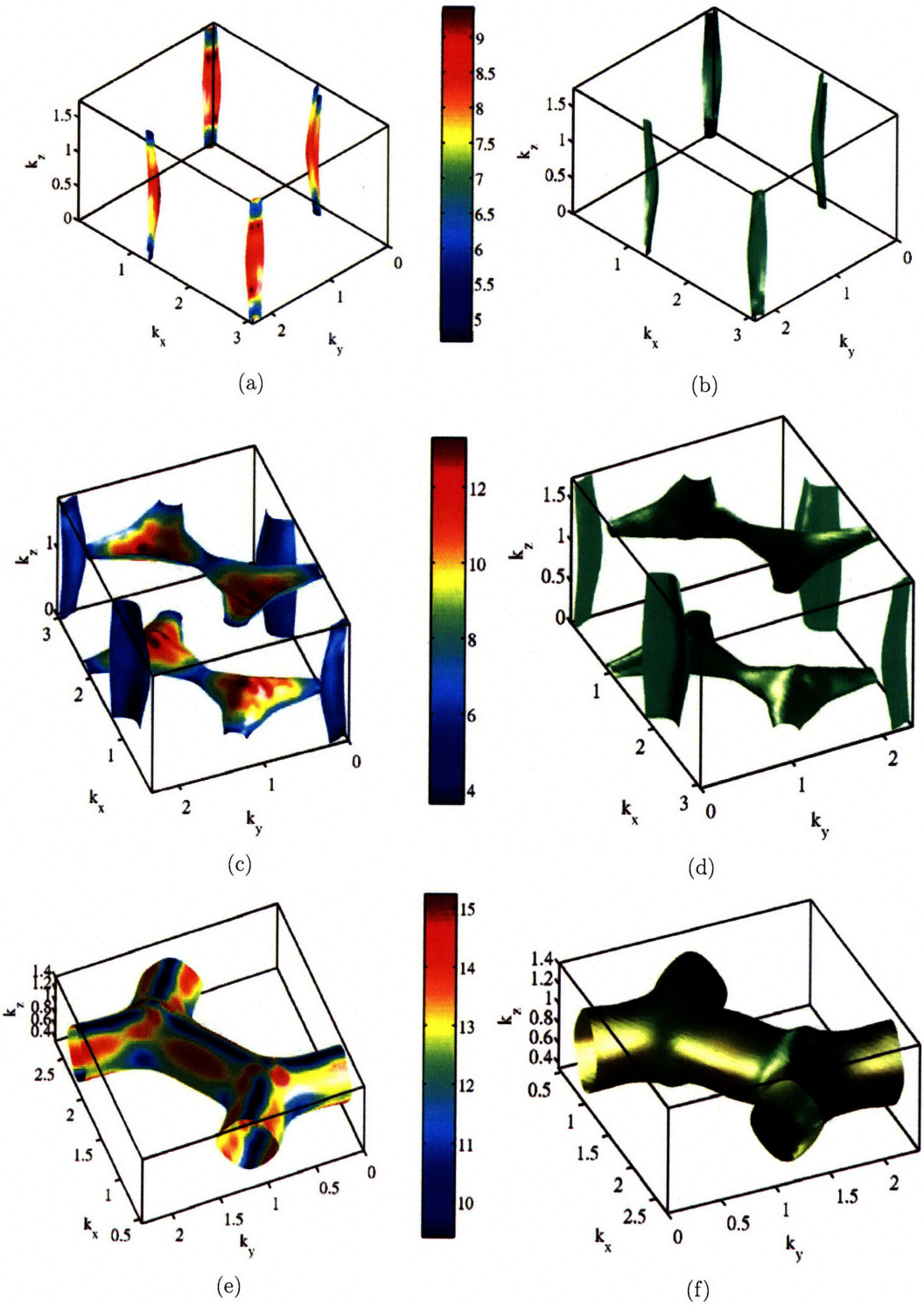

Figure 3-27: Fermi surface of HCP MgB_2: (a), (c), and (e) are color-coded by Fermi velocity; (b), (d), and (f) are color-coded by QO components. (The color bar here is for velocity magnitude with the unit of Å/fs; the color map of QO components is similar to that of Fig. 3-10(b) but with red for Mg's s-like and p-like QOs and green for B's s-like and p-like QOs.)

3.5.7 Quasi-one dimensional material: (5,5)-CNT

Quasi-one dimensional materials are rapidly emerging in recent years due to their various interesting properties which behave totally different from thin films or bulk materials. Carbon nanotube (CNT) is one example obtained by wrapping one or multiple layers of graphite into a cylindrical tube. Single wall carbon nanotube (SWNT) is characterized by chiral vector (n, m) which denotes the number of unit vectors along two directions in the honeycomb crystal lattice of graphene. The chiral vector (n, m) eventually determines both diameter and chiral angle of SWNT.

Here we use SWNT with $n = m = 5$ (armchair) as an example. QOs are constructed with Fermi level shifted up by 2 eV and pseudoatomic $2p$ orbitals rescaled by $e^{-0.5|\mathbf{x}|}$ and renormalized. Some QOs of CNT-(5,5) are constructed and shown in Fig. 3-28 and it is observed that both s and p orbitals are largely "deformed" to the QOs due to strong covalent bonding. The corresponding band structure and density of states are shown in Fig. 3-29(a) and Fig. 3-29(b). As expected, the armchair CNT is metallic with finite density of states around Fermi level. It is noted that some energy points between true Fermi level and shifted Fermi level are not exactly the same as those from DFT calculation. It is possibly due to the strong deformation of atomic orbitals in CNT, therefore the constructed virtual unoccupied subspace is not fully complementary to the subspace below the shifted Fermi level.

3.6 Comparison with Maximal Localized Wannier Function

QO is different from Wannier functions such as MLWF developed by Marzari and Vanderbilt [105]. Both position and shape of MLWF are unknown before the construction is fully finished. It could be like atomic orbital or like bonding orbital, which is determined by the information included in the selected Bloch subspace. Obviously MLWF is the most localized orthogonal Wannier function and it could achieve even more localization if orthogonal condition is relaxed. The localization [141] and

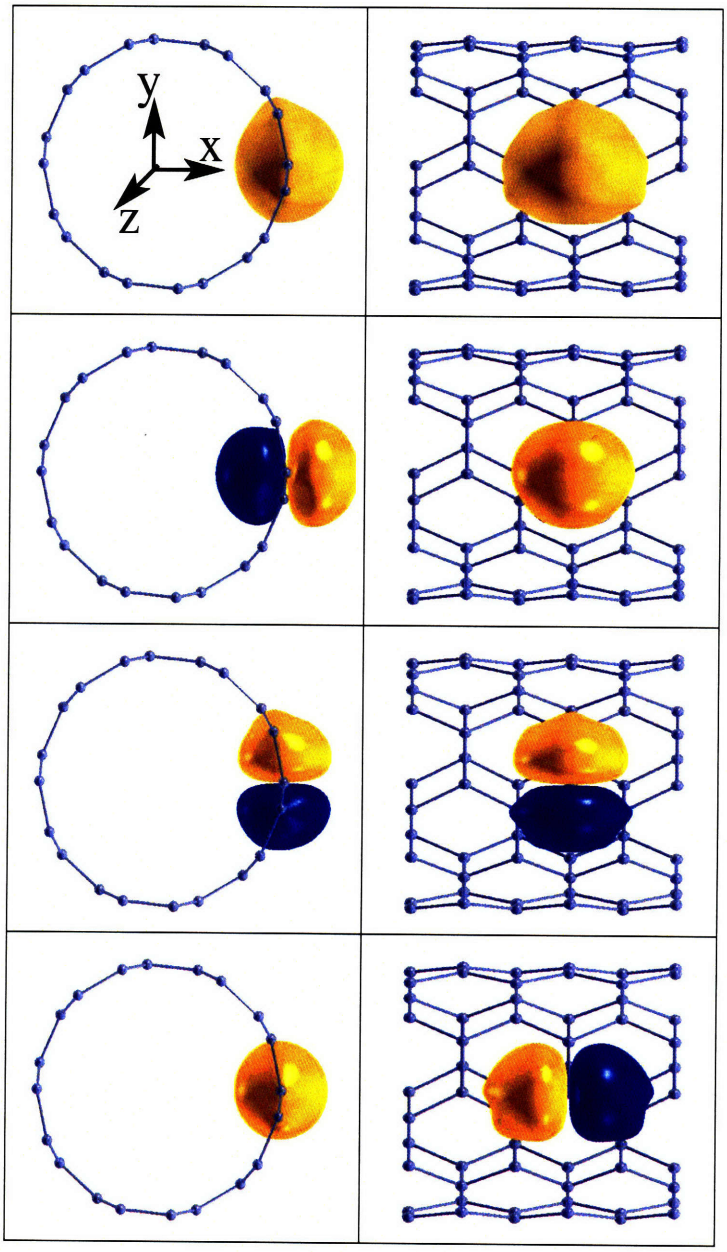

Figure 3-28: QO in carbon nanotube with chiral vector $(n, m) = (5, 5)$. Left column: isosurface viewed from z-direction. Right column: isosurface viewed from x-direction. (absolute isosurface value: 0.06 Å^{-3})

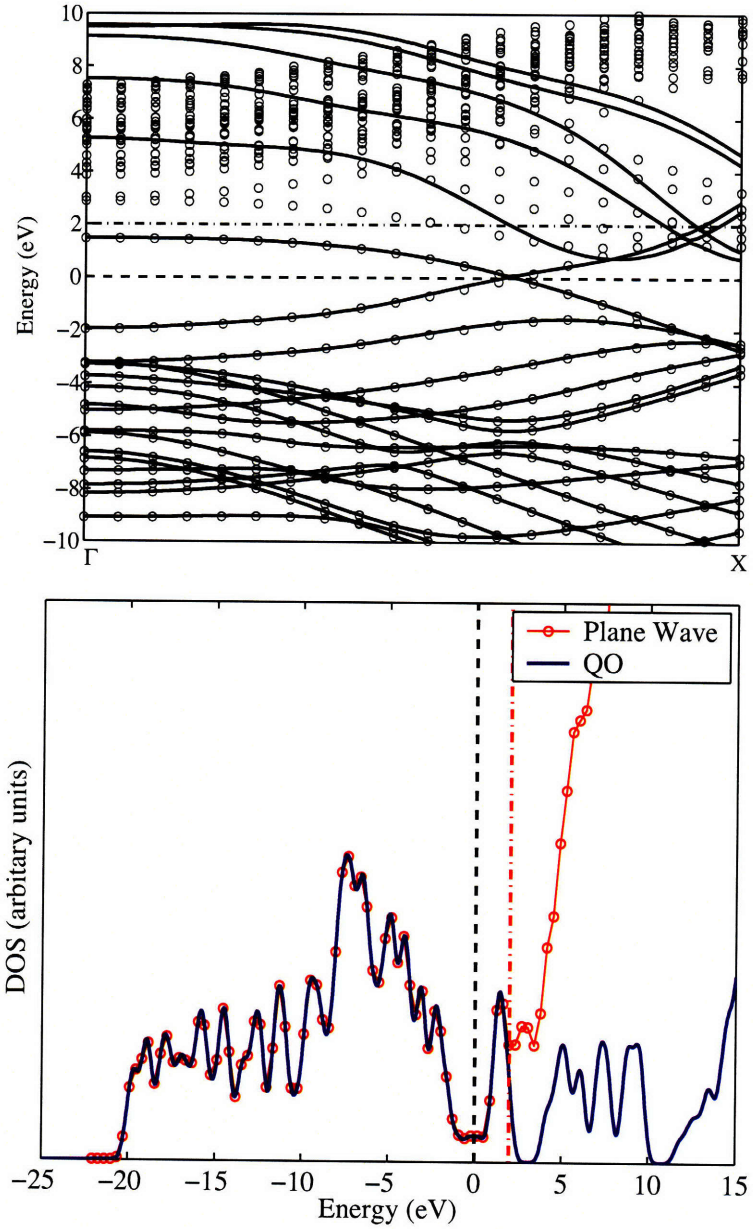

Figure 3-29: (a) Band structure and (b) Density of states of CNT(5,5). (circle dot: planewave DFT calculation; solid line: tight-binding calculation; dashed line: Fermi level; dash-dot line: shifted Fermi level with $E_{\text{shift}} = 2$ eV.)

uniqueness of MLWF are great advantages compared to Lu's QUAMBO and our QO. However, the position and angular momentum of QUAMBO and QO are known *before* the construction, which makes our QO much more transferable.

3.7 Comparison with Quasiatomic Minimal Basis-set Orbital

The original Lu's QUAMBO method [107, 108, 109, 110, 111] selects an optimized combinations of unoccupied Bloch states from DFT calculations to obtain virtual unoccupied Bloch states. This method is also implemented in our code. However, one major disadvantage of Lu's method is that one needs to include enough Kohn-Sham bands to capture all bonding and antibonding Bloch states for the corresponding atomic orbitals. It is difficult to predict where the corresponding highest antibonding Bloch state is. Even if it was predictable, usually this state could be at very high energy. Therefore, with conventional DFT calculations it is very inefficient and memory-consuming to calculate and store such a large number of bands. More importantly, many of these unoccupied bands with other orbital characteristics are not useful at all and in the Lu's scheme most of time could be wasted on calculating atomic projections on these irrelevant bands. However, our new method is totally independent of true unoccupied Bloch states since we *directly* construct the virtual unoccupied Bloch states and the only additional cost is non-self-consistent evaluation of energies of virtual unoccupied Bloch states with Kohn-Sham Hamiltonian.

3.8 Comparison with Projected Atomic Orbital

The construction of unoccupied virtual Bloch subspace from atomic orbital Bloch subspace in our QO scheme is very similar to that in Pulay and Sæbø's PAO scheme [112, 113, 114]. However in general our QO scheme is applicable to molecules, surfaces and solids, which can be embedded in or interfaced to all quantum chemistry packages and all density functional theory packages with norm-conserving pseudopo-

tentials, ultrasoft pseudopotentials or PAW method. As we have shown in the above various applications, QO can be constructed not only in insulators and semiconductors, but also in metallic systems. Another important difference is that here we use the rescaled pseudoatomic orbitals from DFT pseudopotential generators as the projection objects. Therefore, as another advantage we have much less number of basis orbitals to construct and diagonalize in tight-binding calculations. As a result, we can more efficiently perform tight-binding parametrizations, electrical conductance calculations, quasi-particle GW corrections, and many other important applications in electric structure.

3.9 Summary

In this chapter QO with Vanderbilt ultrasoft pseudopotentials and PAW method is derived and constructed for different types of materials. We have implemented and benchmarked QOs in DACAPO and VASP packages with USPP and PAW. The accuracy, efficiency, localization and robustness are demonstrated through various electronic structure properties including band structure, QO-projected band structure, density of states, QO-projected density of states, Fermi surface, QO-projected Fermi surface, Fermi-velocity encoded Fermi surface, bond order and Mülliken charge transfer. The most important property of QO itself is that it keeps electronic structure under certain energy level to be lossless while it has very good localization by including the *directly-constructed* complementary Bloch subspace. Therefore, QO can be used as an accurate localized basis set in linear-scaling electronic structure calculations. For example, it can be applied to calculate electrical conductance of molecular junctions or nanoscale electronics by non-equilibrium Green's function method. With further derivations we can also establish the relation between QO and Berry phase (a geometrical phase) in solids, therefore easily calculate polarization. In general the present work validates the applicability of Slater's linear combinations of atomic orbitals (LCAO) idea, and points to future *ab initio* tight-binding parametrizations.

Chapter 4

Electrical conductance from Green's function method

In the previous chapter we have proposed an efficient method to construct localized quasiatomic orbitals and their corresponding *ab initio* tight-binding Hamiltonian and overlap matrix. With this localized basis-set, Green's function method based on Landauer formalism can be applied to calculate electrical conductance for phase coherent transport in nanoscale materials. We have implemented QO construction and Green's function evaluation in our code and currently it is interfaced to the plane-wave DFT results from VASP [31] and DACAPO [33] in the network common data form(NetCDF).

In this chapter, we will study several applications and explore electron transport mechanism in molecular and nanoscale electronics. The applications include:

- pure one dimensional conductor (Sec. 4.1)
- aluminum and carbon atomic wires between two Al(001) electrodes with finite cross-section (Sec. 4.2)
- benzene dithiolate molecule (BDT) sandwiched by two gold atomic wires (Sec. 4.3.1) and by two Au(001) electrodes with finite cross-section (Sec. 4.3.2)
- phenalenyl molecular bridge between two aluminum atomic wires (Sec. 4.3.3)

- (4,4)-carbon nanotube with and without Si-defect and single vacancy (Sec. 4.4)

Various interesting transport behaviors in these systems will be carefully analyzed, such as zero-dimensional resonant conductance peaks, one-dimensional conductance steps, spin-dependent transport, conductance oscillation, quantum loop current, and the effect of impurity and vacancy in carbon nanotubes.

4.1 One dimensional conductor vs. zero dimensional conductor

Pure one dimensional(1D) conductor can be described by traditional band theory if electron-phonon coupling and quasi-particle effect are not considered. Electron propagates through the 1D conductor via conducting eigenchannels without any dephasing and dissipation. Due to the scattering between pure 1D conductor and electron reservoir, each eigenchannel will contribute one conductance quantum $G_0 = 2e^2/h$. Here the factor of 2 accounts for spin degeneracy. Therefore, the total conductance of pure 1D conductor under zero bias will be $G(E_{\rm F}) = G_0 N(E_{\rm F})$, where $N(E_{\rm F})$ is the number of conducting channels at Fermi level $E_{\rm F}$.

Metallic wire is a typical example of pure 1D conductor. Here we take aluminum atomic wire as an example. The DFT calculation is performed by VASP package in a rectangular unit cell of $2.39 \times 10 \times 10$ Å^3 with one Al atom per unit cell. The Al-Al atomic spacing is $a_0 = 2.39$ Å along the x-direction. Aluminum has 3 valence electrons and the lowest possible orbitals for electron occupation are s and three p orbitals. Thus four corresponding QOs are constructed and shown in Fig. 4-1. Obviously s-QO and p_x-QO have been strongly deformed due to strong σ bonding along x direction while p_y-QO and p_z-QO are less affected. This also can be seen from QO-projected band structure in Fig. 4-2.

In Fig. 4-2 we distinguish four electronic bands from bottom to top: one σ bonding band, two degenerate $pp\pi$ bands, and one σ^* anti-bonding band. The σ bonding band at the bottom changes from pure s bonding at Γ point to pure p_x bonding at X point,

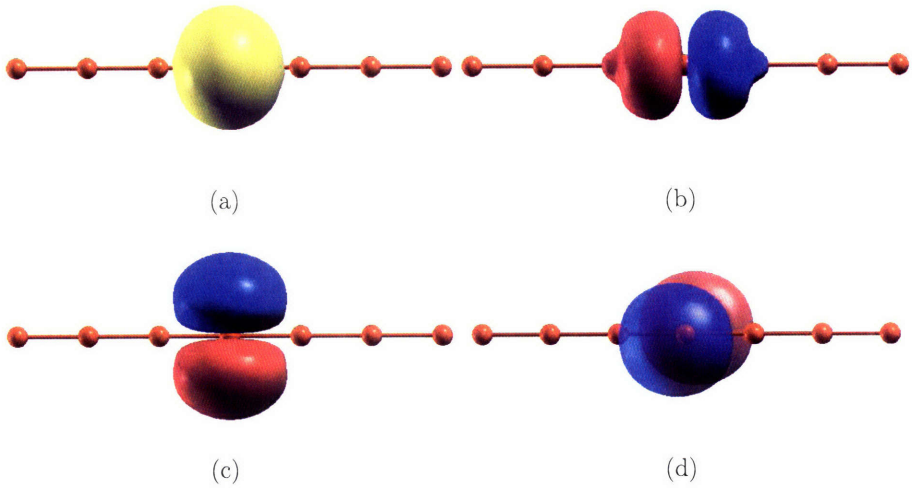

Figure 4-1: QOs in Al atomic wire

while the top σ^* anti-bonding band changes from pure p_x anti-bonding at Γ point to pure s anti-bonding at X point. It is consistent with our physical intuition. Since at Γ point the phase of QOs are each atom is zero, they directly add onto each other and the overall s Bloch wave function has the least number of nodes while p_x has the most number of nodes. Thus at Γ point $ss\sigma$ bonding band has the lowest energy and $p_xp_x\sigma^*$ anti-bonding band has the highest energy. Although this is very simple physical picture, it is much easier to find it out in the QO-projected band structure. Meanwhile the s and p_x bands have larger band width compared to the band with of p_y and p_z bands. That also indicates p_y and p_z-QOs are less affected due to their less important role in chemical bonding in Al atomic wire.

We notice that only p_y and p_z-QO bands are cross the Fermi level. Thus, from the above band counting method we know at Fermi level the total conductance of this Al atomic wire is $G = 2G_0$. This is clearly confirmed by the conductance curve calculated from Green's function method, shown in Fig. 4-3. The main feature of the conductance curve is step-like behavior and correspondingly density of states(DOS) has a sharp peak at each change of steps. DOS does not quickly go to zero and that is the direct consequence of electronic bands along transport directions. Fig. 4-3 shows the important electron transport mechanism in one-dimensional conductor, which is

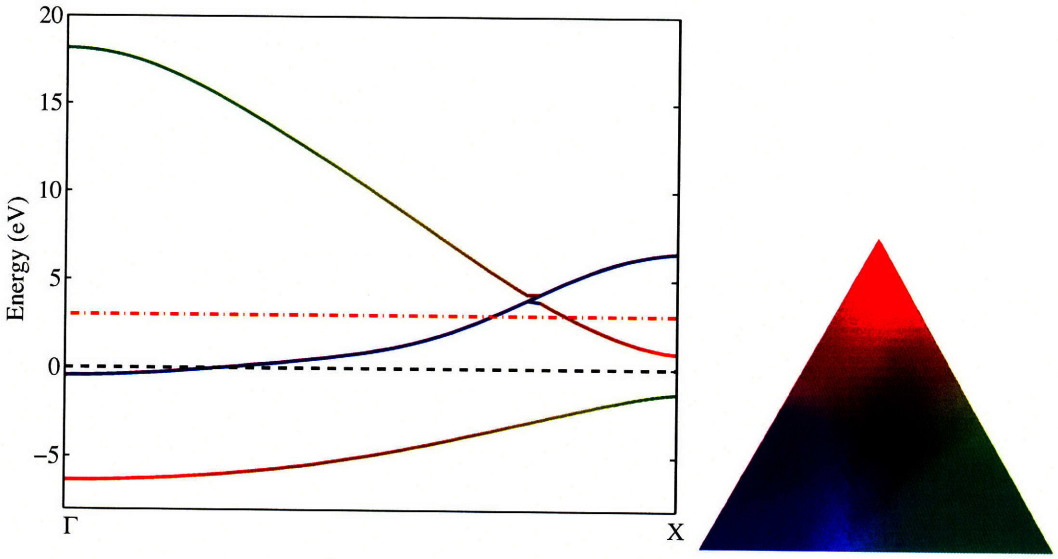

(a) (b)

Figure 4-2: QO-projected band structure (a) of Al atomic wire with the colormap (b): red for s-QO, green for p_x-QO, and blue for p_y-QO and p_z-QO. Black dash line is Fermi level and red dash-dot line is shifted Fermi level with $E_{\text{shift}} = 3$ eV.

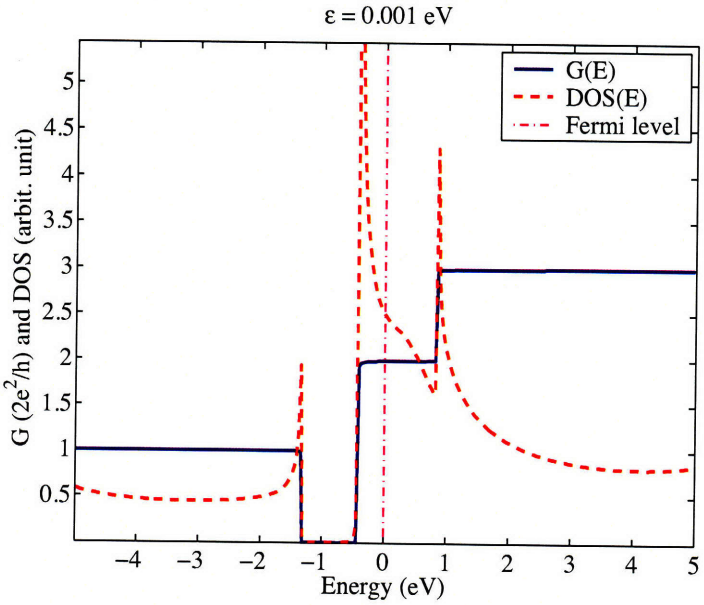

Figure 4-3: Electrical conductance and density of state of Al atomic wire as a function of energy

very different from the transport in zero-dimensional conductor.

In zero-dimensional conductors, the transport mechanism is resonant transport and it can be explained by the well-known Newns-Anderson model [154, 155]. In this model, single-level impurity is directly coupled to host metal and the latter is described by a continuous band. It can be shown that the energy-dependent conductance through the zero-dimensional single-level impurity is a simple Lorentzian function, which is very different from the conductance steps in the 1D case. Its center is the impurity's on-site energy and its width is determined by the coupling between the impurity and the host meal. Different from DOS in the pure 1D conductors, the corresponding density of states in 0D conductors quickly decays to zero.

In addition to the above theoretical comparison between 1D and 0D transport mechanism, we want to know how electrical current and wave functions change through the device. According to quantum mechanics, the current vector $\mathbf{J}(\mathbf{x})$ carried by a wave function $\psi(\mathbf{x})$ at position $\mathbf{x}$ is given by

$$\mathbf{J}(\mathbf{x}) = \frac{e}{2m}\Big[\psi^*[(\mathbf{p} - e\mathbf{A})\psi] + \psi[(\mathbf{p} - e\mathbf{A})\psi]^*\Big], \tag{4.1}$$

where $\mathbf{A}$ is vector potential and $\mathbf{p}$ is momentum operator with $\mathbf{p} = -i\hbar\nabla$. Here we do not consider external magnetic fields. Thus we have

$$\mathbf{J}(\mathbf{x}) = \frac{e\hbar}{m}\mathrm{Im}\Big[\psi^*(\mathbf{x})\nabla\psi(\mathbf{x})\Big] = \frac{e\hbar}{m}\Big|\psi(\mathbf{x})\Big|^2\,\nabla\phi(\mathbf{x}) = \frac{e\hbar}{m}\rho(\mathbf{x})\,\nabla\phi(\mathbf{x}), \tag{4.2}$$

where $\psi(\mathbf{x}) = \Big|\psi(\mathbf{x})\Big|\,\exp\Big[i\phi(\mathbf{x})\Big]$ and $\phi(\mathbf{x})$ is the phase of wave function $\psi(\mathbf{x})$. The total current I_S through surface S is defined as surface integration of current vector $\mathbf{J}(\mathbf{x})$ and surface S is perpendicular to the current direction to be measured. That is,

$$\mathbf{I}_S = \int\int_S \mathbf{J}(\mathbf{x})\,dS. \tag{4.3}$$

Eq. (4.2) and Eq. (4.3) reveal that electrical current in the absence of magnetic fields only depends on two factors. One is the electron density carried by the wave function and the other is the gradient of the phase of wave function. We, therefore, understand

that the phase oscillation is the important signature of current flows. The simplest model is single right-traveling plane-wave electron $\exp(+ikx)$ scattering and tunneling through single square potential barrier. Two extreme cases are immediately obtained. In the limit of infinite high barrier, the incident electron $\exp(+ikx)$ will be completely reflected due to the scattering and the reflected wave function is $\exp(-ikx)$, forming a standing wave $2\cos(kx)$. In the limit of zero barrier, the incident electron $\exp(+ikx)$ will completely transmit through barrier without any scattering and it remains in the original eigen state $\exp(+ikx)$. In the first limit, we have finite electron density on the left, however there is no phase oscillation at all and thus no current exists. In the second limit, we have the complete phase oscillation from left to right and thus the current reaches the maximum. In the middle region with finite barrier, it is obvious that we will have both transmitted and reflected wave functions and thus obtain finite but less than 100% electrical current due to the scattering. We will demonstrate the phase oscillation as the signature of electrical current by various applications below.

4.2 Atomic wires between two electrodes

Atomic size electronics is one of the promising directions for future development toward ultrasmall scale devices. Atomic scale point contact is a simple and natural application to be explored. In the last decade it has been studied by experimentalists using scanning tunneling microscopy(STM) and mechanically controllable break junctions(MCBJ) technique. Conductance measurements of these metal point contacts [156, 157, 158] and metal wires [159, 160, 161, 162, 163, 164, 158] have shown a common behavior with flat conductance plateaus in the unit of quantum conductance (G_0) or half of G_0 for the spin-dependent cases. More interestingly, conductance oscillation behavior in Au, Pt and Ir atomic wires has been observed by Smit *et al.*[165] when two electrodes were pulled apart. On the other hand, conductance oscillations in different atomic wires have been theoretically predicted and analyzed by Pernas [166], Lang [167, 168], and Larade [169]. Several explanations of oscillation behavior were given including standing-wave resonance model [170], potential barrier model

[171], and resonant transport model [172, 173]. Actually these models are consistent with each other and they just treat the same physical problem from different angles.

Here we study two typical types of finite atomic wires between two Al(001) electrodes with finite cross-section. The first one is seven-carbon atomic wire: Al(001)-C_7-Al(001). From this work we show our conductance calculation is consistent with several simulation results from other groups [169, 60, 63, 174] and conducting eigenchannel analysis is performed to understand the physical mechanism. The second one is aluminum atomic wire with various number of Al atoms: Al(001)-Al_n-Al(001). For the spin-degenerate case it does show certain oscillation as other people have shown before although the detailed oscillation shape is different. However we show that in the above system the transport calculation should include spin degree of freedom and the oscillation behavior is significantly changed after the additional spin degree of freedom is included. The fundamental reason of the spin-dependent transport is due to the formation of local magnetic moment inside the atomic wire and this spin dependence plays an important role on the development of spintronics such as spin valve or spin filter.

4.2.1 Al(001)-C_7-Al(001)

The atomic structure of Al(001)-C_7-Al(001) with finite cross section is illustrated in Fig. 4-4, which is exactly the same as the structure used by several other groups [60, 63, 174]. The whole system is put in a rectangular box of $14 \times 14 \times 34.238$ Å^3 and the transport are along the z-direction. The lead part Al(001) is cut from FCC Al with the lattice constant of 4.05 Å and it consists of four atomic layers with 4-5-4-5 Al atoms from left to right. The distance between the edge carbon atom and the nearest 4-Al atomic plane is 1 Å and the C-C distance is 1.323 Å. Both ends of carbon atomic wire are connected to 4-Al atomic planes. Under the periodic boundary condition, the above specific structure of interfaces gives rise to the different number of aluminum atomic layers in the left lead and the right lead in our DFT calculations. That is clearly shown in the figure. Fermi level is shifted to 3 eV above the true Fermi level for the QO construction.

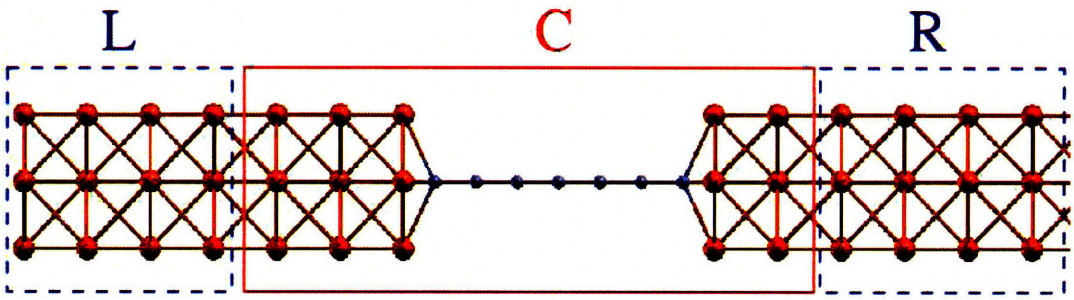

Figure 4-4: Atomic structure of Al(001)-C_7-Al(001). L: the left lead; C: the conductor; R: the right lead.

The band structure, density of states and electrical conductance of the Al(001) lead are shown in Fig. 4-5 (a) and (b). As usual it displays step-like conductance curve and sharp DOS peaks at each change of steps and the total conductance is consistent with band counting method from the band structure. The ground state valence charge density and effective Kohn-Sham potential are shown in Fig. 4-6 and Fig. 4-7. Fig. 4-7 shows high charge density (red) in the narrow carbon wire in contrast to low density (light blue) in the conductor region. This is due to the effective Kohn-Sham potential in Fig. 4-6 forms a very deep and narrow well, which confines the valence electrons of carbon atoms inside the long and small channel. That indeed reflects the strong quantum confinement in such system.

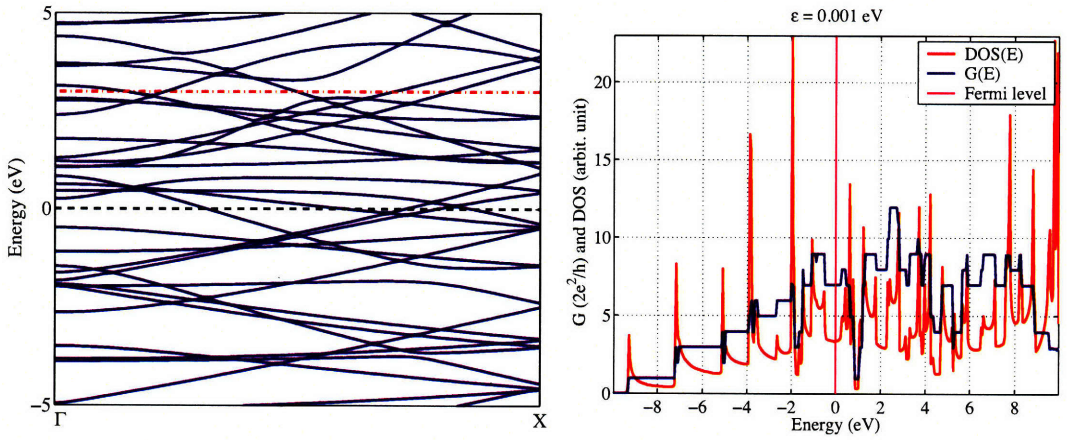

(a) (b)

Figure 4-5: (a) Band structure (black dash line: Fermi level; red dash-dot line: shifted Fermi level.) (b) density of states and electrical conductance (b) of the Al(001) lead.

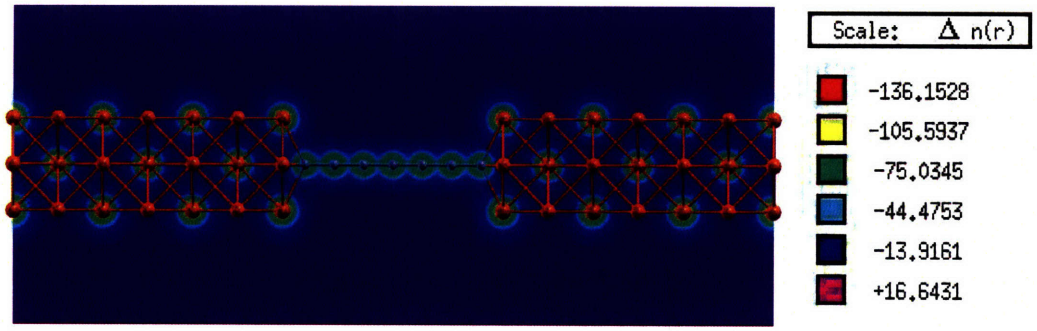

(a) (b)

Figure 4-6: Contour plot of effective Kohn-Sham potential of Al(001)-C_7-Al(001) in the unit of eV

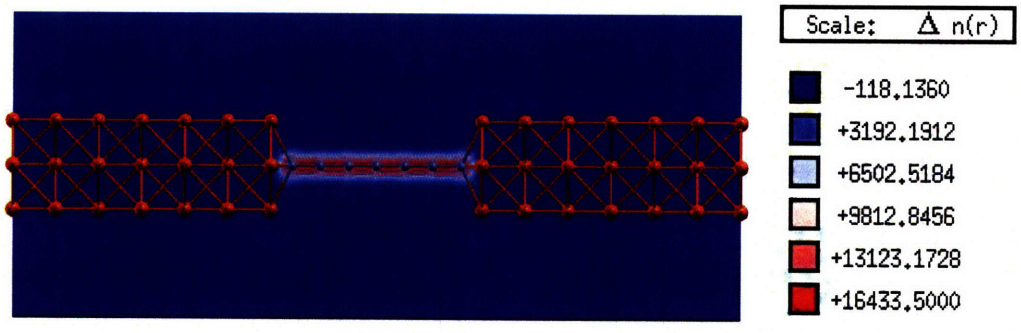

(a) (b)

Figure 4-7: Contour plot of valence electron density of Al(001)-C_7-Al(001)

We then show electrical conductance and density of states as the function of energy in Fig. 4-8 (a) and (b) respectively. The energy-dependent conductance of Al(001)-C_7-Al(001) has also been calculated by Larade *et al.* with MCDCAL package [169], Brandbyge *et al.* with TranSiesta package [60], Ke *et al.* with SIESTA [63], and Smogunov *et al.* with USPP-scattering state approach [174]. Our conductance curve is very similar to their results below 1 eV. The difference above 1 eV could arise from the different DFT packages with different basis-sets (plane-wave basis-set in our case) or exchange-correlation functionals. It may also come from the shifted Fermi level, above which we simply ignore those unoccupied Bloch states.

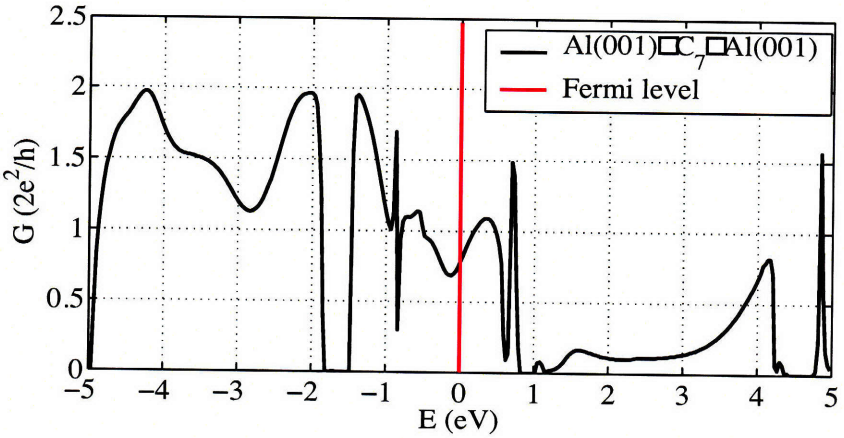

(a)

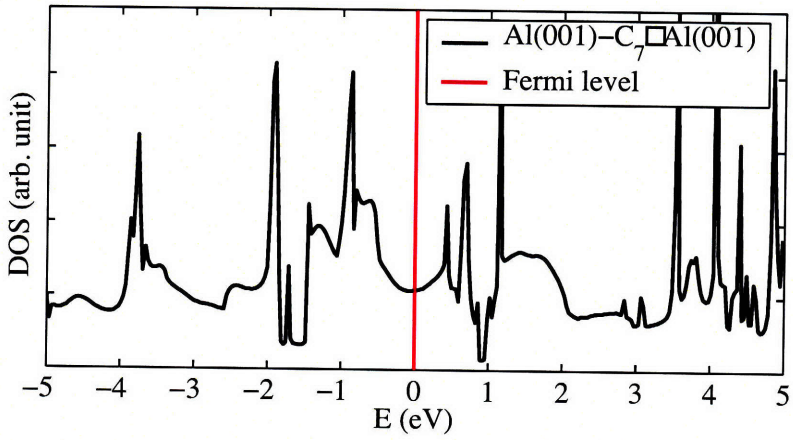

(b)

Figure 4-8: Electrical conductance (a) and density of states (b) of Al(001)-C_7-Al(001)

we can not obtain more detailed transport mechanism from the conductance curve

only. Thus we perform the conducting eigenchannel analysis at various energy levels listed in Table 4.1. We found that there are only two major eigenchannels containing most conductance at all listed energy levels while the remaining channels only contribute about 0.0001 G_0. The corresponding eigenchannels are shown in Fig. 4-9 for five energy levels below Fermi level and Fig. 4-10 for another five energy levels above Fermi level. It should be mentioned that both figures are displaying the plus and minus isosurfaces of real part of all the eigenchannels and they are corresponding to the current flowing from left to right. Here we only plot out the orbital components on the two surface layer and carbon atomic wire.

Table 4.1: Conductance eigenchannel decomposition of Al(001)-C_7-Al(001)

Energy eV ($E_F = 0$)	Total conductance G_0	Channel 1 G_0	Channel 2 G_0
-4.25	1.9730	0.9865	0.9865
-2.85	1.1410	0.5704	0.5706
-2.05	1.9618	0.9809	0.9809
-1.40	1.8877	0.9439	0.9438
-0.866	0.8399	0.4197	0.4201
0	0.8875	0.4439	0.4434
0.7	0.3151	0.1572	0.1579
1.6	0.1994	0.0995	0.0998
4.15	0.7311	0.3662	0.3648
4.854	1.2199	0.7711	0.4487

The first observation of both Fig. 4-9 and Fig. 4-10 is that all the electrons propagate through p_x and p_y-like QOs of carbon atomic wires. That indicates the reason of only two major eigenchannels found in the calculation is really due to the carbon chain can only hold valence electrons inside two degenerate π orbitals while s and p_z-like QOs have formed very low-lying strong σ bonding orbitals which are fully occupied. Immediately we confirm the above point that the maximum of conductance is no more than 2 G_0 in Fig. 4-8 (a) and Table 4.1.

The second generic feature of Fig. 4-9 and Fig. 4-10 is that the conducting channel containing less number of nodes in the wave function has lower energy. This is consistent with our common knowledge about Bloch states in 1D system and atomic

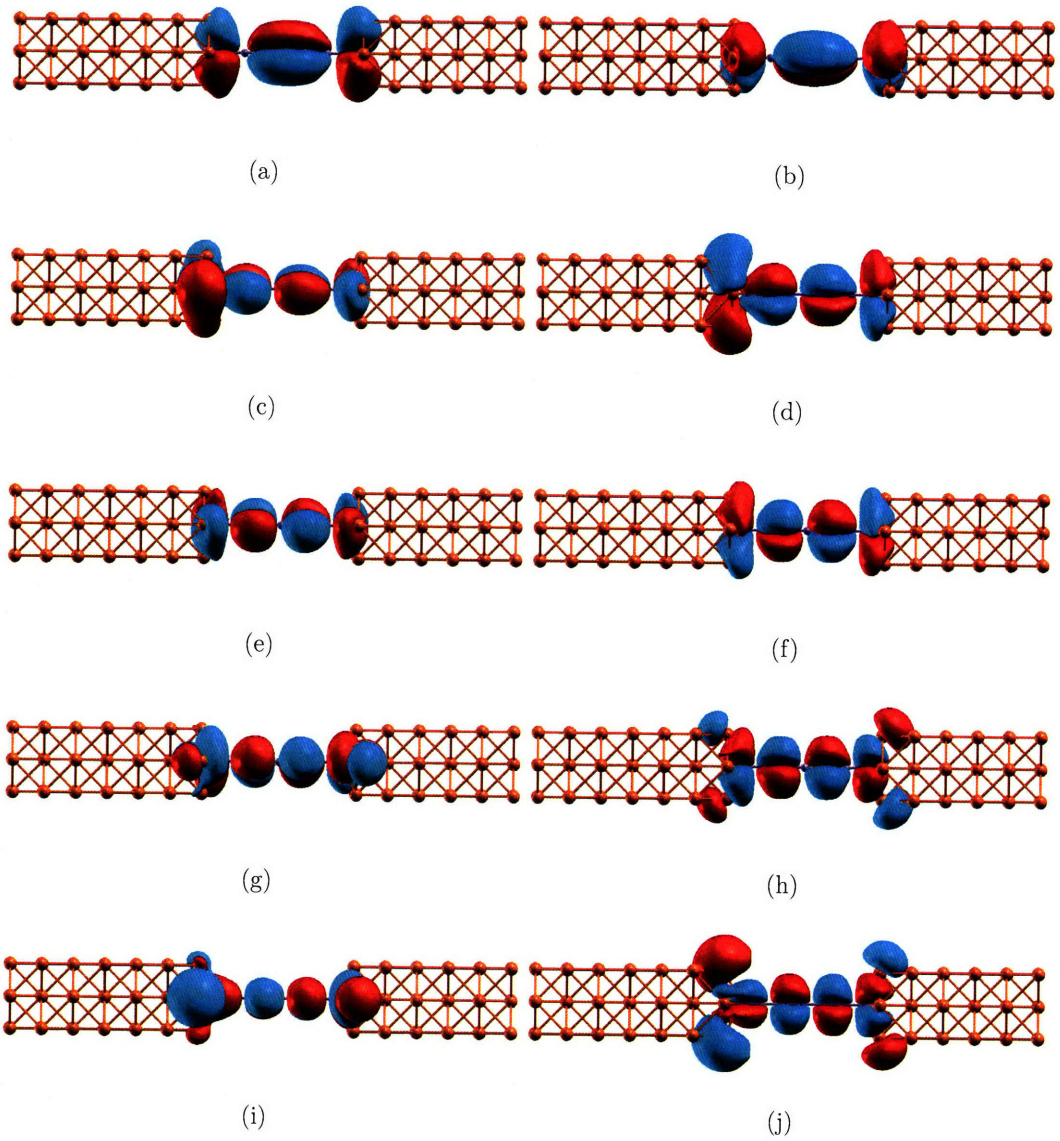

Figure 4-9: Conductance eigenchannel decomposition of Al(001)-C_7-Al(001) for $E < E_F$. The figures on the left-hand side are eigenchannel 1 and those on the right-hand side are eigenchannel 2 at the different energy levels. From top to bottom the corresponding energy levels are -4.25, -2.85, -2.05, -1.40, and -0.866 eV.

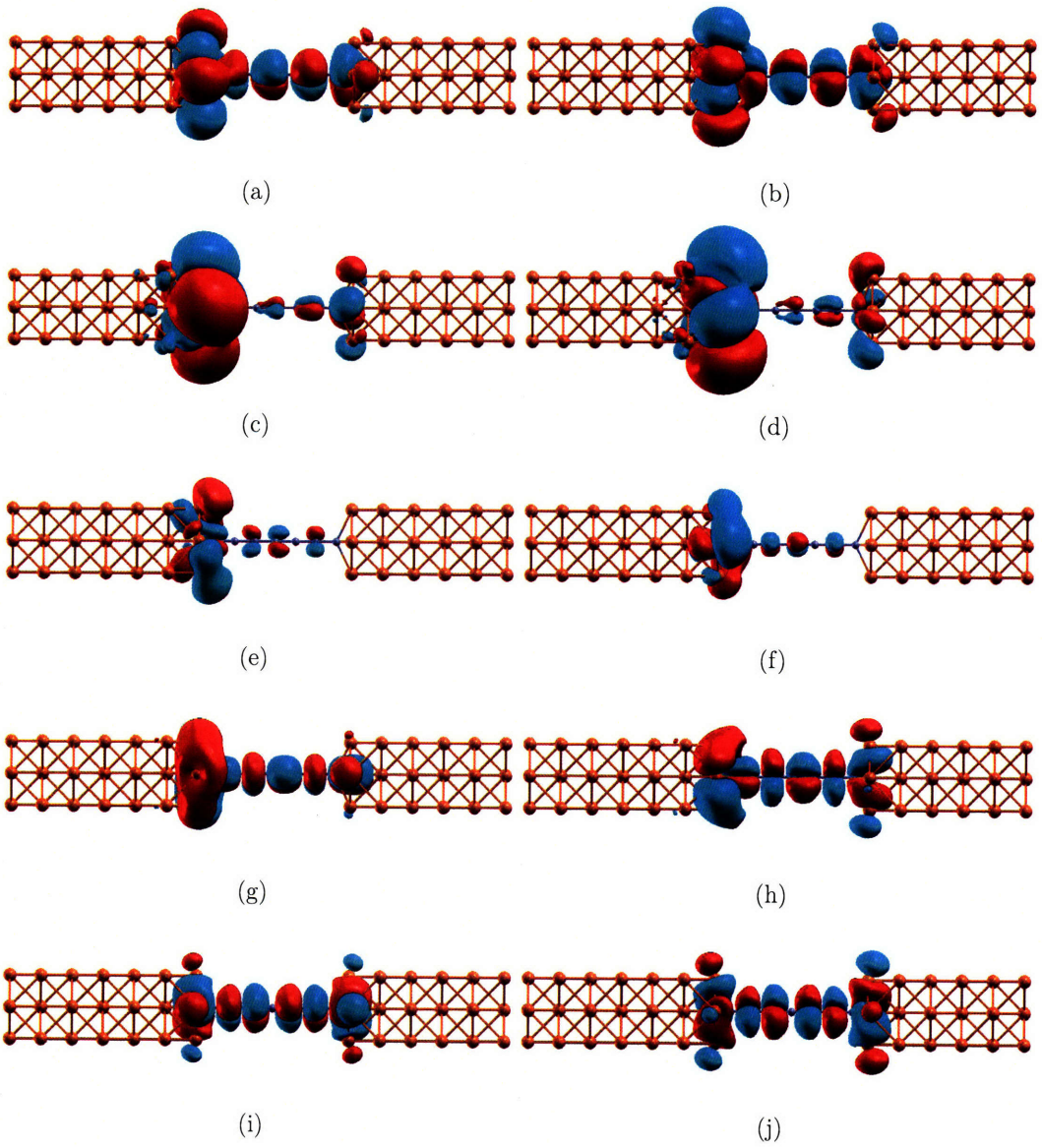

Figure 4-10: Conductance eigenchannel decomposition of Al(001)-C_7-Al(001) for $E \geq E_F$. The figures on the left-hand side are eigenchannel 1 and those on the right-hand side are eigenchannel 2 at different energy levels. From top to bottom the corresponding energy levels are 0, 0.7, 1.6, 4.15 and 4.854 eV.

orbitals in individual atoms.

The third interesting feature is that in general the shape of conducting channels on the left and right are not symmetric, except the channels near maximum conductance ($2G_0$). This is simply due to the scattering between electrons and Kohn-Sham potential when the energy of electrons is away from the perfect resonant level. Generally speaking, there are two situations, in which we will find non-decaying channels. One is the perfect periodic conductor, such as pure 1D conductor we have studied above and its conducting eigenchannels are exactly the Bloch eigenstates. The other is resonant level in the current example and that is further illustrated in Fig. 4-9 (a, b), (e, f) and (g,h) corresponding to the energies at -4.25, -2.05 and -1.40 eV respectively. Especially the size of the above channels on the left and right leads do not change, which is the signature of non-decaying electron transport. Away from the resonant level, the strong scattering makes the conductance deviate from integer quantum conductance. We can easily imagine in this case that part of the current traveling from left to right is reflected by the wire-contact interfaces. Therefore, the size and shape of the same eigenchannel on the left and right conductor-lead interfaces are be different. This is demonstrated in the various channels away from the non-integer quantum conductance in Fig. 4-9 and Fig. 4-10.

The fourth fascinating feature is from the shape of conductance eigenchannels. In Fig. 4-9 (i, j) at $E = -0.866$ eV and Fig. 4-10 (a, b) at $E = 0$ eV and (c, d), droplet tail of the orbitals inside the carbon atomic chain clearly indicates the electrical current flowing from left to right. We believe this is the direct consequence of Fermi liquid characteristics of electron flows inside the atomic wire between two metallic surfaces. In contrast, the orbital shape at the resonant levels is symmetric and electron transport through the resonant level behaves like Fermi gas without any local impedance from the scattering with the Kohn-Sham potential.

The fifth important message is the detailed orbital hybridization between molecular orbitals of carbon atomic wire and surface states of two Al(001) leads. Since we know under small bias the total current is determined by the conductance around the Fermi level, we take the eigenchannels in Fig. 4-10 (a) at Fermi level as an example

to study the orbital interactions. The more detailed plot of that conducting eigenchannel is shown in Fig. 4-11. First, on the left surface layer consisting of four Al atoms, two $pp\sigma$ bonding orbitals are formed on the two pairs of Al-Al bonds and then these two orbitals form an overall anti-bonding state on the whole left surface. Then the surface state is anti-bonded with the three-node anti-bonding π^* state of carbon atomic wire. The mixed p orbital on the right edge of carbon wire forms an overall $pp\sigma$ bonding group orbital with the p orbitals on the four surface atoms of the right lead. Thus it is very clear that the $pp\sigma$ bonding group orbital on the right-hand side is different from the surface state on the left-hand side.

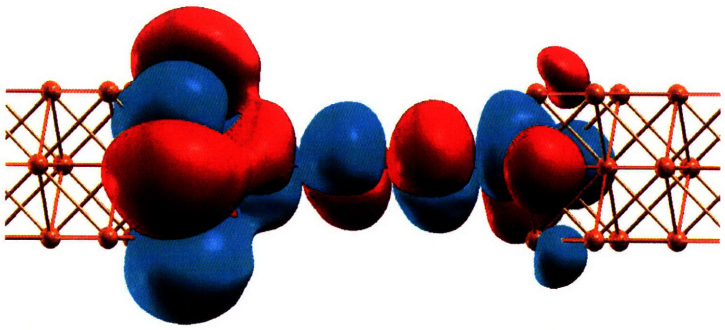

Figure 4-11: Conductance eigenchannel of Al(001)-C_7-Al(001) at Fermi level. [detailed version of Fig. 4-10 (a)]

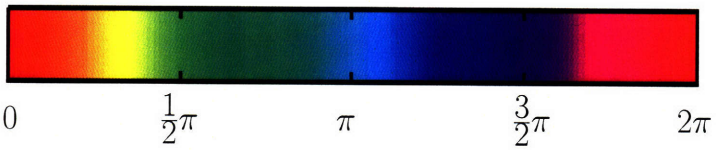

Figure 4-12: Phase colormap for electron wave function

Another striking feature comes from the comparison between the DOS curve and the conductance curve in Fig. 4-8 (a) and (b). We observe that some regions with high DOS have almost zero conductance, such as at $E \in [-1.8, -1.5]$ and $E \in [1.0, 1.2]$. To resolve this puzzle, we then map the phase information on the isosurface of the amplitude of those eigenchannels in the above energy regions. Particularly we pick

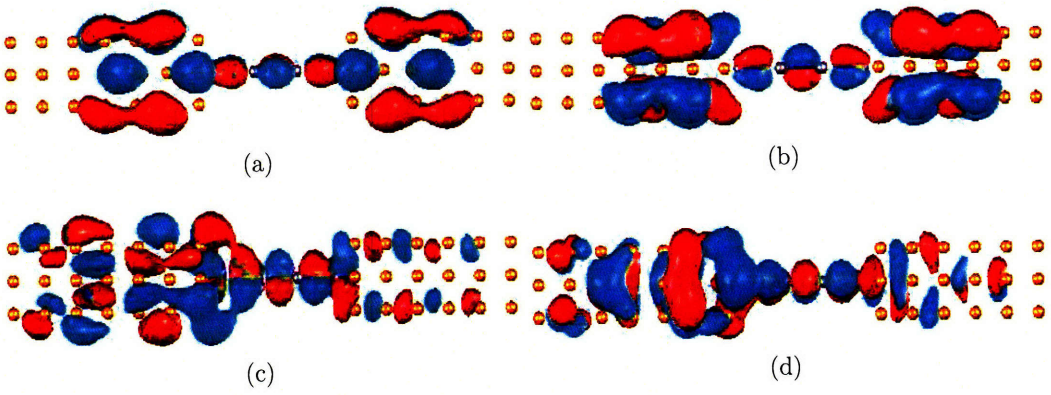

Figure 4-13: Phase-encoded conductance eigenchannels of Al(001)-C_7-Al(001) at (a, b) $E = -1.711$ eV and (c, d) $E = 1.149$ eV. The figures on the left-hand side are eigenchannel 1 and those on the right-hand side are eigenchannel 2.

up two major eigenchannels of one energy level in each region ($E = -1.711$ eV and $E = 1.149$ eV) and they are shown in 4-13(a,b) and (c,d) respectively with their phase colormap illustrated in Fig. 4-12. We again plot out the same type of phase-encoded isosurfaces in Fig. 4-14 and Fig. 4-15 for all the same eigenchannels listed in Fig. 4-9 and Fig. 4-10. Comparing these phase-encoded isosurfaces, we find that these two eigenchannels inside the high DOS but low conductance regions have almost only two colors - red and blue - in the vicinity of the lead-wire-lead structure, corresponding to real wave functions with plus and minus signs. In another word, the imaginary part of those eigenchannels is merely zero. From Eq. (4.2), we know that the probability current $\mathbf{J}$ has the following form

$$\mathbf{J}(\mathbf{x},\mathbf{t}) = -\frac{ie\hbar}{2m}\Big[\psi^*(\nabla\psi) - (\nabla\psi^*)\psi\Big] = \frac{e\hbar}{m}\mathrm{Im}\Big[\psi^*\nabla\psi\Big]. \tag{4.4}$$

As a consequence, the current through the above pure real eigenchannels is zero and thus the transmission T is zero. In contrast, we can see that wave functions of the channels in Fig. 4-14 and Fig. 4-15 have much more imaginary components, and it is particularly clear at the resonant levels shown in Fig. 4-14 (a, b), (e, f) and (g,h). Therefore, although the eigenchannels inside the high DOS but low conductance regions have large wave function components across the lead-wire-lead, fundamentally

they are non-conducting anti-resonant states [175] which almost perfectly reflect the incoming electrons in contrast to the resonant states discussed before. In another word, the electrons in these energy regions will form a static Coulomb potential and block other electron to transport from one side to the other. Moreover, it manifests that phase oscillation of wave functions is the key signature of electrical current in phase-coherent quantum transport.

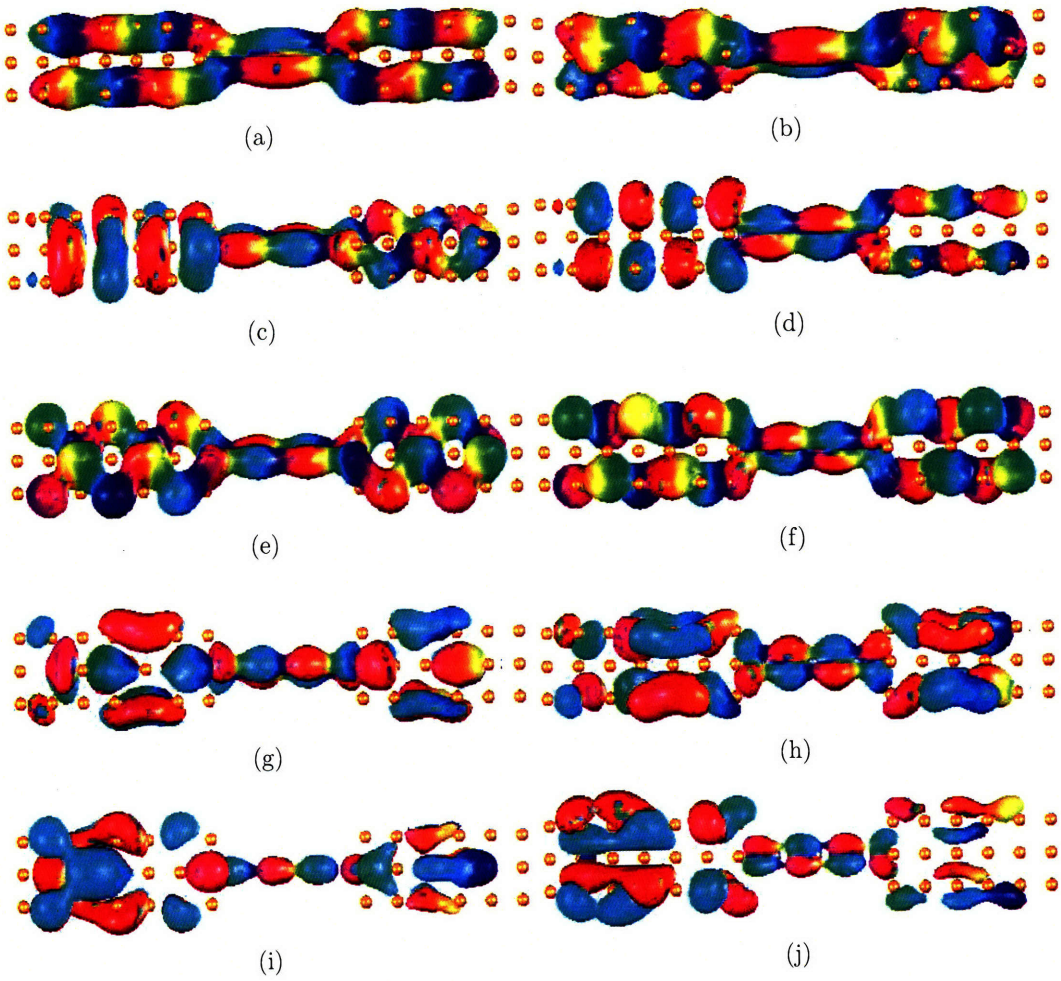

Figure 4-14: Phase-encoded isosurface plot of the magnitude part of conductance eigenchannels of Al(001)-C_7-Al(001) for $E < E_F$. The figures on the left-hand side are eigenchannel 1 and those on the right-hand side are eigenchannel 2 at different energy levels from top to bottom: -4.25, -2.85, -2.05, -1.40, and -0.866 eV. (The corresponding isosurface plot of these channels without phase-encoding is shown in Fig. 4-9.)

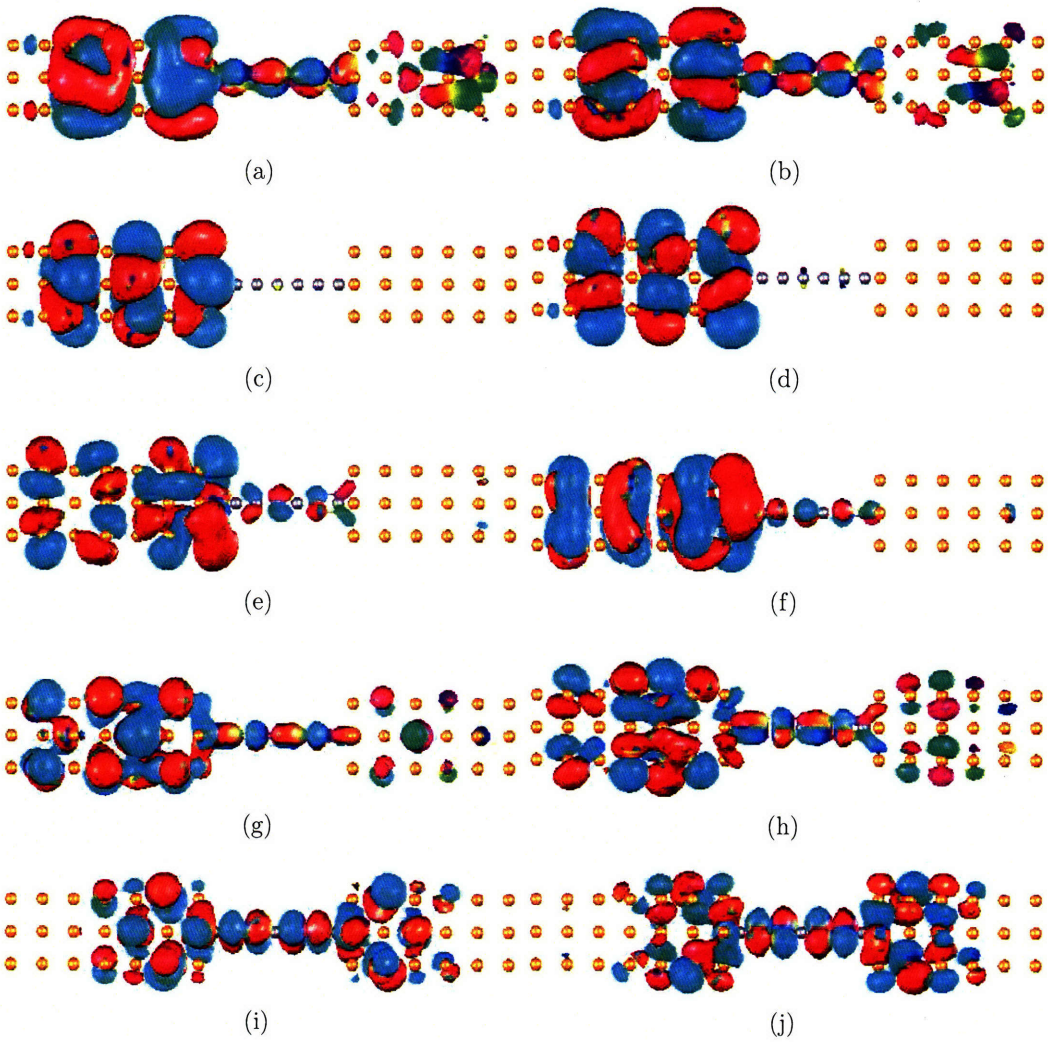

Figure 4-15: Phase-encoded conductance eigenchannel decomposition of Al(001)-C_7-Al(001) for $E \geq E_F$. The figures on the left-hand side are eigenchannel 1 and those on the right-hand side are eigenchannel 2 at different energy levels from top to bottom: 0, 0.7, 1.6, 4.15 and 4.85 eV. (The corresponding isosurface plot of these channels without phase-encoding is shown in Fig. 4-10.)

In summary, we show that our electrical conductance results are consistent with the results from other groups by various different methods. This benchmark proves that our efficient scheme for localized QO construction works very well for electron transport problem. We demonstrate that particular states inside the electron sea of both Al(001) leads hybridize with molecular orbitals of carbon atomic wire and form resonant levels. Conductance at each resonant level will have one quantum of conductance G_0. At the energy away from resonant levels, the scattering potential reduces the total transmission of the electrons traveling from one side to the other. More interestingly, droplet tail of conducting eigenchannel away from resonant levels gives direct evidence to the Fermi liquid characteristics of electron transport. From conducting eigenchannel decomposition and orbital hybridization analysis, we have more detailed understandings of electron transport mechanism in Al(001)-C_7-Al(001). Especially we find the anti-resonant states are responsible for the vanishing conductance at high DOS regions and those states are pure real functions which almost do not carry any current although a large fraction of those real functions are localized on the carbon atomic wire.

4.2.2 Al(001)-Al_n-Al(001)

From the previous case we have already obtained some detailed understandings of electron transport through atomic wire confined between two electrodes. In this section we first study the length-dependent conductance of aluminum atomic wire with different number of Al atoms between two Al(001) electrodes with finite cross-section. We then introduce the spin degree of freedom into conductance calculations and we find that the Al(001)-Al_n-Al(001) system has strong spin-dependent conductance, which, to our knowledge, has not been investigated by other people before.

The structure of our Al(001)-Al_n-Al(001) system is illustrated in Fig. 4-16. In the case of $n = 5$, the whole system is put in a rectangular box of $12 \times 12 \times 37.91$ Å^3 and the transport are along the z-direction. Same as the case of Al(001)-C_7-Al(001) in previous section, the lead part Al(001) is cut from FCC Al with the lattice constant of 4.05 Å and it consists of four atomic layers with 4-5-4-5 Al atoms from left to right.

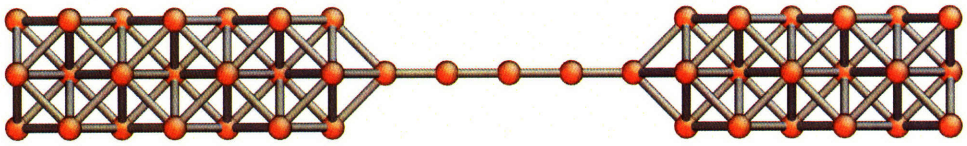

Figure 4-16: Atomic structure of Al(001)-Al_n-Al(001). L: the left lead; C: the conductor; R: the right lead. Here $n = 5$.

The distance between the aluminum atom at the end of the atomic wire and the nearest 4-Al atomic plane is 2.86378 Å and the Al-Al distance inside the aluminum atomic wire is 2.39 Å. Both ends of the atomic wire are connected to 4-Al atomic planes. Virtual Fermi level is shifted 2 eV above the true Fermi level for all QO constructions in both spin-degenerate and spin-nondegenerate cases.

Spin-degenerate transport in Al(001)-Al_n-Al(001)

We first calculate the spin-degenerate ground state and compare our results with other result from several other works. Fig. 4-17 and Fig. 4-18 show the corresponding effective Kohn-Sham potential and valence electron charge density.

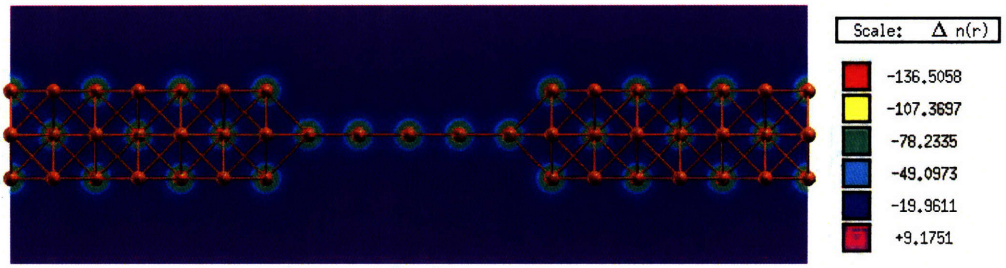

(a) (b)

Figure 4-17: Contour plot of effective Kohn-Sham potential of Al(001)-Al_5-Al(001) in the unit of eV

We then plot out the spin-degenerate electrical conductance of Al(001)-Al_n-Al(001) as a function of energy with $n = 4, 5, \cdots, 15$ and $E_F = 0$ eV. Similar conductance calculations have been performed by other groups [60, 173, 63, 176]. Although the detailed configurations of their calculations are different in some cases, one can still find several common features on all the conductance curves: (a) resonant peak emerges

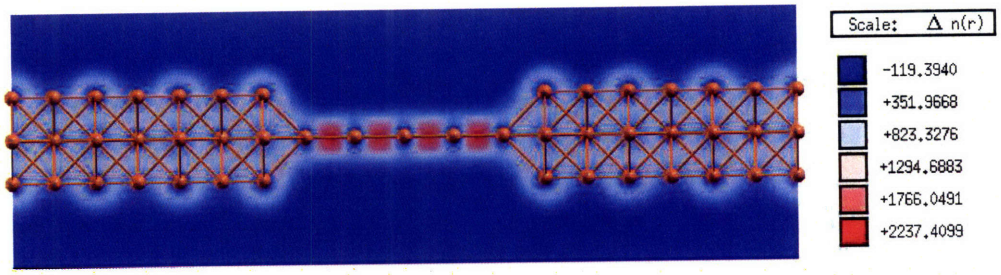

(a) (b)

Figure 4-18: Contour plot of valence electron density of Al(001)-Al_5-Al(001)

one by one with the increase of Al atoms in the atomic wire; (b) conductance value at Fermi level will oscillate with number of Al atoms due to those new resonant peaks which push the existing peaks toward the low energy direction. In Fig. 4-19 we do see the emergence of new resonant peaks when the number of Al atoms in the atomic wire increases. Meanwhile, the conductance oscillation is shown in Table 4.2 and plotted in Fig. 4-20. Our curve does show large oscillation when N varies from 4 to 15, however the periodicity is less significant than that in other people's work [173, 176]. One possible source of the difference is the different interface structure used in Ref. [173]. Another source could be the difference between our plane-wave DFT result and the local orbital result used in Ref. [176] even when the configurations used in calculations are the same.

Spin-nondegenerate transport in Al(001)-Al_n-Al(001)

Although an infinite linear Al atomic wire has a nonmagnetic ground state, the unsupported finite Al chain is predicted to have spontaneous magnetization along elongation[177]. Even after the chain is relaxed into the zigzag wire, it still exhibit the spontaneous magnetization. Therefore the spontaneous magnetization could also exist in the confined geometry of Al(001)-Al_n-Al(001), and electron transport could also depend on spin degree of freedom although none of those previous works has taken spin into account.

In Fig. 4-21 we show the total magnetization of Al(001)-Al_n-Al(001) for $n = 4, 5, \cdots, 9$ in the unit of number of electrons. The largest magnetization happens at

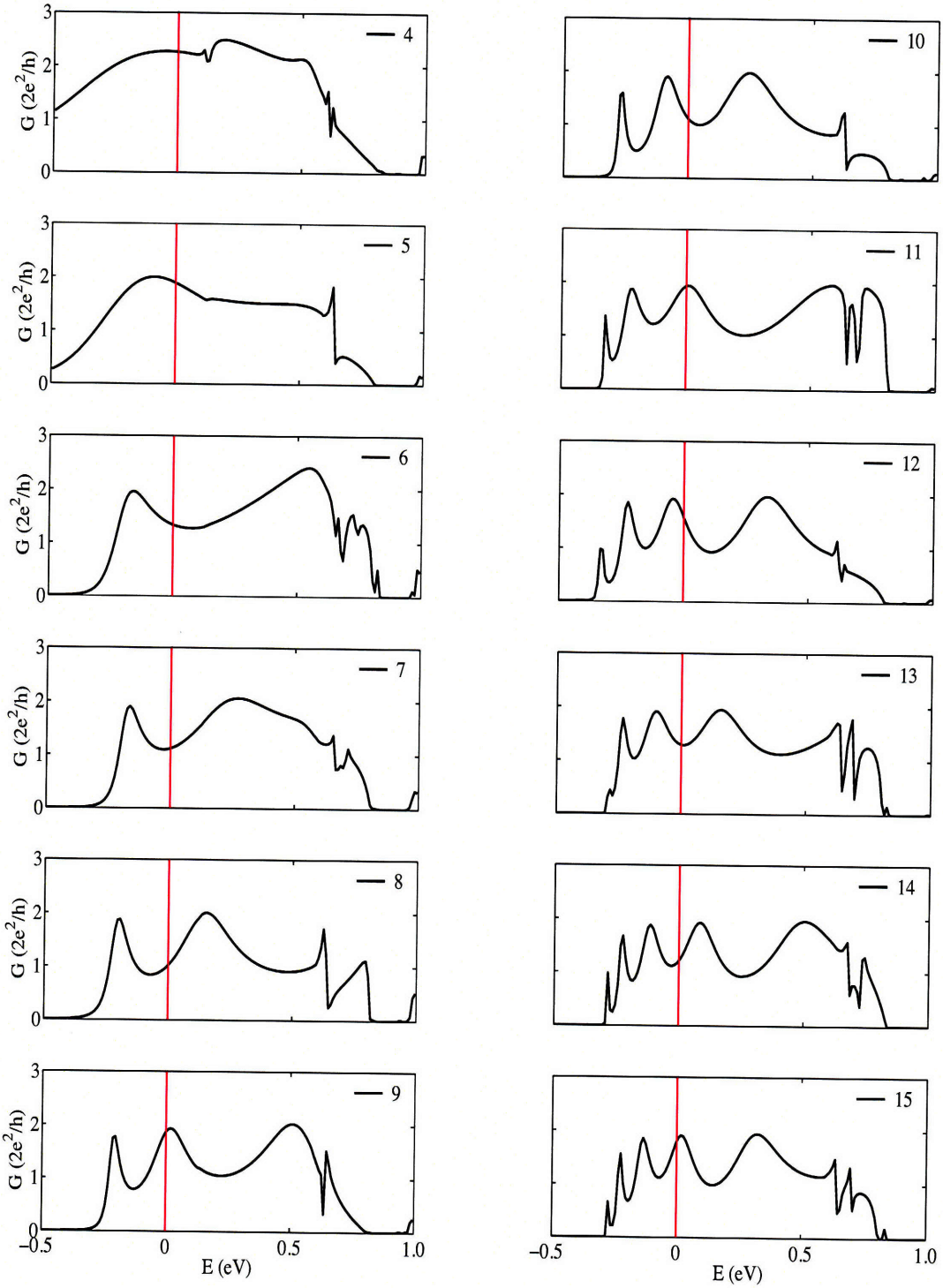

Figure 4-19: Spin-degenerate electrical conductance of Al(001)-Al$_n$-Al(001) as a function of energy with $n = 4, 5, \cdots, 15$ and $E_{\mathrm{F}} = 0$ eV.

Table 4.2: Spin-degenerate electrical conductance of Al(001)-Al_n-Al(001) at Fermi level with different number of atoms

N_{Al}	Total conductance (unit: G_0)
4	2.2653
5	1.8845
6	1.3315
7	1.1173
8	1.0194
9	1.8677
10	1.1131
11	1.9331
12	1.5673
13	1.2901
14	1.2130
15	1.8050

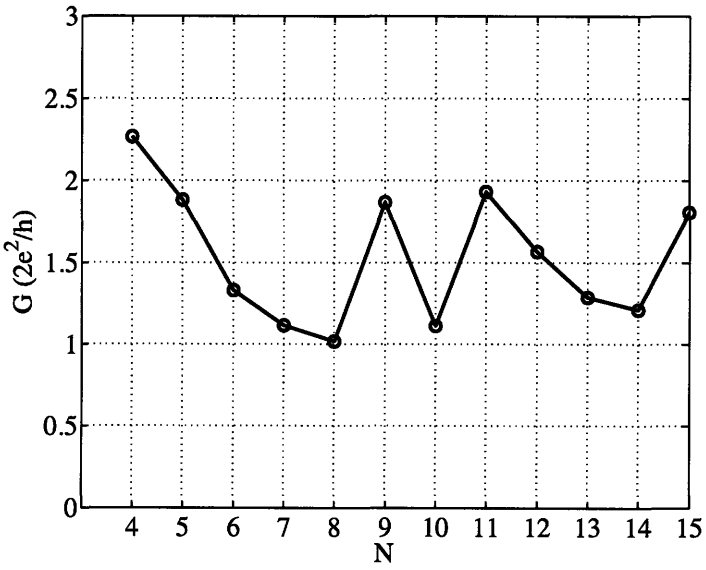

Figure 4-20: Spin-degenerate electrical conductance of Al(001)-Al_n-Al(001) as a function of number of Al atoms in atomic wire at Fermi level $E = 0$ eV.

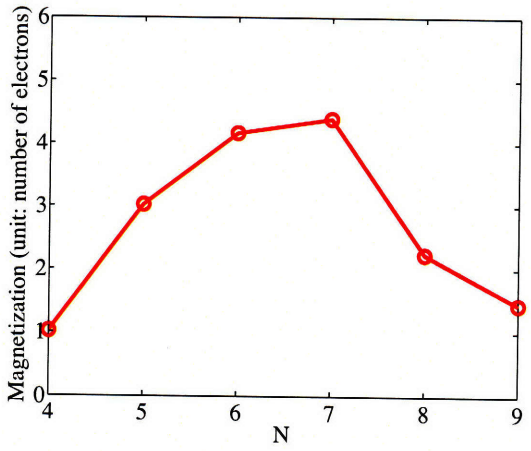

Figure 4-21: Magnetization of Al(001)-Al_n-Al(001) with $n = 4, 5, \cdots, 9$ (unit: number of electrons).

$n = 7$, while at $n = 4$ and $n = 9$ it has the smallest magnetization among all the six cases. To understand the magnetization, we visualize the contour plane of spin density with $n = 4$, 7 and 9 in Fig. 4-22. The contour plane passes through the whole atomic wire. It is obvious that most of the spontaneous magnetization is localized between two interfaces due to the above quantum confinement, which gives rise to the local moment formation. In the case of $n = 4$, the majority spin density (red) wraps around the atomic wire and occupies the $pp\pi$ orbitals formed by p_x and p_y of two center Al atoms (atom 2 and 3), while the minority spin seems to have more weight along the longitudinal direction of atomic wire and occupy the σ bonds. In the case of $n = 7$, it is quite similar to the case of $n = 4$, but a slight difference comes from two fragments majority spin density occupying the $pp\pi$ orbitals formed by atom (2,3) and atom (5,6) inside the seven-atom chain respectively. However, the spin density distribution changes dramatically when n increases to 9. In this case, beside two parts of majority spin density surrounding atom (2,3) and atom(7,8), the minority spin occupies p_x and p_y orbitals of the center atom (atom 5).

Since the significant amount of local moment is formed inside the conductor region, we believe it could directly affect the electrical conductance. We carry out the conductance calculation again while varying the number of Al atoms in the wire. The result is shown in Fig. 4-23 where total conductance, majority spin component, and

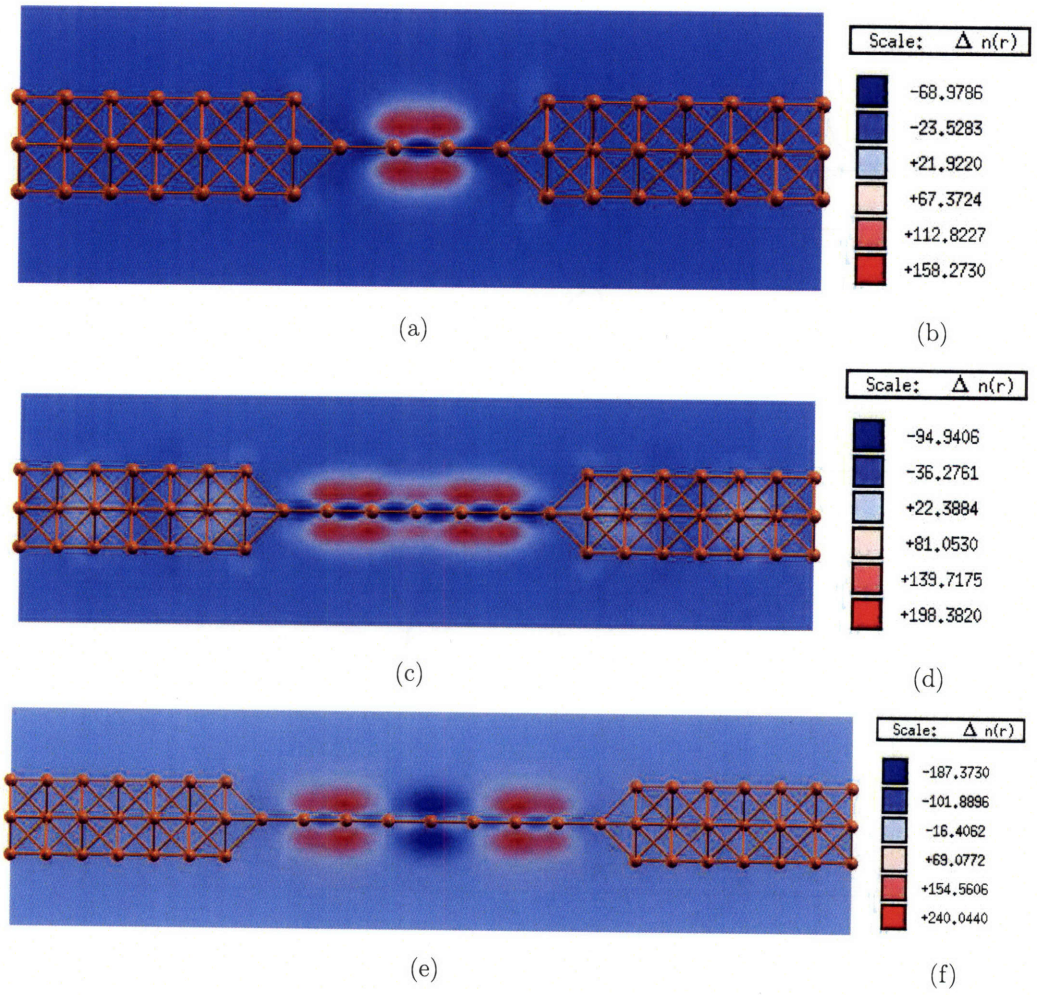

Figure 4-22: Spin density of Al(001)-Al$_n$-Al(001) with $n = 4$, 7, and 9 (red: majority spin; blue: minority spin).

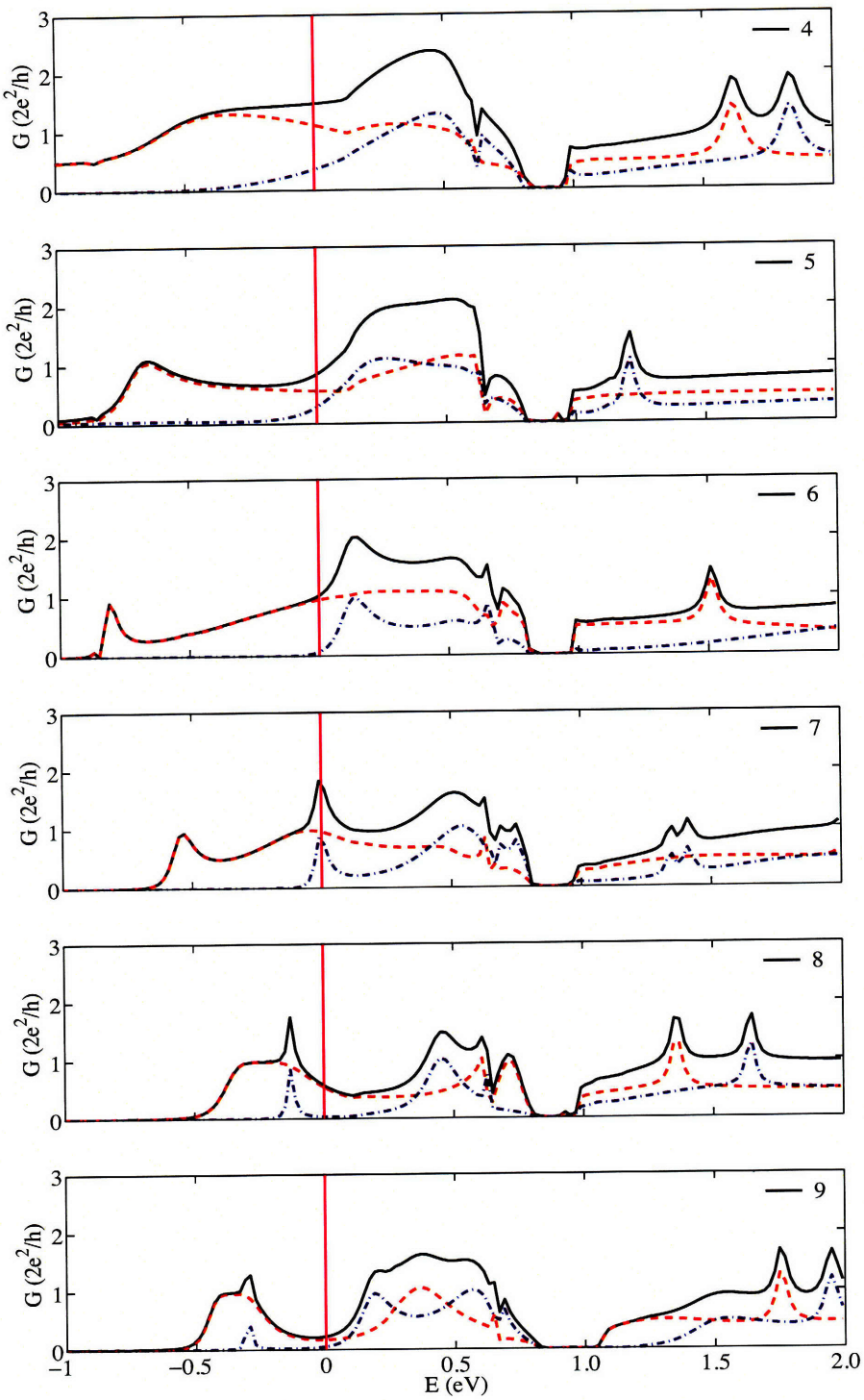

Figure 4-23: Spin-dependent electrical conductance of Al(001)-Al$_n$-Al(001) with $n = 4, 5, \cdots, 9$ and $E_F = 0$ eV. (black solid line: total conductance; red dash line: majority spin; blue dash-dot line: minority spin.)

minority spin component are indicated by black solid line, red dash line and blue dash-dot line, respectively. The result in Fig. 4-23 leads to the following remarkable conclusions:

- The total conductance below the Fermi level is dominated by majority spin component while above the Fermi level both components play important roles.

- With the increased number of Al atoms, both majority and minority spin conductance curves contain more and more resonant peaks. That is consistent with the spin-degenerate case that we have explored before.

- The first resonant peak of majority spin below the Fermi level begins to squeeze from the initial broad shape and move *rightward* but never reach the Fermi level. In contrast, the first resonant peak of minority spin moves *leftward* and does pass the Fermi level. The latter one moves to Fermi level at $n = 7$ and eventually locates below Fermi level when $n = 9$. That is the main reason for the maximum total conductance at $n = 7$ but much smaller values at $n = 4$ and $n = 9$. For a more clear view, Table 4.3 and Fig. 4-24 show the conductance at the Fermi level with varying atoms and a clear peak shows at $n = 7$.

- Compared to the spin-degenerate case shown in Fig. 4-25, we find there is significant difference between the total conductance curves obtained from spin-degenerate and spin-nondegenerate calculations. Especially, our spin-degenerate calculation together with the results from the other groups shows conductance *minimum* around $n = 7$. That obviously contradicts to our spin-nondegenerate result. Therefore, the previous conductance oscillation under spin-degenerate assumption should be carefully re-examined.

The above conclusions come from the most important fact in our calculations that even the original nonmagnetic materials can have local magnetic moment formation due to specific confined geometry such as atomic wire sandwiched between two metal surfaces. It has been ignored in several other works which deal with the same system. The above system is very similar to magnetic Co and Ni nanowires studied by

Smogunov *et al.* [174], who consider more than ground state magnetization. By constraining the magnetization direction and then using scattering state method, they have considered parallel and anti-parallel magnetization and conductance inside two Co or Ni leads. Our method with QOs can be easily extended to these situations if magnetization constrains are treated correctly in plane-wave DFT calculations.

Table 4.3: Spin-dependent electrical conductance of Al(001)-Al$_n$-Al(001) at Fermi level

N_{Al}	Total conductance (unit: G_0)	Spin majority (unit: G_0)	Spin minority (unit: G_0)
4	1.4834	1.1210	0.3624
5	0.8487	0.5586	0.2901
6	1.0228	0.9510	0.0718
7	1.7585	0.9557	0.8028
8	0.5705	0.5363	0.0342
9	0.2249	0.1708	0.0541

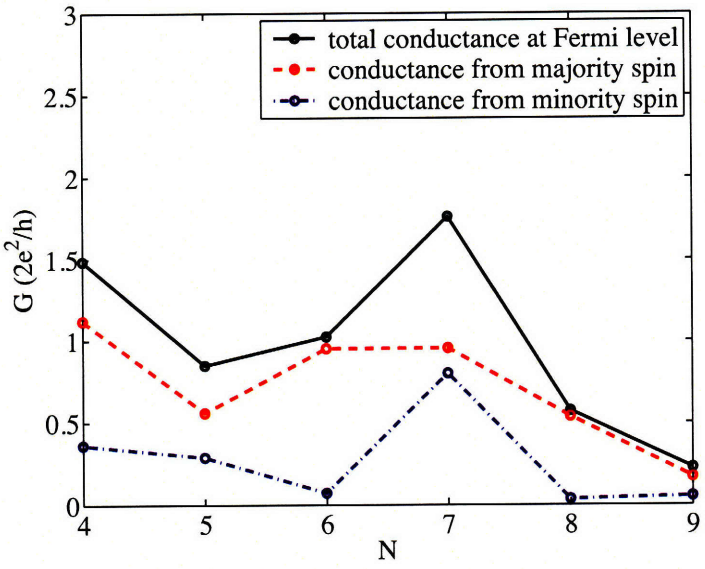

Figure 4-24: Spin-dependent electrical conductance of Al(001)-Al$_n$-Al(001) at $E = 0$ eV as a function of number of Al atoms, $n = 4, 5, \cdots, 9$. (black solid line: total conductance; red dash line: spin majority; blue dash-dot line: spin minority.)

To achieve better understandings of spin-dependent electron transport mechanism, we again perform conducting eigenchannel analysis at various resonant energy levels.

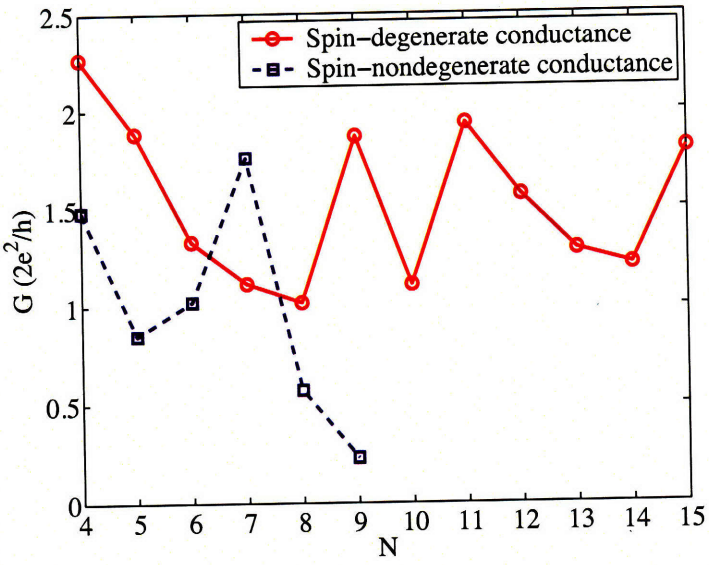

Figure 4-25: Comparison between spin-degenerate conductance (solid line) and spin-nondegenerate conductance (dash line) of Al(001)-Al$_n$-Al(001) as a function of number of Al atoms in atomic wire at Fermi level $E = 0$ eV.

The eigenchannels are shown in Fig. 4-26 for $n = 7$ and Fig. 4-27 for $n = 9$. In both cases, we found only two majority channels are responsible for most of total conductance. In Fig. 4-26 we see that majority-spin channels (a,b) is the same as minority-spin channels in (g,h) and so is the similarity between (c,d) and (i,j) while the only difference is the shifted energy levels of majority spin channel and minority spin channel. It is clearly reflected at resonant peaks in Fig. 4-23. However, there is no corresponding peak in the spin-minority case with respect to Fig. 4-26 (e,f) at E=0.53 eV in the spin-majority case. In another word, majority-spin channel has three resonant peaks while minority-spin channel has only two. In the case of $n = 9$, the situation is reversed. There is no corresponding majority-spin eigenchannel with respect to the lowest minority-spin resonant peak in Fig. 4-27 (e,f). Nonetheless, the correspondence still exists between (a,b) and (g,h) and between (c,d) and (i,j) for $n = 9$.

Another interesting phenomena is that in Fig. 4-23 conductance maximum in the case of $n = 4$ exceeds $2G_0$ limit of pure Al wire. To explain the high conductance we show the spin-dependent conducting eigenchannels in Fig. 4-28 at two resonant

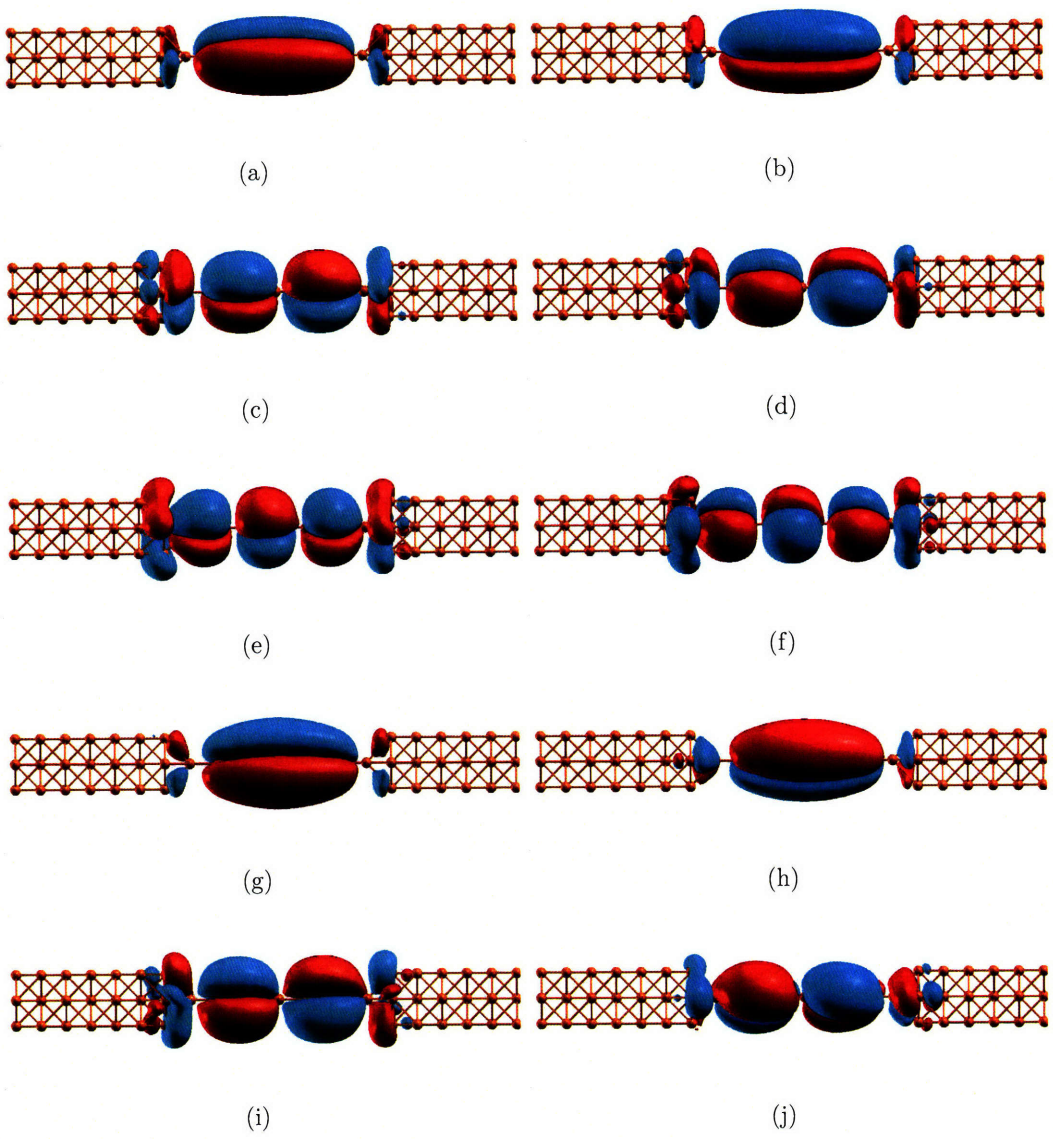

Figure 4-26: Spin-dependent conductance eigenchannel decomposition of Al(001)-Al_7-Al(001) at various resonant levels. The figures on the left-hand side are eigenchannel 1 and those on the right-hand side are eigenchannel 2. The eigenchannels from top to bottom are: six majority-spin channels at $E = -0.53$ eV (a,b), 0 eV (c,d) and 0.53 eV (e,f), and then four minority-spin channels at $E = 0$ eV (g, h) and 0.53 eV (i,j).

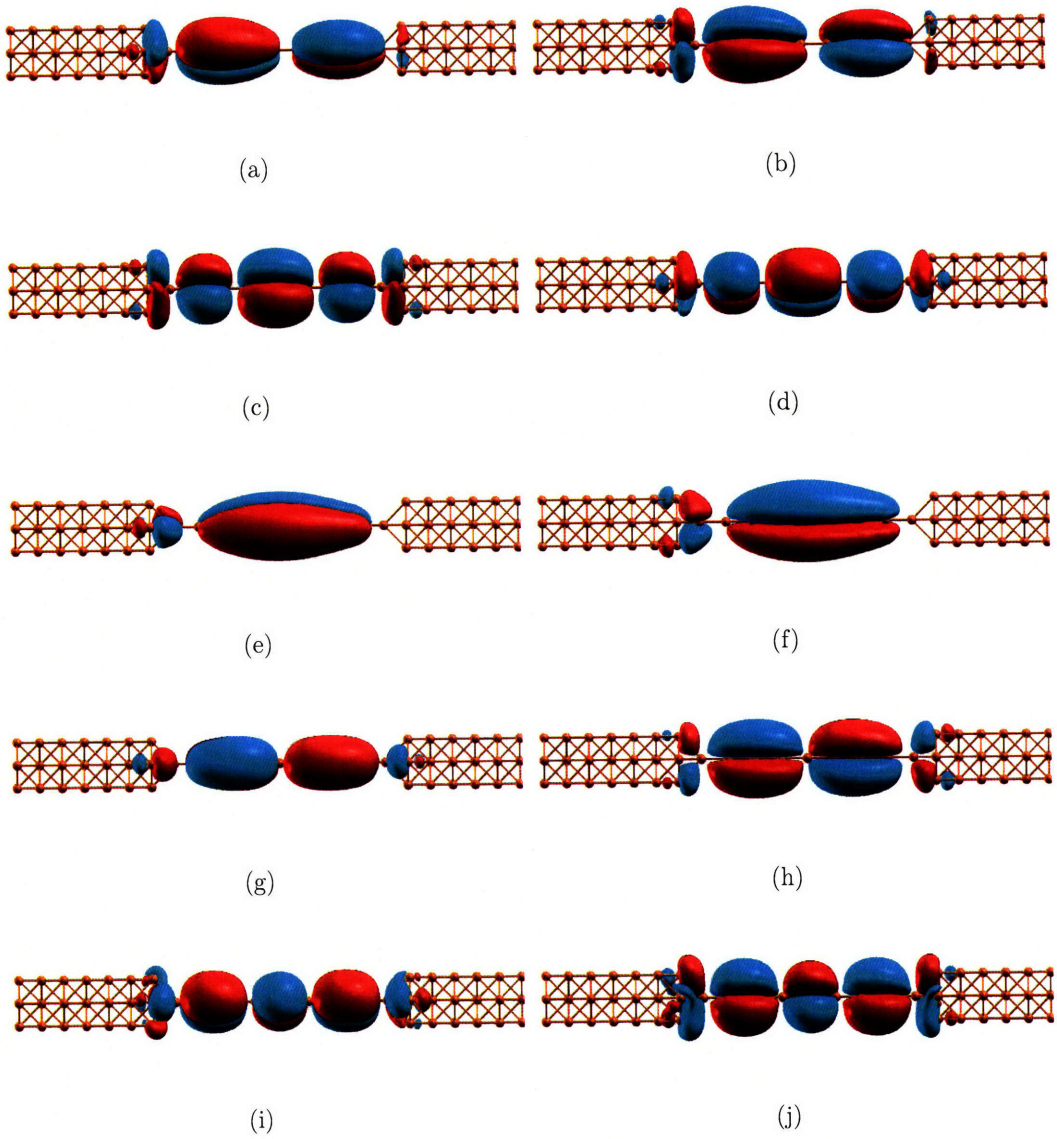

Figure 4-27: Spin-dependent conductance eigenchannel decomposition of Al(001)-Al_9-Al(001) at various resonant levels. The figures on the left-hand side are eigenchannel 1 and those on the right-hand side are eigenchannel 2. The eigenchannels from top to bottom are: four majority-spin channels at $E = -0.29$ eV (a,b) and 0.37 eV (c,d), and then six minority-spin channels at $E = -0.29$ eV (e,f), 0.19 eV (g, h) and 0.57 eV (i,j).

energy levels: $E = -0.35$ and 0.5 eV. We find there are three dominant eigenchannels for majority-spin conductance at $E = -0.35$ and three major channels for majority and minority spin conductance at $E = 0.5$ respectively. Spin-dependent conductance of each eigenchannel is listed Table 4.4 for all the 9 channels. From Fig. 4-28, channel 1 and 2 are easily identified as two degenerate $pp\pi$ bonding states in (a,b) and two degenerate $pp\pi^*$ antibonding states in both (d, e) and (g, h), however channel 3 is single $ss\sigma^*$ antibonding state in (c,f,i) in the conductor region. Therefore, the $ss\sigma^*$ antibonding eigenchannel is the extra channel with an additional conductance, resulting in large total conductance above $2G_0$ limit of pure Al wire.

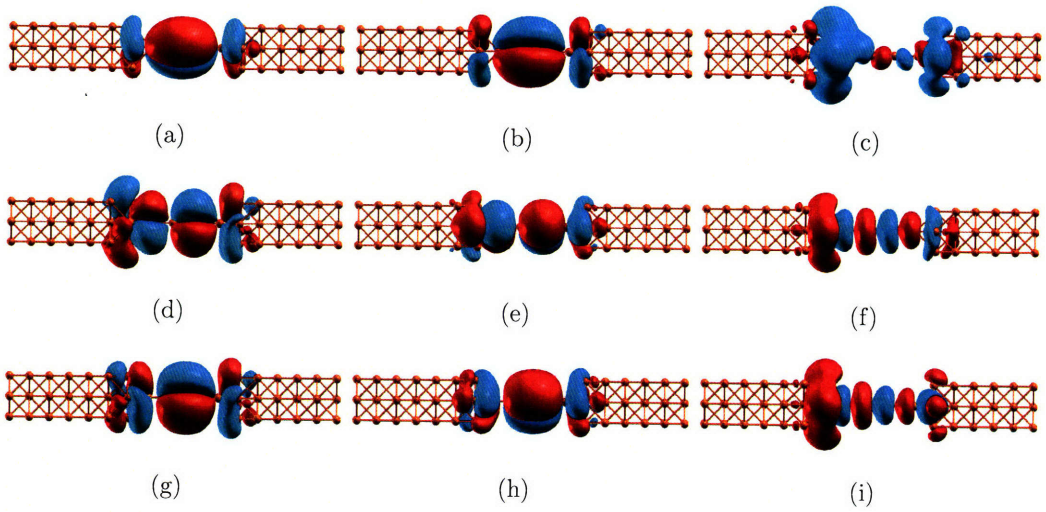

Figure 4-28: Spin-dependent conductance eigenchannel decomposition of Al(001)-Al_4-Al(001) at various resonant levels. The figures on the left, middle and right columns are eigenchannel 1, 2 and 3 respectively. The eigenchannels from top to bottom are: three majority-spin channels at $E = -0.35$ eV (a,b,c), three majority-spin channels at $E = 0.5$ eV (d,e,f), and three minority-spin channels at $E = 0.5$ eV (g, h, i).

Table 4.4: Spin-dependent eigenchannel conductance of Al(001)-Al_4-Al(001) at two resonant energy levels

E	Spin majority (unit: $G_0/2$)			Spin minority (unit: $G_0/2$)		
(eV)	1	2	3	1	2	3
-0.35	0.9458	0.9603	0.6914	0	0	0
0.5	0.4854	0.4773	0.9652	0.9653	0.9590	0.6427

Furthermore, we believe that our observations and conclusions share some similar aspects with quantum point contacts which have been extensively studied [80, 178, 179, 180, 178, 181, 182, 183, 184, 185, 186, 187, 188, 189]. The similarity lies at the spontaneous magnetization or local magnetic moment formation which is believed to be responsible for the conductance plateaus at 0.5 and 0.7 G_0 of the quantum point contact. The latter one is the famous "0.7-structure", being a puzzle for more than one decade. Crook *et al.* [186] showed that even with the absence of magnetic field an induced gallium arsenide (GaAs) quantum wire exhibits an additional conductance plateau at 0.5 quantum conductance in addition to the "0.7-structure". These two plateaus are believed to result from the above spontaneous spin polarization - a ferromagnetic phase. Especially "0.7-structure" is suggested to be a transition stage between two different phases [190, 186, 185] associated with electron spin. It is the similar situation we have encountered in Al(001)-Al_n-Al(001) here. The feature discussed above can be applied to the development of spintronic devices such as *spin-current filter* which generates electric current with specific spin polarization and *spin-current detector* without the help of external magnetic fields or magnetic materials [186].

4.3 Molecular electronics

The development of molecular scale electronic devices has attracted a great deal of interest in the past two decades due to its potential applications in future ultrasmall electronics such as diode, logic gate and memory [191, 49, 192, 193, 194, 195, 196, 197, 50, 198, 51, 52, 53, 199, 200, 201, 202, 203, 204, 205, 206, 207, 208], although major experimental and theoretical challenges still exist. Various experimental techniques are employed including mechanically-controlled break junction method(MCBJ)[49], crossed-wire method[209] and STM break-junction method [200]. However, precise experimental control of molecular conformation is still lacking, resulting in large uncertainties in the measured conductance. Recently local heating or vibrational effect on the conductance has been investigated[210, 211, 212, 213, 209, 214, 215, 66,

216, 217, 218]. On the other hand, theoretical approaches using Green's function method [79], scattering-state approach (theoretically equivalent to Green's function method) [192, 219] and complex band structure method (simplified Landauer formalism) [220, 221] have been developed to calculate electrical conductance in the similar molecular systems [192, 193, 222, 59, 201, 205]. With great efforts from both experimental and theoretical approaches, the previous large discrepancy between conductance magnitude from two approaches has reduced from three orders to two or even one order[208].

Here we investigate three examples of molecular electronics: (a) benzene dithiolate sandwiched by gold chains, (b) benzene dithiolate sandwiched by Au(001) electrodes with finite cross-section and (c) phenalenyl dithiolate-based molecular bridge sandwiched by aluminum chains. From these cases we will demonstrate the effect of the shape of electrodes on conductance curve and source-drain-induced quantum current loop inside molecular system.

4.3.1 Benzene dithiolate molecule sandwiched by gold chains

Figure 4-29: Atomic structure of Au_6-BDT-Au_6.

The structure of benzene dithiolate(BDT) molecule sandwiched by gold chains is illustrated in Fig. 4-29. The bond lengths for Au-Au, Au-S, S-C, C-C, and C-H is 2.88, 2.41, 1.83, 1.39 and 1.1 Å respectively. The contour plots of ground-state effective Kohn-Sham potential and valence charge density are shown in Fig. 4-30 and Fig. 4-31. These plots display a deeper potential well and indicates that the sulfur atoms play a critical role in gluing benzene molecule and metallic gold lead.

The nine quasiatomic orbitals, including five d-QOs, one s-QO and three p-QOs, are constructed for each gold atom in the lead part shown in Fig. 4-32. From the

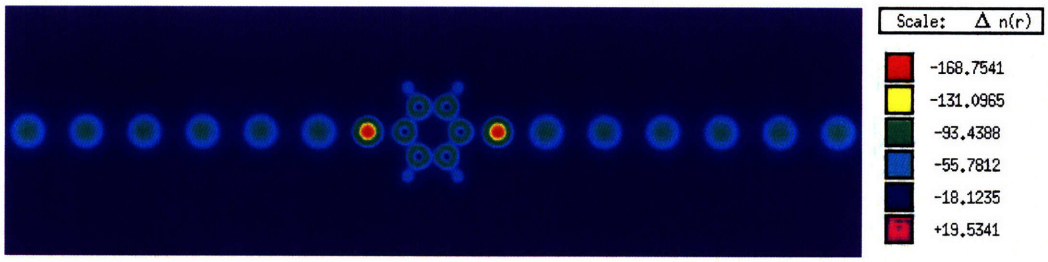

(a) (b)

Figure 4-30: Contour plot of effective Kohn-Sham potential of Au_6-BDT-Au_6 in the unit of eV

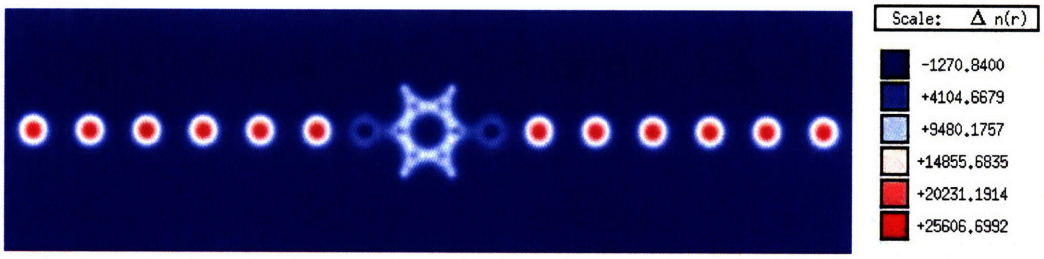

(a) (b)

Figure 4-31: Contour plot of valence electron density of Au_6-BDT-Au_6

orbital shape, we can see d-QOs are less deformed compared to s-QO and p-QOs, especially along the chain or bonding direction. That is also reflected in the QO-projected electronic band structure Fig. 4-33(a). The band width of those bottom red bands and middle blue bands, dominated by d and p_y, p_z-QOs respectively, is very narrow, however the band width of the remaining upper green dominated by s and p_x-QOs is much wider. More significantly the top of antibonding s-QO band at Γ point is around 18 eV above Fermi level. Thus, to capture this high energy antibonding band for band closure in modern Wannier or QUAMBO approaches, we usually need to include so many Kohn-Sham bands at each $\mathbf{k}$-point in ground-state DFT calculations, a lot more than the number of valence orbitals. The conclusion can be also applied to other one-dimensional and two-dimensional structures such as nanowires, nanotubes, and graphene sheets where quantum confinement is extremely important.

The conductance curve of the lead formed by gold chain is plotted in Fig. 4-

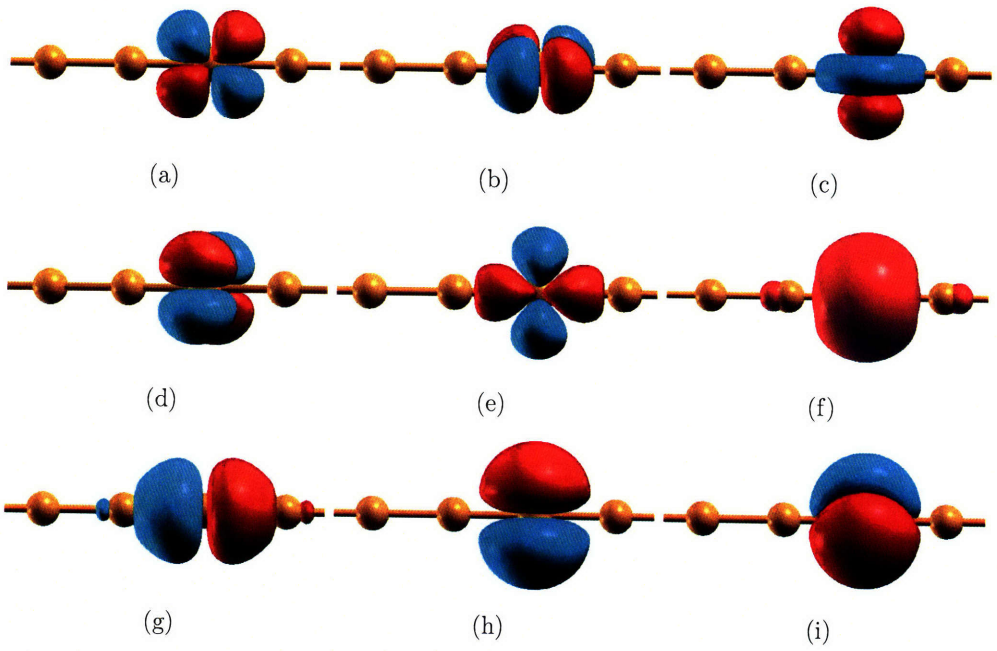

Figure 4-32: 9 QOs in the Au chain including five d-QOs (a-e), one s-QO (f) and three p-QOs (g-i).

33(b). We clearly see that the total conductance again shows the step shape and exactly matches band-counting method from band structure plot in Fig. 4-33(a) along the energy axis. It is clear that the only channel available around Fermi level is not from d or p_y, p_z-QO, but from the Bloch state formed by s and p_x-QOs. However, once the BDT molecule is sandwiched between two gold chains, the conductance curve changes dramatically as shown in Fig. 4-34. Within the energy range from -4 eV to 4 eV (E_F = 0 eV), there exist two broad peaks in the energy range [-3.5, -1.5] eV and [0.5, 4.0] eV and one sharp peak in [-1, -0.2] eV. Although the lead part contains more than one channel in the two same lower energy range, none of three peaks exceeds one G_0, which is the resonant feature of quantum transport through molecules. Or in another word, electron transport in molecular system is through the coupling between molecular orbitals of BDT and the orbitals of leads at discrete molecular orbital energy, therefore it is essentially zero-dimensional resonant transport and can be easily described by the Newns-Anderson model [154, 155].

To understand the above three conductance peaks, we then carry out the conduc-

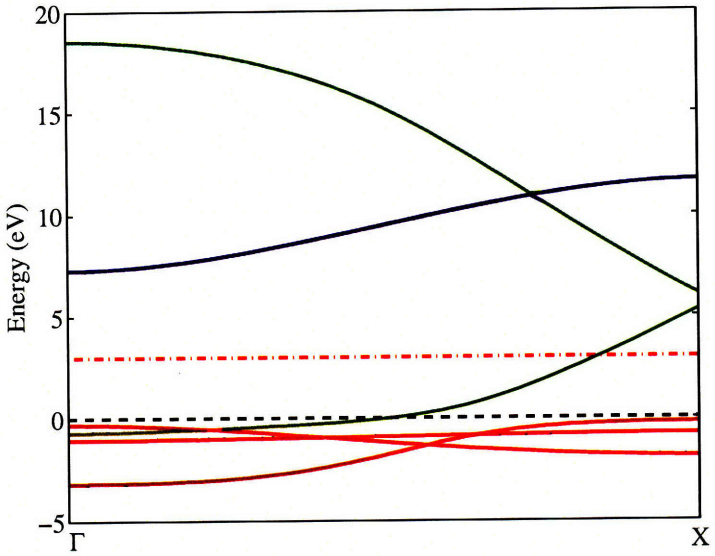

(a)

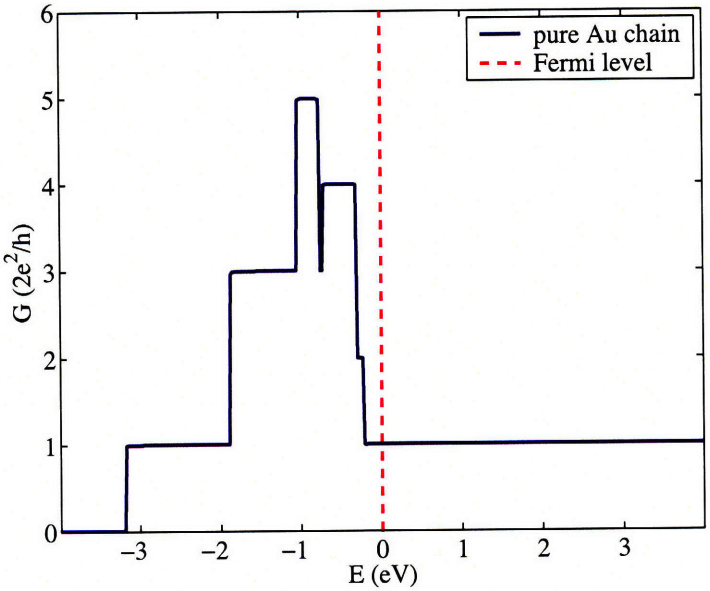

(b)

Figure 4-33: (a) QO-projected band structure of Au chain with its colormap similar to Fig. 4-2(b) but with red for d-QOs, green for s, p_x-QO and blue for p_y, p_z-QOs with x as the chain direction. (black dash line: Fermi level; red dash-dot line: the shifted Fermi level with $E_{\text{shift}} = 3$ eV.) (b) Conductance curve.

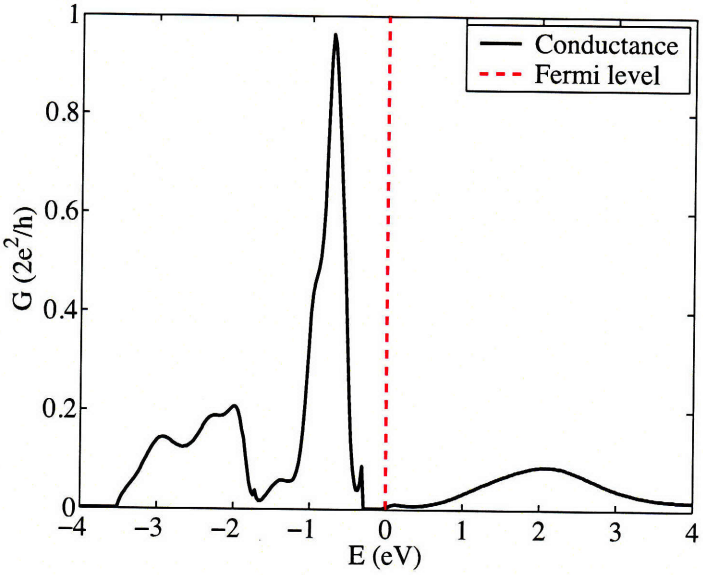

Figure 4-34: Electrical conductance of Au_6-BDT-Au_6.

tance eigenchannel decomposition and find that at each energy level only one major conducting channel is available. Conductance eigenchannels at five energy levels, -2.913, -1.988, -0.713, 0.9 and 2.0 eV, are shown in Fig. 4-35. We clearly see that the lowest channel at E = -2.913 eV, shown in Fig. 4-35(a,b), is from the coupling through the d_{x^2}-QO bonding state of Au atoms in the lead, antibonded with the bonding p_x of S atom and benzene ring. Channel 2 at $E = -1.988$ eV, shown in Fig. 4-35(c,d), is similar to channel 1 but the left lead part contains *partial* antibonding d_{x^2} state and that is the reason for its energy level about 1 eV higher than channel 1. Channel 3 at $E = -0.713$ eV, shown in Fig. 4-35(e,f), has completely different character and the coupling is through the partial d_{xz}-antibonding state in the left lead which is then antibonded with the partial p_z-antibonding molecular orbital of BDT molecule. The channels of the broad peak above Fermi level are mostly from the mixed antibonding $s - p_x$ state in the left lead antibonded with the p_x state of BDT molecule. This peak reaches its maximum at $E = 2.0$ eV. More strikingly, the phase-encoded eigenchannels on the right column of Fig. 4-35 directly demonstrate that the channels (b,d,f) with larger conductance have stronger phase change from 0 to 2π and larger volume in the right lead while the channels (h,j) with lower con-

ductance have smaller volume and less phase change. The more pure red and light blue indicate the eigenchannel wave function contains less imaginary part, forming more static state in the left channel. The perfect limit is no current propagating from left to right. As we have discussed before, the simplest model in this limit is: $2\cos(x) = e^{ikx} + e^{-ikx}$, where e^{ikx} and e^{-ikx} represent the right moving incoming wave and the left moving reflected wave and they form a static $\cos(x)$ wave inside the left lead.

In Fig. 4-35(g,h), we also show the channel at $E = 0.9$ eV with conductance $G = 0.025G_0$, which will be directly compared to our real-time wave propagation result using time-dependent density functional theory(TDDFT) [128] in the next Chapter. Briefly speaking, from the comparison we will show the agreement between Green's function method and TDDFT, not only from the conductance results in the same order, but also from the detailed eigenchannel state and propagating wave function. To our knowledge, this is the first direct comparison between TDDFT and Green's function method in the linear response regime under the rigid band approximation. More details will be shown and explained in the next Chapter.

4.3.2 Benzene dithiolate molecule sandwiched by Au(001) electrodes with finite cross section

From the above results and discussions we have gained some important insights of electron transport through Au chain-BDT-Au chain. Although in experiments gold chain has been formed when pulling the macroscopic gold wire apart, most conductance measurements of BDT junction were done between two surfaces with certain local structures and they are much easier to control than the wire when chemically absorbing BDT molecules. Here we change the chain-like gold electrode to Au(001) lead with finite cross section, similar to what we have done in the aluminum electrode before.

The structure of Au(001)-BDT-Au(001) is shown in Fig. 4-36. The bond lengths of Au-Au, S-C, C-C and C-H are 2.885, 1.83, 1.39 and 1.4 Å respectively while S is

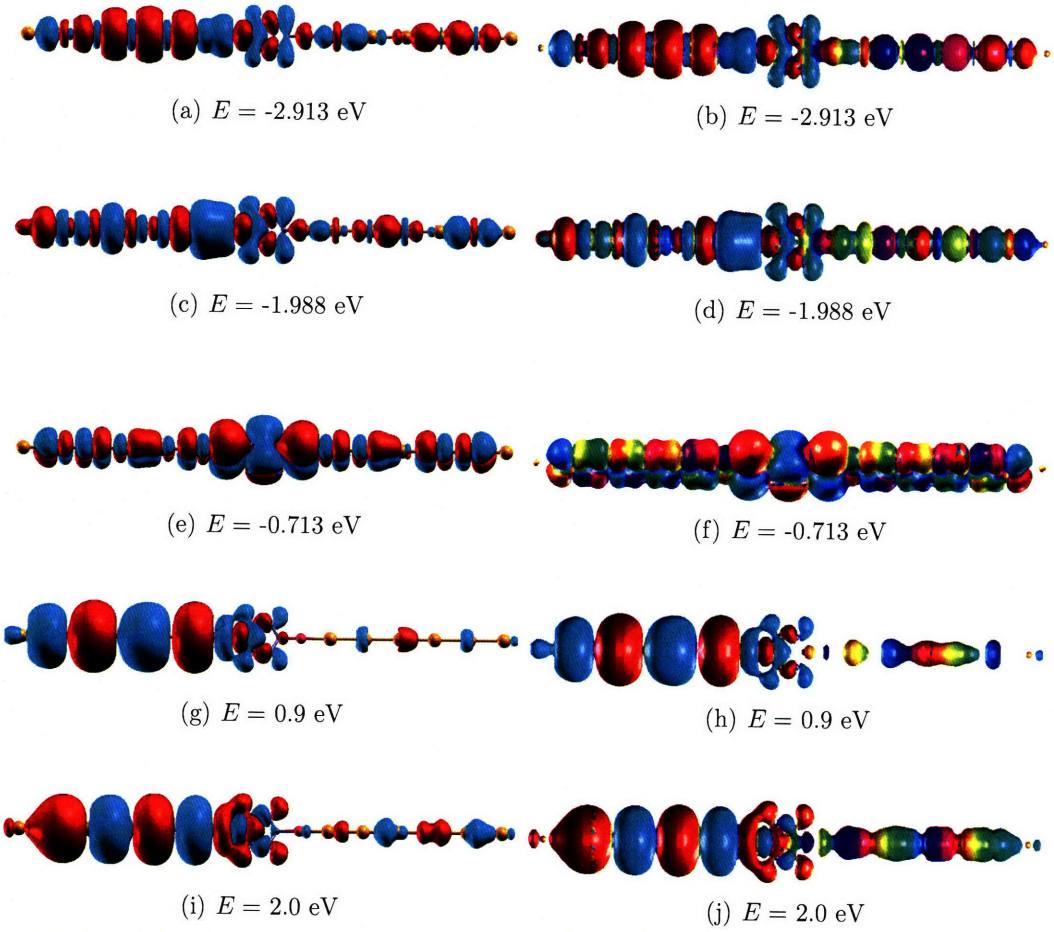

(a) E = -2.913 eV (b) E = -2.913 eV

(c) E = -1.988 eV (d) E = -1.988 eV

(e) E = -0.713 eV (f) E = -0.713 eV

(g) E = 0.9 eV (h) E = 0.9 eV

(i) E = 2.0 eV (j) E = 2.0 eV

Figure 4-35: Conductance eigenchannel decomposition of Au_6-BDT-Au_6 with one major eigenchannel at each energy level. The left column is isosurface plot of real part of two channels, and the right column is phase-encoded isosurface plot of magnitude part. Energy levels of the eigenchannels from (a) to (i) on the left column are: $E = -2.913$, -1.988, -0.713, 0.9, and 2.0 eV with their conductance $G = 0.144$, 0.208, 0.95, 0.025 and 0.086 G_0.

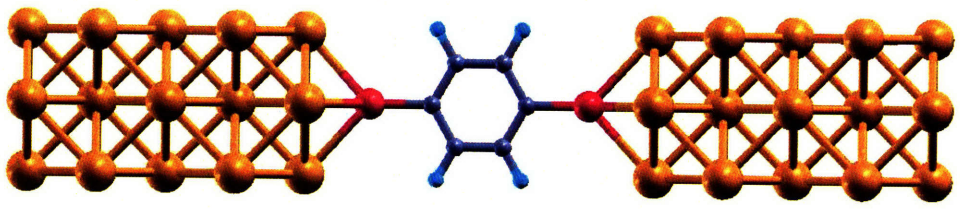

Figure 4-36: Atomic structure of Au(001)-BDT-Au(001) with finite cross section.

1.0 Å away from the near gold surface and the latter contains four Au atoms on the plane perpendicular to the x-direction. Contour plot of charge density on the plane through the benzene plane is shown in Fig. 4-37.

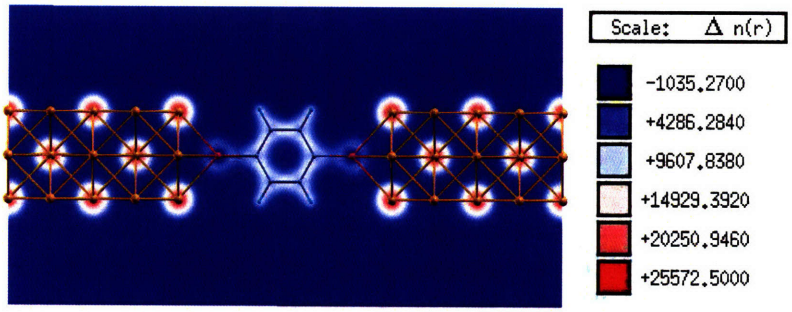

(a) (b)

Figure 4-37: Contour plot of valence electron density of Au(001)-BDT-Au(001) with finite cross section.

Principal layer of the lead part is composed of four layers of Au atoms with the 5-4-5-4 structure. Band structure and conductance curve are shown in Fig. 4-38, which again match exactly with each other. Compared to Au chain, the Au(001) lead with finite cross-section has more channels accessible around Fermi level while below 1.5 eV there are many bulk-like states which gives rise to quick oscillations in the conductance curve.

The conductance curve for Au(001)-BDT-Au(001) with finite cross section is shown in Fig. 4-39. Almost all the peaks contain only one major channel with its conductance less than 1 G_0 and this again demonstrates the resonant transport feature in the device of Au(001)-BDT-Au(001), similar to the Au chain-BDT-Au chain case. Again we plot two eigenchannels at $E = -1.32$ and 0.0 eV in Fig. 4-40 and the corresponding conductance values are 0.981 G_0 and 0.558 G_0, respectively. It is clear that at both channels the resonant transport state is the overall antibonding state of the benzene molecule which is further antibonded to the sulfur atom's p_z orbital. In turn, the incoming state from the left lead changes its phase by the amount of π and leads to the opposite sign of the real part of wave functions on the left and right leads.

The important role of molecular orbitals on the BDT molecule has also been

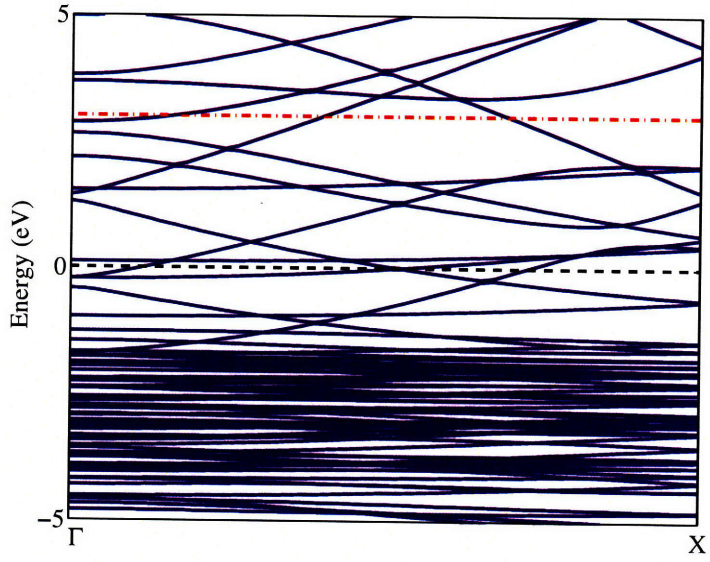

(a)

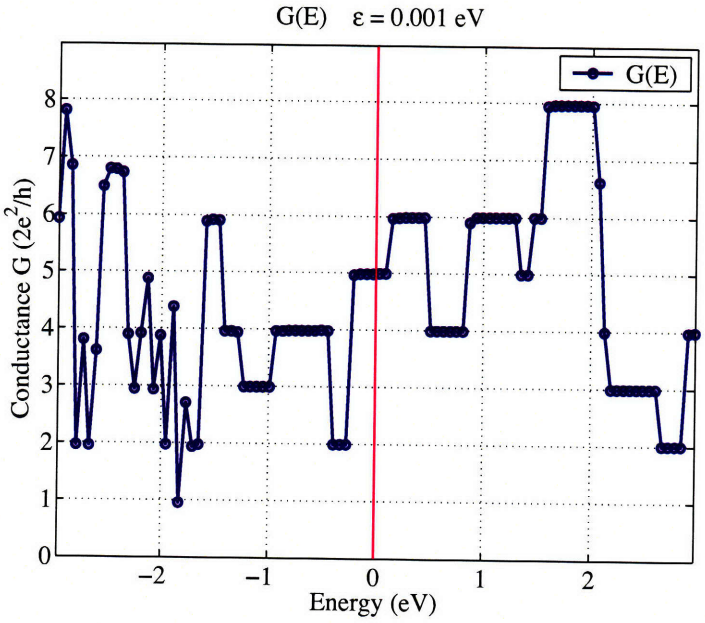

(b)

Figure 4-38: (a) band structure of Au(001) with finite cross-section. Black dash line indicates Fermi level and red dash-dot line indicates shifted Fermi level with $E_{\text{shift}} = 3$ eV. (b) Conductance curve

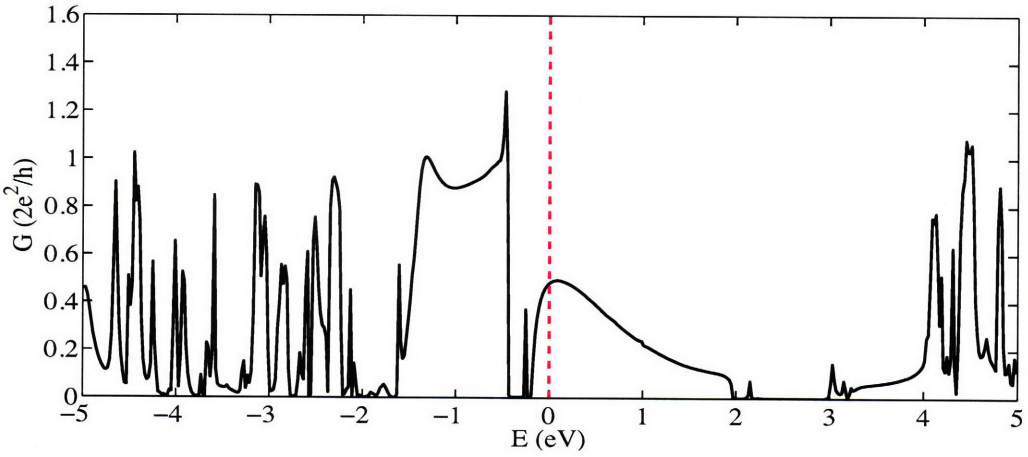

Figure 4-39: Electrical conductance of Au(001)-BDT-Au(001) with finite cross section.

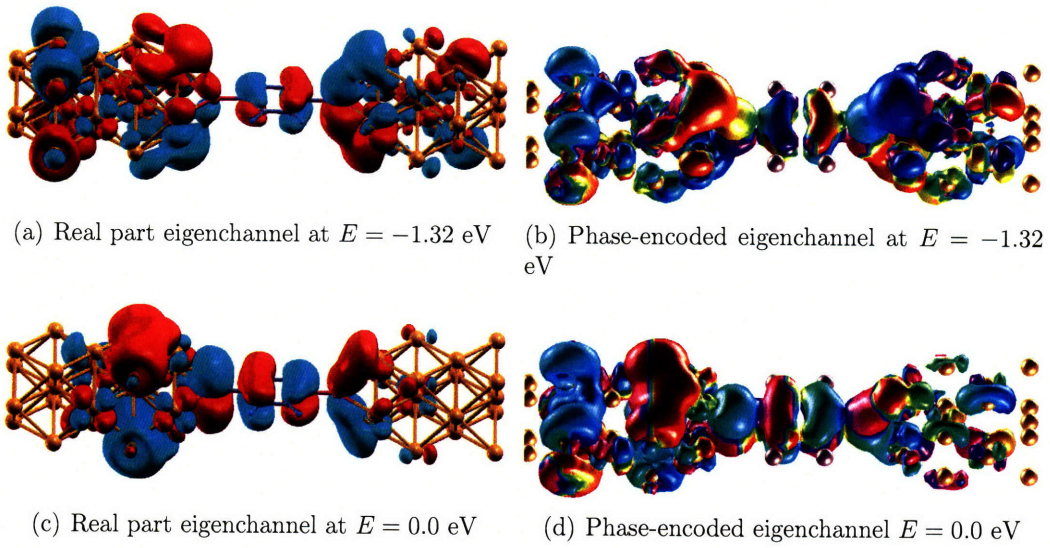

(a) Real part eigenchannel at $E = -1.32$ eV

(b) Phase-encoded eigenchannel at $E = -1.32$ eV

(c) Real part eigenchannel at $E = 0.0$ eV

(d) Phase-encoded eigenchannel $E = 0.0$ eV

Figure 4-40: Conductance eigenchannel decomposition of Au(001)-BDT-Au(001) with finite cross section at different energy levels. The left column is isosurface plot of real part of two channels, and the right column is phase-encoded isosurface plot of magnitude part. These two eigenchannels are at $E = -1.32$ eV with conductance $G = 0.981G_0$ and at $E = 0.0$ eV with conductance $G = 0.558G_0$.

pointed out by Stokbro *et al.* [223] and Thygesen *et al.* [96]. In their case, two Au(111) surface has been used as electrodes, different from our case here. However, the same benzene molecular orbital discussed above seems to dominate the conductance at certain energy level. Moreover, our phase-encoded isosurface plot of two eigenchannels show the large phase oscillations and large volume of wave functions on the right lead, indicating the large conductance. It has been shown by Thygesen *et al.* [96] that transverse **k**-point sampling will smear the large oscillations in conductance curve. Thus, one thing we need to make effort in future is to include the transverse **k**-point sampling in our conductance calculation.

4.3.3 Phenalenyl-based molecular bridge sandwiched by aluminum chains

Instead of focusing on electrical conductance, now we shift our gear a little bit and ask another question: what will be the current map look like if the molecular conductor is asymmetric with respect to electron transport direction? This problem has been already demonstrated by Nakanishi *et al.* [88, 89, 90, 224] using simple tight-binding model. It is shown that fullerene C_{60} and phenalenyl molecule as molecular conductor, asymmetric to the source-drain current, exhibit magic quantum loop current inside the conductor itself. Sometimes that loop current can be even much higher than the source-drain current added on the leads. Consequently from the law of electromagnetic induction the loop current will induce a local magnetic field. However, to our knowledge there is no validation at the first-principles level.

Here we report our Green's function method calculation of phenalenyl-dithiolate based molecular bridge between two aluminum chains using the QO basis-set and its *ab initio* tight-binding Hamiltonian and overlap matrix. Atomic structure of phenalenyl-dithiolate molecular bridge sandwiched between two aluminum chains is shown in Fig. 4-41. Its ground-state effective Kohn-Sham potential and valence charge density are shown in Fig. 4-42 and Fig. 4-43. Again sulfur atoms seem to have a deeper potential than carbon and aluminum atoms.

Figure 4-41: Atomic structure of phenalenyl-based molecular bridge with Al chain as the lead .

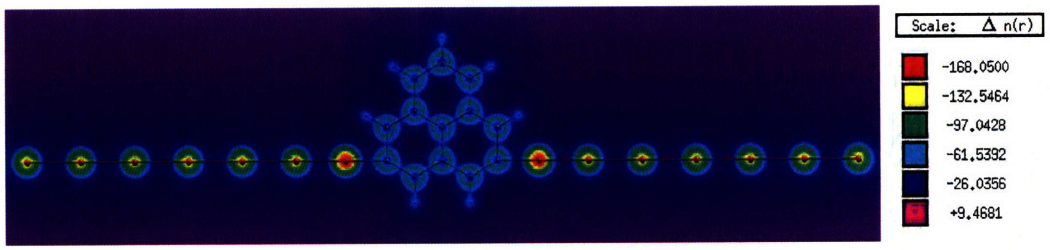

(a) (b)

Figure 4-42: Contour plot of effective Kohn-Sham potential of phenalenyl-based molecular bridge.

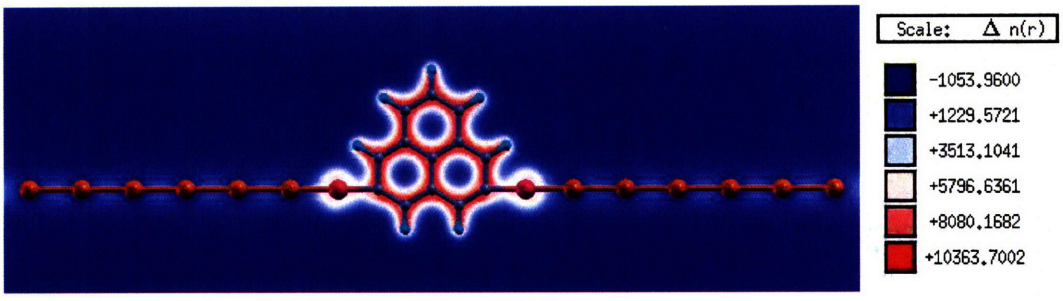

(a) (b)

Figure 4-43: Contour plot of valence electron density of phenalenyl-based molecular bridge.

The conductance curve is plotted in Fig. 4-44. It is not totally unexpected that, similar to the previous BDT case, the conductance curve shows the resonant transport characteristics and most peaks are below 1 G_0. Its discrete single-channel resonant conductance peaks indicate the role of molecular orbitals of phenalenyl-dithiolate coupled to Al chain. There are nine peaks between -5 eV and 4 eV. Two of them are not very clearly separated and they squeeze between -0.078 eV and -0.03 eV.

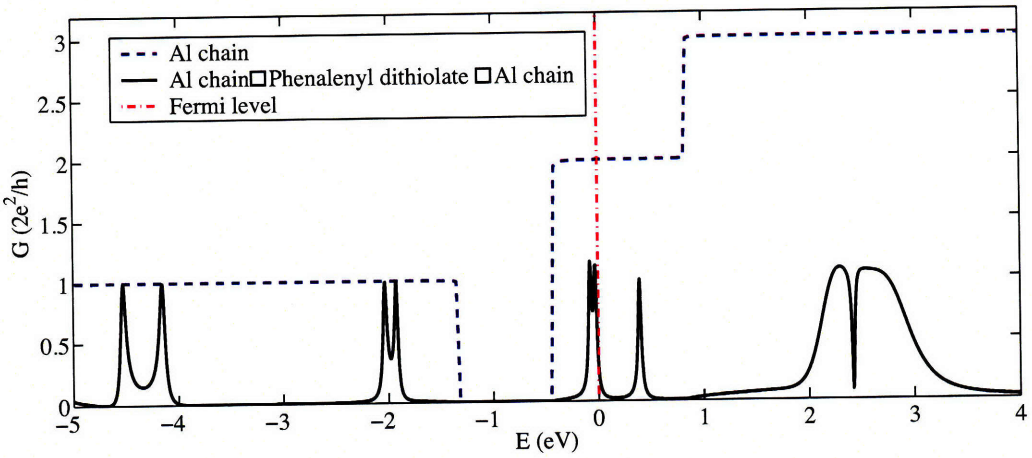

Figure 4-44: Electrical conductance of phenalenyl-based molecular bridge.

We then perform conductance eigenchannel decomposition of the nine peaks. The eigenchannel conductance at each resonant peak is listed in Table 4.5. It is clear that the conductance of all the major eigenchannels has the conductance near 1 G_0. From the table, we see that each of two channels at $E = -0.078$ eV and $E = -0.03$ eV contains one major channel and one minor channel. We can guess that the minor channel comes from dispersion of the major channel at the other resonant energy level.

To further explore the detailed transport mechanism, we then show the phase-encoded conductance eigenchannels in Fig. 4-45. The conductor region in channel (a, b, f) shows the large components of pure red and light blue isosurface, indicating the static wave nature inside these regions mostly composed of real wave function. In contrast, the eigenchannels in Fig. 4-45(h) and (i) show the smooth phase-change of wave functions in the lead *and* phenalenyl molecule. Following the colormap of phase in Fig. 4-12 from red to yellow, green, light blue, blue and then back to red, we can

(a) E = -4.53 eV, $G = 0.913\ G_0$

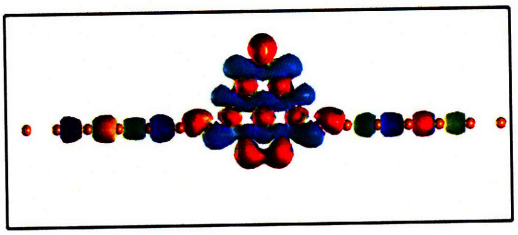

(b) E = -4.15 eV, $G = 0.923\ G_0$

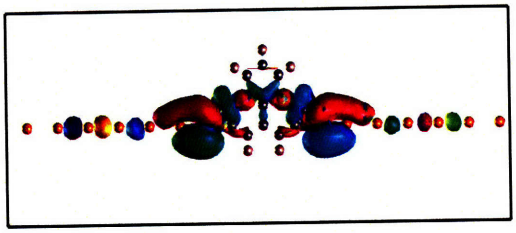

(c) E = -2.03 eV, $G = 0.898\ G_0$

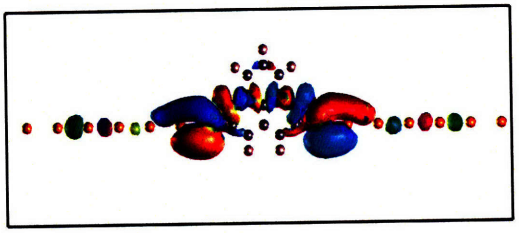

(d) E = -1.93 eV, $G = 0.858\ G_0$

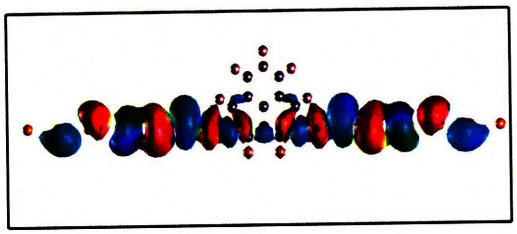

(e) E = -0.078 eV, $G = 0.985\ G_0$

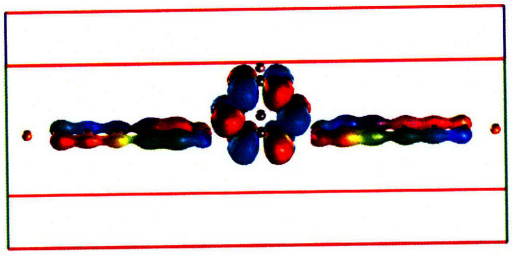

(f) E = -0.03 eV, $G = 0.984\ G_0$

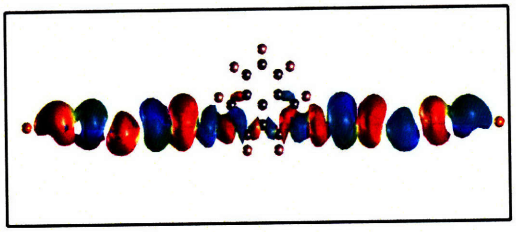

(g) E = 0.39 eV, $G = 0.877\ G_0$

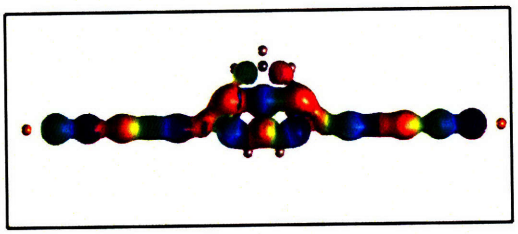

(h) E = 2.29 eV, $G = 0.982\ G_0$

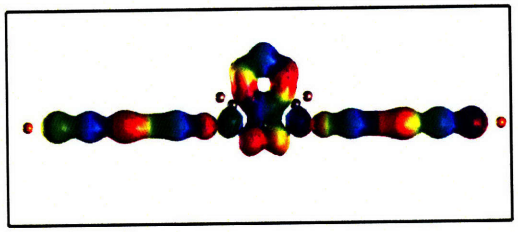

(i) E = 2.55eV, $G = 0.985\ G_0$

Figure 4-45: Phase-encoded conductance eigenchannels of phenalenyl-based molecular bridge at different resonant levels. The energy level and conductance of each channel are indicated in the figure and also listed in Table 4.5.

Table 4.5: Eigenchannel conductance of phenalenyl-based molecular bridge at different resonant levels. Labels (a-i) is the corresponding major conducting channel plotted in Fig. 4-45

E	Channel 1	Channel 2
eV	G_0	G_0
-4.53	0.913 (a)	
-4.15	0.923 (b)	
-2.03	0.898 (c)	
-1.93	0.858 (d)	
-0.078	0.985 (e)	0.155
-0.03	0.131	0.984 (f)
0.39	0.877 (g)	
2.29	0.982 (h)	
2.55	0.985 (i)	

obtain a simple view of the current direction inside the molecule. Current channel (h) in the bottom big ring forms a counterclockwise current loop at $E = 2.29$ eV and current channel (i) in the top small ring forms a clockwise current loop at $E = 2.55$ eV.

To have a clear understanding of the local loop current we calculate the bond current distribution[54] from each conductance eigenchannel. The current magnitude is shown in Table 4.6 and the detailed current map is shown Fig. 4-46 (a) and (b). Immediately we find two almost perfect quantum current loops inside the molecule. However beside the difference in the shape and size, another important difference between two loops are the opposite direction of current-induced magnetic fields, resulting from the law of electromagnetic induction. Since electron current carries negative charges, the magnetic field induced from the red loop points inside the paper while that from the green loop points outside the paper. The calculated ratio between the magnitude of quantum loop current and that of the incoming current is above 3 in each case.

Our quantum loop current is similar to the result of Nakanishi *et al.* [89], however not all the loops that they have predicted from simple tight-binding model show up in our calculation. That difference has to be traced back the fundamental physics

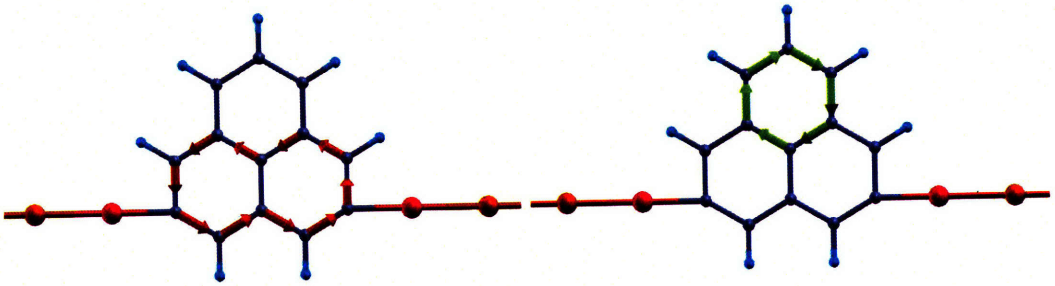

(a) (b)

Figure 4-46: Quantum current loops in the phenalenyl-based molecular bridge at two resonant levels (a) $E = 2.29$ eV and (b) $E = 2.55$ eV. (The red and green loops indicate different directions of magnetic field from the current loops.)

Table 4.6: Quantum current loops in the phenalenyl-based molecular bridge at two resonant levels.

E(eV)	Source-drain current (I_{SD})	Loop current (I_{loop})	Ratio (I_{loop}/I_{SD})
2.29	0.61	2.03	3.35
2.55	0.56	2.21	3.96

of the emergence of quantum loop current. The intrinsic reason is the breaking of time-reversal symmetry under the source-drain bias or current. Just like the previous explanation through the right-moving and left-moving plane-wave model, the static ground-state wave function can be viewed as the exact cancellation of left and right moving waves. With the bias or current added onto the system, the time reversal symmetry of the original ground state is broken, leading to imperfect cancellation between two opposite currents. Finally it results in a net current between two electrodes. Actually the emergence of quantum current loops side the conductor region has an extra requirement. That is the asymmetric geometry of molecular conductor respect to the source-drain current. If the phenalenyl molecule is replaced by benzene molecule in the previous case, we will not see any internal current loop if no external magnetic field and asymmetric interface geometry exist. We immediately realize that the lifting of time-reversal symmetry can also be introduced by external magnetic field while the close relationship between two cases has been shown by Tagami *et al.* [224]. Therefore the absence of the other loops predicted by Nakanishi *et al* is most

probably due to the insufficient time-reversal symmetry breaking.

4.4 Carbon nanotube

Carbon nanotubes(CNTs), first discovered by Iijima[225], have a lot of potential applications in nanoscale electronics. They have attracted a lot of attentions in experiments and theories in the past decade. Particularly single-walled carbon nanotubes(SWNTs) can be excellent conductors replacing traditional electrical wire. Various conductance calculations have been carried out in the last few years to study pristine CNT, defected CNT, or chemically-functionalized CNT [56, 59, 95, 226, 227, 228, 229].

Here we would like to ask two questions: (a) What is the role of spin and specific defect in the CNT conductance? (b) does quantum current loop exist in CNT with and without defects? To answer the above two questions, we have investigated three CNT systems: (a) clean armchair CNT(4,4), (b) CNT(4,4) with single substitutional impurity Si atom with and without atomic structure relaxation, and (c) relaxed CNT(4,4) with single vacancy.

4.4.1 CNT(4,4)

Atomic structure of clean CNT(4,4) is displayed in Fig. 4-47 with long bond length of 1.414 Å and short bond length of 1.399 Å in a rectangular box of $13.512 \times 13.512 \times 14.705$ Å^3. The tube is along the z-direction (the third axis). The corresponding band structure, density of states, and quantum conductance curve are shown in Fig. 4-48. The quantized conductance is the similar feature found in other people's work [56, 59, 95, 226, 227]. It also agrees with the band counting method from the band structure plot. Both curves smoothly pass the Fermi level and that is consistent with one basic rule of CNT. For a given (n, m) carbon nanotube, if $n - m$ is a multiple of 3, the carbon nanotube is metallic. Again DOS of CNT(4,4) shows sharp peaks at each conductance step, indicating extra band inclusion or exclusion. Around Fermi level the conductance is $2G_0$ and that means there are two perfect eigenchannels

responsible for the conductance.

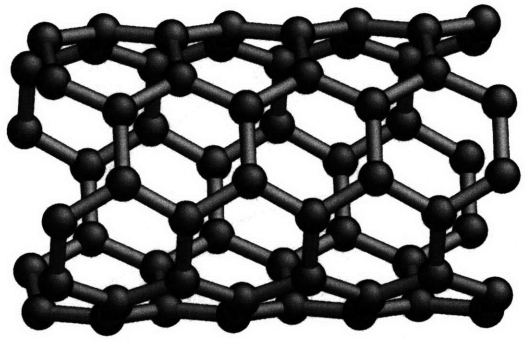

Figure 4-47: Atomic structure of CNT(4,4)

The current map for one of the major conducting eigenchannel is illustrated in Fig. 4-49. It clearly shows the bond current is through the armchair direction or the longitudinal direction while no net current is found along the zigzag direction or the transverse direction. This is also a direct illustration of one-dimensional characteristics of CNT(4,4) from the view of electrical current.

4.4.2 CNT(4,4) with single substitutional impurity Si atom

In this session, we replace one carbon atom with a Si atom in CNT(4,4). The relaxed atomic structure is shown in Fig. 4-50. The ground-state DFT calculation includes the spin degree of freedom.

Electrical conductance curves of both unrelaxed and relaxed CNT(4,4)-Si are plotted in Fig. 4-51. Fig. 4-51(a) shows that there is no significant spin dependence on the conductance curve. However as indicated in Fig. 4-51(b), the total conductance of relaxed structure has large difference from the conductance of the CNT(4,4)-Si without relaxation. It shows a deep and wide dip above Fermi level from 0 to 1 eV. The depth of the conductance dip is about $1G_0$ and that could come from the disappearance of one conducting channel. In the case of unrelaxed CNT(4,4)-Si, we do not find the similar dip at the same energy range. The overall conductance magnitude of relaxed structure from -4 eV to 4 eV is no higher than the unrelaxed one. It is also clear that the conductance in both cases is lower than that of the perfect tube.

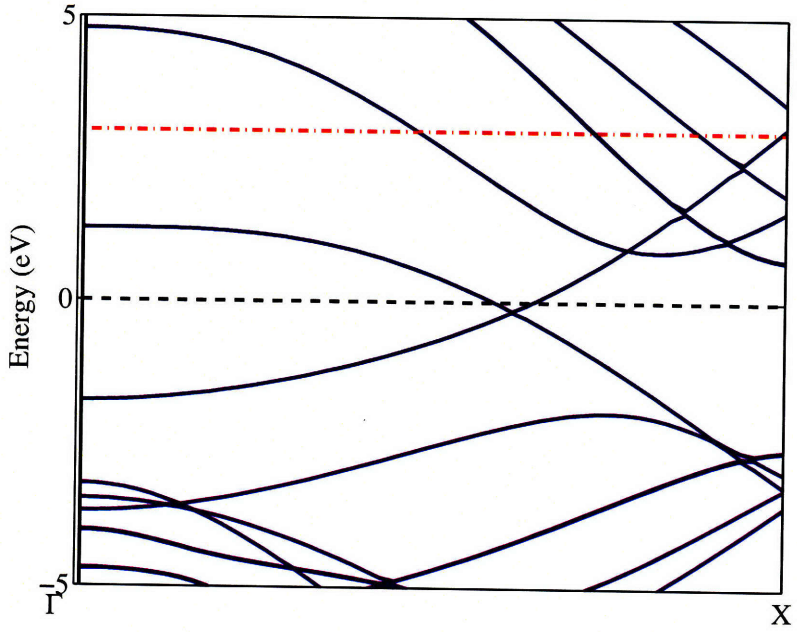

(a)

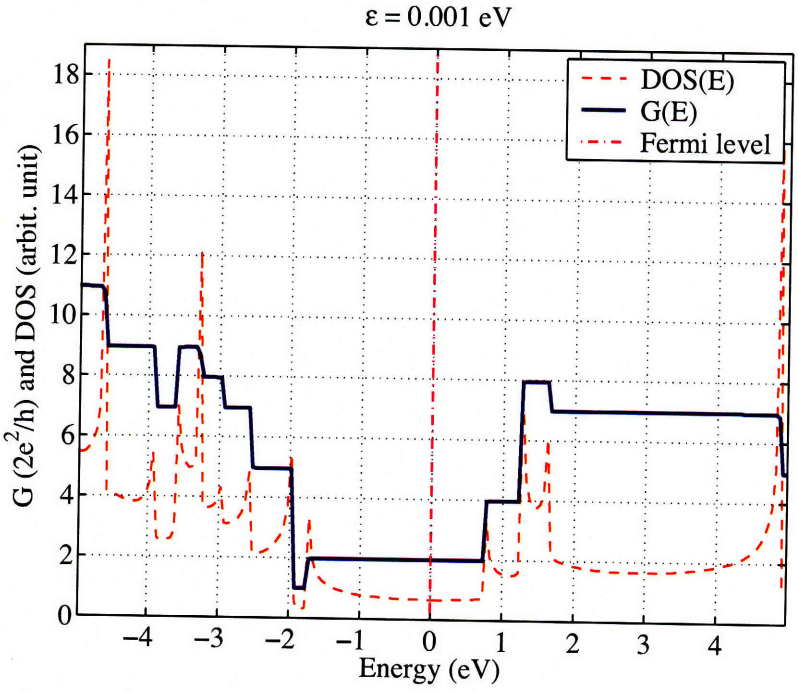

(b)

Figure 4-48: Band structure, density of states and electrical conductance of CNT(4,4). Black dash line and red dash-dot line in the band structure plot are true Fermi level and the shifted Fermi level at 3 eV, respectively.

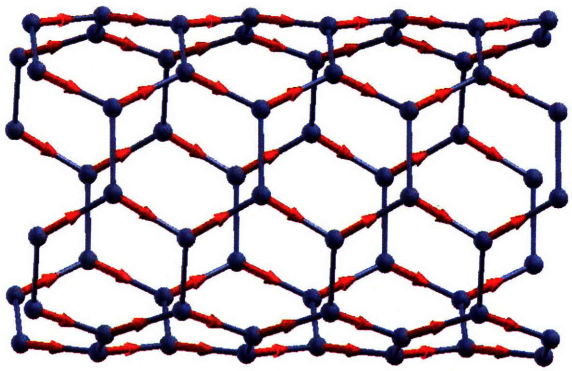

Figure 4-49: Double-degenerate eigenchannel current of CNT(4,4) at Fermi level

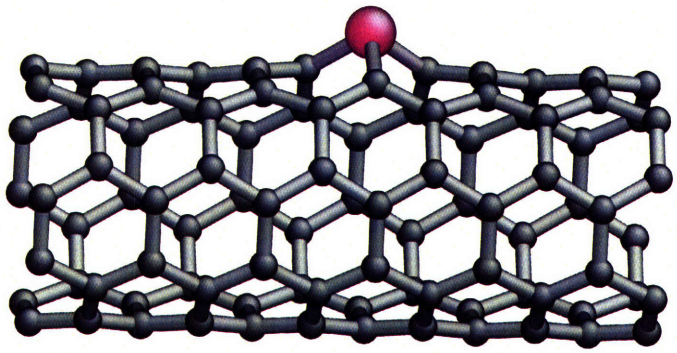

Figure 4-50: Atomic structure of relaxed CNT(4,4) with single substitutional impurity Si atom (purple).

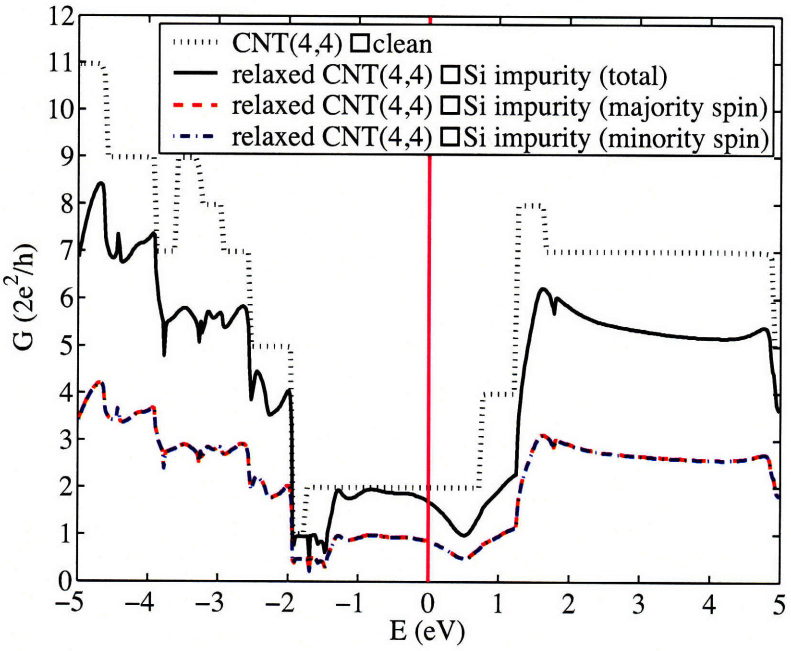

(a) spin-decomposed conductance

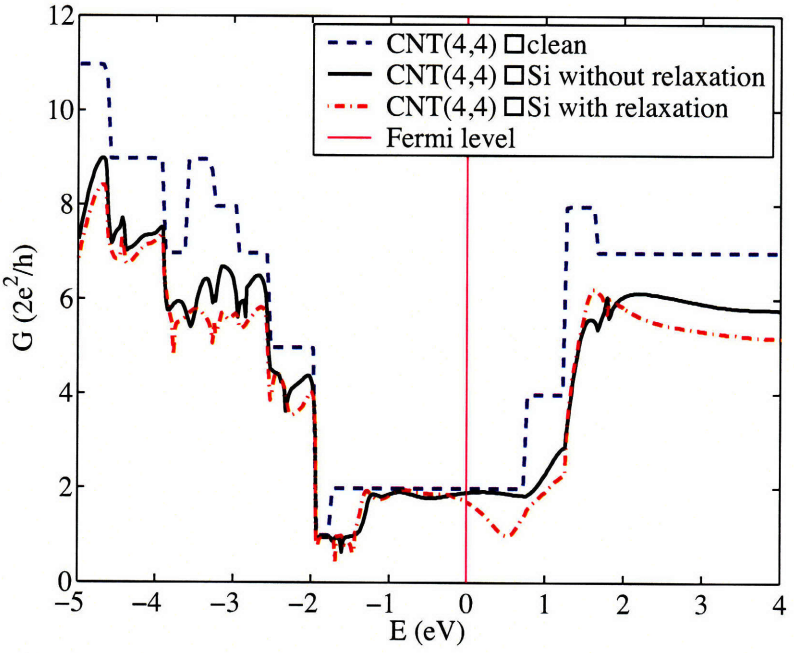

(b) comparison of conductance curves with and without relaxation

Figure 4-51: Electrical conductance of CNT(4,4) with single substitutional impurity Si atom with and without relaxation

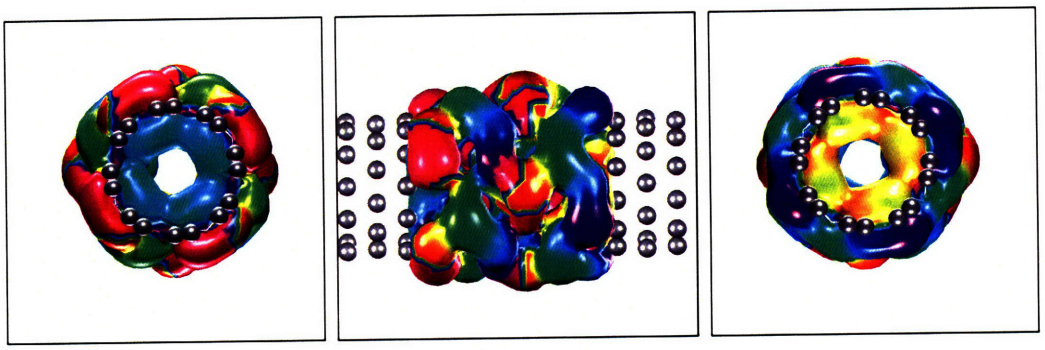

(a) Channel 1 at $E = 0$ eV, $G = 0.917G_0$

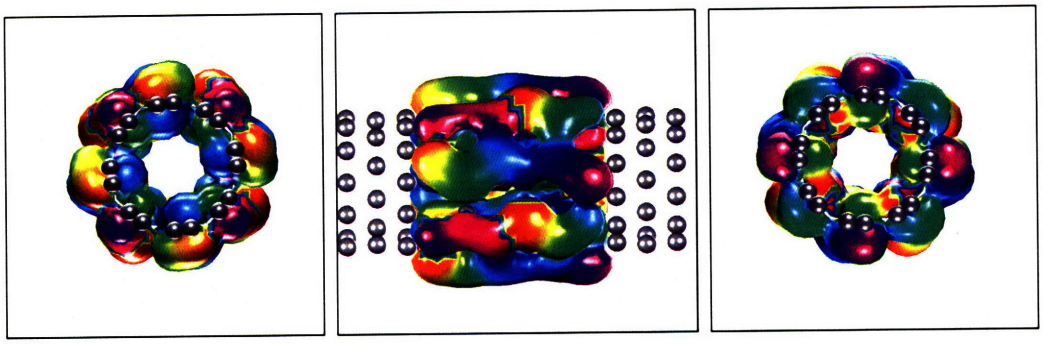

(b) Channel 2 at $E = 0$ eV, $G = 0.987G_0$

Figure 4-52: Phase-encoded conductance eigenchannels of *unrelaxed* CNT(4,4) with single substitutional impurity Si atom. Three figures on each row are the left, top, and right view of the same eigenchannel at Fermi energy ($E = 0$ eV).

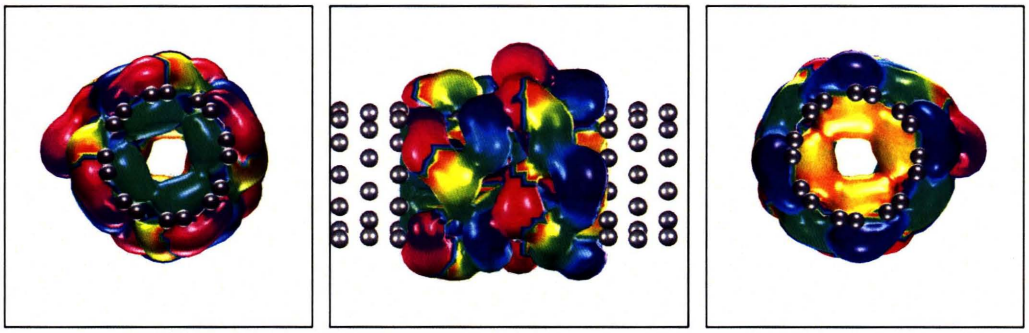

(a) Channel 1 at $E = 0.5$ eV, $G = 0.977G_0$

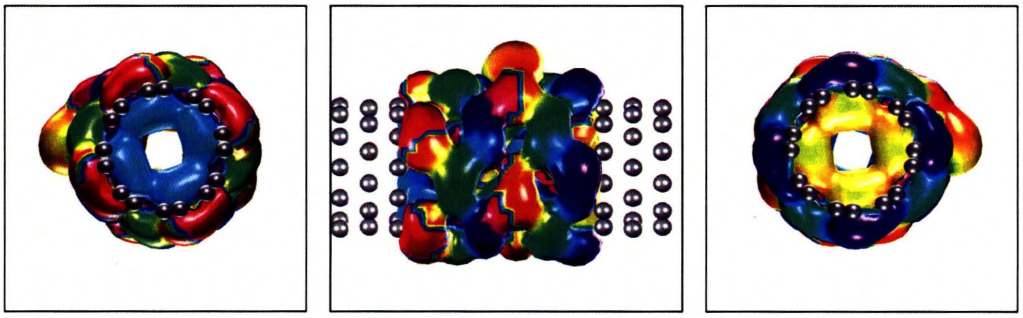

(b) Channel 1 at $E = 0$ eV, $G = 0.955G_0$

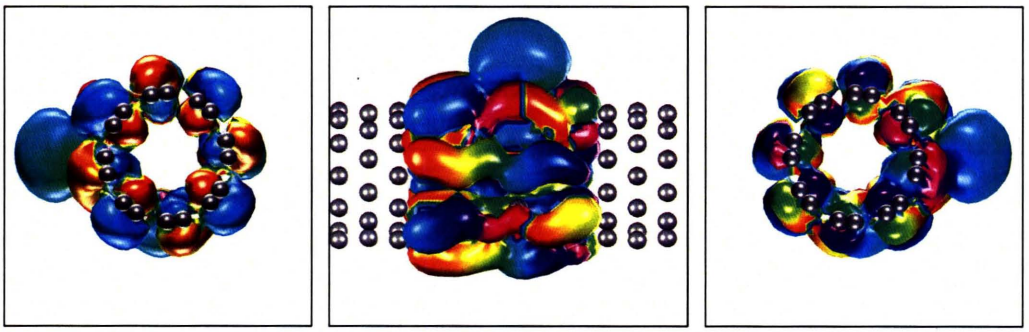

(c) Channel 2 at $E = 0$ eV, $G = 0.740G_0$

Figure 4-53: Phase-encoded conductance eigenchannel of *relaxed* CNT(4,4) with single substitutional impurity Si atom. (Three figures on each row are the left, top, and right view of the same eigenchannel at their corresponding energy level.)

To understand the finite conductance at Fermi level $E = 0$ eV and $E = 0.5$ eV, we have done the eigenchannel decomposition for both structures. The corresponding eigenchannel of unrelaxed structure at $E = 0$ eV is shown in Fig. 4-52 and the eigenchannels of relaxed structure at $E = 0$ eV and $E = 0.5$ eV are shown in Fig. 4-53. It is very clear that at Fermi level both structures have two different major eigenchannels. The channel in Fig. 4-52(a) is almost the same as the channel in Fig. 4-53(b), however the channel in Fig. 4-52(b) is different from Fig. 4-53(c) to some extent. Especially an additional large light blue bump appears at the Si atom and the phase change is less significant than the unrelaxed case, resulting in a smaller conductance less than $1G_0$. Two almost perfect transport eigenchannels in the unrelaxed structure demonstrate that around Fermi level the Si atom plays the similar role as carbon atom and it is well coupled to the Bloch states of CNT(4,4). The situation changes after relaxation and the Si atom is electronically distinguished from carbon atoms. Gradually the second channel of relaxed structure shown in Fig. 4-53(c) disappears at $E = 0.5$ eV. The only one major eigenchannel at that energy level is shown in Fig. 4-53(a), similar to Fig. 4-53(b).

The bond current distribution of each channel at two energy levels in the unrelaxed structure is shown in Fig. 4-54. The basic current topology is similar to the perfect conducting case and we did not find any significant quantum current loop except some changes of current amplitude and the current distribution around the Si atom. Similar situations happen in the relaxed structure at $E = 0.5$ eV, however it does contain clear quantum current loop in the left end of CNT at $E = 0.5$ eV with the magnetization direction pointing to the right, shown in Fig. 4-55 (b). To our knowledge, this is the first prediction of quantum current loop induced by impurity in CNT from first-principles calculations. The emergence of quantum current loop is again due to the time-reversal symmetry breaking while impurities bring the required asymmetry into the system with respect to the source-drain current. We would like to conclude that such quantum loop current should widely exist in many atomic or mesoscopic systems with either structural defects or chemical defects.

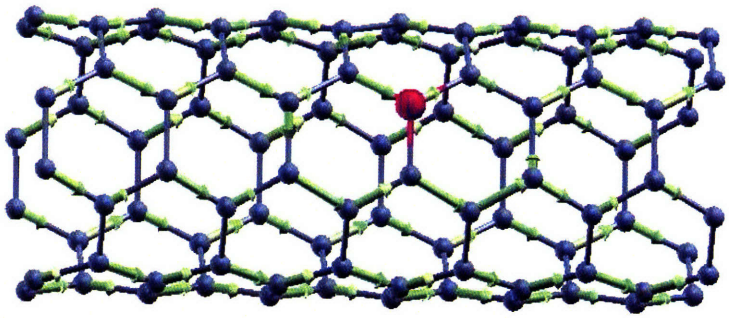

(a) Channel 1 at $E = 0$ eV

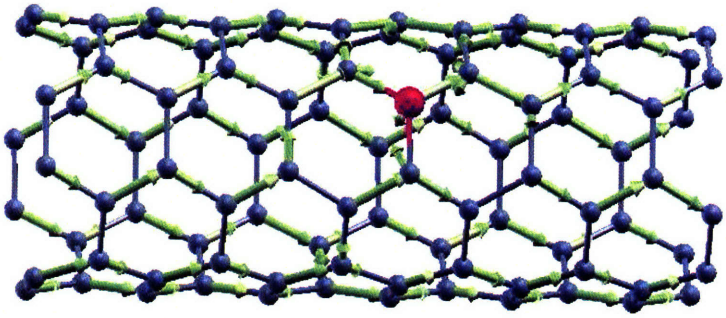

(b) Channel 2 at $E = 0$ eV

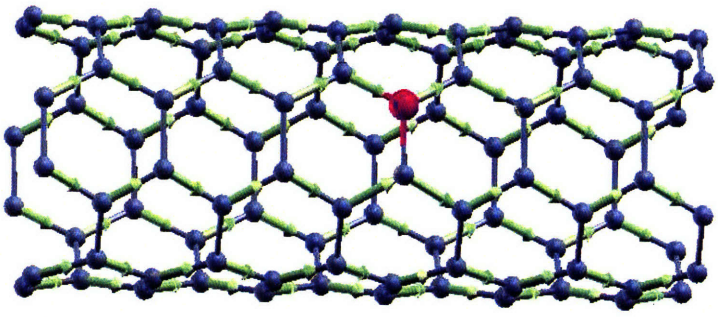

(c) Total current at $E = 0$ eV

Figure 4-54: Eigenchannel current maps of unrelaxed CNT(4,4) with single substitutional impurity Si atom.

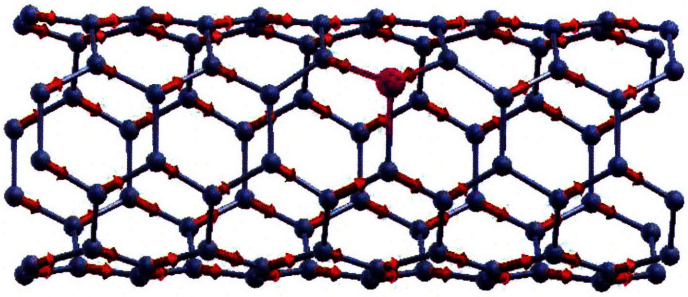

(a) Total current at $E = 0$ eV (two major channels)

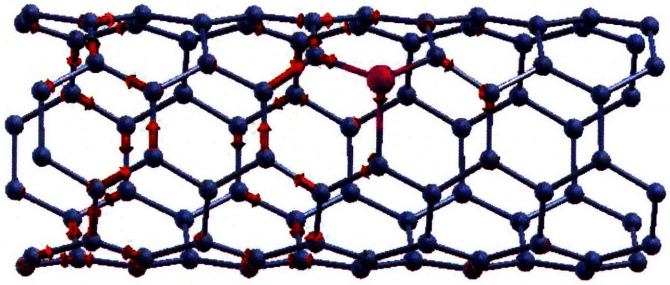

(b) Total current at $E = 0.5$ eV (1 major channel)

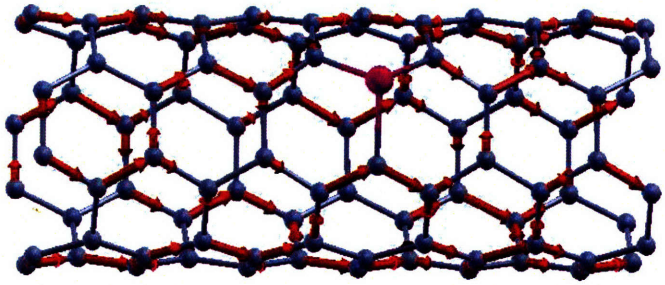

(c) Channel 1 at $E = 0$ eV

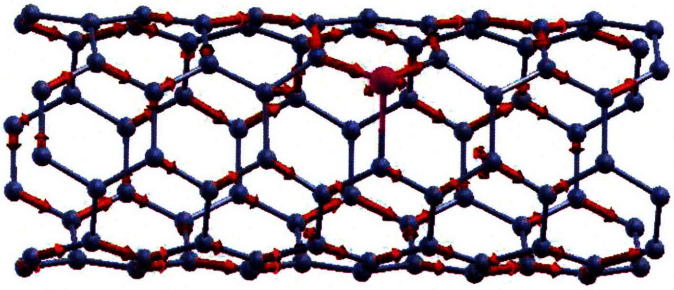

(d) Channel 2 at $E = 0$ eV

Figure 4-55: Eigenchannel current maps of relaxed CNT(4,4) with single substitutional impurity Si atom.

4.4.3 CNT(4,4) with single vacancy

Here we begin to study the role of single vacancy on the conductance of CNT(4,4). The relaxed atomic structure of CNT(4,4)-single vacancy is illustrated in Fig. 4-56. The calculated spin-dependent conductance is shown in Fig. 4-57(a). We do not find strong spin dependence of electrical conductance. However, compared to relaxed CNT(4,4)-Si, the conductance curve has a big difference in the energy range between -2 eV and 1.5 eV. That is shown in Fig. 4-57(b). From the phased-encoded eigenchannel decomposition in Fig. 4-58, we can see that the channels in Fig. 4-58(a) and Fig. 4-58(b) are the same eigenchannel at different energies while the channel in Fig. 4-58(c) disappears at $E = -0.6$ eV. This is the same channel which disappears in the relaxed CNT(4,4) with single substitutional impurity Si atom at $E = 0.5$ eV shown Fig. 4-53(c). More interestingly, here this channel shows up above Fermi level while it also shows up below Fermi level in the relaxed CNT(4,4) with single substitutional impurity Si atom.

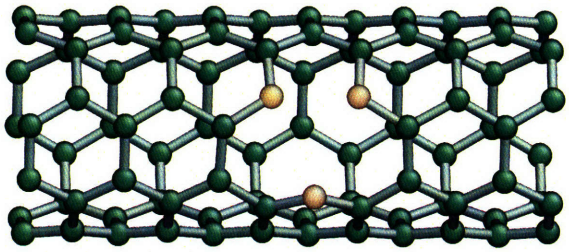

Figure 4-56: Atomic structure of relaxed CNT(4,4) with single substitutional impurity Si atom

We also plot out the bond current distribution map in Fig. 4-59. Similar to previous case, we did not find significant quantum loop current at $E = 0$ eV. However, again we find the quantum loop current at $E = -0.6$ eV surrounding the vacancy region of CNT(4,4).

Another observation of the current map in both relaxed CNT(4,4)-Si and relaxed CNT(4,4)-vacancy at $E = 0$ eV is that, although the total current from two major channels does not show significant current loop, the current map of each channel does show asymmetric current along transverse direction. It is the cancellation effect

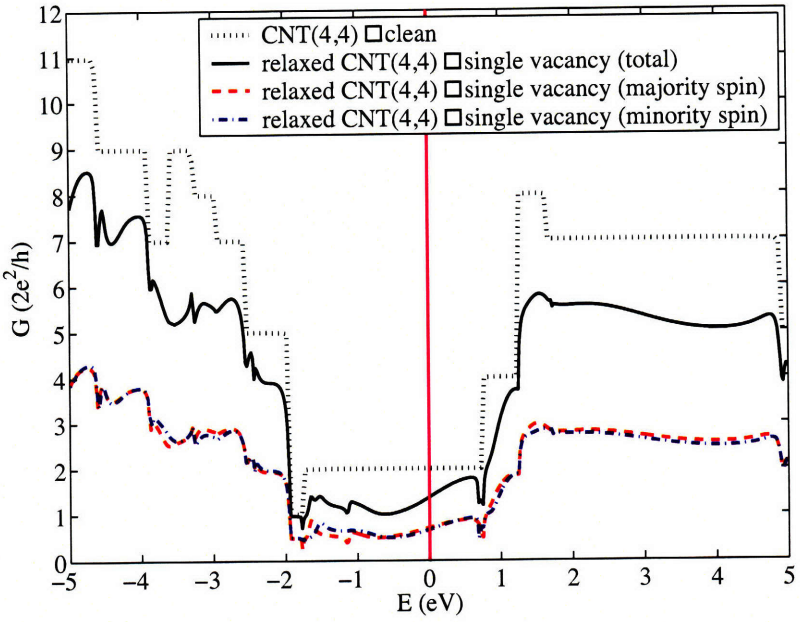

(a)

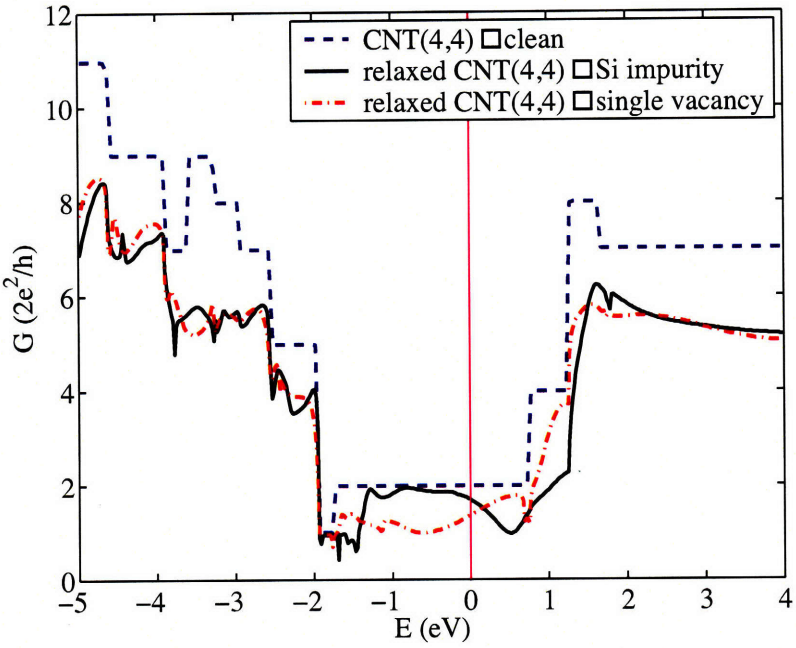

(b)

Figure 4-57: (a) Electrical conductance of relaxed CNT(4,4) with single vacancy. (b) Comparison of electrical conductance among pure CNT(4,4), relaxed CNT(4,4) with single vacancy, and relaxed CNT(4,4) with single substitutional impurity Si atom

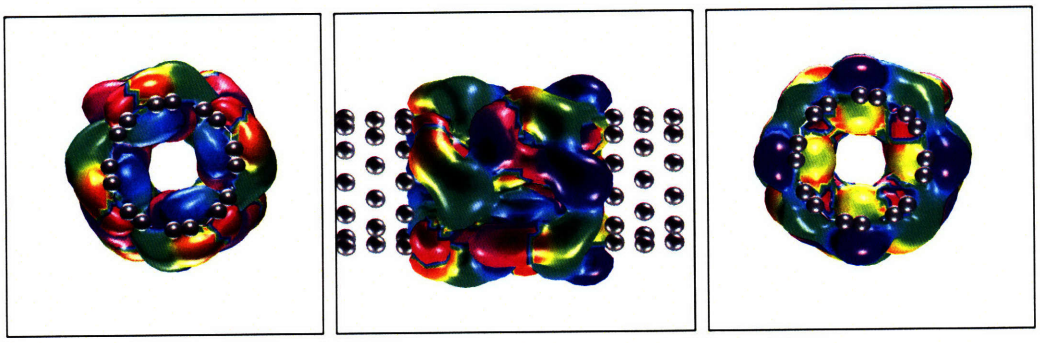

(a) Channel 1 at $E = -0.6$ eV, $G = 0.981G_0$

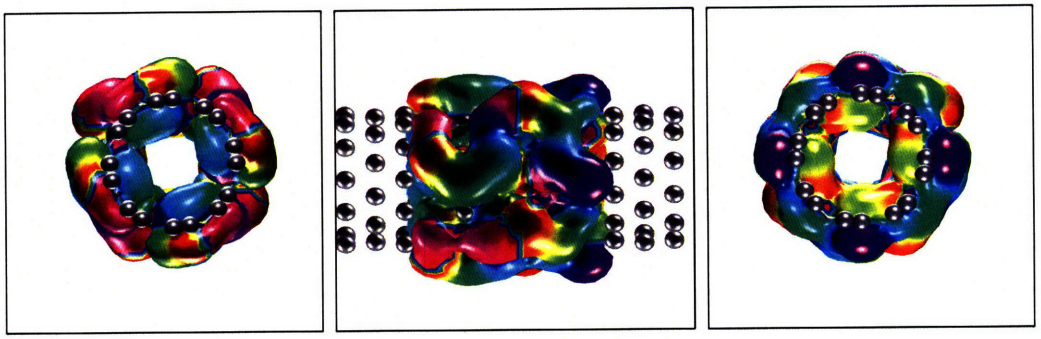

(b) Channel 1 at $E = 0$ eV, $G = 0.986G_0$

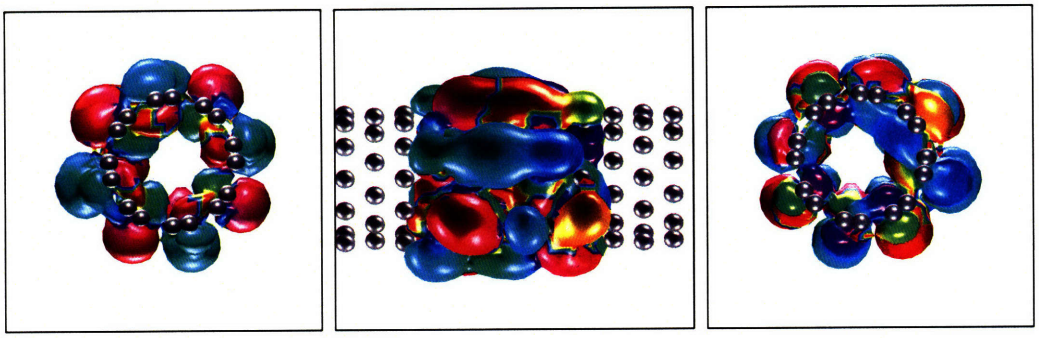

(c) Channel 2 at $E = 0$ eV, $G = 0.429G_0$

Figure 4-58: Phase-encoded conductance eigenchannel of relaxed CNT(4,4) with single vacancy. (Three figures on each row are the left, top, and right view of the same eigenchannel at their corresponding energy level.)

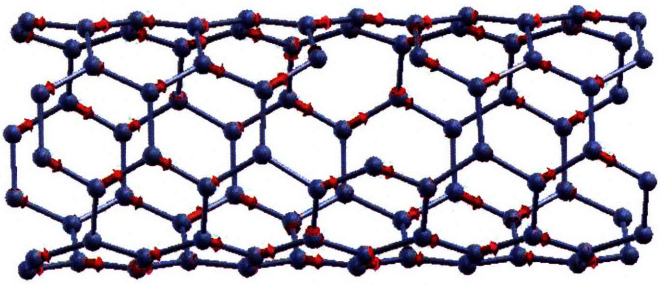

(a) Total current at $E = 0$ eV (two major channels)

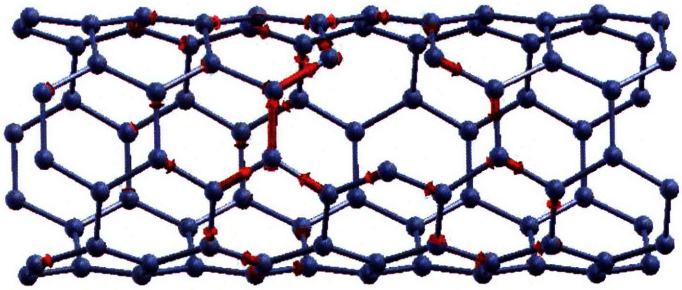

(b) Total current at $E = -0.6$ eV (one major channel)

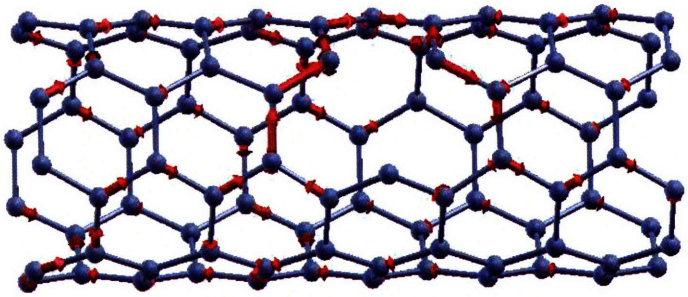

(c) Channel 1 at $E = 0$ eV

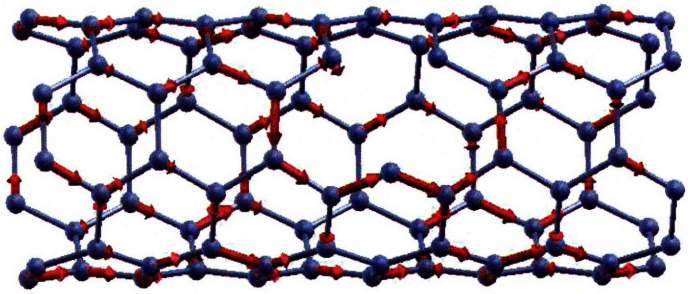

(d) Channel 2 at $E = 0$ eV

Figure 4-59: Eigenchannel current maps of relaxed CNT(4,4) with single vacancy.

which leads to the effective total current without clear quantum current loop.

More importantly, if we look at the phase-encoded eigenchannels for all three situations, unrelaxed CNT(4,4)-Si, relaxed CNT(4,4)-Si, and relaxed CNT(4,4) with single vacancy, we immediately find the reason why the second channel will disappear while the first channel always exists. The shape of the first conductance eigenchannel in all the three cases are intrinsically like *large armchairs*, which provides a smart way to bypass the effect of Si atom or single vacancy. However the second channel is a direct and small armchair-like channel, which is easily broken when it encounters relaxed single Si atom or relaxed single vacancy. This is a remarkable microscopic view of the robustness of conducting channels in nanoscale electronics, which, to our knowledge, has not been mentioned before.

4.5 Summary

In this chapter, we have shown several examples of electron transport in zero dimensional and one dimensional molecular and nanoscale electronics. Resonant transport is widely observed in several molecular electronic systems and those resonant peaks are due to the coupling between various *discrete* molecular level and continuous states in metal leads. We found that the typical confined aluminum wires have remarkable spin-dependent conductance because of local magnetic moment formation. We predict that such spin-dependent transport should widely exist in confined systems. More strikingly, the phase-encoded conductance eigenchannel gives a direct and visual understanding of electron transport. In one limit, it shows the static standing wave with complete refection while in the other limit it gives perfect phase-oscillation with complete transmission. We further explore electron transport in phenalenyl molecule and carbon nanotube with and without defects. In these systems, quantum loop currents are found due to time-reversal symmetry breaking and the asymmetry between the conductor geometry and source-drain current. We predict that source-drain current could introduce much larger local loop current in defected or disordered systems with asymmetric current paths, leading to the induced local magnetic fields.

Chapter 5

Electrical conductance from TDDFT

Green's function (GF) method has achieved many successes in describing electron transport at the meso [54, 55] and molecular [57, 58, 59, 62, 63] scales, issues such as dynamical electron correlation and large electron-phonon coupling effects [65, 66] are far from fully resolved. It is therefore desirable to exploit alternative approaches [230, 193, 231, 232, 233, 234, 235, 128, 236] for comparison with the mainstream GF calculations. In this chapter, we describe a step[128] towards this goal by computing how an electron propagates through a molecular junction in real time, based on the time-dependent density functional theory [36] (TDDFT).

5.1 Introduction

Density functional theory (DFT) [5] with the Kohn-Sham reference kinetic energy functional of a fictitious non-interacting electron system [6] is a leading method for treating many electrons in solids and molecules. [7]. While initially formulated to describe only the electronic ground state [5, 6], it has been rigorously extended by Runge and Gross [36] to treat time-dependent driven systems (excited states). TDDFT is therefore a natural theoretical platform for studying electron conduction at the nanoscale. There are two flavors in which TDDFT is implemented. One is direct

numerical integration [37, 38, 39, 40, 41, 42, 237] of the time-dependent Kohn-Sham (TDKS) equations. The other is a *Gedanken experiment* of the former with an added assumption of infinitesimal time-dependent perturbation, so a linear response function may be first derived in closed form [43, 44, 45, 237], which is then evaluated numerically. These two implementations should give exactly the same result when the external perturbation field is infinitesimal. The latter implementation can be computationally more efficient once the linear-response function has been analytically derived, while the former can treat non-infinitesimal perturbations and arbitrary initial states.

Presently, most electronic conductance calculations based on the Landauer transmission formalism [68, 69] have assumed a static molecular geometry. In the Landauer picture, dissipation of the conducting electron energy is assumed to take place in the metallic leads (electron reservoirs), not in the narrow molecular junction (channel) itself. [71] Inelastic scattering, however, does occur in the molecular junctions themselves, the effects appearing as peaks or dips in the measured inelastic electron tunneling spectra (IETS) [214] at molecular vibrational eigen-frequencies. Since heating is always an important concern for high-density electronics, and because molecular junctions tend to be mechanically more fragile compared to larger, semiconductor-based devices, the issue of electron-phonon coupling warrants detailed calculations [214, 215] (here we use the word phonon to denote general vibrations when there is no translational symmetry). In the case of long π-conjugated polymer chain junctions, strong electron-phonon coupling may even lead to elementary excitations and spin or charge carriers, called soliton/polaron [65, 66, 238, 239, 240], where the electronic excitation is so entangled with phonon excitation that separation is no longer possible.

In view of the above background, there is a need for efficient TDDFT implementations that can treat complex electron-electron and electron-phonon interactions in the time domain. Linear-response type analytic derivations can become very cumbersome, and for some problems [241] may be entirely infeasible. A direct time-stepping method [37, 38, 39, 40, 42, 41] analogous to molecular dynamics for electrons as well

as ions may be more flexible and intuitive in treating some of these highly complex and coupled problems, *if* the computational costs can be managed. Such a direct time-stepping code also can be used to double-check the correctness of analytic approaches such as the non-equilibrium Green's function (NEGF) method and electron-phonon scattering calculations [214, 215], most of which explicitly or implicitly use the same set of TDDFT approximations (most often an adiabatic approximation such as TDLDA).

We note that similar to surface catalysis problems, metal-molecule interaction at contact is the key for electron conduction across molecular junctions. Therefore it seems reasonable to explore how TDDFT, specifically TDKS under the adiabatic approximation, performs in the USPP/PAW framework, which may achieve similar cost-performance benefits. This is the main distinction between our approach and the software package Octopus [40, 42], a ground-breaking TDDFT program with direct time stepping, but which uses norm-conserving Troullier-Martins (TM) pseudopotentials [242], and real-space grids. We will address the theoretical formulation of TD-USPP (TD-PAW) in sec. 5.2, and the numerical implementation of TD-USPP in the direct time-stepping flavor in sec. 5.3.

To validate that the direct time-integration USPP-TDDFT algorithm indeed works, we calculate the optical absorption spectra of sodium dimer and benzene molecule in sec. 5.4 and compare them with experimental results and other TDLDA calculations. As an application, we perform a computer experiment in sec. 5.5 which is a verbatim implementation of the original Landauer picture [69, 71]. An electron wave pack comes from the left metallic lead (1D Au chain) with an energy that is exactly the Fermi energy of the metal (the Fermi electron), and undergoes scattering by the molecular junction (benzene-(1,4)-dithiolate, or BDT). The probability of electron transmission is carefully analyzed in density vs. $(\mathbf{x}, t)$ plots. The point of this exercise is to check the stability and accuracy of the time integrator, rather than to obtain new results about the Au-BDT-Au junction conductance. We check the transmission probability thus obtained with simple estimate from complex band structure calculations [220, 221], and Green's function calculations at small bias volt-

ages. Both seem to be consistent with our calculations. In sec. 5.6, we give a detailed comparison between the result from TDDFT and the result from Green's function method. Especially we will show the similar electron propagation channels in both cases. Lastly, we give a brief summary in sec. 5.7.

5.2 TDDFT formalism with ultrasoft pseudopotentials

We have reviewed the basic formalism of ultrasoft pseudopotentials in Chap. 1. To extend the ground-state USPP formalism to the time-dependent case, we note that the $\hat{S}$ operator in (1.139) depends on the ionic positions $\{\mathbf{X}_I\}$ only and *not* on the electronic charge density. In the case that the ions are not moving, the following dynamical equations are equivalent:

$$\hat{H}(t)\psi_n(t) = i\hbar\partial_t(\hat{S}\psi_n(t)) = \hat{S}(i\hbar\partial_t\psi_n(t)), \tag{5.1}$$

whereby we have replaced the ε_n in (1.139) by the $i\hbar\partial_t$ operator, and $\hat{H}(t)$ is updated using the time-dependent $\rho(\mathbf{x}, t)$. However when the ions are moving,

$$i\hbar\partial_t\hat{S} \neq \hat{S}(i\hbar\partial_t) \tag{5.2}$$

with difference proportional to the ionic velocities. To resolve this ambiguity, we note that $\hat{S}$ can be split as

$$\hat{S} = (\hat{S}^{1/2}\hat{U})(\hat{U}^\dagger\hat{S}^{1/2}), \tag{5.3}$$

where $\hat{U}$ is a unitary operator, $\hat{U}\hat{U}^\dagger = \hat{I}$, and we can rewrite (1.139) as

$$(\hat{U}^\dagger\hat{S}^{-1/2})\hat{H}(\hat{S}^{-1/2}\hat{U})(\hat{U}^\dagger\hat{S}^{1/2})\psi_n = \varepsilon_n(\hat{U}^\dagger\hat{S}^{1/2})\psi_n. \tag{5.4}$$

Referring to the PAW formulation [28], we can select $\hat{U}$ such that $\hat{U}^\dagger \hat{S}^{1/2}$ is the PAW transformation operator

$$\hat{U}^\dagger \hat{S}^{1/2} = \hat{T} \equiv 1 + \sum_{i,I} (|\tilde{\psi}_i^I\rangle - |\psi_i^I\rangle)\langle \beta_i^I| : \quad \tilde{\psi}_n = \hat{T}\psi_n, \tag{5.5}$$

that maps the pseudowavefunction to the true wavefunction. So we can rewrite (5.4) as,

$$(\hat{U}^\dagger \hat{S}^{-1/2})\hat{H}(\hat{S}^{-1/2}\hat{U})\tilde{\psi}_n \equiv \hat{\tilde{H}}\tilde{\psi}_n = \varepsilon_n \tilde{\psi}_n, \tag{5.6}$$

where $\hat{\tilde{H}}$ is then the true all-electron Hamiltonian (with core-level electrons frozen). In the all-electron TDDFT procedure, the above ε_n is replaced by the $i\hbar\partial_t$ operator. It is thus clear that a physically meaningful TD-USPP equation in the case of moving ions should be

$$(\hat{U}^\dagger \hat{S}^{-1/2})\hat{H}(\hat{S}^{-1/2}\hat{U})(\hat{U}^\dagger \hat{S}^{1/2})\psi_n = i\hbar\partial_t((\hat{U}^\dagger \hat{S}^{1/2})\psi_n), \tag{5.7}$$

or

$$(\hat{U}^\dagger \hat{S}^{-1/2})\hat{H}\psi_n = i\hbar\partial_t((\hat{U}^\dagger \hat{S}^{1/2})\psi_n). \tag{5.8}$$

In the equivalent PAW notation, it is simply,

$$(\hat{T}^\dagger)^{-1}\hat{H}\psi_n = i\hbar\partial_t(\hat{T}\psi_n). \tag{5.9}$$

Or, in pseudized form amenable to numerical calculations,

$$\hat{H}\psi_n = i\hbar\hat{T}^\dagger(\partial_t(\hat{T}\psi_n)) = i\hbar(\hat{T}^\dagger\hat{T}(\partial_t\psi_n) + \hat{T}^\dagger(\partial_t\hat{T})\psi_n). \tag{5.10}$$

Differentiating (5.5), there is,

$$\partial_t\hat{T} = \sum_{i,I}\left(\frac{\partial(|\tilde{\psi}_i^I\rangle - |\psi_i^I\rangle)}{\partial \mathbf{X}_I}\langle\beta_i^I| + (|\tilde{\psi}_i^I\rangle - |\psi_i^I\rangle)\frac{\partial\langle\beta_i^I|}{\partial \mathbf{X}_I}\right)\cdot\dot{\mathbf{X}}_I, \tag{5.11}$$

and so we can define and calculate

$$\hat{P} \equiv -i\hbar\hat{T}^{\dagger}(\partial_t\hat{T}) = \sum_I \hat{\mathbf{P}}^I \cdot \dot{\mathbf{X}}_I \tag{5.12}$$

operator, similar to analytic force calculation [27], where

$$\hat{\mathbf{P}}^I \equiv -i\hbar\hat{T}^{\dagger}\sum_i \left(\frac{\partial(|\tilde{\psi}_i^I\rangle - |\psi_i^I\rangle)}{\partial \mathbf{X}_I}\langle\beta_i^I| + (|\tilde{\psi}_i^I\rangle - |\psi_i^I\rangle)\frac{\partial\langle\beta_i^I|}{\partial \mathbf{X}_I} \right). \tag{5.13}$$

The TD-USPP / TD-PAW equation therefore can be rearranged as,

$$(\hat{H} + \hat{P})\psi_n = i\hbar\hat{S}(\partial_t\psi_n), \tag{5.14}$$

with $\hat{P}$ proportional to the ionic velocities. It is basically the same as traditional TDDFT equation, but taking into account the moving spatial "gauge" due to ion motion. As such it can be used to model electron-phonon coupling [215], cluster dynamics under strong laser field [241], etc., as long as the pseudopotential cores are not overlapping, and the core-level electrons are not excited.

At each timestep, one should update $\rho(\mathbf{x}, t)$ as

$$\rho(\mathbf{x}, t) = \sum_n \left\{ |\psi_n(\mathbf{x}, t)|^2 + \sum_{i,j,I} Q_{ji}^I(\mathbf{x})\langle\psi_n(t)|\beta_j^I\rangle\langle\beta_i^I|\psi_n(t)\rangle \right\} f_n. \tag{5.15}$$

Note that while $\psi_n(\mathbf{x}, t = 0)$ may be an eigenstate if we start from the ground-state wavefunctions, $\psi_n(\mathbf{x}, t > 0)$ generally is no longer so with the external field turned on. n is therefore merely used as a label based on the initial state rather than an eigenstate label at $t > 0$. f_n on the other hand always maintains its initial value, $f_n(t) = f_n(0)$, for a particular simulation run.

One may define projection operator $\hat{t}_I$ belonging to atom I:

$$\hat{t}_I \equiv \sum_i (|\tilde{\psi}_i^I\rangle - |\psi_i^I\rangle)\langle\beta_i^I|. \tag{5.16}$$

$\hat{t}_I$ spatially has finite support, and so is

$$\frac{\partial \hat{t}_I}{\partial \mathbf{X}_I} = -\frac{\partial \hat{t}_I}{\partial \mathbf{x}} = -\frac{\partial (1+\hat{t}_I)}{\partial \mathbf{x}} = (1+\hat{t}_I)\nabla - \nabla(1+\hat{t}_I). \tag{5.17}$$

Therefore $\hat{\mathbf{P}}^I$ in (5.12) is,

$$\begin{aligned}
\hat{\mathbf{P}}^I &= -i\hbar \hat{T}^\dagger \frac{\partial \hat{t}_I}{\partial \mathbf{X}_I} \\
&= -i\hbar(1+\hat{t}_I^\dagger)\frac{\partial \hat{t}_I}{\partial \mathbf{X}_I} \\
&= -i\hbar(1+\hat{t}_I^\dagger)((1+\hat{t}_I)\nabla - \nabla(1+\hat{t}_I)) \\
&= (1+\hat{t}_I^\dagger)(1+\hat{t}_I)\mathbf{p} - (1+\hat{t}_I^\dagger)\mathbf{p}(1+\hat{t}_I),
\end{aligned} \tag{5.18}$$

where $\mathbf{p}$ is the electron momentum operator. Unfortunately $\hat{\mathbf{P}}^I$ and therefore $\hat{P}$ are not Hermitian operators. This means that the numerical algorithm for integrating (5.14) may be different from the special case of immobile ions:

$$\hat{H}(t)\psi_n \;=\; i\hbar \hat{S}(\partial_t \psi_n). \tag{5.19}$$

Even if the same time-stepping algorithm is used, the error estimates would be different. In section III we discuss algorithms for integrating (5.19) only, and postpone detailed discussion of integration algorithm and error estimates for coupled ion-electron dynamics (5.14) under USPP to a later development.

5.3 Time-stepping algorithms in the case of immobile ions

In this section we focus on the important limiting case of (5.19), where the ions are immobile or can be approximated as immobile. We may rewrite (5.19) formally as

$$\hat{S}^{-1/2}\hat{H}(t)\hat{S}^{-1/2}(\hat{S}^{1/2}\psi_n) \;=\; i\hbar\partial_t(\hat{S}^{1/2}\psi_n). \tag{5.20}$$

And so the time evolution of (5.19) can be formally expressed as

$$\psi_n(t) \;=\; \hat{S}^{-1/2}\hat{\mathcal{T}}\left[\exp\left(-\frac{i}{\hbar}\int_0^t dt'\hat{S}^{-1/2}\hat{H}(t')\hat{S}^{-1/2}\right)\right]\hat{S}^{1/2}\psi_n(0), \tag{5.21}$$

with $\hat{\mathcal{T}}$ the time-ordering operator. Algebraic expansions of different order are then performed on the above propagator, leading to various numerical time-stepping algorithms.

5.3.1 First-order implicit Euler integration scheme

To first-order accuracy in time there are two well-known propagation algorithms, namely, the explicit (forward) Euler

$$i\hbar\hat{S}\frac{\psi_n(t+\Delta t)-\psi_n(t)}{\Delta t} = \hat{H}\psi_n(\mathbf{x},t) \tag{5.22}$$

and implicit (backward) Euler

$$i\hbar\hat{S}\frac{\psi_n(t+\Delta t)-\psi_n(\mathbf{x},t)}{\Delta t} = \hat{H}\psi_n(t+\Delta t) \tag{5.23}$$

schemes. Although the explicit scheme (5.22) is less expensive computationally, our test runs indicate that it always diverges numerically. The reason is that (5.19) has poles on the imaginary axis, which are marginally outside of the stability domain ($\mathrm{Re}(z\Delta t) < 0$) of the explicit algorithm. Therefore only the implicit algorithm can be used, which upon rearrangement is,

$$\left[\hat{S}+\frac{i}{\hbar}\hat{H}\Delta t\right]\psi_n(t+\Delta t) = \hat{S}\psi_n(t). \tag{5.24}$$

In the above, we still have the choice of whether to use $\hat{H}(t)$ or $\hat{H}(t+\Delta t)$. Since this is a first-order algorithm, neither choice would influence the order of the local truncation error. Through numerical tests we found that the implicit time differentiation in (5.23) already imparts sufficient stability that the $\hat{H}(t+\Delta t)$ operator is not needed.

Therefore we will solve

$$\left[\hat{S} + \frac{i}{\hbar}\hat{H}(t)\Delta t\right]\psi_n(t+\Delta t) = \hat{S}\psi_n(t) \tag{5.25}$$

at each timestep. Direct inversion turns out to be computationally infeasible in large-scale planewave calculations. We solve (5.25) iteratively using matrix-free linear equation solvers such as the conjugate gradient method. Starting from the wavefunction of a previous timestep, we find that typically it takes about three to five conjugate gradient steps to achieve sufficiently convergent update.

One serious drawback of this algorithm is that norm conservation of the wavefunction

$$\langle\psi_n(t+\Delta t)|\hat{S}|\psi_n(t+\Delta t)\rangle \;=\; \langle\psi_n(t)|\hat{S}|\psi_n(t)\rangle \tag{5.26}$$

is not satisfied exactly, even if there is perfect floating-point operation accuracy. So one has to renormalize the wavefunction after several timesteps.

5.3.2 First-order Crank-Nicolson integration scheme

We find the following Crank-Nicolson expansion [243, 244, 42] of propagator (5.21)

$$\hat{S}^{\frac{1}{2}}\psi_n(t+\Delta t) = \frac{1 - \frac{i}{2\hbar}\hat{S}^{-\frac{1}{2}}\hat{H}(t)\hat{S}^{-\frac{1}{2}}\Delta t}{1 + \frac{i}{2\hbar}\hat{S}^{-\frac{1}{2}}\hat{H}(t)\hat{S}^{-\frac{1}{2}}\Delta t}\hat{S}^{\frac{1}{2}}\psi_n(t) \tag{5.27}$$

stable enough for practical use. The norm of the wavefunction is conserved explicitly in the absence of roundoff errors, because of the spectral identity

$$\left\|\frac{1 - \frac{i}{2\hbar}\hat{S}^{-\frac{1}{2}}\hat{H}\hat{S}^{-\frac{1}{2}}\Delta t}{1 + \frac{i}{2\hbar}\hat{S}^{-\frac{1}{2}}\hat{H}\hat{S}^{-\frac{1}{2}}\Delta t}\right\| = 1. \tag{5.28}$$

Therefore (5.26) is satisfied in an ideal numerical computation, and in practice one does not have to renormalize the wavefunctions in thousands of timesteps.

Writing out the (5.27) expansion explicitly, we have:

$$\left[\hat{S} + \frac{i}{2\hbar}\hat{H}(t)\Delta t\right]\psi_n(t+\Delta t) = \left[\hat{S} - \frac{i}{2\hbar}\hat{H}(t)\Delta t\right]\psi_n(t). \tag{5.29}$$

Similar to (5.25), we solve Eq. (5.29) using the conjugate gradient linear equations solver. This algorithm is still first-order because we use $\hat{H}(t)$, not $(\hat{H}(t)+\hat{H}(t+\Delta t))/2$, in (5.29). In the limiting case of time-invariant charge density, $\rho(\mathbf{x},t) = \rho(\mathbf{x},0)$ and $\hat{H}(t+\Delta t) = \hat{H}(t)$, the algorithm has second-order accuracy. This may happen if there is no external perturbation and we are simply testing whether the algorithm is stable in maintaining the eigenstate phase oscillation: $\psi_n(t) = \psi_n(0)e^{-i\omega t}$, or in the case of propagating a test electron, which carries an infinitesimal charge and would not perturb $\hat{H}(t)$.

5.3.3 Second-order Crank-Nicolson integration scheme

We note that replacing $\hat{H}(t)$ by $(\hat{H}(t)+\hat{H}(t+\Delta t))/2$ in (5.27) would enhance the local truncation error to second order, while still maintaining norm conservation. In practice we of course do not know $\hat{H}(t+\Delta t)$ exactly, which depends on $\rho(t+\Delta t)$ and therefore $\psi_n(t+\Delta t)$. However a sufficiently accurate estimate of $\rho(t+\Delta t)$ can be obtained by running (5.29) first for one step, from which we can get:

$$\rho'(t+\Delta t) = \rho(t+\Delta t)+\mathcal{O}(\Delta t^2), \quad \hat{H}'(t+\Delta t) = \hat{H}(t+\Delta t)+\mathcal{O}(\Delta t^2). \tag{5.30}$$

After this "predictor" step, we can solve:

$$\left[\hat{S}+\frac{i(\hat{H}(t)+\hat{H}'(t+\Delta t))\Delta t}{4\hbar}\right]\psi_n(t+\Delta t) = \left[\hat{S}-\frac{i(\hat{H}(t)+\hat{H}'(t+\Delta t))\Delta t}{4\hbar}\right]\psi_n(t), \tag{5.31}$$

to get the more accurate, second-order estimate for $\psi_n(t+\Delta t)$, that also satisfies (5.26).

5.4 Optical absorption spectra

Calculating the optical absorption spectra of molecules, clusters and solids is one of the most important applications of TDDFT [245, 43, 44, 37, 38, 39, 246, 40, 41, 247]. Since many experimental and standard TDLDA results are available for comparison,

we compute the spectra for sodium dimer (Na_2) and benzene molecule (C_6H_6) to validate our direct time-stepping USPP-TDDFT scheme.

We adopt the method by Bertsch *et al.* [37, 246] whereby an impulse electric field $\mathbf{E}(t) = \epsilon\hbar\hat{\mathbf{k}}\delta(t)/e$ is applied to the system at $t = 0$, where $\hat{\mathbf{k}}$ is unit vector and ϵ is a small quantity. The system, which is at its ground state at $t = 0^-$, would undergo transformation

$$\tilde{\psi}_n(\mathbf{x}, t = 0^+) \;=\; e^{i\epsilon\hat{\mathbf{k}}\cdot\mathbf{x}}\tilde{\psi}_n(\mathbf{x}, t = 0^-), \tag{5.32}$$

for all its occupied electronic states, $n = 1..N$, at $t = 0^+$. Note that the true, unpseudized wavefunctions should be used in (5.32) if theoretical rigor is to be maintained.

One may then evolve $\{\tilde{\psi}_n(\mathbf{x}, t), n = 1..N\}$ using a time stepper, with the total charge density $\rho(\mathbf{x}, t)$ updated at every step. The electric dipole moment $\mathbf{d}(t)$ is calculated as

$$\mathbf{d}(t) \;=\; e\int d^3\mathbf{x}\rho(\mathbf{x}, t)\mathbf{x}. \tag{5.33}$$

In a supercell calculation one needs to be careful to have a large enough vacuum region surrounding the molecule at the center, so no significant charge density can "spill over" the PBC boundary, thus causing a spurious discontinuity in $\mathbf{d}(t)$.

The dipole strength tensor $\mathbf{S}(\omega)$ can be computed by

$$\mathbf{S}(\omega)\hat{\mathbf{k}} \;=\; \mathbf{m}(\omega) \equiv \frac{2m_e\omega}{e\hbar\pi}\lim_{\epsilon,\gamma\to 0}\frac{1}{\epsilon}\int_0^\infty dt\sin(\omega t)e^{-\gamma t^2}[\mathbf{d}(t) - \mathbf{d}(0)], \tag{5.34}$$

where γ is a small damping factor and m_e is the electron mass. In reality, the time integration is truncated at t_f, and γ should be chosen such that $e^{-\gamma t_\mathrm{f}^2} \ll 1$. The merit of this and similar time-stepping approaches [46] is that the entire spectrum can be obtained from just one calculation.

For a molecule with no symmetry, one needs to carry out Eq. (5.32) with subsequent time integration for three independent $\hat{\mathbf{k}}$'s: $\hat{\mathbf{k}}_1, \hat{\mathbf{k}}_2, \hat{\mathbf{k}}_3$, and obtain three different $\mathbf{m}_1(\omega), \mathbf{m}_2(\omega), \mathbf{m}_3(\omega)$ on the right-hand side of Eq. (5.34). One then solves the matrix

equation:

$$\mathbf{S}(\omega)[\hat{\mathbf{k}}_1\ \hat{\mathbf{k}}_2\ \hat{\mathbf{k}}_3] = [\mathbf{m}_1(\omega)\ \mathbf{m}_2(\omega)\ \mathbf{m}_3(\omega)] \tag{5.35}$$

$$\rightarrow\ \mathbf{S}(\omega) = [\mathbf{m}_1(\omega)\ \mathbf{m}_2(\omega)\ \mathbf{m}_3(\omega)][\hat{\mathbf{k}}_1\ \hat{\mathbf{k}}_2\ \hat{\mathbf{k}}_3]^{-1}. \tag{5.36}$$

$\mathbf{S}(\omega)$ satisfies the Thomas-Reiche-Kuhn f-sum rule,

$$N\delta_{ij} = \int_0^\infty d\omega S_{ij}(\omega). \tag{5.37}$$

For gas-phase systems where the orientation of the molecule or cluster is random, the isotropic average of $\mathbf{S}(\omega)$

$$S(\omega) \equiv \frac{1}{3}\mathrm{Tr}\mathbf{S}(\omega) \tag{5.38}$$

may be calculated and plotted.

In actual calculations employing norm-conserving pseudopotentials [40], the pseudo-wavefunctions $\psi_n(\mathbf{x}, t)$ are used in (5.32) instead of the true wavefunctions. And so the oscillator strength $\mathbf{S}(\omega)$ obtained is not formally exact. However, the f-sum rule Eq. (5.37) is still satisfied exactly. With the USPP/PAW formalism [25, 26, 27, 28], formally we should solve

$$\hat{T}\psi_n(\mathbf{x}, t = 0^+) = e^{i\epsilon\hat{\mathbf{k}}\cdot\mathbf{x}}\hat{T}\psi_n(\mathbf{x}, t = 0^-), \tag{5.39}$$

using linear equation solver to get $\psi_n(\mathbf{x}, t = 0^+)$, and then propagate $\psi_n(\mathbf{x}, t)$. However, for the present work we skip this step, and replace $\tilde{\psi}_n$ by ψ_n in (5.32) directly. This "quick-and-dirty fix" makes the oscillator strength not exact and also breaks the sum rule slightly. However, the peak positions are still correct.

For the Na_2 molecule, we use the norm-conserving TM pseudopotential, treated as a special case ($\hat{S} = 1$) in our USPP-TDDFT code. The supercell is a tetragonal box of $12 \times 10 \times 10$ $\mathrm{\AA}^3$ and the Na_2 cluster is along the x-direction with a bond length of 3.0 Å. The planewave basis has a kinetic energy cutoff of 300 eV. The time integration is carried out for $10,000$ steps with a timestep of $\Delta t = 1.97$ attoseconds,

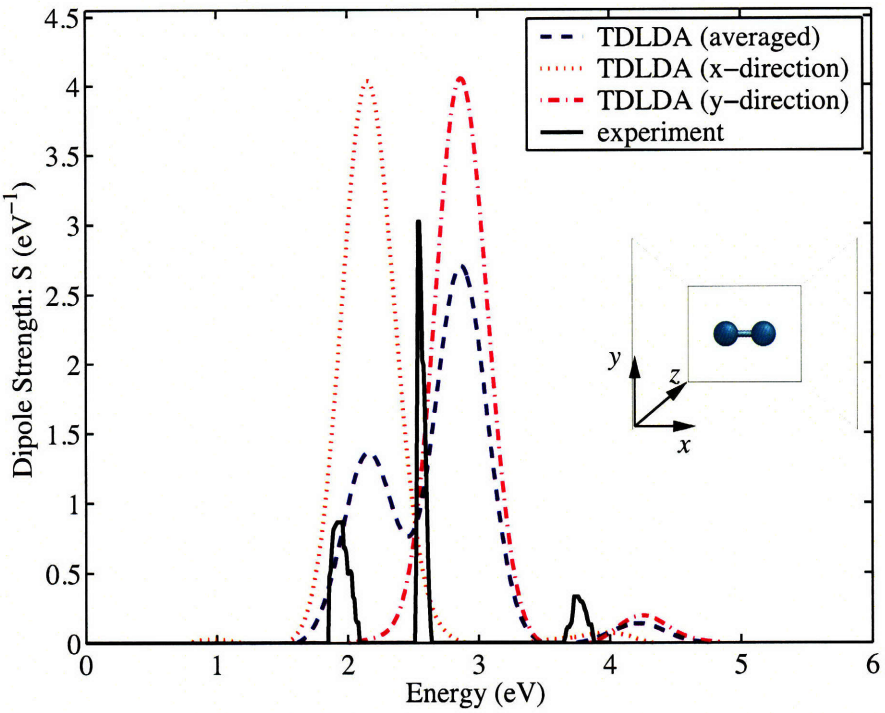

Figure 5-1: Optical absorption spectra of Na_2 cluster obtained from direct time-stepping TDLDA calculation using norm-conserving TM pseudopotentials. The results should be compared with Fig. 1 of Marques et al. [246].

and $\epsilon = 0.01/\text{Å}$, $\gamma = 0.02\text{eV}^2/\hbar^2$. In the dipole strength plot (Fig. 5-1), the three peaks agree very well with TDLDA result from Octopus [246], and differ by ~ 0.4 eV from the experimental peaks [248, 249, 246]. In this case, the f-sum rule is verified to be satisfied to within 0.1% numerically.

For the benzene molecule, ultrasoft pseudopotentials are used for both carbon and hydrogen atoms. The calculation is performed in a tetragonal box of $12.94 \times 10 \times 7$ Å^3 with the benzene molecule placed on the $x-y$ plane. The C-C bond length is 1.39 Å and the C-H bond length is 1.1 Å. The kinetic energy cutoff is 250 eV, $\epsilon = 0.01/\text{Å}$, $\gamma = 0.1\text{eV}^2/\hbar^2$, and the time integration is carried out for 5000 steps with a timestep of $\Delta t = 2.37$ attoseconds. In the dipole strength function plot (Fig. 5-2), the peak at 6.95 eV represents the $\pi \rightarrow \pi^*$ transition and the broad peak above 9 eV corresponds to the $\sigma \rightarrow \sigma^*$ transition. The dipole strength function agrees very well with other TDLDA calculations [38, 40] and experiment [250]. The slight difference is mostly due

to our *ad hoc* approximation that ψ_n's instead of $\tilde{\psi}_n$'s are used in (5.32). The more formally rigorous implementation of the electric impulse perturbation, Eq. (5.39), will be performed in future work.

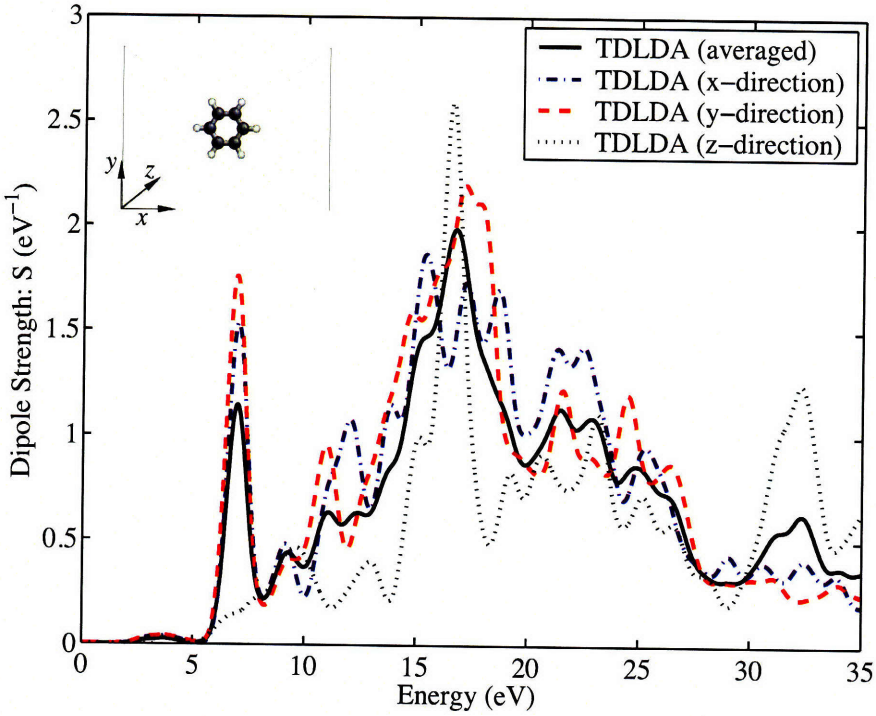

Figure 5-2: Optical absorption spectrum of benzene (C_6H_6) molecule. The results should be compared with Fig. 2 of Marques et al. [40]

In this section we have verified the soundness of our time stepper with planewave basis through two examples of explicit electronic dynamics, where the charge density and effective potential are updated at every timestep, employing both norm-conserving and ultrasoft pseudopotentials. This validation is important for the following non-perturbative propagation of electrons in more complex systems. Recently Walker and Gebauer [251] combined the USPP-TDDFT scheme [128] and the closed form of linear response function [43, 44, 45] based on Lanczos algorithms[252], and they demonstrated that USPP-based TDDFT calculations benefit not only from the smaller size of plane-wave basis-set but also from the faster convergence. Their method has been used to efficiently calculate optical absorption spectra of the fullerene C_{60}. However, it should be emphasized that the real-time propagation method can

treat non-infinitesimal perturbations and arbitrary initial states, which is not true for linear-response method.

5.5 Fermi electron transmission

We first briefly review the setup of the Landauer transmission equation, [68, 69, 71] before performing an explicit TDDFT simulation. In its simplest form, two identical metallic leads (see Fig. (5-3)) are connected to a device. The metallic lead is so narrow in y and z that only one channel (lowest quantum number in the y, z quantum well) needs to be considered. In the language of band structure, this means that one and only one branch of the 1D band structure crosses the Fermi level $E_{\rm F}$ for $k_x > 0$. Analogous to the universal density of states expression $dN = 2\Omega dk_x dk_y dk_z/(2\pi)^3$ for 3D bulk metals, where Ω is the volume and the factor of 2 accounts for up- and down-spins, the density of state of such 1D system is simply

$$dN = \frac{2Ldk_x}{2\pi}. \tag{5.40}$$

In other words, the number of electrons per unit length with wave vector $\in (k_x, k_x + dk_x)$ is just dk_x/π. These electrons move with group velocity [253]:

$$v_{\rm G} = \frac{dE(k_x)}{\hbar dk_x}, \tag{5.41}$$

so there are $(dk_x/\pi)(dE(k_x)/(\hbar dk_x)) = 2dE/h$ such electrons hitting the device from either side per unit time.

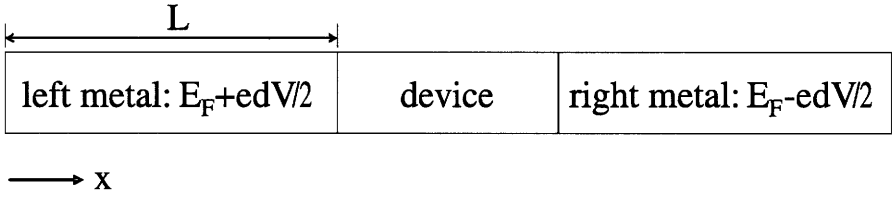

Figure 5-3: Illustration of the Landauer transmission formalism.

Under a small bias voltage dV, the Fermi level of the left lead is raised to $E_{\rm F} +$

$edV/2$, while that of the right lead drops to $E_{\rm F} - edV/2$. The number of electrons hitting the device from the left with wave vector $(k_x, k_x + dk_x)$ is exactly equal to the number of electrons hitting the device from the right with wave vector $(-k_x, -k_x - dk_x)$, except in the small energy window $(E_{\rm F} - edV/2, E_{\rm F} + edV/2)$, where the right has no electrons to balance against the left. Thus, a net number of $2(edV)/h$ electrons will attempt to cross from left and right, whose energies are very close to the original $E_{\rm F}$. Some of them are scattered back by the device, and only a fraction of $T \in (0, 1]$ gets through. So the current they carry is:

$$\left.\frac{dI}{dV}\right|_{V=0} = \frac{2e^2}{h} T(E_{\rm F}), \tag{5.42}$$

where $2e^2/h = 77.481\mu S = (12.906k\Omega)^{-1}$.

Clearly, if the device is also of the same material and structure as the metallic leads, then $T(E_{\rm F})$ should be 1, when we ignore electron-electron and electron-phonon scattering. This can be used as a sanity check of the code. For a nontrivial device however such as a molecular junction, $T(E_{\rm F})$ would be smaller than 1, and would sensitively depend on the alignment of the molecular levels and $E_{\rm F}$, as well as the overlap between these localized molecular states and the metallic states.

Here we report two USPP-TDDFT case studies along the line of the above discussion. One is an infinite defect-free gold chain (Fig. 5-4(a)). The other case uses gold chains as metallic leads and connects them to a -S-C_6H_4-S- (benzene-(1,4)-dithiolate, or BDT) molecular junction (Fig. 5-4(b)).

In the semi-classical Landauer picture explained above, the metallic electrons are represented by very wide Gaussian wavepacks [253] moving along with the group velocity $v_{\rm G}$, and with negligible rate of broadening compare to $v_{\rm G}$. Due to limitation of computational cost, we can only simulate rather small systems. In our experience with 1D lithium and gold chains, a Gaussian envelop of 3-4 lattice constants in full width half maximum is sufficient to propagate at the Fermi velocity $v_{\rm G}(k_{\rm F})$ with 100% transmissions and maintain its Gaussian-profile envelop with little broadening for several femto-seconds.

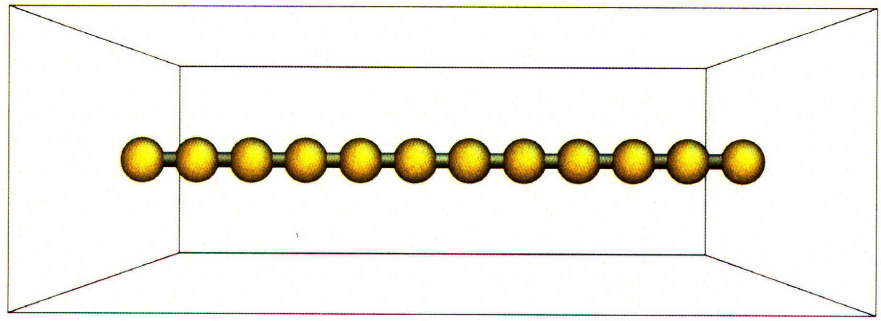

(a)

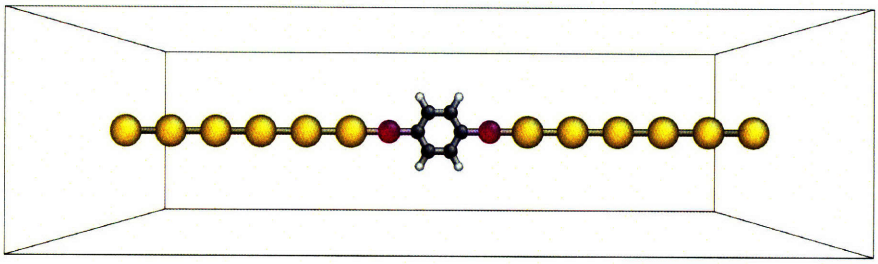

(b)

Figure 5-4: Atomistic configurations of our USPP-TDDFT simulations visualized by AtomEye [152]. Au: yellow (light gray), S: magenta (large dark gray), C: black (small dark gray), and H: white. (a) 12-atom Au chain. Bond length: Au-Au 2.88 Å. (b) BDT (-S-C_6H_4-S-) junction connected to Au chain contacts. Bond lengths: Au-Au 2.88 Å, Au-S 2.41 Å, S-C 1.83 Å, C-C 1.39 Å, and C-H 1.1 Å.

5.5.1 Fermi electron propagation in gold chain

The ground-state electronic configurations of pure gold chains are calculated using the free USPP-DFT package DACAPO, [33, 34, 35] with local density functional (LDA) [8, 9] and planewave kinetic energy cutoff of 250 eV. The ultrasoft pseudopotentials are generated using the free package USPP (ver. 7.3.3) [25, 26, 27], with $5d$, $6s$, $6p$, and auxiliary channels. Fig. 5-4(a) shows a chain of 12 Au atoms in a tetragonal supercell ($34.56 \times 12 \times 12$ Å^3), with equal Au-Au bond length of $a_0 = 2.88$ Å. Theoretically, 1D metal is always unstable against period-doubling Peierls distortion [253, 22]. However, the magnitude of the Peierls distortion is so small in the Au chain that room-temperature thermal fluctuations will readily erase its effect. For simplicity, we constrain the metallic chain to maintain single periodicity. Only the Γ-point wavefunctions are considered for the 12-atom configuration.

The Fermi level $E_{\rm F}$ is found to be -6.65 eV, which is confirmed by a more accurate calculation of a one-Au-atom system with **k**-sampling (Fig. 5-5). The Fermi state is doubly degenerate due to the time-inversion symmetry, corresponding to two Bloch wavefunctions of opposite wave vectors $k_{\rm F}$ and $-k_{\rm F}$.

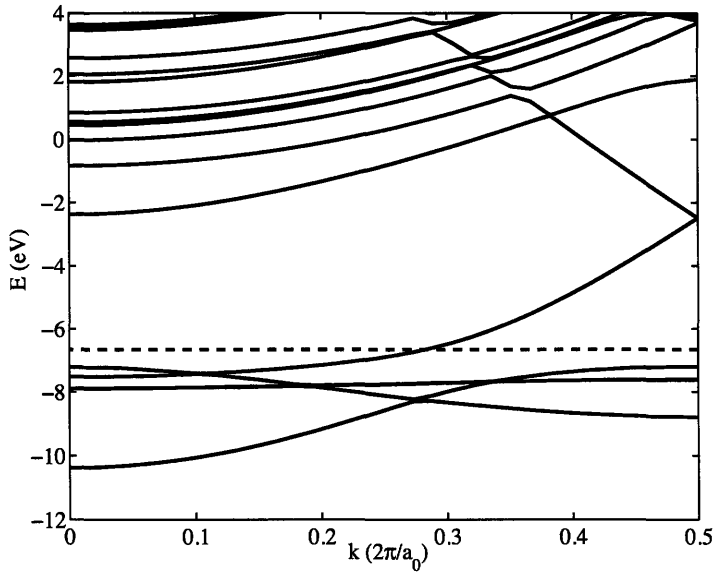

Figure 5-5: Band structure of a one-atom Au chain with 64 Monkhorst-Pack[23] **k**-sampling in the chain direction. The Fermi level, located at -6.65 eV, is marked as the dashed line.

From the Γ-point calculation, two energetically degenerate and real eigen wavefunctions, $\psi_+(\mathbf{x})$ and $\psi_-(\mathbf{x})$, are obtained. The complex traveling wavefunction is reconstructed as

$$\psi_{k_{\rm F}}(\mathbf{x}) = \frac{\psi_+(\mathbf{x}) + i\psi_-(\mathbf{x})}{\sqrt{2}}. \tag{5.43}$$

The phase velocity of $\psi_{k_{\rm F}}(\mathbf{x}, t)$ computed from our TDLDA runs matches the Fermi frequency $E_{\rm F}/\hbar$. We use the integration scheme (5.29) and a timestep of 2.37 attoseconds.

We then calculate the Fermi electron group velocity $v_{\rm G}(k_{\rm F})$ by adding a perturbation modulation of

$$\tilde{\psi}_{k_{\rm F}}(\mathbf{x}, t=0) \;=\; \psi_{k_{\rm F}}(\mathbf{x})(1 + \lambda \sin(2\pi x/L)) \tag{5.44}$$

to the Fermi wavefunction $\psi_{k_F}(\mathbf{x})$, where λ is 0.02 and L is the x-length of the supercell. Fig. 5-6 shows the electron density plot along two axes, x and t. From the dashed line connecting the black-lobe edges, one can estimate the Fermi electron group velocity to be ~10.0 Å/fs. The Fermi group velocity can also be obtained analytically from Eq. (5.41) at $k_x = k_F$. A value of 10 Å/fs is found according to Fig. 5-5, consistent with the TDLDA result.

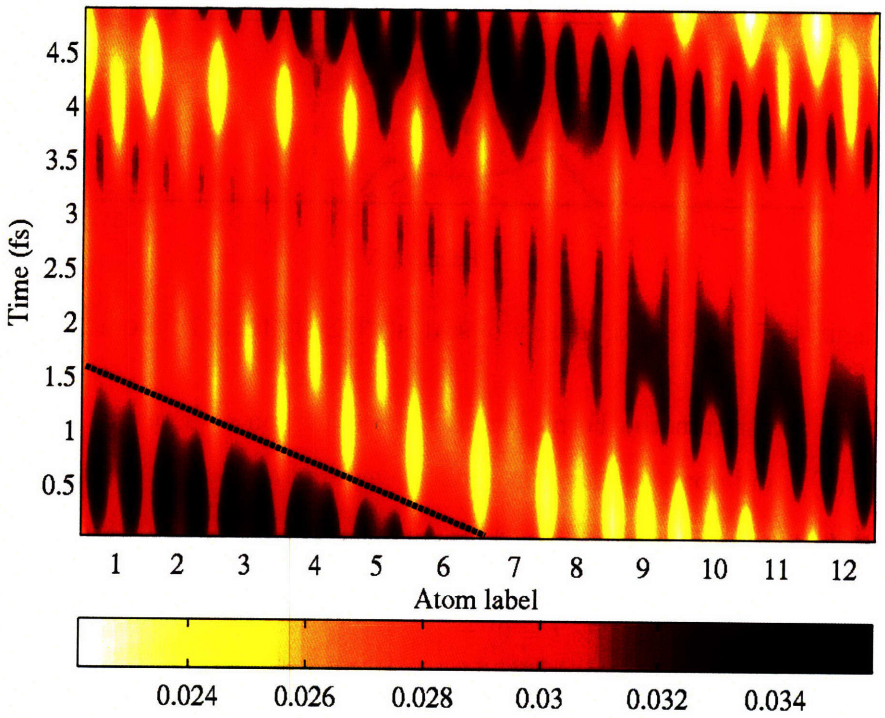

Figure 5-6: Evolution of modulated Fermi electron density in time along the chain direction. The electron density, in the unit of $Å^{-1}$, is an integral over the perpendicular y-z plane and normalized along the x direction, which is then color coded.

Lastly, the angular momentum projected densities of states are shown in Fig. 5-7, which indicate that the Fermi wavefunction mainly has s and p_x characteristics.

5.5.2 Fermi electron transmission through Au-BDT-Au junction

At small bias voltages, the electric conductance of a molecular junction (Fig. 5-4(b)) is controlled by the transmission of Fermi electrons, as shown in Eq. (5.42). In this

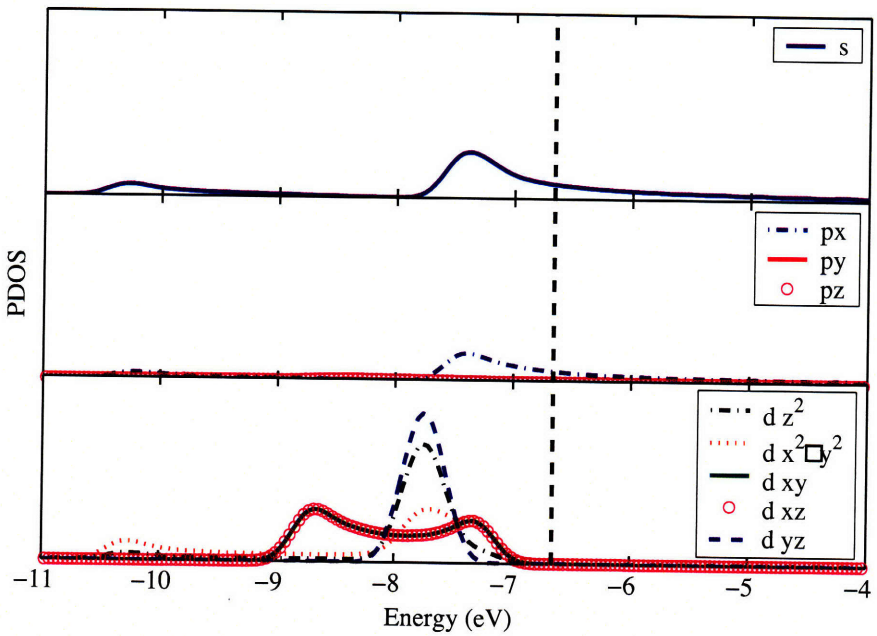

Figure 5-7: Projected density of states(PDOS) of the 12-atom Au chain.

section, we start from the Fermi electron wavefunction of a perfect 1D gold chain (Fig. 5-4(a)), and apply a Gaussian window centered at $\mathbf{x}_0$ with a half width of σ, to obtain a localized wave pack

$$\tilde{\psi}_{k_F}(\mathbf{x}, t=0) = \psi_{k_F}(\mathbf{x}) G\left(\frac{\mathbf{x}-\mathbf{x}_0}{\sigma}\right), \tag{5.45}$$

at the left lead. This localized Fermi electron wave pack is then propagated in real time by the TDLDA-USPP algorithm (5.29) with a timestep of 2.37 attoseconds, leaving from the left Au lead and traversing across the -S-C_6H_4-S- molecular junction (Fig. 5-4(b)). While crossing the junction the electron will be scattered, after which we collect the electron density entering the right Au lead to compute the transmission probability $T(E_F)$ literally. The calculation is performed in a tetragonal box ($42.94 \times 12 \times 12$ Å^3) with a kinetic energy cutoff of 250 eV.

Fig. 5-8 shows the Fermi electron density evolution in x-t. A group velocity of 10 Å/fs is obtained from the initial wave pack center trajectory, consistent with the perfect Au chain result. This *free* propagation lasts for about 0.8 fs, followed by a sharp density turnover that indicates the occurrence of strong electron scattering

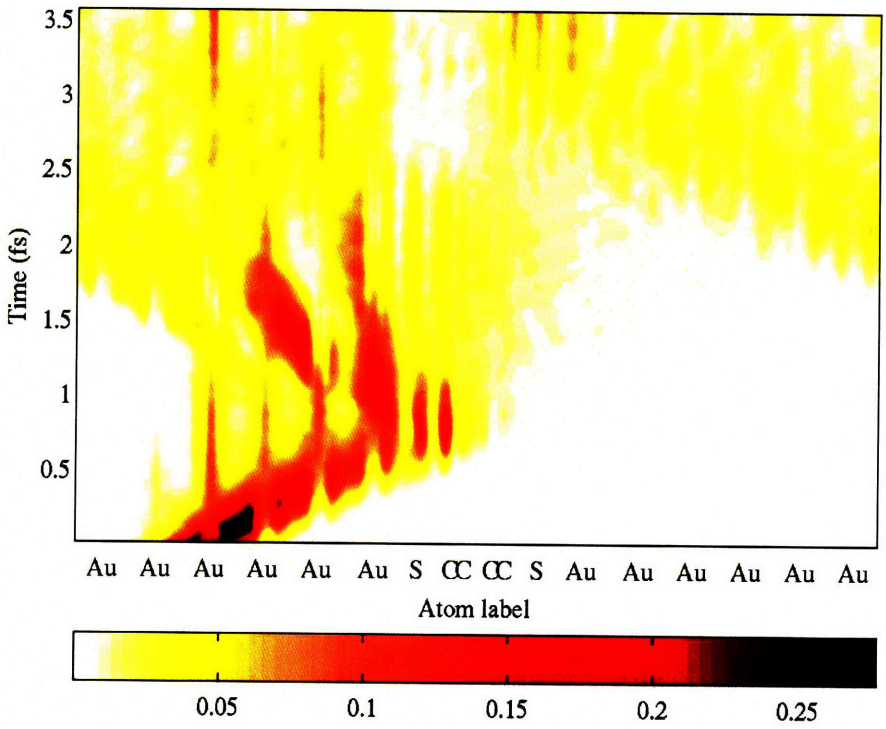

Figure 5-8: Evolution of filtered wave package density in time along the chain direction. The electron density, in the unit of Å^{-1}, is a sum over the perpendicular y-z plane and normalized along the x direction. The normalized electron density is color coded by the absolute value.

at the junction. A very small portion of the wave pack goes through the molecule. After about 1.7 fs, the reflected portion of the wave pack enters the right side of the supercell through PBC.

To separate the transmitted density from the reflected density as clearly as possible, we define and calculate the following cumulative charge on the right side

$$R(x',t) \equiv \int_{x_S}^{x'} dx \int_0^{L_y} dy \int_0^{L_z} dz \rho(x,y,z,t), \tag{5.46}$$

where x_S is the position of the right sulfur atom. $R(x',t)$ is plotted in Fig. 5-9 for ten x'-positions starting from the right sulfur atom up to the right boundary L_x. A shoulder can be seen in all 10 curves, at t = 1.5-2 fs, beyond which $R(x',t)$ starts to rise sharply again, indicating that the reflected density has entered from the right boundary. Two solid curves are highlighted in Fig. 5-9. The lower curve is at

$x' = x_S + 7.2$ Å, which shows a clear transmission plateau of about 5%. The upper curve, which is for x' exactly at the right PBC boundary, shows $R(x', t) \approx 7\%$ at the shoulder. From these two curves, we estimate a transmission probability $T(E_F)$ of 5-7%, which corresponds to a conductance of 4.0-5.6 μS according to Eq. (5.42). This result from planewave TDLDA-USPP calculation is comparable to the transmission probability estimate of 10% from complex band structure calculation [220, 221] for one benzene linker (-C_6H_4-) without the sulfur atoms, and the non-equilibrium Green's function estimate of 5 μS [62] for the similar system. However it should be mentioned here the electrical lead is pure gold chain while in other people's work they use the bulk lead with Au(111) surfaces. So more physical comparison should be done in the same system. That will be shown in the next section.

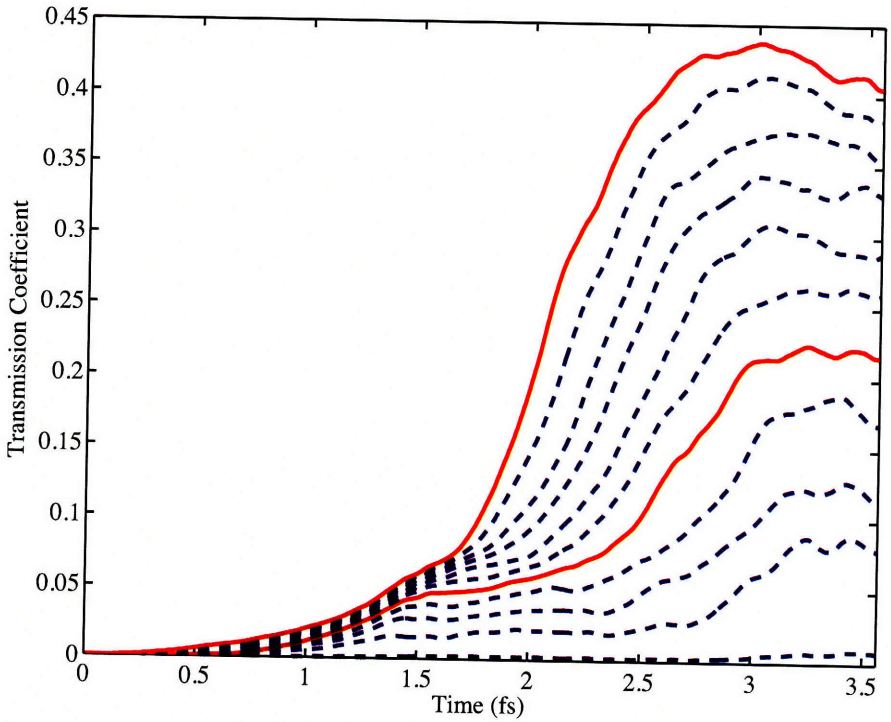

Figure 5-9: $R(x', t)$ versus time plot. Curves are measured in 10 different regions with different x' positions, which equally divide the region from the right S atom to the boundary on the right hand side.

5.6 Direct comparison between TDDFT result and Green's function method result

The transmission value from our Green's function calculation is 0.025 shown in Fig. 4-35(g, h), while the corresponding transmission coefficient from real-time TDDFT wave propagation is 0.05 to 0.07. The two-time difference may come from the tiny Gaussian wavepacket of Fermi electron, which is known to add more kinetic energy due to the localization of Gaussian wave function. Therefore it will give rise to a higher transmission value.

Here we plot the real-time propagation of wave function at four different time points shown in Fig. 5-10. Compared to those eigenchannels in Fig. 4-35(g, h) at the corresponding energy level, we find very good agreement between the shape of two different sets of wave functions. Particularly we see the composition of the incoming electron is from the coupled $s - p_x$ state, and it transfers to the other side through the orbitals of benzene ring along the bond direction. There is some fraction of electron density "jammed" around the hydrogen atoms and in the end only a very small fraction of electron reaches the other side. This is very similar to the conductance eigenchannel shown in Fig. 4-35(g, h). To our knowledge, this is the first direct comparison between the result from real-time TDDFT method and that from Green's function method. However, we would like to emphasize that, although the conductance at Fermi level from Green's function method and TDDFT is in good agreement, a better voltage or current boundary condition needs to be developed to have the correct conductance value in the end. Otherwise, the Gaussian wavepacket will lead to higher transmission coefficients as we have seen in the above example.

5.7 Summary

In this chapter we develop the TDDFT method based on Vanderbilt ultrasoft pseudopotentials [128] and benchmark this USPP-TDDFT scheme by calculating optical absorption spectra, which agree with both experiments and other TDDFT calcula-

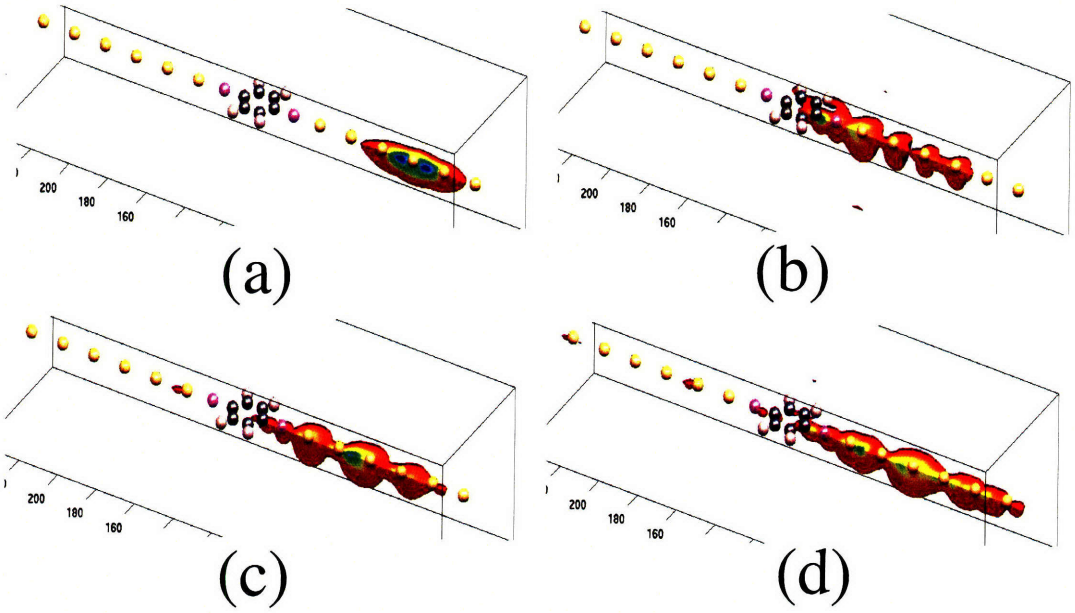

Figure 5-10: Real-time propagation of wave function: (a, b, c, d) are the contour plot of magnitude of wave functions in the right-bottom zone at four different time points: 0 fs, 1.4 fs, 2.16 fs, and 2.49 fs. The propagating direction is from right to left.

tions. We also demonstrate a practical approach to compute the electrical conductance through single-molecule junction via wave pack propagation using TDDFT. The small conductance of 4.0-5.6 μS is a result of our fixed band approximation, assuming the electron added was a small testing electron and therefore generated little disturbing effects of the incoming electrons on the electronic structure of the junction. This result is of the same order of magnitude as the results given by the Green's function and the complex band approaches, both requiring similar assumptions. We would like to mention that (a) the USPP-TDDFT scheme can easily extend to PAW-TDDFT with proper treatment of the projectors; (b) to fully implement TDDFT for periodic system with finite bias potential we need to either include vector potential to drive the system or implement certain current pump, which are effectively same.

Chapter 6

Summary and outlook

In this thesis we have developed two approaches based on the first-principles method toward more accurate simulations of phase-coherent electron transport in molecular and nanoscale electronics. The comparison between two methods verifies the equivalence in the limit of rigid band without dynamical correlations.

Our first approach is based on Green's function method within Landauer formalism. The efficiency of Green's function method relies on localization of basis-sets while the accuracy depends on the electronic ground-state. To achieve both of them at the same time, we have developed a minimal basis-set of quasiatomic orbitals from plane-wave density functional theory (DFT) results with norm-conserving pseudopotentials (NCPP), ultrasoft pseudopotentials (USPP), and projector augmented wave method (PAW). Our scheme is different from conventional methods by optimizing finite occupied Bloch space and large unoccupied Bloch space under the criteria of maximal localization or maximal atomic-orbital projection. Instead, the large unoccupied Bloch space is directly constructed from the space spanned by atomic orbitals but perpendicular to occupied Bloch space under maximal atomic-like criteria. We have mathematically proved that this method can reproduce the result of maximal atomic-orbital projection method with infinite Bloch space while accurately reproducing all electronic structures of occupied Bloch space. More importantly, it resembles quasi-angular momentum characteristics in solid state systems as that in atoms. This further validates Slater's original idea of linear combinations of atomic orbitals

(LCAO). We numerically show that there exists finite quantum numbers of orbital angular momentum for most materials. Our localized orbitals are always guaranteed to be atomic-orbital-like and have more flexibility and chemical transferability for *ab initio* tight-binding modeling. Based on these short-ranged tight-binding Hamiltonian and overlap matrices, band structure, Fermi surface, Mülliken charge, bond order, and quasiatomic orbitals-projected band structure and Fermi surfaces demonstrate the accuracy, efficiency and stability of our scheme.

With our minimal basis-set, quantum conductance and density of states of coherent electron transport are calculated by Green's function method within the Landauer formalism. We show several examples of electron transport in zero-dimensional and one-dimensional molecular and nanoscale electronics. Resonant transport is widely observed in several molecular electronic systems and those resonant peaks are due to the coupling between various *discrete* molecular level and continuous states in metal leads. We found that the typical confined aluminum wires have remarkable spin-dependent conductance because of local magnetic moment formation. We predict that such spin-dependent transport should widely exist in confined systems. More strikingly, the phase-encoded conductance eigenchannel gives a direct and visual understanding of electron transport. In one limit, it shows the static standing wave with complete refection while in the other limit it gives complete phase-oscillation with complete transmission. We further explore electron transport in phenalenyl molecule and carbon nanotube with and without defects. Quantum loop current due to time-reversal symmetry breaking is found in these systems. We predict that source-drain current could introduce current loop in defected or disordered systems with asymmetric current paths.

Our second approach naturally arises due to the fact that electron transport is not ground state, but an excited state property. Time-dependent density functional theory (TDDFT) is a fundamental approach to account for dynamical correlations of wave functions and correct band gap in DFT. In our second approach, we mainly focus on the mathematical formulation and algorithm development of TDDFT with ultrasoft pseudopotentials and projector augmented wave method. Calculated optical

absorption spectrum gives the correct positions and shapes of excitation peaks compared to experimental results and other TDDFT results with norm-conserving pseudopotentials. It is further applied to the study of Fermi electron transmission through benzene dithiolate molecular junction sandwiched by two gold nanowires. It is first verified that Fermi electron's group velocity in gold nanowire obtained by TDDFT agrees with band structure theory. Then under rigid band and zero bias approximations, a tiny Fermi electron wave packet is injected into the molecular junction. Transmission coefficient evaluated after scattering process is around 5%. From the comparison between real-time TDDFT method and Green's function method, both methods agree with each other not only because of the transmission coefficient on the same order, but also because of the similar characteristic propagation channels. The nice agreement verifies that Green's function approach based on DFT reaches the TDDFT result without dynamical correlations.

Compared to experiments, calculated electrical conductance of various molecular electronics is still not accurate although sometimes the shapes of current-voltage curves are very similar. Unknown detailed geometry in experiments is one critical factor since different binding sites on metallic surfaces can change the conductance dramatically. In theoretical development several issues need to be improved including exchange-correlation functional, electron-phonon coupling, and dynamical electron correlation.

- Exchange-correlation functional can often affect band gap and energy level of molecular orbitals, thus significantly affect the electrical conductance. However, it should be mentioned that even with exact exchange-correlation functional the band gap is still not correct due to the missing derivative discontinuity of the functional. One traditional way is to use LDA+U method which modifies the on-site Coulomb interactions to normal ground-state LDA calculations.

- Dynamical electron correlation is another important ingredient. As we have mentioned above, electron transport is indeed an excited state property and it can not be described in the static single-particle picture any more. Therefore,

quasi-particle correction from many-body perturbation theory such as GW approximation [254, 255] is a very promising candidate to systematically improve the accuracy of electrical conductance, even including electron-hole excitation by solving Bethe-Salpeter equation [256]. Meanwhile, time-dependent density functional theory is an alternative approach to include dynamical electron correlation. However appropriate current or voltage boundary condition needs to be developed for efficient electron transport simulations.

- Electron-phonon coupling is also very critical for a more accurate current-voltage curve since self-energy correction due to electron-phonon coupling can also modify the conductor Hamiltonian. More importantly new transport mechanism could emerge because of the additional degrees of freedom from electron-phonon couplings. One interesting example is soliton transport in one dimensional organic polymer such as polyacetylene, where an additional gap state, an self-trapped electron-phonon mode, is formed. Electron transport via soliton can be slower but much more efficient when the electron-phonon coupling is strong.

We believe that our quasiatomic orbitals can serve as a minimal basis-set for both GW quasi-particle corrections of electronic structure in the non-equilibrium Green's function (NEGF) method and efficient electron propagation in TDDFT. More importantly, a combined method with GW-NEGF and TDDFT will provide a more accurate and efficient way to study various molecular and nanoscale electronic devices including transistors, chemical sensors, electromechanical devices, magnetic memory, strong-correlated materials, and optical electronics.

Bibliography

[1] M. Born and J. R. Oppenheimer. Zur quantentheorie der molekeln. *Ann. d. Physik*, 84:457, 1927.

[2] M. Born and K. Huang. *Dynamical Theory of Crystal Lattices.* Oxford University Press, 1954.

[3] J. C. Slater. A Simplification of the Hartree-Fock Method. *Phys. Rev.*, 81:385–390, 1951.

[4] Richard D. Mattuck. *A Guide to Feynman Diagrams in the Many-Body Problem.* Dover Publications, INC., New York, 2nd edition, 1992.

[5] P. Hohenberg and W. Kohn. Inhomogeneous electron gas. *Phys. Rev.*, 136:B864–B871, 1964.

[6] W. Kohn and L. J. Sham. Self-consistent equations including exchange and correlation effects. *Phys. Rev.*, 140:A1133–A1138, 1965.

[7] R. G. Parr and W. Yang. *Density-Functional Theory of Atoms and Molecules.* Clarendon Press, Oxford, 1989.

[8] D. M. Ceperley and B. J. Alder. Ground-state of the electron-gas by a stochastic method. *Phys. Rev. Lett.*, 45:566–569, 1980.

[9] J. P. Perdew and A. Zunger. Self-interaction correction to density-functional approximations for many-electron systems. *Phys. Rev. B*, 23:5048–5079, 1981.

[10] J. P. Perdew and Y. Wang. Accurate and simple analytic representation of the electron-gas correlation energy. *Phys. Rev. B*, 45:13244–13249, 1992.

[11] A. D. Becke. Density-functional exchange-energy approximation with correct asymptotic behavior. *Phys. Rev. A*, 38:3098–3100, 1988.

[12] J. P. Perdew, J. A. Chevary, S. H. Vosko, K. A. Jackson, M. R. Pederson, D. J. Singh, and C. Fiolhais. Atoms, molecules, solids, and surfaces: Applications of the generalized gradient approximation for exchange and correlation. *Phys. Rev. B*, 46:6671–6687, 1992.

[13] J. P. Perdew, K. Burke, and M. Ernzerhof. Generalized gradient approximation made simple. *Phys. Rev. Lett.*, 77:3865–3868, 1996.

[14] A. D. Becke. Density-functional thermochemistry. III. The role of exact exchange. *J. Chem. Phys.*, 98:5648, 1993.

[15] C. Lee, W. Yang, and R. G. Parr. Development of the Colle-Salvetti correlation-energy formula into a functional of the electron density. *Phys. Rev. B*, 37:785, 1988.

[16] S. H. Vosko, L. Wilk, and M. Nusair. Accurate spin-dependent electron liquid correlation energies for local spin density calculations: a critical analysis. *Can. J. Phys.*, 58:1200, 1980.

[17] P. J. Stephens, F. J. Devlin, C. F. Chabalowski, and Frisch M. J. *Ab initio* calculation of vibrational absorption and circular dichroism spectra using density functional force fields. *J. Phys. Chem.*, 98:11623–11627, 1994.

[18] J. Paier, M. Marsman, and G. Kresse. Why does the B3LYP hybrid functional fail for metals? *J. Chem. Phys*, 127:024103, 2007.

[19] L. J. Sham and M. Schluter. Density-functional theory of the energy-gap. *Phys. Rev. Lett.*, 51:1888–1891, 1983.

[20] J. P. Perdew and M. Levy. Physical content of the exact kohn-sham orbital energies - band-gaps and derivative discontinuities. *Phys. Rev. Lett.*, 51:1884–1887, 1983.

[21] Neil W. Ashcroft and N. David Mermin. *Solid State Physics*. Thomson Learning, 1976.

[22] M. P. Marder. *Condensed Matter Physics*. Wiley-Interscience Publication, 2000.

[23] H. J. Monkhorst and J. D. Pack. Special points for Brillouin-zone integrations. *Phys. Rev. B*, 13:5188–5192, 1976.

[24] James C. Phillips and Leonard Kleinman. New method for calculating wave functions in crystals and molecules. *Phys. Rev.*, 116:287–294, 1959.

[25] D. Vanderbilt. Soft self-consistent pseudopotentials in a generalized eigenvalue formalism. *Phys. Rev. B*, 41:7892–7895, 1990.

[26] K. Laasonen, R. Car, C. Lee, and D. Vanderbilt. Implementation of ultrasoft pseudopotentials in *ab initio* molecular-dynamics. *Phys. Rev. B*, 43:6796–6799, 1991.

[27] K. Laasonen, A. Pasquarello, R. Car, C. Lee, and D. Vanderblit. Car-Parrinello molecular-dynamics with Vanderbilt ultrasoft pseudopotentials. *Phys. Rev. B*, 47:10142–10153, 1993.

[28] P. E. Blöchl. Projector augmented-wave method. *Phys. Rev. B*, 50:17953–17979, 1994.

[29] D. R. Hamann, M. Schluter, and C. Chiang. Norm-conserving pseudopotentials. *Phys. Rev. Lett.*, 43:1494–1497, 1979.

[30] G. B. Bachelet, D. R. Hamann, and M. Schluter. Pseudopotentials that work - from H to Pu. *Phys. Rev. B*, 26:4199–4228, 1982.

[31] VASP. *http://cms.mpi.univie.ac.at/vasp/.*

[32] G. Kresse and J. Furthmuller. Efficient iterative schemes for *ab initio* total-energy calculations using a plane-wave basis set. *Phys. Rev. B*, 54:11169–11186, 1996.

[33] DACAPO. *http://dcwww.camp.dtu.dk/campos/dacapo/.*

[34] B. Hammer, L. B. Hansen, and J. K. Nørskov. Improved adsorption energetics within density-functional theory using revised perdew-burke-ernzerhof functionals. *Phys. Rev. B*, 59:7413–7421, 1999.

[35] S. R. Bahn and K. W. Jacobsen. An object-oriented scripting interface to a legacy electronic structure code. *Comput. Sci. Eng.*, 4:56–66, 2002.

[36] E. Runge and E. K. U. Gross. Density-functional theory for time-dependent systems. *Phys. Rev. Lett.*, 52:997–1000, 1984.

[37] K. Yabana and G. F. Bertsch. Time-dependent local-density approximation in real time. *Phys. Rev. B*, 54:4484–4487, 1996.

[38] K. Yabana and G. F. Bertsch. Time-dependent local-density approximation in real time: Application to conjugated molecules. *Int. J. Quantum Chem.*, 75:55–66, 1999.

[39] G. F. Bertsch, J. I. Iwata, A. Rubio, and K. Yabana. Real-space, real-time method for the dielectric function. *Phys. Rev. B*, 62:7998–8002, 2000.

[40] M. A. L. Marques, A. Castro, G. F. Bertsch, and A. Rubio. Octopus: a first-principles tool for excited electron-ion dynamics. *Comput. Phys. Commun.*, 151:60–78, 2003.

[41] A. Tsolakidis, D. Sánchez-Portal, and R. M. Martin. Calculation of the optical response of atomic clusters using time-dependent density functional theory and local orbitals. *Phys. Rev. B*, 66:235416–, 2002.

[42] A. Castro, M. A. L. Marques, and A. Rubio. Propagators for the time-dependent Kohn-Sham equations. *J. Chem. Phys.*, 121:3425, 2004.

[43] R. Bauernschmitt and R. Ahlrichs. Treatment of electronic excitations within the adiabatic approximation of time dependent density functional theory. *Chem. Phys. Lett.*, 256:454–464, 1996.

[44] M. E. Casida, C. Jamorski, K. C. Casida, and D. R. Salahub. Molecular excitation energies to high-lying bound states from time-dependent density-functional response theory: Characterization and correction of the time-dependent local density approximation ionization threshold. *J. Chem. Phys.*, 108:4439–4449, 1998.

[45] J. R. Chelikowsky, L. Kronik, and I. Vasiliev. Time-dependent density-functional calculations for the optical spectra of molecules, clusters, and nanocrystals. *J. Phys.-Condes. Matter*, 15:R1517–R1547, 2003.

[46] J. Li and S. Yip. Order-N method to calculate the local density of states. *Phys. Rev. B*, 56:3524–3527, 1997.

[47] G. Vignale and W. Kohn. Current-dependent exchange-correlation potential for dynamical linear response theory. *Phys. Rev. Lett.*, 77:2037–2040, 1996.

[48] X. M. Tong and S. I. Chu. Time-dependent density-functional theory for strong-field multiphoton processes: Application to the study of the role of dynamical electron correlation in multiple high-order harmonic generation. *Phys. Rev. A*, 57:452–461, 1998.

[49] M. A. Reed, C. Zhou, C. J. Muller, T. P. Burgin, and J. M. Tour. Conductance of a molecular junction. *Science*, 278:252–254, 1997.

[50] R. H. M. Smit, Y. Noat, C. Untiedt, N. D. Lang, M. C. van Hemert, and J. M. van Ruitenbeek. Measurement of the conductance of a hydrogen molecule. *Nature*, 419:906–909, 2002.

[51] C. Joachim, J. K. Gimzewski, and A. Aviram. Electronics using hybrid-molecular and mono-molecular devices. *Nature*, 408:541–548, 2000.

[52] A. Nitzan. Electron transmission through molecules and molecular interfaces. *Annu. Rev. Phys. Chem.*, 52:681–750, 2001.

[53] J. R. Heath and M. A. Ratner. Molecular electronics. *Phys. Today*, 56:43–49, 2003.

[54] Supriyo Datta. *Electronic Transport in Mesoscopic Systems.* Cambridge University Press, Cambridge, 1995.

[55] Yoseph Imry. *Introdution to Mesoscopic Physics.* Oxford University Press, Oxford, 2nd edition, 2002.

[56] M. B. Nardelli. Electronic transport in extended systems: Application to carbon nanotubes. *Phys. Rev. B*, 60:7828–7833, 1999.

[57] P. A. Derosa and J. M. Seminario. Electron transport through single molecules: Scattering treatment using density functional and Green function theories. *J. Phys. Chem. B*, 105:471–481, 2001.

[58] P. S. Damle, A. W. Ghosh, and S. Datta. Unified description of molecular conduction: From molecules to metallic wires. *Phys. Rev. B*, 64:201403, 2001.

[59] J. Taylor, H. Guo, and J. Wang. *Ab initio* modeling of quantum transport properties of molecular electronic devices. *Phys. Rev. B*, 63:245407, 2001.

[60] M. Brandbyge, J. L. Mozos, P. Ordejon, J. Taylor, and K. Stokbro. Density-functional method for nonequilibrium electron transport. *Phys. Rev. B*, 65:165401, 2002.

[61] K. Stokbro, J. Taylor, M. Brandbyge, and P. Ordejon. TranSIESTA - A spice for molecular electronics. *Ann. N. Y. Acad. Sci.*, 1006:212–226, 2003.

[62] Y. Q. Xue and M. A. Ratner. Microscopic study of electrical transport through individual molecules with metallic contacts. I. Band lineup, voltage drop, and high-field transport. *Phys. Rev. B*, 68:115406, 2003.

[63] S. H. Ke, H. U. Baranger, and W. T. Yang. Electron transport through molecules: Self-consistent and non-self-consistent approaches. *Phys. Rev. B*, 70:085410, 2004.

[64] Supriyo Datta. *Quantum Transport: Atom to Transistor.* Cambridge University Press, Cambridge, 2005.

[65] M. Galperin, M. A. Ratner, and A. Nitzan. Hysteresis, switching, and negative differential resistance in molecular junctions: A polaron model. *Nano Lett.*, 5:125–130, 2005.

[66] M. Galperin, A. Nitzan, M. A. Ratner, and D. R. Stewart. Molecular transport junctions: Asymmetry in inelastic tunneling processes. *J. Phys. Chem. B*, 109:8519–8522, 2005.

[67] Y. Meir and N. S. Wingreen. Landauer formula for the current through an interacting electron region. *Phys. Rev. Lett.*, 68:2512–2515, 1992.

[68] R. Landauer. Spatial variation of currents and fields due to localized scatters in metallic conduction. *IBM. J. Res. Dev.*, 1:223–231, 1957.

[69] R. Landauer. Electrical resistance of disordered one-dimensional lattices. *Philos. Mag.*, 21:863–867, 1970.

[70] D. S. Fisher and P. A. Lee. Relation between conductivity and transmission matrix. *Phys. Rev. B*, 23:6851–6854, 1981.

[71] Y. Imry and R. Landauer. Conductance viewed as transmission. *Rev. Mod. Phys.*, 71:S306–S312, 1999.

[72] H. Haug and A. P. Jauho. *Quantum Kinetics in Transport and Optics of Semiconductors.* Springer, Berlin, 1996.

[73] M. Buttiker. Four-terminal phase-coherent conductance. *Phys. Rev. Lett.*, 57:1761–1764, 1986.

[74] A. Ferretti, A. Calzolari, R. Di Felice, F. Manghi, M. J. Caldas, M. B. Nardelli, and E. Molinari. First-principles theory of correlated transport through nano-junctions. *Phys. Rev. Lett.*, 94:116802, 2005.

[75] A. Ferretti, A. Calzolari, R. Di Felice, and F. Manghi. First-principles theoretical description of electronic transport including electron-electron correlation. *Phys. Rev. B*, 72:125114, 2005.

[76] K. S. Thygesen and A. Rubio. Nonequilibrium GW approach to quantum transport in nano-scale contacts. *J. Chem. Phys.*, 126:091101, 2007.

[77] L. V. Keldysh. Diagram technique for nonequilibrium processes. *Sov. Phys. JETP*, 20:1018–1026, 1965.

[78] A. P. Jauho, N. S. Wingreen, and Y. Meir. Time-dependent transport in interacting and noninteracting resonant-tunneling systems. *Phys. Rev. B*, 50:5528–5544, 1994.

[79] Y. Q. Xue, S. Datta, and M. A. Ratner. First-principles based matrix Green's function approach to molecular electronic devices: general formalism. *Chem. Phys.*, 281:151–170, 2002.

[80] B. J. Vanwees, H. Vanhouten, C. W. J. Beenakker, J. G. Williamson, L. P. Kouwenhoven, D. Vandermarel, and C. T. Foxon. Quantized conductance of point contacts in a two-dimensional electron-gas. *Phys. Rev. Lett.*, 60:848–850, 1988.

[81] B. J. Vanwees, L. P. Kouwenhoven, H. Vanhouten, C. W. J. Beenakker, J. E. Mooij, C. T. Foxon, and J. J. Harris. Quantized conductance of magnetoelectric subbands in ballistic point contacts. *Phys. Rev. B*, 38:3625–3627, 1988.

[82] M. P. L. Sancho, J. M. L. Sancho, and J. Rubio. Quick iterative scheme for the calculation of transfer-matrices - application to Mo(100). *J Phys-F-Metal Phys*, 14:1205–1215, 1984.

[83] M. P. L. Sancho, J. M. L. Sancho, and J. Rubio. Highly convergent schemes for the calculation of bulk and surface Green-functions. *J Phys-F-Metal Phys*, 15:851–858, 1985.

[84] M. P. L. Sancho, J. M. L. Sancho, and J. Rubio. A non-orthogonal-basis calculation of the spectral density of surface-states for the (100) and (110) faces of tungsten. *J Phys-C-Solid State Phys*, 18:1803–1815, 1985.

[85] J. Harris. Simplified method for calculating the energy of weakly interacting fragments. *Phys. Rev. B*, 31:1770–1779, 1985.

[86] W. Matthew, C. Foulkes, and R. Haydock. Tight-binding models and density-functional theory. *Phys. Rev. B*, 39:12520–12536, 1989.

[87] M. Paulsson and M. Brandbyge. Transmission eigenchannels from nonequilibrium Green's functions. *Phys. Rev. B*, 76:115117, 2007.

[88] S. Nakanishi, R. Tamura, and M. Tsukada. Ballistic transport in artificial nano-circuits. *Jpn. J. Appl. Phys. Part 1 - Regul. Pap. Short Notes Rev. Pap.*, 37:3805–3808, 1998.

[89] S. Nakanishi and M. Tsukada. The theory of microscopic current distribution in molecular bridge structures. *Surf. Sci.*, 438:305–310, 1999.

[90] S. Nakanishi and M. Tsukada. Quantum loop current in a C_{60} molecular bridge. *Phys. Rev. Lett.*, 87:126801, 2001.

[91] S. Goedecker. Linear scaling electronic structure methods. *Rev. Mod. Phys.*, 71:1085–1123, 1999.

[92] A. J. Williamson, R. Q. Hood, and J. C. Grossman. Linear-scaling quantum Monte Carlo calculations. *Phys. Rev. Lett.*, 87:246406, 2001.

[93] J. M. Soler, E. Artacho, J. D. Gale, A. Garcia, J. Junquera, P. Ordejon, and D. Sanchez-Portal. The SIESTA method for *ab initio* order-N materials simulation. *J. Phys.-Condes. Matter*, 14:2745–2779, 2002.

[94] R. Iftimie, J. W. Thomas, and M. E. Tuckerman. On-the-fly localization of electronic orbitals in Car-Parrinello molecular dynamics. *J. Chem. Phys.*, 120:2169–2181, 2004.

[95] A. Calzolari, N. Marzari, I. Souza, and M. B. Nardelli. *Ab initio* transport properties of nanostructures from maximally localized Wannier functions. *Phys. Rev. B*, 69:035108, 2004.

[96] K. S. Thygesen and K. W. Jacobsen. Molecular transport calculations with Wannier functions. *Chem. Phys.*, 319:111–125, 2005.

[97] Z. Y. Li and D. S. Kosov. First-principles calculations of conductance within a plane wave basis set via non-orthogonal Wannier-type atomic orbitals. *J. Phys.-Condes. Matter*, 18:1347–1358, 2006.

[98] R. Resta. Why are insulators insulating and metals conducting? *J. Phys.-Condes. Matter*, 14:R625–R656, 2002.

[99] T. Thonhauser, D. Ceresoli, D. Vanderbilt, and R. Resta. Orbital magnetization in periodic insulators. *Phys. Rev. Lett.*, 95:137205, 2005.

[100] I. Schnell, G. Czycholl, and R. C. Albers. Hubbard-U calculations for Cu from first-principle Wannier functions. *Phys. Rev. B*, 65:075103, 2002.

[101] S. Fabris, S. de Gironcoli, S. Baroni, G. Vicario, and G. Balducci. Taming multiple valency with density functionals: A case study of defective ceria. *Phys. Rev. B*, 71:041102, 2005.

[102] A. Yamasaki, M. Feldbacher, Y. F. Yang, O. K. Andersen, and K. Held. Pressure-induced metal-insulator transition in $LaMnO_3$ is not of Mott-Hubbard type. *Phys. Rev. Lett.*, 96:166401, 2006.

[103] E. J. Bylaska, K. Tsemekhman, and F. Gao. New development of self-interaction corrected DFT for extended systems applied to the calculation of native defects in 3C-SiC. *Phys. Scr.*, T124:86–90, 2006.

[104] G. H. Wannier. The structure of electronic excitation levels in insulating crystals. *Phys. Rev.*, 52:191–197, 1937.

[105] N. Marzari and D. Vanderbilt. Maximally localized generalized Wannier functions for composite energy bands. *Phys. Rev. B*, 56:12847–12865, 1997.

[106] I. Souza, N. Marzari, and D. Vanderbilt. Maximally localized Wannier functions for entangled energy bands. *Phys. Rev. B*, 65:035109, 2001.

[107] W. C. Lu, C. Z. Wang, M. W. Schmidt, L. Bytautas, K. M. Ho, and K. Ruedenberg. Molecule intrinsic minimal basis sets. I. Exact resolution of *ab initio* optimized molecular orbitals in terms of deformed atomic minimal-basis orbitals. *J. Chem. Phys.*, 120:2629–2637, 2004.

[108] W. C. Lu, C. Z. Wang, M. W. Schmidt, L. Bytautas, K. M. Ho, and K. Ruedenberg. Molecule intrinsic minimal basis sets. II. Bonding analyses for Si_4H_6 and Si_2 to Si_{10}. *J. Chem. Phys.*, 120:2638–2651, 2004.

[109] W. C. Lu, C. Z. Wang, T. L. Chan, K. Ruedenberg, and K. M. Ho. Representation of electronic structures in crystals in terms of highly localized quasiatomic minimal basis orbitals. *Phys. Rev. B*, 70:041101, 2004.

[110] W. C. Lu, C. Z. Wang, K. Ruedenberg, and K. M. Ho. Transferability of the Slater-Koster tight-binding scheme from an environment-dependent minimal-basis perspective. *Phys. Rev. B*, 72:205123, 2005.

[111] T.-L. Chan, Y. X. Yao, C. Z. Wang, W. C. Lu, J. Li, X. F. Qian, S. Yip, and K. M. Ho. Highly localized quasiatomic minimal basis orbitals for Mo from *ab initio* calculations. *Phys. Rev. B*, 76:205119, 2007.

[112] P. Pulay. Localizability of dynamic electron correlation. *Chem. Phys. Lett.*, 100:151–154, 1983.

[113] S. Sæbø and P. Pulay. Local configuration-interaction — an efficient approach for larger molecules. *Chem. Phys. Lett.*, 113:13–18, 1985.

[114] S. Sæbø and P. Pulay. Local treatment of electron correlation. *Annu. Rev. Phys. Chem.*, 44:213–236, 1993.

[115] XCrySDen. *http://www.xcrysden.org/.*

[116] A. Kokalj. XCrySDen - a new program for displaying crystalline structures and electron densities. *J. Mol. Graph.*, 17:176, 1999.

[117] A. Kokalj. Computer graphics and graphical user interfaces as tools in simulations of matter at the atomic scale. *Comput. Mater. Sci.*, 28:155–168, 2003.

[118] M. S. Tang, C. Z. Wang, C. T. Chan, and K. M. Ho. Environment-dependent tight-binding potential model. *Phys. Rev. B*, 53:979–982, 1996.

[119] H. Haas, C. Z. Wang, M. Fahnle, C. Elsasser, and K. M. Ho. Environment-dependent tight-binding model for molybdenum. *Phys. Rev. B*, 57:1461–1470, 1998.

[120] C. Z. Wang, B. C. Pan, and K. M. Ho. An environment-dependent tight-binding potential for si. *J. Phys.-Condes. Matter*, 11:2043–2049, 1999.

[121] J. Li, D. Y. Liao, S. Yip, R. Najafabadi, and L. Ecker. Force-based many-body interatomic potential for ZrC. *J. Appl. Phys.*, 93:9072–9085, 2003.

[122] S. Yip, editor. *Handbook of Materials Modeling.* Springer, Dordrecht, 2005.

[123] Walter A. Harrison. *Electronic Structure and the Properties of Solids: the Physics of the Chemical Bond.* Freeman, San Francisco, 1980.

[124] M. C. Payne, M. P. Teter, D. C. Allan, T. A. Arias, and J. D. Joannopoulos. Iterative minimization techniques for *ab initio* total-energy calculations - molecular-dynamics and conjugate gradients. *Rev. Mod. Phys.*, 64:1045–1097, 1992.

[125] W. J. Hehre, R. F. Stewart, and J. A. Pople. Self-consistent molecular-orbital methods. I. Use of Gaussian expansions of Slater-type atomic orbitals. *J. Chem. Phys.*, 51:2657, 1969.

[126] J. C. Slater and G. F. Koster. Simplified LCAO method for the periodic potential problem. *Phys. Rev.*, 94:1498–1524, 1954.

[127] O. K. Andersen and T. Saha-Dasgupta. Muffin-Tin orbitals of arbitrary order. *Phys. Rev. B*, 62:R16219–R16222, 2000.

[128] X. F. Qian, J. Li, X. Lin, and S. Yip. Time-dependent density functional theory with ultrasoft pseudopotentials: Real-time electron propagation across a molecular junction. *Phys. Rev. B*, 73:035408, 2006.

[129] G. Kresse and D. Joubert. From ultrasoft pseudopotentials to the projector augmented-wave method. *Phys. Rev. B*, 59:1758–1775, 1999.

[130] Quasiatomic Orbitals. *http://alum.mit.edu/www/liju99/QO.*

[131] G. F. Koster and J. C. Slater. Wave functions for impurity levels. *Phys. Rev.*, 95:1167–1176, 1954.

[132] W. Kohn. Analytic properties of Bloch waves and Wannier functions. *Phys. Rev.*, 1:809–821, 1959.

[133] W. Kohn. Construction of wannier functions and applications to energy-bands. *Phys. Rev. B*, 7:4388–4398, 1973.

[134] G. Berghold, C. J. Mundy, A. H. Romero, J. Hutter, and M. Parrinello. General and efficient algorithms for obtaining maximally localized Wannier functions. *Phys. Rev. B*, 61:10040–10048, 2000.

[135] J. J. Mortensen and M. Parrinello. Localized non-orthogonal orbitals in silicon. *J. Phys.-Condes. Matter*, 13:5731–5741, 2001.

[136] C. M. Zicovich-Wilson, R. Dovesi, and V. R. Saunders. A general method to obtain well localized Wannier functions for composite energy bands in linear combination of atomic orbital periodic calculations. *J. Chem. Phys.*, 115:9708–9719, 2001.

[137] K. S. Thygesen, L. B. Hansen, and K. W. Jacobsen. Partly occupied Wannier functions. *Phys. Rev. Lett.*, 94:026405, 2005.

[138] R. A. Evarestov, D. E. Usvyat, and V. P. Smirnov. Wannier-type atomic orbitals for periodic systems. *Theor. Chem. Acc.*, 114:19–28, 2005.

[139] U. Birkenheuer and D. Izotov. Localization of Wannier functions for entangled energy bands. *Phys. Rev. B*, 71:125116, 2005.

[140] J. Bhattacharjee and U. V. Waghmare. Localized orbital description of electronic structures of extended periodic metals, insulators, and confined systems: Density functional theory calculations. *Phys. Rev. B*, 73:1211102, 2006.

[141] C. Brouder, G. Panati, M. Calandra, C. Mourougane, and N. Marzari. Exponential localization of Wannier functions in insulators. *Phys. Rev. Lett.*, 98:046402, 2007.

[142] L. X. He and D. Vanderbilt. Exponential decay properties of Wannier functions and related quantities. *Phys. Rev. Lett.*, 86:5341–5344, 2001.

[143] J. W. Thomas, R. Iftimie, and M. E. Tuckerman. Field theoretic approach to dynamical orbital localization in *ab initio* molecular dynamics. *Phys. Rev. B*, 69:125105, 2004.

[144] R. Iftimie, P. Minary, and M. E. Tuckerman. *Ab initio* molecular dynamics: Concepts, recent developments, and future trends. *Proc. Natl. Acad. Sci. U. S. A.*, 102:6654–6659, 2005.

[145] J. M. Foster and S. F. Boys. Canonical configurational interaction procedure. *Rev. Mod. Phys.*, 32:300–302, 1960.

[146] S. Baroni, A. Dal Corso, S. de Gironcoli, P. Giannozzi, C. Cavazzoni, G. Ballabio, S. Scandolo, G. Chiarotti, P. Focher, A. Pasquarello, K. Laasonen, A. Trave, R. Car, N. Marzari, and A. Kokalj. PWscf. *http://www.pwscf.org.*

[147] CPMD. *http://www.cpmd.org.*

[148] P. E. Blöchl, C. J. Först, and J. Schimpl. Projector augmented wave method: *ab initio* molecular dynamics with full wave functions. *Bull. Mat. Sci.*, 26:33–41, 2003.

[149] X. Gonze, J. M. Beuken, R. Caracas, F. Detraux, M. Fuchs, G. M. Rignanese, L. Sindic, M. Verstraete, G. Zerah, F. Jollet, M. Torrent, A. Roy, M. Mikami, P. Ghosez, J. Y. Raty, and D. C. Allan. First-principles computation of material properties: the ABINIT software project. *Comput. Mater. Sci.*, 25:478–492, 2002.

[150] K. Ruedenberg, M. W. Schmidt, M. M. Gilbert, and S. T. Elbert. Are atoms intrinsic to molecular electronic wavefunctions? I. The FORS model. *Chem. Phys.*, 71:41–49, 1982.

[151] J. C. Slater. Atomic radii in crystals. *J. Chem. Phys.*, 41:3199, 1964.

[152] J. Li. Atomeye: an efficient atomistic configuration viewer. *Model. Simul. Mater. Sci. Eng.*, 11:173–177, 2003.

[153] H. J. Choi, D. Roundy, H. Sun, M. L. Cohen, and S. G. Louie. The origin of the anomalous superconducting properties of mgb2. *Nature*, 418:758–760, 2002.

[154] P. W. Anderson. Localized magnetic states in metals. *Phys. Rev.*, 124:41–53, 1961.

[155] D. M. Newns. Self-consistent model of hydrogen chemisorption. *Phys. Rev.*, 178:1123–1135, 1969.

[156] J. M. Krans, C. J. Muller, I. K. Yanson, T. C. M. Govaert, R. Hesper, and J. M. Vanruitenbeek. One-atom point contacts. *Phys. Rev. B*, 48:14721–14724, 1993.

[157] N. Agrait, J. G. Rodrigo, and S. Vieira. Conductance steps and quantization in atomic-size contacts. *Phys. Rev. B*, 47:12345–12348, 1993.

[158] N. Agrait, A. L. Yeyati, and J. M. van Ruitenbeek. Quantum properties of atomic-sized conductors. *Phys. Rep.-Rev. Sec. Phys. Lett.*, 377:81–279, 2003.

[159] J. M. Krans, J. M. vanRuitenbeek, and L. J. deJongh. Atomic structure and quantized conductance in metal point contacts. *Physica B*, 218:228–233, 1996.

[160] J. M. Krans, J. M. Vanruitenbeek, V. V. Fisun, I. K. Yanson, and L. J. Dejongh. The signature of conductance quantization in metallic point contacts. *Nature*, 375:767–769, 1995.

[161] K. Hansen, E. Lægsgaard, I. Stensgaard, and F. Besenbacher. Quantized conductance in relays. *Phys. Rev. B*, 56:2208–2220, 1997.

[162] J. L. Costa-Krämer. Conductance quantization at room temperature in magnetic and nonmagnetic metallic nanowires. *Phys. Rev. B*, 55:R4875–R4878, 1997.

[163] J. L. Costa-Krämer, N. García, P. García-Mochales, P. A. Serena, M. I. Marqués, and A. Correia. Conductance quantization in nanowires formed between micro and macroscopic metallic electrodes. *Phys. Rev. B*, 55:5416–5424, 1997.

[164] H. Ohnishi, Y. Kondo, and K. Takayanagi. Quantized conductance through individual rows of suspended gold atoms. *Nature*, 395:780–783, 1998.

[165] R. H. M. Smit, C. Untiedt, G. Rubio-Bollinger, R. C. Segers, and J. M. van Ruitenbeek. Observation of a parity oscillation in the conductance of atomic wires. *Phys. Rev. Lett.*, 91:076805, 2003.

[166] P. L. Pernas, A. Martin-Rodero, and F. Flores. Electrochemical-potential variations across a constriction. *Phys. Rev. B*, 41:8553–8556, 1990.

[167] N. D. Lang. Anomalous dependence of resistance on length in atomic wires. *Phys. Rev. Lett.*, 79:1357–1360, 1997.

[168] N. D. Lang and P. Avouris. Oscillatory conductance of carbon-atom wires. *Phys. Rev. Lett.*, 81:3515–3518, 1998.

[169] B. Larade, J. Taylor, H. Mehrez, and H. Guo. Conductance, I-V curves, and negative differential resistance of carbon atomic wires. *Phys. Rev. B*, 64:075420, 2001.

[170] E. G. Emberly and G. Kirczenow. Electron standing-wave formation in atomic wires. *Phys. Rev. B*, 60:6028–6033, 1999.

[171] Y. J. Lee, M. Brandbyge, M. J. Puska, J. Taylor, K. Stokbro, and R. M. Nieminen. Electron transport through monovalent atomic wires. *Phys. Rev. B*, 69:125409, 2004.

[172] H. W. Lee, H. S. Sim, D. H. Kim, and K. J. Chang. Towards unified understanding of conductance of stretched monatomic contacts. *Phys. Rev. B*, 68:075424, 2003.

[173] K. S. Thygesen and K. W. Jacobsen. Four-atom period in the conductance of monatomic al wires. *Phys. Rev. Lett.*, 91:146801, 2003.

[174] A. Smogunov, A. Dal Corso, and E. Tosatti. Ballistic conductance of magnetic Co and Ni nanowires with ultrasoft pseudopotentials. *Phys. Rev. B*, 70:045417, 2004.

[175] X. R. Wang, Y. P. Wang, and Z. Z. Sun. Antiresonance scattering at defect levels in the quantum conductance of a one-dimensional system. *Phys. Rev. B*, 65:193402, 2002.

[176] Y. Xu, X. Q. Shi, Z. Zeng, Z. Y. Zeng, and B. W. Li. Conductance oscillation and quantization in monatomic Al wires. *J. Phys.-Condes. Matter*, 19:056010, 2007.

[177] A. Ayuela, H. Raebiger, M. J. Puska, and R. M. Nieminen. Spontaneous magnetization of aluminum nanowires deposited on the NaCl(100) surface. *Phys. Rev. B*, 66:035417, 2002.

[178] Y. Meir, N. S. Wingreen, and P. A. Lee. Low-temperature transport through a quantum dot - the anderson model out of equilibrium. *Phys. Rev. Lett.*, 70:2601–2604, 1993.

[179] S. M. Cronenwett, H. J. Lynch, D. Goldhaber-Gordon, L. P. Kouwenhoven, C. M. Marcus, K. Hirose, N. S. Wingreen, and V. Umansky. Low-temperature fate of the 0.7 structure in a point contact: A kondo-like correlated state in an open system. *Phys. Rev. Lett.*, 88:226805, 2002.

[180] Y. Meir, K. Hirose, and N. S. Wingreen. Kondo model for the "0.7 anomaly" in transport through a quantum point contact. *Phys. Rev. Lett.*, 89:196802, 2002.

[181] H. D. Chopra, M. R. Sullivan, J. N. Armstrong, and S. Z. Hua. The quantum spin-valve in cobalt atomic point contacts. *Nat. Mater.*, 4:832–837, 2005.

[182] M. R. Sullivan, D. A. Boehm, D. A. Ateya, S. Z. Hua, and H. D. Chopra. Ballistic magnetoresistance in nickel single-atom conductors without magnetostriction. *Phys. Rev. B*, 71:024412, 2005.

[183] T. Rejec and Y. Meir. Magnetic impurity formation in quantum point contacts. *Nature*, 442:900–903, 2006.

[184] A. D. Klironomos, J. S. Meyer, and K. A. Matveev. Spontaneous spin polarization in quantum wires. *Europhys. Lett.*, 74:679–685, 2006.

[185] L. P. Rokhinson, L. N. Pfeiffer, and K. W. West. Spontaneous spin polarization in quantum point contacts. *Phys. Rev. Lett.*, 96:156602, 2006.

[186] R. Crook, J. Prance, K. J. Thomas, S. J. Chorley, I. Farrer, D. A. Ritchie, M. Pepper, and C. G. Smith. Conductance quantization at a half-integer plateau in a symmetric GaAs quantum wire. *Science*, 312:1359–1362, 2006.

[187] A. Sokolov, C. J. Zhang, E. Y. Tsymbal, J. Redepenning, and B. Doudin. Quantized magnetoresistance in atomic-size contacts. *Nat. Nanotechnol.*, 2:171–175, 2007.

[188] A. M. Bychkov and T. M. Stace. 0.4 and 0.7 conductance anomalies in quantum point contacts. *Nanotechnology*, 18:185403, 2007.

[189] S. Luscher, L. S. Moore, T. Rejec, Y. Meir, H. Shtrikman, and D. Goldhaber-Gordon. Charge rearrangement and screening in a quantum point contact. *Phys. Rev. Lett.*, 98:196805, 2007.

[190] P. Roche, J. Segala, D. C. Glattli, J. T. Nicholls, M. Pepper, A. C. Graham, K. J. Thomas, M. Y. Simmons, and D. A. Ritchie. Fano factor reduction on the 0.7 conductance structure of a ballistic one-dimensional wire. *Phys. Rev. Lett.*, 93:116602, 2004.

[191] A. Aviram and M. A. Ratner. Molecular rectifiers. *Chem. Phys. Lett.*, 29:277–283, 1974.

[192] E. G. Emberly and G. Kirczenow. Theoretical study of electrical conduction through a molecule connected to metallic nanocontacts. *Phys. Rev. B*, 58:10911–10920, 1998.

[193] M. Di Ventra, S. T. Pantelides, and N. D. Lang. First-principles calculation of transport properties of a molecular device. *Phys. Rev. Lett.*, 84:979–982, 2000.

[194] J. C. Ellenbogen and J. C. Love. Architectures for molecular electronic computers: 1. logic structures and an adder designed from molecular electronic diodes. *Proc. IEEE*, 88:386–426, 2000.

[195] X. D. Cui, A. Primak, X. Zarate, J. Tomfohr, O. F. Sankey, A. L. Moore, T. A. Moore, D. Gust, G. Harris, and S. M. Lindsay. Reproducible measurement of single-molecule conductivity. *Science*, 294:571–574, 2001.

[196] X. D. Cui, A. Primak, X. Zarate, J. Tomfohr, O. F. Sankey, A. L. Moore, T. A. Moore, D. Gust, L. A. Nagahara, and S. M. Lindsay. Changes in the electronic properties of a molecule when it is wired into a circuit. *J. Phys. Chem. B*, 106:8609–8614, 2002.

[197] R. L. Carroll and C. B. Gorman. The genesis of molecular electronics. *Angew. Chem.-Int. Edit.*, 41:4379–4400, 2002.

[198] W. J. Liang, M. P. Shores, M. Bockrath, J. R. Long, and H. Park. Kondo resonance in a single-molecule transistor. *Nature*, 417:725–729, 2002.

[199] A. Nitzan and M. A. Ratner. Electron transport in molecular wire junctions. *Science*, 300:1384–1389, 2003.

[200] X. Y. Xiao, B. Q. Xu, and N. J. Tao. Measurement of single molecule conductance: benzenedithiol and benzenedimethanethiol. *Nano Lett.*, 4:267–271, 2004.

[201] J. Tomfohr and O. F. Sankey. Theoretical analysis of electron transport through organic molecules. *J. Chem. Phys.*, 120:1542–1554, 2004.

[202] F. Chen, J. He, C. Nuckolls, T. Roberts, J. E. Klare, and S. Lindsay. A molecular switch based on potential-induced changes of oxidation state. *Nano Lett.*, 5:503–506, 2005.

[203] J. He, F. Chen, J. Li, O. F. Sankey, Y. Terazono, C. Herrero, D. Gust, T. A. Moore, A. L. Moore, and S. M. Lindsay. Electronic decay constant of carotenoid polyenes from single-molecule measurements. *J. Am. Chem. Soc.*, 127:1384–1385, 2005.

[204] J. He, F. Chen, P. A. Liddell, J. Andreasson, S. D. Straight, D. Gust, T. A. Moore, A. L. Moore, J. Li, O. F. Sankey, and S. M. Lindsay. Switching of a photochromic molecule on gold electrodes: single-molecule measurements. *Nanotechnology*, 16:695–702, 2005.

[205] Y. Q. Xue and M. A. Ratner. Theoretical principles of single-molecule electronics: A chemical and mesoscopic view. *Int. J. Quantum Chem.*, 102:911–924, 2005.

[206] J. He, O. Sankey, M. Lee, N. J. Tao, X. L. Li, and S. Lindsay. Measuring single molecule conductance with break junctions. *Faraday Discuss.*, 131:145–154, 2006.

[207] S. M. Lindsay. Molecular wires and devices: Advances and issues. *Faraday Discuss.*, 131:403–409, 2006.

[208] S. M. Lindsay and M. A. Ratner. Molecular transport junctions: Clearing mists. *Adv. Mater.*, 19:23–31, 2007.

[209] J. G. Kushmerick, J. Lazorcik, C. H. Patterson, R. Shashidhar, D. S. Seferos, and G. C. Bazan. Vibronic contributions to charge transport across molecular junctions. *Nano Lett.*, 4:639–642, 2004.

[210] T. N. Todorov, J. Hoekstra, and A. P. Sutton. Current-induced forces in atomic-scale conductors. *Philos. Mag. B-Phys. Condens. Matter Stat. Mech. Electron. Opt. Magn. Prop.*, 80:421–455, 2000.

[211] A. Troisi, M. A. Ratner, and A. Nitzan. Vibronic effects in off-resonant molecular wire conduction. *J. Chem. Phys.*, 118:6072–6082, 2003.

[212] A. Troisi and M. A. Ratner. Modeling the inelastic electron tunneling spectra of molecular wire junctions. *Phys. Rev. B*, 72:033408, 2005.

[213] J. K. Viljas, J. C. Cuevas, F. Pauly, and M. Hafner. Electron-vibration interaction in transport through atomic gold wires. *Phys. Rev. B*, 72:245415, 2005.

[214] M. Galperin, M. A. Ratner, and A. Nitzan. Inelastic electron tunneling spectroscopy in molecular junctions: Peaks and dips. *J. Chem. Phys.*, 121:11965–11979, 2004.

[215] T. Frederiksen, M. Brandbyge, N. Lorente, and A. P. Jauho. Inelastic scattering and local heating in atomic gold wires. *Phys. Rev. Lett.*, 93:256601, 2004.

[216] M. Paulsson, T. Frederiksen, and M. Brandbyge. Inelastic transport through molecules: Comparing first-principles calculations to experiments. *Nano Lett.*, 6:258–262, 2006.

[217] M. Galperin, A. Nitzan, and M. A. Ratner. Resonant inelastic tunneling in molecular junctions. *Phys. Rev. B*, 73:045314, 2006.

[218] T. Frederiksen, M. Paulsson, M. Brandbyge, and A. P. Jauho. Inelastic transport theory from first principles: Methodology and application to nanoscale devices. *Phys. Rev. B*, 75:205413, 2007.

[219] H. J. Choi and J. Ihm. *Ab initio* pseudopotential method for the calculation of conductance in quantum wires. *Phys. Rev. B*, 59:2267–2275, 1999.

[220] J. K. Tomfohr and O. F. Sankey. Complex band structure, decay lengths, and fermi level alignment in simple molecular electronic systems. *Phys. Rev. B*, 65:245105, 2002.

[221] J. K. Tomfohr and O. F. Sankey. Simple estimates of the electron transport properties of molecules. *Phys. Status Solidi B-Basic Res.*, 233:59–69, 2002.

[222] H. J. Choi, J. Ihm, S. G. Louie, and M. L. Cohen. Defects, quasibound states, and quantum conductance in metallic carbon nanotubes. *Phys. Rev. Lett.*, 84:2917–2920, 2000.

[223] K. Stokbro, J. Taylor, M. Brandbyge, J. L. Mozos, and P. Ordejon. Theoretical study of the nonlinear conductance of di-thiol benzene coupled to Au(111) surfaces via thiol and thiolate bonds. *Comput. Mater. Sci.*, 27:151–160, 2003.

[224] K. Tagami and M. Tsukada. A novel viewpoint for source-drain driven current inside triangular nanographene: close relationship with magnetic current. *J. Surf. Sci. Nanotech.*, 2:205, 2004.

[225] S. Iijima. Helical microtubules of graphitic carbon. *Nature*, 354:56–58, 1991.

[226] S. Latil, S. Roche, D. Mayou, and J. C. Charlier. Mesoscopic transport in chemically doped carbon nanotubes. *Phys. Rev. Lett.*, 92:256805, 2004.

[227] Y. S. Lee, M. B. Nardelli, and N. Marzari. Band structure and quantum conductance of nanostructures from maximally localized Wannier functions: The case of functionalized carbon nanotubes. *Phys. Rev. Lett.*, 95:076804, 2005.

[228] Y. S. Lee and N. Marzari. Cycloaddition functionalizations to preserve or control the conductance of carbon nanotubes. *Phys. Rev. Lett.*, 97:116801, 2006.

[229] J. C. Charlier, X. Blase, and S. Roche. Electronic and transport properties of nanotubes. *Rev. Mod. Phys.*, 79:677–732, 2007.

[230] N. D. Lang. Resistance of atomic wires. *Phys. Rev. B*, 52:5335, 1995.

[231] N. Sai, Zwolak M., Vignale G., and M. Di Ventra. Dynamical corrections to the DFT-LDA electron conductance in nanoscale systems. *Phys. Rev. Lett.*, 94:186810, 2005.

[232] S. Kurth, G. Stefanucci, C.-O. Almbladh, A. Rubio, and E. K. U. Gross. Time-dependent quantum transport: A practical scheme using density functional theory. *Phys. Rev. B*, 72:035308, 2005.

[233] G. Stefanucci and C.-O. Almbladh. Time-dependent quantum transport: An exact formulation based on TDDFT. *Europhys. Lett.*, 67:14, 2004.

[234] R. Baer and D. Neuhauser. *Ab initio* electrical conductance of a molecular wire. *Int. J. Quantum Chem.*, 91:524, 2003.

[235] R. Baer, T. Seideman, S. Ilani, and D. Neuhauser. *Ab initio* study of the alternating current impedance of a molecular junction. *J. Chem. Phys.*, 120:3387, 2004.

[236] C. L. Cheng, J. S. Evans, and T. Van Voorhis. Simulating molecular conductance using real-time density functional theory. *Phys. Rev. B*, 74:155112, 2006.

[237] K. Yabana, T. Nakatsukasa, J. I. Iwata, and G. F. Bertsch. Real-time, real-space implementation of the linear response time-dependent density-functional theory. *Phys. Status Solidi B-Basic Solid State Phys.*, 243:1121–1138, 2006.

[238] A. J. Heeger, S. Kivelson, J. R. Schrieffer, and W. P. Su. Solitons in conducting polymers. *Rev. Mod. Phys.*, 60:781–850, 1988.

[239] X. Lin, J. Li, E. Smela, and S. Yip. Polaron-induced conformation change in single polypyrrole chain: An intrinsic actuation mechanism. *Int. J. Quantum Chem.*, 102:980–985, 2005.

[240] X. Lin, J. Li, and S. Yip. Controlling the conformation of conjugated polymers via soliton. *Phys. Rev. Lett.*, 95:198303, 2005.

[241] F. Calvayrac, P. G. Reinhard, E. Suraud, and C. A. Ullrich. Nonlinear electron dynamics in metal clusters. *Phys. Rep.-Rev. Sec. Phys. Lett.*, 337:493–578, 2000.

[242] N. Troullier and J. L. Martins. Efficient pseudopotentials for plane-wave calculations. *Phys. Rev. B*, 43:1993–2006, 1991.

[243] J. Crank and P. Nicolson. A practical method for numerical evaluation of solutions of partial differential equations of the heat conduction type. *Proc. Cambridge Phil. Soc.*, 43:50–64, 1947.

[244] Steven E. Koonin and Dawn C. Meredith. *Computational Physics.* Addison-Wesley, Reading, Mass., 1990.

[245] A. Zangwill and P. Soven. Density-functional approach to local-field effects in finite systems: Photoabsorption in the rare gases. *Phys. Rev. A*, 21:1561–1572, 1980.

[246] M. A. L. Marques, A. Castro, and A. Rubio. Assessment of exchange-correlation functionals for the calculation of dynamical properties of small clusters in time-dependent density functional theory. *J. Chem. Phys.*, 115:3006–3014, 2001.

[247] G. Onida, L. Reining, and A. Rubio. Electronic excitations: density-functional versus many-body Green's-function approaches. *Rev. Mod. Phys.*, 74:601–659, 2002.

[248] S. P. Sinha. Ultra-Violet bands of Na_2. *Proc. Phys. Soc. A*, 62:124–130, 1949.

[249] W. R. Fredrickson and W. W. Watson. The sodium and potassium absorption bands. *Phys. Rev.*, 30:429–437, 1927.

[250] E. E. Koch and A. Otto. Optical absorption of benzene vapour for photon energies from 6 eV to 35 eV. *Chem. Phys. Lett.*, 12:476–480, 1972.

[251] B. Walker and R. Gebauer. Ultrasoft pseudopotentials in time-dependent density-functional theory. *J. Chem. Phys.*, 127:164106, 2007.

[252] B. Walker, A. M. Saitta, R. Gebauer, and S. Baroni. Efficient approach to time-dependent density-functional perturbation theory for optical spectroscopy. *Phys. Rev. Lett.*, 96:113001, 2006.

[253] Rudolf Ernst Peierls. *Quantum Theory of Solids.* Oxford University Press, Oxford, 1955.

[254] L. Hedin. New method for calculating the one-particle Green's function with application to the electron-gas problem. *Phys. Rev.*, 139:A796–A823, 1965.

[255] M. S. Hybertsen and S. G. Louie. First-principles theory of quasiparticles: Calculation of band gaps in semiconductors and insulators. *Phys. Rev. Lett.*, 55:1418–1421, 1985.

[256] E. E. Salpeter and H. A. Bethe. A relativistic equation for bound-state problems. *Phys. Rev.*, 84:1232–1242, 1951.